Modelling and calculation for shear-driven rotating turbulence, with multiscale and directional approach

Ying Zhu

Numéro National de Thèse: 2019LYSEC002

THÈSE DE DOCTORAT DE L'UNIVERSITÉ DE LYON

opérée par

L'ÉCOLE CENTRALE DE LYON

École Doctorale MEGA (ED 162)

Mécanique, Energétique, Génie civil et Acoustique

Spécialité: Mécanique des Fluides

Soutenue le 15/05/2019 par **Ying Zhu**

Modelling and calculation for shear-driven rotating turbulence, with multiscale and directional approach

Devant le jury composé de:

Julian SCOTT	Professeur, LMFA, ECL, Ecully	Président
Susan KURIEN	Directrice de Recherche, LANL, New Mexico, USA	Rapporteure
Pierre SAGAUT	Professeur, M2P2, Marseille	Rapporteur
Benoît-Joseph GRÉA	Directeur de Recherche, CEA, DAM, Arpajon	Examinateur
Claude CAMBON	Directeur de Recherche CNRS, LMFA, ECL, Ecully	Directeur
Fabien GODEFERD	Directeur de Recherche CNRS, LMFA, ECL, Ecully	Co-directeur
Jacques MAGNAUDET	Directeur de Recherche, IMFT, Toulouse	Invité
Daniel LIVESCU	Directeur de Recherche, LANL, New Mexico, USA	Invité

Abstract

Stability and turbulence in rotating shear flows is essential in many contexts ranging from engineering—as in e.g. turbomachinery or hydraulic energy production—to geophysics and astrophysics. Apart from inhomogeneous effects which we discard in the present study, these flows are complex because they involve an anisotropic dynamics which is difficult to represent at the level of one-point statistics. In this context, the properties of these flows, such as scale-by-scale anisotropy or turbulent cascade can be studied via two-point statistical models of Homogeneous Anisotropic Turbulence (HAT), in which the distorting mean flow is represented by uniform mean velocity and density gradients, and by body forces as the Coriolis one. The context of HAT can be relevant for flows in a plane channel with spanwise rotation, or for a Taylor-Couette flow.

We propose a new model for predicting the dynamics of homogeneous sheared rotating turbulence. The model separates linear distortion effects from nonlinear turbulent dynamics, so that each contribution can be treated with an adapted model.

Our model deals with equations governing the spectral tensor of two-point second-order velocity correlations, and is developed for arbitrary mean velocity gradients with or without system rotation. The direct linear effect of mean gradients is exact in our model, whereas nonlinear effects come from two-point third-order correlations which are closed by an anisotropic EDQNM model. In the closure, the anisotropy is restricted to an expansion in terms of low-degree angular harmonics (Mons *et al.*, 2016). The present model has been validated in the linear regime, by comparison to the accurate solution of viscous Rapid Distortion Theory (vRDT), in several cases, stabilizing, destabilizing or neutral.

In contrast with pseudo-spectral DNS adapted to shear flow by Rogallo (1981) in engineering and by Lesur & Longaretti (2005) in astrophysics, the advection operator is not solved by following characteristic lines in spectral or physical space, but by an original high-order finite-difference scheme for calculating derivatives $\frac{\partial}{\partial k_i}$ with respect to the wave vector $\boldsymbol{k}$. One thus avoids mesh deformation and remeshing, thus one can easily extract angular

harmonics at any time since physical or spectral space are not distorted.

With this new approach, we are able to improve the prediction of the previous model by Mons *et al.* (2016), in which the linear resolution is questioned at large time, especially in the case without rotation.

The proposed new model is versatile since it is implemented for several cases of mean velocity gradients consistent with the homogeneity approximation. Validations have been done for several cases of plane deformations. In the case of sheared turbulence, whose modelling resists most one-point approaches and even the two-point model by Mons, we propose an adaptation of our two-point model in a new hybrid model, in which return-to-isotropy is explicitly introduced in the guise of Weinstock (2013)'s model. Predictions of the new hybrid model are extremely good.

Résumé

Les écoulements cisaillés en rotation sont fréquents en ingénierie — par exemple en turbomachines et dans la production d'énergie hydraulique — et en géophysique et astrophysique. L'étude de leurs propriétés de stabilité en lien avec la production de turbulence est donc essentielle. Dans la présente étude, nous ne considérons pas d'éventuels effets inhomogènes, et nous nous concentrons sur la complexité de la dynamique anisotrope, qui ne peut se représenter facilement par les seuls modèles statistiques en un point. La thèse porte donc sur l'étude des propriétés de la turbulence homogène anisotrope (HAT) avec champ moyen uniforme et effet Coriolis, à l'aide de modèles statistiques en deux points. Un modèle original est proposé qui permet de prédire la dynamique de la turbulence cisaillée en rotation, et sépare les effets de déformation linéaire de la dynamique turbulente non linéaire, afin de proposer un traitement adapté pour chaque contribution.

Le modèle proposé porte sur les équations qui régissent l'évolution du tenseur spectral du second ordre des corrélations de vitesse en deux points. Il permet d'aborder les gradients de vitesse moyenne arbitraires, avec ou sans rotation d'ensemble du système. L'effet direct linéaire des gradients moyens est exact dans le modèle, alors que les effets non linéaires constitués des corrélations d'ordre trois en deux points sont fermés par un modèle anisotrope de type EDQNM. Dans ce modèle de fermeture, l'anisotropie est restreinte à un développement tronqué en termes d'harmoniques angulaires d'ordre bas Mons *et al.* (2016). Notre nouveau modèle est validé pour le régime linéaire par comparaison à une solution trés précise de distorsion rapide visqueuse (vRDT) dans plusieurs cas de cisaillement: stabilisant, déstabilisant ou neutre.

Le modèle diffère des approches de simulation numérique directe (DNS) pseudo-spectrale pour les écoulements cisaillés proposées par Rogallo (1981) en ingénierie et par Lesur & Longaretti (2005) en astrophysique, en ce que l'opérateur de convection n'est pas résolu en suivant les courbes caractéristiques moyennes spectrales ou physiques, mais grâce à un schéma original de type différences finies d'ordre élevé qui permet de calculer les dérivées $\frac{\partial}{\partial k_i}$

par rapport au vecteur d'onde $\boldsymbol{k}$. On évite ainsi la déformation du maillage et l'obligation de remailler, ce qui autorise l'obtention aisée des harmoniques angulaires à chaque instant, grâce au fait que l'espace physique ou spectral n'est pas déformé.

La capacité de prédiction de cette nouvelle approche est significativement améliorée par rapport au modèle de Mons *et al.* (2016), pour lequel la solution linéaire peut être remise en cause à grand temps d'évolution, particulièrement pour le cas non tournant. Le nouveau modèle est suffisamment universel puisqu'il est implémenté pour plusieurs cas de gradients de vitesse moyenne compatibles avec l'approximation homogène. Les validations ont notamment été réalisées dans des cas de déformation plane. Pour la turbulence cisaillée, dont la modélisation est demeurée jusqu'à présent un point dur des approches en un point et aussi de l'approche en deux points de Mons, nous proposons une version adaptée de notre modèle en deux points, en l'hybridant avec un modèle de retour à l'isotropie proposé par Weinstock (2013). Ce nouveau modèle hybride pour la turbulence cisaillée fournit des résultats extrêmement satisfaisants.

Acknowledgements

When I was a child, I was asked what to do when growing up. My answer was to be a scientist, although I had no idea of science and scientists at that time. Fortunately, I have met many good mentors and friends along the way.

My first Chinese teacher, a sweet old lady, always encouraged me to be the best. I am very grateful to all the mathematics and physics teachers in my primary and secondary school years, who opened my curiosity about the scientific world and the addiction to the laws themselves and the exploration for the laws. Particularly, Mr. Wu, my math teacher in high school, the experience of taking part in the mathematical Olympiad for two years under his guidance, was an adventure trip to pursue the intellectual limit. And Mrs. Wang, my physics teacher in high school, she always emphasized that we should not take physics phenomena for granted and we must analyze everything with rational thinking. These maybe the first scientific skills and scientific literacy training I received.

My high school days had a great influence on me. On the one hand, my fervent curiosity at that time made me hungry for all knowledge and acquired good general knowledge education. At the same time, I also developed a strong interest in social sciences, such as history and philosophy. On the other hand, I have met some of the most important friends in my life, Meiling, Shixi, Xiaodan, Peng Tian, my history teacher, Mrs. Zhang, and Jing Zhang, who helped me polish this short acknowledgement. Thank them for their accompany and encouragement all the time. To the friendship of more than ten years!

Thanks to Professor Wei, who taught calculus in college, her class was always so great. She also made me realize that scientists should have their own manners, sense of responsibility and attitudes towards society. Thanks to Professor Jing, in the second year of fluid mechanics class, I first heard about 'turbulence'. The teacher said, this is a unsolved mystery of physics, hopefully that some of the students will be able to make a contribution to this in the future. From then on, sowed a seed in my heart.

One year after college, the work as an aeronautical engineer made me realize that if I didn't make any change, I would really say goodbye to my dream of being a scientist. Thanks to my graduate supervisor, Professor Fang, who helped me prepare for future doctoral research career, including basic turbulence theory and numerical simulation techniques, and also the application for the doctoral position.

I am so lucky to have such two excellent doctoral supervisors. Mr. Claude Cambon and Mr. Godeferd. They fully respect my research interests and never force me to do the work that I do not want to do. Mr. Cambon is the role model for scientists in my mind. He is diligent, intelligent, dedicated and modest, cautious about research, but so easy-going. I am very proud to be his last doctoral student. Mr. Godeferd, thank him for all the support and convenience he has offered me in the working environment, and for teaching me some basic skills of researchers, such as how to make presentations and how to write scientific articles word by word. The two supervisors always try their best to offer me all the possible help, not only on knowledge and skills, but also on how to be a researcher.

Lots of thanks to Professor Sagaut, who promised to be one of the reporters for my thesis, in his busy schedule. Also lots of thanks to Doctor Kurien, who is the other reporter. I am also very grateful to Doctor Livescu, Doctor Magnaudet and Doctor Gréa for being a member of the jury. My special thanks to Professor Scott for his efforts of being the chairman.

This nearly three years of life in Ecully is calm, easy, sometimes boring. Thanks to the company of Yi Hui, Jianzhao, Yifan and all other friends. Special thanks to Haining and Zecong in the next office. In the past three years, we have been sharing knowledge, technology and standpoints, supporting each other and learning from each other. Especially during the period when I was writing my thesis, they took good care of my life. I will never forget the colorful clouds in Lyon that I looked upon after work. I will also never forget the nights when the three of us came home from the laboratory with moonlight.

Pay tribute to my idol Faye Wong, pay tribute to “Friends” and “Crayon Shinchan”, pay tribute to all the people who created beautiful music. These not only enrich my entertainment, but also enrich my life. Special thanks to Sijia Yu for being a best friend of each other for more than ten years, as a confidant, sometimes like family, sometimes like a soulmate. Wish her a successful completion of her doctoral career. Thanks to my brother and sister-in-law for taking care of our parents, so that I can concentrate on my own research. I have the best brother in the world. He not only supports me in pursuing self but also is the original guide of my cognition of the world and my literature enlightenment teacher. Dedicate this thesis to my parents, even if they may not understand a word. They gave me life and wisdom. They support me with love and teach me to be a good person. They are always the most important people in the world to me.

Thank all the people who have helped me, inspired me and made me feel the beauty of this world. I know that finishing my PhD is just the beginning, and curiosity and scientific exploration are endless. Finally, attached my two favorite quotes:

> "Be the change that you wish to see in the world."—Mahatma Gandhi
> "spur with long accumulation."—Chinese idiom

Ecully
November 25th, 2018

Contents

Nomenclature

Abbreviations

1D	One-Dimensional
3D	Three-Dimensional
DNS	Direct Numerical Simulation
EDQNM	Eddy-Damped Quasi-Normal Markovian
FDS	Finite Difference Scheme
FFT	Fast Fourier Transform
HAT	Homogeneous Anisotropic Turbulence
HIT	Homogeneous Isotropic Turbulence
LRR	The model developed by B. E. Launder, G. J. Reece and W. Rodi
MCS	The model developed by Mons, Cambon and Sagaut
MHD	MagnetoHydroDynamics
MPI	Message Passing Interface
OpenMP	Open Multi-Processing
RANS	Reynolds Averaged Navier-Stokes
RDT	Rapid Distortion Theory
RK4	Fourth-order Runge-Kutta
RSM	Reynolds Stress Models
RST	Reynolds Stress Tensor
RTI	Return-To-Isotropy
RTT	Rayleigh-Taylor Turbulence
SLT	Spectral Linear Theory
SPMD	Single Program Multiple Data
SSH	Scalar spherical harmonics
USHT	Unstable Stratified Homogeneous Turbulence

VSHF Vertically Sheared Horizontal Flow

VSH Vectorial spherical harmonics

ZCG The model developed by Zhu, Cambon and Godeferd

Symbols

$*$	convolution
$\boldsymbol{\Omega}$	system angular velocity
$\boldsymbol{F}$	body force per mass unit
$\boldsymbol{f}$	fluctuating body force per mass unit
$\boldsymbol{W}$	mean vorticity
$\delta(x)$	Dirac function
δ_{ij}	Kronecker delta
ϵ_{ijn}	permutation tensor
$\hbar(\boldsymbol{r})$	two-point helicity correlation
$\imath$	imaginary root
$\mathcal{K}$	turbulent kinetic energy
$\mathcal{R}_{ij}$	Reynolds Stress Tensor
$\hat{\mathbf{R}}$	two-point second-order spectral velocity correlation tensor
$\mathbf{A}$	mean-velocity gradient
$\mathbf{F}$	Cauchy matrix
$\mathbf{G}$	Green's function tensor
$\mathbf{R}$	two-point second-order velocity correlation tensor
$\mathbf{S}$	symmetric part of mean-velocity gradient
∇^2	Laplace operator
ε	viscous dissipation rate of kinetic energy
B	Bradshaw number
h	turbulence helicity
k	wave number
P	static pressure
p	fluctuating pressure
R	ratio of system vorticity to shear-induced vorticity
S	mean shear rate
t	time
$\boldsymbol{x}$	position vector
$\hat{p}$	spectral pressure
$\boldsymbol{U}$	velocity
$\langle\cdot\rangle$	ensemble average
$\langle\boldsymbol{U}\rangle$	mean velocity

$\hat{\boldsymbol{u}}$	spectral velocity
$\boldsymbol{u}$	fluctuating velocity
$(.)$	tensorial inner product

List of Figures

List of Tables

Introduction

“Turbulence is the last unsolved problem in classical physics”, this has been repeated for so many times since more than half a century ago. Until today, no scientist can say that this phenomenon has been captured completely. Turbulence is still an attractive mystery for human beings, although most people have no idea what turbulence is and how turbulence influences their daily lives, or even the remote universe. Indeed, it is so difficult to understand, to predict, even to control turbulence, for its extreme non linearity that may be beyond the scope of today's mathematics. Some researchers quit this field, while fortunately, some others persist with their work and there are always new researchers starting to devote themselves to this problem. Turbulence may be not one of the hottest science topics at present, but I believe that the studies on turbulence will never be ‘out of fashion’. Anyway, being more and more close to the ‘truth’ is one of the most attractive aspects of science.

In the past century, we have already made amazing advances in our knowledge. Many researchers have contributed much on applied fluid mechanics. They have changed our lifestyles, such as in transportation industry, in the energy industry, even the way of making war, by experiments and numerical simulations on real flows. At the same time, some scientists work on turbulent theories with advanced mathematics, in order to figure out the fundamental physical mechanisms, and they have pictured this phenomenon more and more vividly.

It is a pity that there is still a huge gap between turbulent theories and practical applications. The theories, usually developed in the canonical case of homogeneous isotropic turbulence (**HIT**), are difficult to help build more universal practical models for complicated real flows in engineering, environmental sciences, astrophysics and geophysics. Thanks to the rapid development of supercomputers and the progresses on numerical methods, the theories are able to describe more complex flows with small computational cost compared to direct numerical simulation (**DNS**). The first milestone towards real flows is perhaps the breakthrough from isotropic turbulence to anisotropic turbulence. Our research group has been devoted to homogeneous anisotropic turbulence (**HAT**) for decades and has achieved remarkable results. It is too ambitious to say we are attempting at the methodology on how to use theoretical results to improve practical models, but we are indeed trying to build a systems approach to capture the feedback from the turbulent field to the averaged field, possibly initiated by this thesis work.

The thesis is structured as follows.

In chapter 1, we introduce our systems approach to turbulence research, disentangling the modeling levels based on consideration of three interactions between the mean flow and fluctuating flow. The classical spectral theory with two-point approach for homogeneous turbulent flow is recalled, including the linear spectral theory and nonlinear models. Single-point models are revisited to capture the counteraction to mean flow from the so-called turbulence field, and the general results of stability analysis for homogeneous rotating shear turbulence in linear limit are presented.

We follow the footsteps in our research group to model shear-driven homogeneous anisotropic turbulence in chapter 2. The three-dimensional (**3D**) spectral model EDQNM-1 (Eddy-Damped Quasi-Normal Markovian) and the spherically-averaged model by Mons *et al.* (2016) (denoted as **MCS** for Mons, Cambon & Sagaut hereinafter) is revisited. We propose the present model in this thesis work, retaining exact 3D linear operators as in EDQNM-1 and simplified nonlinear closure as in MCS, and a hybrid model is proposed partly combined with Weinstock's model that has forced return-to-isotropy (**RTI**) mechanism.

The numerical simulation method for the present model is introduced in chapter 3. A straightforward numerical method with finite difference scheme (**FDS**) is employed on advection terms rather than conventional characteristic method, in order to improve the computational accuracy and develop the algorithm compatibility to arbitrary mean flow velocity gradients. All the details on numerical implementation and some preliminary tests are exhibited.

The validation of the present model is performed in chapter 4, started by considering different flows in both the inviscid and viscous linear limits. The results are compared with those from Salhi *et al.* (2014), which are obtained by the characteristics technique, and with results of MCS. We compare fully nonlinear results provided by different models and non-linear closure techniques: the proposed model by Zhu, Cambon and Godeferd (**ZCG**), the proposed hybrid model, the MCS model, Weinstock's model, and direct numerical simulations by Salhi *et al.* (2014). All the comparisons show excellent agreement between present model and linear spectral theory (**SLT**) in linear limit, and also remarkable improvements compared to MCS both in linear limit and with fully nonlinear terms. The hybrid model achieved final exponential growth of turbulent kinetic energy correctly in the case without system rotation.

In chapter 5, we introduce the SO^3-type decompositions for scalar in form of tensorial expansions and spherical harmonics decomposition. The equivalency of the tensorial expansion and spherical harmonics decomposition is validated in homogeneous rotating sheared flow. In linear limit, we observe the effects of 'stropholysis' term. The fully nonlinear results are calculated with hybrid model, and the interaction between linear and nonlinear mechanisms are studied in the view of evolution of anisotropy in high degrees.

The shear flow without system rotation is the most challenging case to model in this thesis. Further analysis on pure shear flow is continued in chapter 6. The essential difference and connections among ZCG, Weinstock's model and the hybrid model, even the isotropic nonlinear transfer terms are discussed. We exploit the impacts of various initial conditions and preliminary Reynolds number effects are obtained as well.

This PhD work has led to several conference articles and journal articles, published, submitted or in preparation:

- Ying Zhu, Claude Cambon, and Fabien Godeferd. "Rotating shear-driven turbulent flows: Towards a spectral model with angle-dependent linear interactions." S31-Turbulence (2017).

- Ying Zhu, Claude Cambon, and Fabien Godeferd. "A new model for rotating shear flow: from the rotating channel to geophysics and astrophysics." ETMM12 (2018).

- Ying Zhu, C. Cambon, F. S. Godeferd and A. Salhi. "Nonlinear spectral model for rotating sheared turbulence."*Journal of Fluid Mechanics* 866 (2019): 5-32.

- Y. Zhu, C. Cambon and F. S. Godeferd. "High degree anisotropy analysis with spherical harmonics decomposition on homogeneous rotating shear turbulence". In preparation.

- Y. Zhu, C. Cambon and F. S. Godeferd. "Study on dynamics of homogeneous flow with mean shear based on fully non linear spectral model". In preparation.

- Y. Zhu, C. Cambon and F. S. Godeferd. "Improvements on single-point model for rotating shear flow with fully non linear spectral model". In preparation.

- Y. Zhu, C. Cambon and F. S. Godeferd. "Mixed finite difference and pseudo-spectral method for DNS in homogeneous turbulent flow". In preparation.

In this thesis, vectors are denoted with bold italic font, such as $\boldsymbol{k}$, and tensors and matrices are denoted with bold sloping sans-serif font, such as $\boldsymbol{\mathsf{A}}$, while their components are denoted with italic font as k_i and A_{ij}. Colored boxes are used for some short supplementation of the main body or detailed discussions.

Chapter 1

Systems approach to turbulence modeling for homogeneous rotating shear flow and beyond

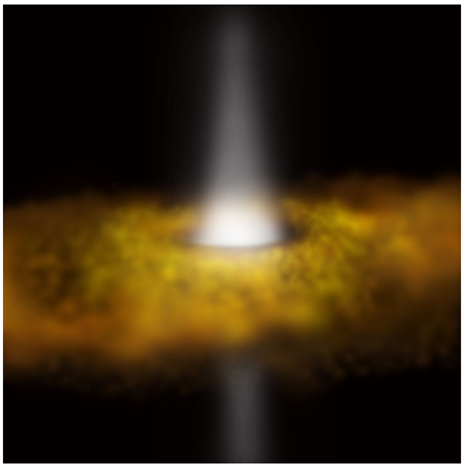

Artist's view of a star with accretion disk. From Wikipedia.

Turbulence and stability in rotating shear flows is essential in many different contexts ranging from engineering as in e.g. turbomachinery or hydroelectric power to geophysics and astrophysics. Among various combinations of mean flow gradients and system rotation, the case with mean plane shear rotating in spanwise direction is well-known for its widespread applications. Stabilization and destabilization of turbulence are found in these flows depending on cyclonic or anticyclonic asymmetries of mean shear vorticity and system vorticity, for instance in the experimental study of rotating plane channel flow by Johnston *et al.* (1972). Similar effects are also exhibited in rotating Couette flows (Hiwatashi *et al.*, 2007) and rotating wakes (Dong *et al.*, 2007; Perret *et al.*, 2006) with the interaction of mean shear and Coriolis force. Therefore, modelling and investigating the dynamics of rotating shear turbulent flow with mean plane shear rotating in spanwise direction is the principle application of the proposed model in this thesis.

In this chapter, we firstly introduce our systems approach to turbulence research, disentangling the modeling levels based on consideration of three interactions between the mean flow and fluctuating flow. Following the directions given by this approach, discarding the feedback from fluctuation, we zoom in the scope to homogeneous turbulence so that the classical spectral theory with two-point approach is recalled. The linear spectral theory focuses on the influence on fluctuation from mean field, whereas the nonlinear models attempt to describe the interaction between fluctuation and itself. Then, single-point models are revisited to capture the counteraction to mean flow from the so-called turbulence field. The connection among mathematical hypotheses, physical implications and relevance to real flows is specified. Then, the general results of stability analysis for homogeneous rotating shear turbulence in linear limit is presented. Finally, I introduce the original proposals for the thesis work.

1.1 The systems approach to turbulence

We start with the Navier-Stokes equations for incompressible flow,

$$\frac{\partial U_i}{\partial t} + U_j \frac{\partial U_i}{\partial x_j} = -\frac{\partial P}{\partial x_i} + \nu \frac{\partial^2 U_i}{\partial x_j x_j} + F_i \tag{1.1a}$$

$$\frac{\partial U_i}{\partial x_i} = 0, \tag{1.1b}$$

where t is time, $\boldsymbol{x}$ is position vector, $\boldsymbol{U} = \boldsymbol{U}(\boldsymbol{x}, t)$ is velocity, ν is kinetic viscosity, $P = P(\boldsymbol{x}, t)$ is static pressure (divided by density) and $\boldsymbol{F} = \boldsymbol{F}(\boldsymbol{x}, t)$ is body force per unit mass. Eq.(1.1a) and Eq.(1.1b) are yielded from momentum conservation, mass conservation and incompressibility condition respectively.

We then split the velocity and pressure fields into mean and fluctuating components. From Eq.(1.1) one can derive the following evolution equations for the mean field,

$$\frac{\partial \langle U_i \rangle}{\partial t} + \langle U_j \rangle \frac{\partial \langle U_i \rangle}{\partial x_j} = -\frac{\partial \langle P \rangle}{\partial x_i} + \nu \frac{\partial^2 \langle U_i \rangle}{\partial x_j x_j} - \underbrace{\frac{\partial \langle u_i u_j \rangle}{\partial x_j}}_{\text{Reynolds stress term}} + \langle F_i \rangle \tag{1.2a}$$

$$\frac{\partial \langle U_i \rangle}{\partial x_i} = 0, \tag{1.2b}$$

and the equations for the fluctuating field,

$$\frac{\partial u_i}{\partial t} + \langle U_j \rangle \frac{\partial u_i}{\partial x_j} + u_j \frac{\partial \langle U_i \rangle}{\partial x_j} = \underbrace{\frac{\partial}{\partial x_j} \left(\langle u_i u_j \rangle - u_i u_j \right)}_{\text{Nonlinear term}} \overbrace{-\frac{\partial p}{\partial x_i}}^{\text{Pressure term}} + \underbrace{\nu \frac{\partial^2 u_i}{\partial x_j x_j}}_{\text{Viscous term}} + f_i \tag{1.3a}$$

$$\frac{\partial u_i}{\partial x_i} = 0, \tag{1.3b}$$

with supposition that the field is good enough in mathematical quality to exchange derivation and ensemble average operator $\langle \cdot \rangle$. $\langle \boldsymbol{U} \rangle$, $\langle P \rangle$ and $\langle \boldsymbol{F} \rangle$ are the mean velocity, static pressure and body force, while $\boldsymbol{u}$, p and $\boldsymbol{f}$ are the corresponding fluctuating quantities, usually interpreted as representing turbulence (Sagaut & Cambon, 2018). Eq.(1.2) is usually named as Reynolds-averaged Navier-Stokes (**RANS**) equations. Neither the Reynolds-averaged equations nor the fluctuating equations are closed because of the existence of Reynolds stress term and nonlinear term, which is one of the prominent characteristic for turbulence research.

The equations (1.2) and (1.3) show us the complexity of turbulent interplay clearly. Reynolds stress term in the mean equations reflects the influence from fluctuations to mean field, while the counteraction arises in the fluctuation equations with opposite sign. The

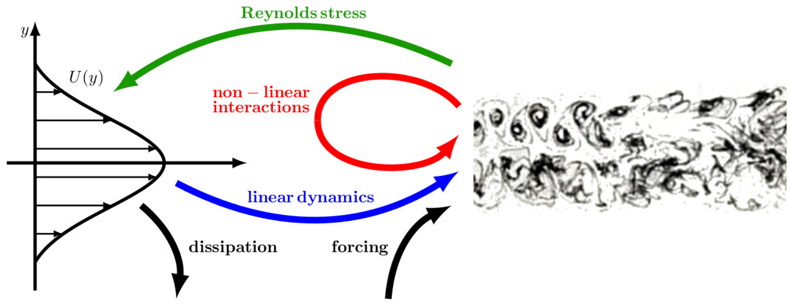

Figure 1.1: Illustration of the three interactions between mean flow and fluctuation. Courtesy from Tomas Tangarife and Freddy Bouchet, ENS-Lyon.

situation in Eq.(1.3) is more complex indeed. $\langle U_j \rangle \dfrac{\partial u_i}{\partial x_j}$ and $u_j \dfrac{\partial \langle U_i \rangle}{\partial x_j}$ are the linear terms of advection and production induced by mean flow, whereas $\dfrac{\partial}{\partial x_j} \left(\langle u_i u_j \rangle - u_i u_j \right)$ represents the nonlinear interaction between fluctuation and itself.

It is worthwhile to mention the pressure term here. Taking the divergence of equation (1.3) and neglecting the body force leads to

$$\nabla^2 p = -\frac{\partial^2}{\partial x_i x_j} \left(u_i \langle U_j \rangle + \langle U_i \rangle u_j + u_i u_j - \langle u_i u_j \rangle \right), \tag{1.4}$$

in which ∇^2 is the Laplace operator. The Poisson equation is obtained with incompressibility constraint. The solution is based on a Green's function expressing p in terms of an integral over the whole domain and on all boundaries, which gathers both linear and nonlinear, nonlocal contribution from fluctuation. The intrinsic feature of nonlocality resulted from incompressibility makes turbulence modeling even harder.

It is generally accepted that, for theoretical study of turbulence, taking account all the interactions at once is not practical. A feasible strategy is to investigate single interaction separately for the sake of simplicity in order to observe fundamental physical mechanisms firstly. The next step is to couple different interactions together to describe more complex flows. Classical mathematical hypotheses have specific physical implications, e.g. homogeneous isotropic turbulence focuses on only the interaction between fluctuation and itself, while the rapid distortion theory (**RDT**) observes the linear action on fluctuation from mean flow, and single-point models mainly study the evolution of Reynolds Stress Tensor (**RST**) $\langle u_i u_j \rangle$ which gives the feedback from fluctuations to mean flow. One could trace the strategy clearly in the following three sections with the review of previous study on rotating shear turbulent flow.

The systems approach to turbulence is illustrated by studies that extend the classical hydrodynamic stability analysis to rather complex flow. The best examples are for planetary circulation and for near-wall turbulence (Smits *et al.*, 2011), as illustrated by figure 1.1, and will be re-discussed further. The Reynolds decomposition is essential, and the mean flow is not known a priori, in contrast with the base flow in hydrodynamic stability. As in conventional single-point techniques in RANS, the three interactions are relevant, but the fluctuating flow is described with a multiscale approach, possibly identifying its main dynamical modes. In this sense, the linear interaction (mean to fluctuation) is close to what is referred to 'Rapid Distortion Theory', but the feedback interaction (fluctuation to mean) is important, in contrast with *homogeneous* RDT. In these approaches to complex flows, however, the third purely non-linear interaction (fluctuation to fluctuation) is very rough, assuming effective diffusivity, as in $\mathcal{K}$-ε models.

As an example, the scheme in 1.1 illustrates some quasi-2D flows in planetary circulation: the mean flow is identified by zonal averaging, resulting in a (mean) meridional profile of zonal velocity. (Incidentally, the arrows 'dissipation' and 'forcing' ought to be exchanged). The interaction from mean flow to fluctuation, the feedback from fluctuation to mean flow and the interaction between fluctuation and itself are represented in blue, green and red respectively. The counterpart of RDT is the so-called *adiabatic reduction.* It is difficult now to move from our homogeneous approach for shear-driven flows to such a complete systems approach in shear-driven turbulence, but we have the very encouraging study in our team of buoyancy-driven flows, collaboration with CEA (French atomic center) from USHT (**USHT**) to developed, weakly inhomogeneous Rayleigh-Taylor turbulence (**RTT**). In the last case, the turbulent mixing zone resulting from the vertical mixing of heavy fluid and light fluid has a typical finite length scale, the mean flow is obtained by horizontal averaging, and the feed-back (green interaction) results from the vertical buoyancy flux: it renders possible a time-evolution of the stratification frequency, that is a constant fixed a priori in USHT. The rapid acceleration model (Gréa, 2013) ignores the explicit nonlinear interaction, but linear analysis and emergence of dominant modes of fluctuation are affected by the feed-back. Finally, the most complete analysis reintroduces in RTT the nonlinear spectral model by anisotropic multimodal EDQNM inherited from USHT. Our research group, the best example in progress is not yet on shear-driven flows, but on buoyancy-driven flows (Cambon, 2001; Cambon *et al.*, 2017): unstable stratified turbulence, from the homogeneous case with specified N (stratification frequency) to Rayleigh-Taylor turbulence with variable N and feedback from the gradient of vertical concentration flux, see figure 1.1

1.2 Homogeneous rotating shear turbulence in astrophysics and engineering

1.2.1 Homogeneity assumption and mean flow velocity gradient tensor

The common background in this thesis is to consider the mean flow filling all the space with space-uniform velocity gradient (see Craik & Criminale, 1986), which is consistent with statistical homogeneity (Batchelor & Proudman, 1954) that all the averaged quantities are spatially uniform. In addition, Craya (1957) gave a very complete statistical approach, with equations for two-point second-order velocity correlations and for three-point third order correlations, in this HAT context. It is important to point out that statistical homogeneity is restricted to *fluctuations* and has no sense for the mean flow. Correspondingly, the trace free mean velocity-gradient tensor can be represented as

$$\frac{\partial \langle U_i \rangle}{\partial x_j} = A_{ij}(t) \tag{1.5a}$$

$$\text{and} \quad u_i(\boldsymbol{x}) = U_i(\boldsymbol{x}) - A_{ij}(t)x_j, \tag{1.5b}$$

in which the explicit time dependency of $\boldsymbol{A}$ is omitted thereafter for convenience. In rotational steady flow ($\boldsymbol{A}$ is dissymmetric and time-independent), $\boldsymbol{A}$ can be written as

$$\boldsymbol{A} = \begin{bmatrix} 0 & D-W & 0 \\ D+W & 0 & 0 \\ 0 & 0 & 0 \end{bmatrix}, \tag{1.6}$$

with appropriate axes, where $D, W \geq 0$. This form is usually applied in linear analysis with combination of vorticity $2W$ and irrotational strain D (The flow is called irrotational when $\boldsymbol{A}$ is symmetric) (see Sagaut & Cambon, 2018): For $D > W$, the mean flow streamlines are open and hyperbolic, while the flow is strain dominated; for $D < W$, the mean flow streamlines are closed and elliptic about the stagnation point at the origin, and the flow is vorticity dominated; the limit case, $D = W$, corresponds to flow with mean plan shear. Equivalently,

$$A_{ij} = S_{ij} + \frac{1}{2}\epsilon_{imj}W_m, \tag{1.7}$$

combines contributions from strain S_{ij}, the symmetric part, and mean vorticity $\boldsymbol{W}$ (vector $\boldsymbol{W}$, different from preceding scalar W), the antisymmetric part, where ϵ_{imj} represents the permutation tensor. With this decomposition, various combinations of mean strain and mean vorticity can be considered. In addition, the whole flow can be seen in a rotating frame with angular velocity $\boldsymbol{\Omega}$ for various applications, such as rotating shear or precessing flows.

On account of the homogeneity simplification, all the statistical quantities are spatially uniform, so that

$$\frac{\partial\langle u_i u_j\rangle}{\partial x_j} = 0. \tag{1.8}$$

That means the context of homogeneous anisotropic turbulence drops the Reynolds stress tensor in both Eq.(1.2) and (1.3). In other words, there is no feedback from fluctuating field to mean flow while the linear action by mean flow on fluctuations remains.

In addition with the mean velocity-gradient tensor $\dfrac{\partial\langle U_i\rangle}{\partial x_j} = A_{ij}(t)$ and the Coriolis force $\boldsymbol{f} = -2\boldsymbol{\Omega}\times\boldsymbol{u}$ introduced by system rotation $\boldsymbol{\Omega}$ (centrifugal force $-\boldsymbol{\Omega}\times(\boldsymbol{\Omega}\times\boldsymbol{u})$ induced by frame rotation is incorporated in the pressure term), the Navier-Stokes equation for homogeneous turbulence—along with a rotating reference frame—can be investigated:

$$\frac{\partial u_i}{\partial t} + A_{ij}u_j + A_{jk}x_k\frac{\partial u_i}{\partial x_j} + 2\epsilon_{imn}\Omega_m u_n + u_j\frac{\partial u_i}{\partial x_j} = -\frac{\partial p}{\partial x_i} + \nu\frac{\partial^2 u_i}{\partial x_j x_j} \tag{1.9a}$$

$$\frac{\partial u_i}{\partial x_i} = 0, \tag{1.9b}$$

as well as the pressure equation

$$\nabla^2 p = -2A_{ij}\frac{\partial u_i}{\partial x_j} + 2\epsilon_{imn}\Omega_m\frac{\partial u_n}{\partial x_i} - \frac{\partial(u_i u_j)}{\partial x_i x_j}. \tag{1.10}$$

Eq.(1.9) illustrates that the energy is injected directly through mean velocity-gradient rather than solid body rotation of the frame for Coriolis force produces no work. It is also indicated by Eq.(1.10) that fluctuating pressure field is governed by linear operator, rotation effects and nonlinear interaction jointly.

1.2.2 Accretion disc and rotating channel flow

This simple model for spatially uniform turbulent shear flow is used in astrophysics for the study of turbulent accretion discs, which can be seen as Taylor-Couette flow (figure 1.2). According to the shearing sheet approximation by Balbus & Hawley (1998)—also called the local shearing box—the rotation rate Ω is approximately uniform and the shear rate S can be represented by differential rotation at a specific radial position r_0, namely $\Omega\sim\Omega(r_0)$ and $S = r\frac{\mathrm{d}\Omega}{\mathrm{d}r}|_{r_0}$. The simple model of homogeneous turbulent rotating shear flow is also useful in engineering for interblades flow in turbomachinery, and in geophysical flows. Figure 1.3

illustrates how the context of homogeneous anisotropic turbulence can be locally relevant for rotating channel flow, e.g. in the center region where constant mean shear rate S and uniform spanwise rotation Ω apply.

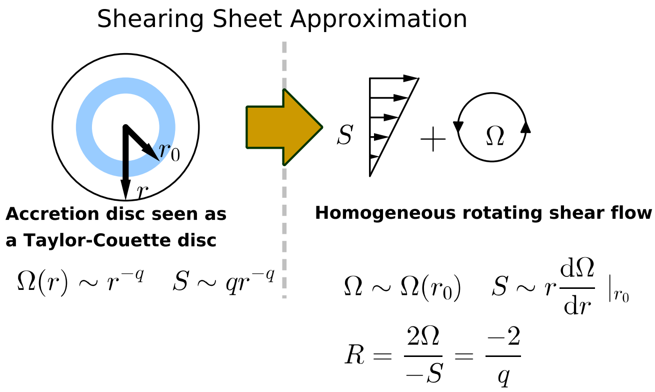

Figure 1.2: Sketch for SSA

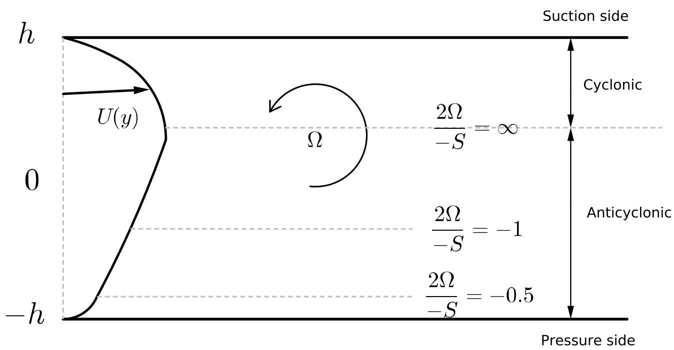

Figure 1.3: Rotating channel flow

It must be clarified that the homogeneity simplification is not only a marginal domain in the theoretical study of turbulence to discarding the feedback from fluctuating field to mean field, it has clear physical relevance on real flows, at least for linear analysis. When the region in which the mean gradient is almost constant, is restricted to a domain which is large with respect to the size of represented turbulent structures, or the time scale of mean flow is larger than that of fluctuation, the flow can be modeled as HAT, just as the geometrical simplification in accretion disc and rotating channel flow.

1.3 Spectral theory with two-point approach for homogeneous turbulence

Spectral theory with a two-point statistical approach is very popular for the study of HAT, in which the distorting mean flow is represented by uniform mean-velocity and density gradients, and by body forces as the Coriolis one (Sagaut & Cambon, 2018). Why two-point approach is preferable with respect to single-point statistics for HAT? Two main reasons are given here: Anisotropic dynamics can act differently depending on the involved length scales. However the single-point closures, e.g. the basic two-equations $\mathcal{K}-\epsilon$ model, altogether ignore the effect of rotation in the rotating shear case, while others take it into account to some extent. This is the case of the Reynolds stress models (**RSM**, e.g. Launder *et al.* (1975), or of the more sophisticated structure-based models (Kassinos *et al.*, 2001); in addition, from the point of view of linear dynamics, the passage from a two-point spectral description to a single-point one implies a loss of nonlocality in the pressure/velocity relationship in physical space. As a consequence, modeling the 'rapid' pressure-strain rate tensor in RSM equations is very difficult and partly hopeless (detailed discussion is in §1.4.1).

1.3.1 Spectral approach

Fourier transformation is a paradigmatic tool to deal with equations of homogeneous flow, with which the fluctuating velocity can be written as:

$$u_i(\boldsymbol{x},t) = \iiint \hat{u}_i(\boldsymbol{k},t)\exp\left(\imath\boldsymbol{k}\cdot\boldsymbol{x}\right)\mathrm{d}^3\boldsymbol{k}, \tag{1.11a}$$

$$\text{while}\quad \hat{u}_i(\boldsymbol{k},t) = \frac{1}{(2\pi)^3}\iiint u_i(\boldsymbol{x},t)\exp\left(-\imath\boldsymbol{k}\cdot\boldsymbol{x}\right)\mathrm{d}^3\boldsymbol{x}, \tag{1.11b}$$

where $\boldsymbol{k}$ is the wavevector in Fourier space, $\imath$ is the imaginary unit with $\imath^2 = -1$ and $\hat{u}_i(\boldsymbol{k},t)$ is the Fourier coefficient of $u_i(\boldsymbol{x},t)$ at wavevector $\boldsymbol{k}$. As we know, the classical Fourier transformation is a rather narrow class of functions which decrease sufficiently rapidly to zero in the neighborhood of infinity to ensure the existence of the Fourier integral. However, it is not the situation in homogeneous turbulence since the velocity is defined in whole space. We are not supposed to discus too much about the convergence in this thesis but to extend the classical Fourier transformation in terms of the classical generalized function, Dirac delta function($\boldsymbol{\delta}$ function different from Kronecker delta δ_{ij}) (see Sagaut & Cambon, 2018), which considerably enlarges the class of functions that could be transformed and removes many obstacles. The readers who have interests of mathematical discussion on the convergence problem could check references Lighthill (1958); Mathieu & Scott (2000). One-dimensional (**1D**) Dirac function is defined as

$$\delta(x) = \begin{cases} +\infty, & x = 0; \\ 0 & x \neq 0, \end{cases} \tag{1.12}$$

which is constrained to satisfy

$$\int_{-\infty}^{+\infty} \delta(x)\,\mathrm{d}x = 1, \tag{1.13}$$

and to the measurement property

$$\int_{-\infty}^{+\infty} f(x)\delta(x)\,\mathrm{d}x = f(0). \tag{1.14}$$

Now let us move on to the Navier-Stokes equations with Coriolis force in spectral space:

$$\frac{\partial \hat{u}_i}{\partial t} - A_{ln}k_l\frac{\partial \hat{u}_i}{\partial k_n} + A_{ij}\hat{u}_j + 2\epsilon_{imn}\Omega_m\hat{u}_n + \nu k^2\hat{u}_i = -\imath k_i\hat{p} - \imath k_j\widehat{u_i u_j} \tag{1.15a}$$

$$k_i\hat{u}_i = 0. \tag{1.15b}$$

in which k is the modulus of wavevector $\boldsymbol{k}$ and the convolution term $\widehat{u_i u_j}$ arises from multiplication of velocity in physical space. Convolution is denoted as

$$\widehat{f_1 f_2}(\boldsymbol{k}) = f_1(\boldsymbol{k}) * f_2(\boldsymbol{k}) = \iiint\limits_{\boldsymbol{p}+\boldsymbol{q}=\boldsymbol{k}} f_1(\boldsymbol{p})f_2(\boldsymbol{q})\,\mathrm{d}^3\boldsymbol{p}. \tag{1.16}$$

It is worthwhile to notice that the incompressibility condition turns into the orthogonality of spectral velocity $\hat{\boldsymbol{u}}$ and wavevector $\boldsymbol{k}$, benefiting from the derivative property of Fourier transformation. In addition, decoupled equation for spectral fluctuating pressure $\hat{p}$ can be given in follows:

$$\hat{p} = \frac{1}{k^2}\left(2\imath k_i A_{ij}\hat{u}_j + 2\imath k_i\Omega_{imn}\Omega_m\hat{u}_n - k_i k_j\widehat{u_i u_j}\right). \tag{1.17}$$

Final simplified momentum equation can be derived by plugging Eq.(1.17) into Eq. (1.15):

$$\frac{\partial \hat{u}_i}{\partial t} - A_{ln}k_l\frac{\partial \hat{u}_i}{\partial k_n} + \nu k^2\hat{u}_i + M_{in}\hat{u}_n = -\imath P_{imn}\widehat{u_m u_n}. \tag{1.18}$$

In the above equation, $M_{ij}(\boldsymbol{k},t) = (\delta_{il} - 2\alpha_i\alpha_j)\,A_{lj} + 2P_{in}\epsilon_{nlj}\Omega_l$ gathers linear distortion and pressure terms, in which δ_{ij} is Kronecker delta or represents the second-order unit tensor, $\boldsymbol{\alpha} = \frac{\boldsymbol{k}}{k}$ is the unit vector along $\boldsymbol{k}$ direction. The third-order tensor $P_{imn}(\boldsymbol{k}) = \frac{1}{2}\left(P_{im}(\boldsymbol{k}) + P_{in}(\boldsymbol{k})\right)$, where $P_{ij}(\boldsymbol{k}) = \delta_{ij} - \alpha_i\alpha_j$ is the projection normal to $\boldsymbol{k}$. It is certain that even the Navier-Stokes equation in spectral space is not closed as well.

1.3.2 Equations for spectral velocity-correlation tensor

The basic concept in two-point approach is the two-point second order velocity correlation tensor

$$R_{ij}(\boldsymbol{r},t) = \langle u_i(\boldsymbol{x},t)u_j(\boldsymbol{x}+\boldsymbol{r},t)\rangle, \tag{1.19}$$

in which the dependency of $\boldsymbol{x}$ vanishes because of statistical homogeneity. The expansion in terms of Fourier components is

$$R_{ij}(\boldsymbol{r},t) = \iiint \hat{R}_{ij}(\boldsymbol{k},t)\exp\left(\imath\boldsymbol{k}\cdot\boldsymbol{r}\right)\mathrm{d}^3\boldsymbol{k}, \tag{1.20a}$$

$$\text{while}\quad \hat{R}_i(\boldsymbol{k},t) = \frac{1}{(2\pi)^3}\iiint R_{ij}(\boldsymbol{x},t)\exp\left(-\imath\boldsymbol{k}\cdot\boldsymbol{r}\right)\mathrm{d}^3\boldsymbol{r}, \tag{1.20b}$$

in which $\hat{R}_{ij}(\boldsymbol{k},t)(\boldsymbol{k},t)$ is the Fourier counterpart of $R_{ij}(\boldsymbol{r},t)$. Following are some important properties for $\boldsymbol{R}(\boldsymbol{r},t)$ and $\hat{\boldsymbol{R}}(\boldsymbol{k},t)$:

$$R_{ij}(-\boldsymbol{r}) = R_{ji}(\boldsymbol{r}),\quad \hat{R}_{ij}(\boldsymbol{k}) = \hat{R}^*_{ij}(\boldsymbol{k}),\quad k_i\hat{R}_{ij}(\boldsymbol{k}) = \hat{R}_{ij}(\boldsymbol{k})k_j = \boldsymbol{0}. \tag{1.21}$$

Two alternative ways can be used to derive the equations for statistical quantities, e.g. the equation of $\hat{R}_{ij}$. Obtain the equation of $R_{ij}(\boldsymbol{r},t)$ from Navier-Stokes equations directly in physical space, then use the relationship in Eq. (1.20b) as in Craya (1957). Another way is to transform the fluctuating Navier-Stokes equations to Fourier space firstly, then get the final equation with the relationship

$$\hat{R}_{ij}(\boldsymbol{k},t)\delta(\boldsymbol{k}+\boldsymbol{p}) = \langle\hat{u}_i(\boldsymbol{p},t)\hat{u}_j(\boldsymbol{k},t)\rangle, \tag{1.22}$$

as in this thesis. Firstly we have

$$\frac{\partial\langle\hat{u}_i(\boldsymbol{p},t)\hat{u}_j(\boldsymbol{k},t)\rangle}{\partial t} = \delta(\boldsymbol{k}+\boldsymbol{p})\frac{\partial\hat{R}_{ij}(\boldsymbol{k},t)}{\partial t} = \underbrace{\langle\frac{\partial\hat{u}_i(\boldsymbol{p},t)}{\partial t}\hat{u}_j(\boldsymbol{k},t)\rangle}_{①} + \underbrace{\langle\hat{u}_i(\boldsymbol{p},t)\frac{\partial\hat{u}_j(\boldsymbol{k},t)}{\partial t}\rangle}_{②} \tag{1.23}$$

in which

$$\begin{aligned} ① =&\langle A_{ln}k_l\frac{\partial\hat{u}_i(\boldsymbol{p},t)}{\partial k_n}\hat{u}_j(\boldsymbol{k},t)\rangle - \langle\nu k^2\hat{u}_i(\boldsymbol{p},t)\hat{u}_j(\boldsymbol{k},t)\rangle \\ &- \langle M_{in}(\boldsymbol{k})\hat{u}_n(\boldsymbol{p},t)\hat{u}_j(\boldsymbol{k},t)\rangle + \langle ik_mP_{in}(\boldsymbol{k})\widehat{u_mu_n}(\boldsymbol{p},t)\hat{u}_j(\boldsymbol{k},t)\rangle \end{aligned} \tag{1.24a}$$

$$\begin{aligned} ② =&\langle A_{ln}k_l\hat{u}_i(\boldsymbol{p},t)\frac{\partial\hat{u}_j(\boldsymbol{k},t)}{\partial k_n}\rangle - \langle\nu k^2\hat{u}_i(\boldsymbol{p},t)\hat{u}_j(\boldsymbol{k},t)\rangle \\ &- \langle M_{jn}(\boldsymbol{k})\hat{u}_i(\boldsymbol{p},t)\hat{u}_n(\boldsymbol{k},t)\rangle - \langle ik_mP_{jn}(\boldsymbol{k})\hat{u}_i(\boldsymbol{p},t)\widehat{u_mu_n}(\boldsymbol{k},t)\rangle, \end{aligned} \tag{1.24b}$$

if $\boldsymbol{k}+\boldsymbol{p}=\mathbf{0}$. Eq.(1.18) and properties of Dirac function yield the governing equation of two-point spectral tensor,

$$\begin{aligned}&\delta(\boldsymbol{k}+\boldsymbol{p})\left(\left(\frac{\partial}{\partial t}-\lambda_{ln}k_l\frac{\partial}{\partial k_n}+2\nu k^2\right)\hat{R}_{ij}(\boldsymbol{k},t)+M_{in}(\boldsymbol{k})\hat{R}_{nj}(\boldsymbol{k},t)+M_{jn}(\boldsymbol{k})\hat{R}_{in}(\boldsymbol{k},t)\right)\\&=\langle ik_mP_{in}(\boldsymbol{k})\widehat{u_mu_n}(\boldsymbol{p},t)\hat{u}_j(\boldsymbol{k},t)\rangle-\langle ik_mP_{jn}(\boldsymbol{k})\hat{u}_i(\boldsymbol{p},t)\widehat{u_mu_n}(\boldsymbol{k},t)\rangle.\end{aligned} \tag{1.25}$$

To deal with the right-hand side of Eq.(1.25), we can define the three-point third-order correlation tensor as

$$S_{ijn}(\boldsymbol{r},\boldsymbol{s},t)=\langle u_i(\boldsymbol{x},t)u_j(\boldsymbol{x}+\boldsymbol{r},t)u_n(\boldsymbol{x}+\boldsymbol{s},t)\rangle. \tag{1.26}$$

Correspondingly, the spectral tensor is

$$\hat{S}_{ijn}(\boldsymbol{k},\boldsymbol{p},t)=\frac{1}{(2\pi)^6}\iiint\exp\left(-i\boldsymbol{p}\cdot\boldsymbol{s}\right)\,\mathrm{d}^3\boldsymbol{s}\iiint S_{ijn}(\boldsymbol{r},\boldsymbol{s},t)\exp\left(-i\boldsymbol{k}\cdot\boldsymbol{r}\right)\,\mathrm{d}^3\boldsymbol{r}, \tag{1.27}$$

and the corresponding relationship in Fourier space is

$$\delta(\boldsymbol{k}+\boldsymbol{p}+\boldsymbol{q})\hat{S}_{ijn}(\boldsymbol{k},\boldsymbol{p},t)=\imath\langle\hat{u}_i(\boldsymbol{q},t)\hat{u}_j(\boldsymbol{k},t)\hat{u}_n(\boldsymbol{p},t)\rangle. \tag{1.28}$$

On the one hand, the two-point third-order correlation could be regarded as $\boldsymbol{s}=\mathbf{0}$ in definition (1.26), which leads to the relationship between three-point third-order and two-point third-order correlations

$$\begin{aligned}&\langle u_i(\boldsymbol{x},t)u_j(\boldsymbol{x}+\boldsymbol{r},t)u_n(\boldsymbol{x},t)\rangle\\&=\iiint\left[\iiint\hat{R}_{ijn}(\boldsymbol{k},\boldsymbol{p},t)\,\mathrm{d}^3\boldsymbol{p}\right]e^{i\boldsymbol{k}\cdot\boldsymbol{r}}\,\mathrm{d}^3\boldsymbol{k},\end{aligned} \tag{1.29}$$

so that one can get

$$\mathcal{F}\left(\langle u_i(\boldsymbol{x},t)u_j(\boldsymbol{x}+\boldsymbol{r},t)u_n(\boldsymbol{x},t)\rangle\right)=\iiint\hat{R}_{ijn}(\boldsymbol{k},\boldsymbol{p},t)\,\mathrm{d}^3\boldsymbol{p}. \tag{1.30}$$

On the other hand, we can get another formula similar to equation (1.22)

$$\delta(\boldsymbol{k}+\boldsymbol{p})\mathcal{F}\left(\langle u_i(\boldsymbol{x},t)u_j(\boldsymbol{x}+\boldsymbol{r},t)u_n(\boldsymbol{x},t)\rangle\right)=\langle\widehat{u_nu_i}(\boldsymbol{p},t)\hat{u}_j(\boldsymbol{k},t)\rangle. \tag{1.31}$$

The above two equations together lead to the important relationship as follows:

$$\langle\widehat{u_nu_i}(\boldsymbol{p},t)\hat{u}_j(\boldsymbol{k},t)\rangle=\delta(\boldsymbol{k}+\boldsymbol{p})\iiint\hat{S}_{ijn}(\boldsymbol{k},\boldsymbol{p},t)\,\mathrm{d}^3\boldsymbol{p} \tag{1.32a}$$

$$\langle\widehat{u_nu_i}(\boldsymbol{k},t)\hat{u}_j(\boldsymbol{p},t)\rangle=\imath\delta(\boldsymbol{k}+\boldsymbol{p})\iiint\hat{S}^*_{ijn}(\boldsymbol{k},\boldsymbol{p},t)\,\mathrm{d}^3\boldsymbol{p}. \tag{1.32b}$$

Taking Eq.(1.32) into (1.25), the most important governing equation in two-point spectral theory is obtained as:

$$\left(\frac{\partial}{\partial t}-\lambda_{ln}k_l\frac{\partial}{\partial k_n}+2\nu k^2\right)\hat{R}_{ij}(\boldsymbol{k},t)+M_{in}(\boldsymbol{k})\hat{R}_{nj}(\boldsymbol{k},t)+M_{jn}(\boldsymbol{k})\hat{R}_{in}(\boldsymbol{k},t)=T_{ij}(\boldsymbol{k},t), \quad (1.33)$$

and

$$T_{ij}(\boldsymbol{k},t)=P_{in}(\boldsymbol{k})\tau_{nj}(\boldsymbol{k},t)+P_{jn}(\boldsymbol{k})\tau^*_{ni}(\boldsymbol{k},t)=\tau_{ij}(\boldsymbol{k},t)+\tau^*_{ji}(\boldsymbol{k},t)\underbrace{-\frac{k_ik_n}{k^2}\tau_{nj}(\boldsymbol{k},t)-\frac{k_jk_n}{k^2}\tau^*_{ni}(\boldsymbol{k},t)}_{W_{ij}(\boldsymbol{k},t)}, \quad (1.34)$$

where

$$\tau_{ij}(\boldsymbol{k},t)=ik_n\iiint\hat{S}_{ijn}(\boldsymbol{k},\boldsymbol{p},t)\,\mathrm{d}^3\boldsymbol{p}. \quad (1.35)$$

The transfer tensor $T_{ij}(\boldsymbol{k},t)$ in terms of two-point third-order correlations, gathers nonlinear triadic interactions between vectors $\boldsymbol{k}$, $\boldsymbol{p}$ and $\boldsymbol{q}$, which can form a triangle. $\tau_{ij}(\boldsymbol{k},t)+\tau^*_{ji}(\boldsymbol{k},t)$ is a 'true' transfer term with zero integral over $\boldsymbol{k}$ spheres, whereas the integral of $W_{ij}(\boldsymbol{k},t)$ over $\boldsymbol{k}$ spheres is the so-called 'slow' pressure-strain rate tensor that contains a possible return-to-isotropy mechanism. In addition, integrating the spectral kinetic energy density $\frac{1}{2}\hat{R}_{ij}$ over spheres defines the kinetic energy spectrum, similarly one can define the transfer spectrum:

$$E(k,t)=\iint_{S_{\boldsymbol{k}}}\frac{1}{2}\hat{R}_{ij}(\boldsymbol{k},t)\,\mathrm{d}^2\boldsymbol{k},\quad T(k,t)=\iint_{S_{\boldsymbol{k}}}\frac{1}{2}T_{ij}(\boldsymbol{k},t)\,\mathrm{d}^2\boldsymbol{k}, \quad (1.36)$$

which gives the spherical definitions.

In analogy with Eq.(1.33), the dynamics for three-point third-order correlation $\hat{S}_{ijn}(\boldsymbol{k},\boldsymbol{p},t)$ is illustrated in following:

$$\begin{aligned}&\left(\frac{\partial}{\partial t}+\nu(k^2+p^2+q^2)-A_{lm}\left(k_l\frac{\partial}{\partial k_m}+p_l\frac{\partial}{\partial p_m}\right)\right)S_{ijn}(\boldsymbol{k},\boldsymbol{p},t)+M_{im}(\boldsymbol{q})S_{mjn}(\boldsymbol{k},\boldsymbol{p},t)\\&+M_{jm}(\boldsymbol{k})S_{imn}(\boldsymbol{k},\boldsymbol{p},t)+M_{nm}(\boldsymbol{p})S_{ijm}(\boldsymbol{k},\boldsymbol{p},t)=T_{ijn}(\boldsymbol{k},\boldsymbol{p},t),\end{aligned} \quad (1.37)$$

where $\boldsymbol{k}+\boldsymbol{p}+\boldsymbol{q}=\boldsymbol{0}$, k, p are moduli of $\boldsymbol{k}$ and $\boldsymbol{p}$ respectively, and $T_{ijn}(\boldsymbol{k},\boldsymbol{p},t)$ actually gathers the contribution from three-point fourth-order moments and is expressed in terms of a fourth-order spectral tensor

$$\begin{aligned}T_{ijn}(\boldsymbol{k},\boldsymbol{p},t)&=P_{imp}(\boldsymbol{q})\iiint S_{mpjn}(\boldsymbol{r},\boldsymbol{k},\boldsymbol{p},t)d^3\boldsymbol{r}\\&+P_{jmp}(\boldsymbol{k})\iiint S_{mpin}(\boldsymbol{r},\boldsymbol{q},\boldsymbol{p},t)d^3\boldsymbol{r}+P_{nmp}(\boldsymbol{p})\iiint S_{mpij}(\boldsymbol{r},\boldsymbol{q},\boldsymbol{k},t)d^3\boldsymbol{r},\end{aligned} \quad (1.38)$$

with

$$\langle \hat{u}_i(\boldsymbol{q})\hat{u}_j(\boldsymbol{q'})\hat{u}_m(\boldsymbol{k})\hat{u}_n(\boldsymbol{p})\rangle = S_{ijmn}(\boldsymbol{q},\boldsymbol{k},\boldsymbol{p})\delta(\boldsymbol{q}+\boldsymbol{q'}+\boldsymbol{k}+\boldsymbol{p}). \tag{1.39}$$

The derivation for equation (1.38) can be found in Appendix A. Obviously, the right-hand sides of Eq.(1.33) and (1.37) are both not closed.

1.3.3 Spectral linear theory

The interplay between linear and nonlinear mechanisms can be very complex and subtle. Even when nonlinearity is significant, the behaviour of the linear operators acting on fluctuating field has significant influence, which is important to understand the linear mechanism firstly. For linear terms, spectral linear theory is very efficient for solving linear operators of homogeneous turbulence. It was originally introduced as 'Rapid Distortion Theory' for irrotational mean flows by (Batchelor & Proudman, 1954), and was applied to the shear flow case by Moffatt (1967). SLT was then extended to rotating shear flows by Salhi & Cambon (1997), and to stratified shear flows by Hanazaki & Hunt (2004) using a refined analytical approach. Salhi & Cambon (2010) unified this approach for the case of rotating stratified shear flows.

Neglecting nonlinearity entirely implies that the effects of the interaction of turbulence with itself are supposed to be small compared with those resulting from mean-flow distortion of turbulence. It can be assumed that, after a sudden change in the mean flow, the turbulent flow is governed by the so-called 'rapid terms' corresponding to linear processes linked to the mean flow, whereas 'slow terms' corresponding to nonlinear processes as triadic interactions and energy cascade may be neglected for short times. For instance, weak turbulence encounters a sudden contraction in a channel or in flows around an airfoil. The underlying implicit assumption is that the time required for a significant distortion by the mean flow to develop is short compared with that for the turbulent evolution in the absence of distortion effect, so that the linear theory is restricted to:

$$\frac{\mathcal{K}||\boldsymbol{A}||}{\varepsilon} \gg 1, \tag{1.40}$$

in which $||\boldsymbol{A}||^{-1} = (A_{ij}A_{ij})^{-1}$ (spatially uniform in our study for homogeneous turbulence) and $\frac{\mathcal{K}}{\varepsilon}$ represents the characteristic times of linear and nonlinear processes respectively, where $\mathcal{K}$ is the turbulent kinetic energy and ε is the viscous dissipation rate of kinetic energy both defined in §1.4.1. The linear theory can also be relevant, at least over short enough times, if physical influences leading to linear terms in the fluctuating equations dominate turbulent flows, such as in strongly stratified or rotating fluid or a conducting fluid in a strong magnetic field. The extended discussion can be found in Sagaut & Cambon (2018).

The purely linear theory closes the equations, leading to

$$\frac{\partial u_i}{\partial t} + \underbrace{A_{jk} x_k \frac{\partial u_i}{\partial x_j}}_{Advection} + A_{ij} u_j + \frac{\partial p}{\partial x_i} = 0, \tag{1.41}$$

in physical space. One may imagine following a particle convected by the mean velocity, which gets

$$\frac{\mathrm{d} u_i(\boldsymbol{x}(t), t)}{\mathrm{d}t} + A_{ij} u_j(\boldsymbol{x}(t), t) + \frac{\partial p(\boldsymbol{x}(t), t)}{\partial x_i} = 0, \tag{1.42}$$

under simple ordinary differential equations

$$\dot{x}_i = \frac{\mathrm{d} x_i}{\mathrm{d}t} = A_{ik} x_k, \tag{1.43}$$

with $(\dot{\ })$ that represents Lagrangian derivation and used as $\dfrac{\mathrm{d}}{\mathrm{d}t}$ indiscriminately in this thesis report. The corresponding linear equation in Fourier space is

$$\frac{\partial \hat{u}_i(\boldsymbol{k}, t)}{\partial t} - A_{ln} k_l \frac{\partial \hat{u}_i(\boldsymbol{k}, t)}{\partial k_n} + M_{in}(\boldsymbol{k}) \hat{u}_n(\boldsymbol{k}, t) = 0, \tag{1.44}$$

and it can be similarly written as

$$\frac{\mathrm{d} \hat{u}_i(\boldsymbol{k}(t), t)}{\mathrm{d}t} = -M_{in}(\boldsymbol{k}(t)) \hat{u}_n(\boldsymbol{k}(t), t), \tag{1.45}$$

with the characteristic lines defined by

$$\dot{k}_i = \frac{\mathrm{d} k_i}{\mathrm{d}t} = -A_{ji} k_j. \tag{1.46}$$

It is not difficult to find that the eikonal equation (1.46), that defines the characteristic lines in Fourier space, is the counterpart of Eq.(1.43) in physical space—which gives the mean flow trajectories.

The solution of (1.43) is obtained as $x_i = F_{ij}(t, t_0) X_j$ with Cauchy matrix, or semi-Lagrangian gradient of displacement $F_{ij}(t, t_0) = \dfrac{\partial x_i^L}{\partial X_j}$, in which $\boldsymbol{X} = \boldsymbol{x}(t_0)$ (see Eringen, 1976). For the sake of brevity, the superscript 'L' is omitted in this report. It is easy to obtain

$$k_i(t) = F_{ji}^{-1}(t, t_0) K_j, \quad \text{where} \quad K_j = k_j(t_0), \tag{1.47}$$

and conservation of $\boldsymbol{k} \cdot \boldsymbol{x} (= \boldsymbol{K} \cdot \boldsymbol{X})$. The linear solution for $\hat{u}_i(\boldsymbol{k}(t), t)$ is therefore formally given by

$$\hat{u}_i(\boldsymbol{k}(t), t) = G_{ij}(\boldsymbol{k}, t, t_0) \hat{u}_j(\boldsymbol{K}, t_0), \tag{1.48}$$

with

$$G_{ij}(\boldsymbol{k}, t_0, t_0) = \delta_{ij} - \frac{K_i K_j}{K^2}. \tag{1.49}$$

One can notice the following properties of $\boldsymbol{F}$ and of Green's function tensor $\boldsymbol{G}$:

$$F^{-1}_{ij}(t, t_0) = F_{ij}(t_0, t), \quad \dot{G}_{ij} = -M_{in} G_{nj}. \tag{1.50}$$

The Green tensor G_{ij} is particularly simple when A_{ij} is symmetric, namely for irrotational flows:

$$G_{ij}(\boldsymbol{k}, t, t_0) = P_{il}(\boldsymbol{k}) F^{-1}_{jl}(t, t_0). \tag{1.51}$$

If viscous effect is considered (Cambon *et al.*, 1985), the linear solution for $\hat{u}_i(\boldsymbol{k}(t), t)$ then turns to

$$\hat{u}_i(\boldsymbol{k}(t), t) = V_0(\boldsymbol{k}, t) G_{ij}(\boldsymbol{k}, t, t_0) \hat{u}_j(\boldsymbol{K}, t_0), \tag{1.52}$$

where

$$V_0(\boldsymbol{k}, t) = \exp\left(-\nu \int_{t_0}^{t} k^2(\tau)\, \mathrm{d}\tau\right) = \exp\left(-\nu k_l k_n \int_{t_0}^{t} F_{li}(\tau, t) F_{ni}(\tau, t)\, \mathrm{d}\tau\right). \tag{1.53}$$

The relationship (1.52) yields the prediction of statistical moments though products of Green's functions, so that the general solution for the second-order spectral tensor when knowing $\boldsymbol{G}$ is

$$\hat{R}_{ij}(\boldsymbol{k}, t) = V_0^2(\boldsymbol{k}, t) G_{ik}(\boldsymbol{k}, t, t_0) G_{jl}(\boldsymbol{k}, t, t_0) \hat{R}_{kl}(\boldsymbol{K}, t_0)\ . \tag{1.54}$$

SLT allows an analytical computation of the fluctuating velocity and its moments. For a given mean flow, $G_{ij}(\boldsymbol{k}, t, t_0)$ is deterministic and can in principle be calculated. Consequently, the evolution of linear system can be predicted with given initial field. In inviscid linear limit, only the orientation of the wavevector is relevant, but this is no longer the case in viscous linear limit. In fact, it is not a simple task to solve $\boldsymbol{G}$ analytically, especially when system rotation is considered. Salhi & Cambon (1997) discussed the analytical solution for linearly rotating shear flow and gave out simple results with very special cases. In rotating shear flow, the effect of 'stropholysis term'—as will be explained in §2.1—is extremely difficult for analytical SLT, even inviscid, whereas STL for irrotational mean flow ignores the 'stropholysis term' simply. An alternative method is to solve the linear equations numerically as in Salhi *et al.* (2014). Appendix 1.3.3 presents some analytical SLT solutions for special mean flow velocity gradients which are related to this PhD work.

1.3.4 Nonlinear spectral models: from HIT to HAT

We now have the governing equations for $\hat{u}_i(\boldsymbol{k},t)$, $\hat{R}_{ij}(\boldsymbol{k},t)$ and $\hat{S}_{ijn}(\boldsymbol{k},\boldsymbol{p},t)$, which illustrate the open hierarchy usually formally written as:

$$\begin{aligned} \frac{\partial}{\partial t}u =&\langle uu\rangle \\ \frac{\partial}{\partial t}\langle uu\rangle =&\langle uuu\rangle \\ \frac{\partial}{\partial t}\langle uuu\rangle =&\langle uuuu\rangle \\ \cdots =&\cdots . \end{aligned} \tag{1.55}$$

In brief, the closure problem for statistical moments is that the $N+1$-th order moments arise in the nonlinear operators for N-th order moments' equations.

Regarding nonlinear closures of HIT, a few models are based on Heisenberg's transfer model, e.g. Canuto & Dubovikov (1996*a*,*b*); Canuto *et al.* (1996). Other more sophisticated and successful models employ high-order closures using the Eddy-Damped Quasi-Normal Markovian technique, firstly proposed by Orszag (1969). The infinite hierarchy is stopped by quasi-normal (**QN**) relationship in the governing equation for $\hat{S}_{ijn}(\boldsymbol{k},\boldsymbol{p},t)$—in which all the linear terms related to mean velocity gradient vanish because of isotropy—assuming that quadratic moments can be expressed as products of second-order ones. So that the nonlinear term in Eq.(1.37) becomes

$$\begin{aligned} T_{ijn}^{(\mathrm{QN})}(\boldsymbol{k},\boldsymbol{p},t) =&2\big(P_{iml}(\boldsymbol{q})\hat{R}_{mj}(\boldsymbol{k},t)\hat{R}_{ln}(\boldsymbol{p},t)+P_{jml}(\boldsymbol{k})\hat{R}_{mn}(\boldsymbol{p},t)\hat{R}_{li}(\boldsymbol{q},t) \\ &+P_{nml}(\boldsymbol{p})\hat{R}_{mi}(\boldsymbol{q},t)\hat{R}_{lj}(\boldsymbol{k},t)\big), \end{aligned} \tag{1.56}$$

with

$$\begin{aligned} \langle\hat{u}_i(\boldsymbol{q})\hat{u}_j(\boldsymbol{q}')\hat{u}_m(\boldsymbol{k})\hat{u}_n(\boldsymbol{p})\rangle =&\langle\hat{u}_i(\boldsymbol{q})\hat{u}_j(\boldsymbol{q}')\rangle\langle\hat{u}_m(\boldsymbol{k})\hat{u}_n(\boldsymbol{p})\rangle+\langle\hat{u}_i(\boldsymbol{q})\hat{u}_m(\boldsymbol{k})\rangle\langle\hat{u}_j(\boldsymbol{q}')\hat{u}_n(\boldsymbol{p})\rangle \\ &+\langle\hat{u}_i(\boldsymbol{q})\hat{u}_n(\boldsymbol{p})\rangle\langle\hat{u}_m(\boldsymbol{k})\hat{u}_j(\boldsymbol{q}')\rangle. \end{aligned} \tag{1.57}$$

QN assumption, as a common feature of triadic closures, is also used in the most sophisticated Kraichnan's theories (Kraichnan, 1959; Kraichnan & Herring, 1978).

However, numerical simulation results by Ogura (1963) exhibited that a negative zone appeared at small k in the energy spectrum for a long time evolution. This loss of realizability indicated a too strong transfer from largest structures, which is corrected by adding an eddy-damping (**ED**) term proposed by Orszag (1969), namely

$$T_{ijn}^{(\mathrm{EDQN})}(\boldsymbol{k},\boldsymbol{p})=T_{ijn}^{(\mathrm{QN})}(\boldsymbol{k},\boldsymbol{p})-\left(\eta(k,t)+\eta(p,t)+\eta(q,t)\right)\hat{S}_{ijn}(\boldsymbol{k},\boldsymbol{p},t). \tag{1.58}$$

The damping term represents a contribution from fourth-order cumulants, which express the departure of Gaussianity. The eddy-damping coefficient $\eta(k,t)$ is usually chosen as

$$\eta(k,t) = A\sqrt{\int_0^k p^2 E(p,t)\,\mathrm{d}p}, \tag{1.59}$$

following Pouquet *et al.* (1975) , which is an improved variant of Orszag (1969)'s proposal. The constant is fixed at A = 0.36 to recover a well-admitted value of the Kolmogorov constant (André & Lesieur, 1977). One can obtain that, with eddy-damping correction, the fourth-order cumulants act as a linear relaxation of triple correlations, which will reinforce the dissipative operator in Eq.(1.37) when added to the purely viscous terms on its left-hand side. So that the dissipative terms are gathered into a single one:

$$\mu_{kpq} = \nu(k^2+p^2+q^2) + \eta(k,t) + \eta(p,t) + \eta(q,t). \tag{1.60}$$

Then the solution of (1.37) can be found as

$$\begin{aligned}\hat{S}_{ijn}(\boldsymbol{k},\boldsymbol{p},t) =& \exp\left[-\mu_{kpq}(t-t_0)\right]\hat{S}_{ijn}(\boldsymbol{k},\boldsymbol{p},t_0)\\ &+\int_{t_0}^{t}\exp\left[-\int_{t'}^{t}\mu_{kpq}(t'')\,\mathrm{d}t''\right]\left[T^{(\mathrm{QN})}_{ijn}(\boldsymbol{k},\boldsymbol{p},t)\right]\,\mathrm{d}t',\end{aligned} \tag{1.61}$$

with time integrals, treating $T^{(\mathrm{QN})}_{ijn}(\boldsymbol{k},\boldsymbol{p},t)$ as a source term.

The last procedure, called as Markovianization (**M**), amounts to truncating the proper time memory of triple correlations. That means the proper time-scale of triple correlations is much larger than the one of the double correlations embedded in the quasi-normal term. In other words, $\hat{\boldsymbol{R}}$ and $T^{(\mathrm{QN})}$ are considered as slowly varying quantities so that one can take $t' = t$ in them, whereas the exponential term is considered damping rapidly. Different levels of Markovianization can give out different final closure results, but yield the same form in HIT:

$$\frac{\partial E(k,t)}{\partial t} + 2\nu k^2 E(k,t) = T(k,t), \tag{1.62}$$

with different expressions of $T(k,t)$. The preceding equation is called *Lin equation* (Von Kármán & Lin, 1951), in which

$$\int_0^{+\infty} T(k,t) = 0. \tag{1.63}$$

From HIT to HAT, there is a rather large literature on generalized EDQNM, for shear-driven and for buoyancy-driven flows, even with coupled fields, such as buoyancy scalar and magnetic field (in Magneto-hydrodynamics) in addition to velocity, as reviewed recently in e.g. Cambon *et al.* (2017) and Sagaut & Cambon (2018). In such cases, different versions can be proposed, depending on the flow regimes, and on the computational resources available. Briefly speaking, such EDQNM strategy, for HAT and beyond, may involve physical assumptions, which are difficult to justify at their highest degree generally, but can be checked on results and a purely technical treatment. Actually, it is definitely a hard task to extend the preceding physical assumptions to HAT, even only velocity field is considered. Following are some difficulties which anisotropic closures have to account for:

1. Explicit anisotropic linear terms, absent in HIT, can be neglected in the equations for triple correlations, only when the linear effects induced by mean-flow gradients have no essential qualitative effects on the dynamics of triple correlations compared with the induced production effects in the equations for second-order correlations. It is not always the situation in some flows, e.g. obviously questioned in purely rotating turbulence, where the Coriolis force does not affect the energy equation directly, namely there is no production for second-order correlations.

2. The eddy damping term is in a quasi-isotropic form, by means of a single eddy damping coefficient $\eta(k, t)$, and is difficult to consider further anisotropic damping.

3. Markovianization is conserved. It is classically stated that the over dissipation of triple correlations induced by the eddy-damping term amounts to break the proper memory of these correlations. Much less classical is the case of wave turbulence theory: in this case, as in strongly rotating turbulence, the phase-mixing due to interacting inertial waves severely damps the inertial transfers, and there is no need for an 'ad-hoc' eddy-damping.

In our case of homogeneous shear-driven turbulence, the generalized 3D EDQNM-1 procedure is employed, which closes $\hat{S}_{ijn}(\boldsymbol{k}, \boldsymbol{p}, t)$ as in HIT. At this stage, the complexity and the numerical cost of the model remains very high, because of the anisotropy, even if axial symmetry is prescribed. This anisotropy renders all two-point quantities mentioned above dependent on the orientation of the wavevector and not only on its modulus. In addition, the generalized transfer terms involve 3D convolution, in which the orientation of the plane of the triad has to be taken into account numerically. In order to derive a much more tractable model, the description of anisotropy was simplified, using a low-degree expansion in terms of angular harmonics for the second-order spectral tensor. This allowed to pass from a model in terms of $\boldsymbol{k}$-vector to a model in terms of spherically-averaged descriptors, only dependent on the modulus of the wavevector. The model MCS by Mons *et al.* (2016) was readily derived from the 3D EDQNM-1 model, retaining the first two degrees of anisotropy. Even if the MCS model was validated in different flow cases, first comparisons to both SLT and DNS for sufficiently long times suggested that the projection on a base of spherical harmonics at low degree was much less satisfactory for the linear terms inherited from SLT than for the nonlinear closure.

The model by Weinstock (1982, 2013) for the pure plane shear without system rotation is particularly interesting. This model is on the $\boldsymbol{k}$-space description like EDQNM-1, based on exact treatment of linear terms in the governing equation of $\hat{\boldsymbol{R}}$, and relies on purely isotropic EDQNM model for the energy transfer, with a weakly anisotropic part giving a forced return to isotropy. However it still needs to be quantitatively evaluated.

All the details on EDQNM-1, MCS and Weinstock's model are presented in the next chapter.

1.4 Single-point models for rotating shear turbulent flow

In fact, the most popular closure models for practical applications especially for engineering, are aiming at Reynolds-averaged Navier-Stokes equations. In addition to simple closure models such as models of turbulent viscosity using a mixing length assumption, second-order single-point models offer both a dynamical and a statistical description of the turbulent field. The governing equations for the Reynolds stress tensor, turbulent kinetic energy, and for its dissipation rate can reflect the effects of convection, diffusion distortion, pressure and viscous stresses, which are present in the equations that govern the fluctuating field u_i. In this section, we will return to physical space and recall the fundamental of single-point models. Further discussion can be obtained in Sagaut & Cambon (2018).

1.4.1 RST equations without system rotation

The exact evolution equation for the Reynolds Stress tensor $\mathcal{R}_{ij} = \langle u_i u_j \rangle$ can be derived from Eq.(1.3)

$$\frac{\partial \mathcal{R}_{ij}}{\partial t} + \langle U_k \rangle \frac{\partial \mathcal{R}_{ij}}{\partial x_k} = \mathcal{P}_{ij} + \Pi_{ij} - \varepsilon_{ij} - \frac{\partial D_{ijk}}{\partial x_k}, \tag{1.64}$$

in which

$$\mathcal{P}_{ij} = -\frac{\partial \langle U_i \rangle}{\partial x_k} \mathcal{R}_{kj} - \frac{\partial \langle U_j \rangle}{\partial x_k} \mathcal{R}_{ki}, \tag{1.65}$$

in terms of basic one-point variables $\langle U_i \rangle$ and $\mathcal{R}_{ij}$ is referred to the production tensor and is the only closed term on the right-hand side of RST equations.

The second term on the right-hand side is

$$\Pi_{ij} = \langle p \left(\frac{\partial u_i}{\partial x_j} + \frac{\partial u_j}{\partial x_i} \right) \rangle, \tag{1.66}$$

consisting of one-point correlations between the fluctuating pressure and rate of strain tensor. As discussed in the beginning of this chapter, p is nonlocally determined from the velocity field by the Poisson equation (1.4) and which in principle requires multi-point methods for its treatment. Π_{ij} is usually decomposed into three trace-free parts

$$\Pi_{ij} = \Pi_{ij}^{(\mathrm{r})} + \Pi_{ij}^{(\mathrm{s})} + \Pi_{ij}^{(\mathrm{w})}, \tag{1.67}$$

corresponding to the three components of the Green's function solution of (1.4). Briefly, the first term arises from the linear part of the Poisson equation, known as 'rapid' pressure component, which is also present in linear theory; the second term coming from the nonlinear part of Eq.(1.4), is the 'slow' component; $\Pi_{ij}^{(\mathrm{w})}$ is the wall component and corresponds to a surface integral over the boundaries of the flow in the Green's function solution for p, which is additional to the volume integrals expressing the 'rapid' and 'slow' components. The three components are assumed to represent physically distinct mechanisms. Hence, they are modeled separately. In simple models, a mechanism of isotropization of the production is attributed to $\Pi_{ij}^{(\mathrm{r})}$, and a mechanism of return-to-isotropy, or isotropization of the Reynolds stress tensor, is attributed to $\Pi_{ij}^{(\mathrm{s})}$.

The dissipation tensor

$$\varepsilon_{ij} = 2\nu \langle \frac{\partial u_i}{\partial x_k} \frac{\partial u_j}{\partial x_k} \rangle, \tag{1.68}$$

accounts for the destruction of kinetic energy by viscous effects. The usual scalar dissipation rate, denoted as ε, is defined as

$$\varepsilon \equiv \frac{1}{2} \varepsilon_{ii}. \tag{1.69}$$

The last term in Eq.(1.64) vanishes in homogeneous turbulence. This term is expressed as a flux of a third-order correlation tensor D_{ijk}, which gathers triple velocity correlations, pressure-velocity terms and viscous diffusion terms.

It is useful to introduce the paradigmatic trace-deviator decomposition for the Reynolds stress tensor

$$\mathcal{R}_{ij} = 2\mathcal{K} \left(\frac{\delta_{ij}}{3} + b_{ij} \right), \quad \mathcal{K} = \frac{1}{2} \mathcal{R}_{ii}, \quad b_{ij} = \frac{\mathcal{R}_{ij}}{2\mathcal{K}} - \frac{\delta_{ij}}{3}, \tag{1.70}$$

where the deviatoric tensor b_{ij} represents the anisotropy of RST. Here, the classical $\mathcal{K}$-ε model is revisited. The evolution equation for the kinetic energy derived from the RST equation is

$$\frac{\partial \mathcal{K}}{\partial t} + \langle U_k \rangle \frac{\partial \mathcal{K}}{\partial x_k} = \mathcal{P} - \varepsilon - \frac{\partial D_{ijk}}{\partial x_k}, \tag{1.71}$$

and a similar one for b_{ij}. Whereas only the scalar dissipation rate ε is considered as an independent variable, which is governed by its own equation.

Single-point closure models are very popular, flexible and easy to use. They illustrate the three interactions in a systems approach, but cannot offer a detailed multiscale description. In addition, the linear, so-called RDT limit is missed due to the nonlocal (in physical space) effect of pressure fluctuation. When system rotation is added, at least the production term is affected and also the 'rapid' pressure-strain rate tensor. However, the basic two-equations $\mathcal{K}$-ε model altogether ignore the effect of rotation in the rotating shear case. The simpler single-point model proposed by Launder *et al.* (1975) will be recalled (see perspectives and Appendix G).

As introduced before, in homogeneous turbulence, the Reynolds stress term in Reynolds-averaged Navier-Stokes equations vanishes because of homogeneity. Then how the homogeneous spectral theory contributes to single-point modeling? Actually, $\mathcal{R}_{ij}$ can be seen as $R_{ij}(\boldsymbol{r})$ when $\boldsymbol{r} = \boldsymbol{0}$, so that we have

$$\mathcal{R}_{ij} = \iiint \hat{R}_{ij}(\boldsymbol{k})\,\mathrm{d}^3\boldsymbol{k}. \tag{1.72}$$

As a consequence, at least all the homogeneous contribution from RST modeling can be validated and corrected by homogeneous spectral models, especially for the nonlocal pressure term, which is difficult to be modeled with single-point approach.

1.4.2 RTI effects and exponential growth of kinetic energy in pure shear flow

When system rotation is omitted, the analysis of RST equation governed by mean shear indicates interesting results to turbulent kinetic energy evolution. Suppose

$$\boldsymbol{A} = \begin{bmatrix} 0 & S & 0 \\ 0 & 0 & 0 \\ 0 & 0 & 0 \end{bmatrix}, \tag{1.73}$$

then the non-zero components of RST equations can be written as:

$$\begin{cases} \dfrac{\partial\langle u_1u_1\rangle}{\partial t} = -2S\langle u_1u_2\rangle + \quad \Pi_{11} - \varepsilon_{11} \\ \dfrac{\partial\langle u_2u_2\rangle}{\partial t} = \qquad\qquad\quad \Pi_{22} - \varepsilon_{22} \\ \dfrac{\partial\langle u_3u_3\rangle}{\partial t} = \qquad\qquad\quad \Pi_{33} - \varepsilon_{33} \\ \dfrac{\partial\langle u_1u_2\rangle}{\partial t} = -2S\langle u_2u_2\rangle + \quad \Pi_{12} - \varepsilon_{12}, \end{cases} \tag{1.74}$$

with isotropic initial fields. Correspondingly, the evolution of kinetic energy is

$$\frac{\partial\mathcal{K}}{\partial t} = -S\langle u_1u_2\rangle - \varepsilon, \tag{1.75}$$

which indicates that the cross-gradient component of RST $\langle u_1u_2\rangle$ plays an important role.

After large elapsed time and at large Reynolds number, the exponential growth of $\mathcal{K}$ can be predicted with

$$\frac{1}{S\mathcal{K}}\frac{\partial\mathcal{K}}{\partial t} = -2b_{12} - \frac{\varepsilon}{S\mathcal{K}}. \tag{1.76}$$

Provided a correct asymptotic value is assumed for b_{12}, reasonable asymptotic values for the shear rapidity term in the preceding equation and also in ε equation

$$\frac{1}{S\varepsilon}\frac{\partial\varepsilon}{\partial t} = C_{\varepsilon 1}\left(-2b_{12}\right) - C_{\varepsilon 2}\frac{\varepsilon}{S\mathcal{K}}, \tag{1.77}$$

can be obtained.

Actually, Reynolds stress models with conventional closure techniques perform satisfactorily in the shear flow case, because the dynamics is dominated by a simple production to dissipation balance (or partial imbalance), and it is not very sensitive to the modeling of the pressure-strain rate tensor, especially to the most difficult rapid part. Eq.(1.74) illustrates the couplings between different non-vanishing Reynolds stresses in the pure shear case. To be specific, the equations for cross stress component can be written as

$$\frac{\partial\langle u_1u_2\rangle}{\partial t} = -2S\langle u_2u_2\rangle + \Pi_{12}^{(\mathrm{r})} + \Pi_{12}^{(\mathrm{s})}, \tag{1.78}$$

with isotropic dissipation tensor, where $\langle u_2^2\rangle$ is governed by

$$\frac{\partial\langle u_2u_2\rangle}{\partial t} = \Pi_{22}^{(\mathrm{r})} + \Pi_{22}^{(\mathrm{s})} - \frac{2}{3}\varepsilon. \tag{1.79}$$

The effect of the linear term $\Pi_{12}^{(\mathrm{r})}$ is modeled to reduce the production, and is perhaps not so important, at least qualitatively. In contrast, the conventional return-to-isotropy effect of the modeled nonlinear term $\Pi_{22}^{(\mathrm{s})}$ is essential for allowing an exponential growth rate in a fully

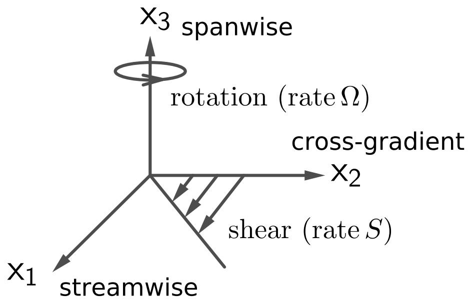

Figure 1.4: Illustration for flow with pure plane mean shear rotating in spanwise direction

nonlinear regime. In the absence of nonlinear terms (and without significant dissipation), Reynolds stress equations are consistent with an algebraic growth of the turbulent kinetic energy. In this regime, $\langle u_2^2 \rangle$ remains very small. The presence of the nonlinear pressure-strain rate, modeled in agreement with the return-to-isotropy principle, will redistribute the energy between the diagonal components of the Reynolds stress tensor, therefore feeding the smallest component $\langle u_2^2 \rangle$. This effect will reinforce the production term of the cross gradient component $\langle u_1 u_2 \rangle$ through a strong positive $\Pi_{22}^{(s)}$ term, which is the most efficient nonlinear effect to enhance $\langle u_2^2 \rangle$ and therefore to allow a dramatic increase of production, consistent with an eventual exponential growth.

1.5 Stability analysis for rotating shear turbulence

The studies in terms of SLT show the global relevance of the Bradshaw number B (Bradshaw, 1969) for the stability. $B = R(R+1)$, in which $R = \dfrac{2\Omega}{-S}$ is the ratio of system vorticity 2Ω to shear-induced-vorticity $-S$ (under typical coordinate system in engineering as shown in figure 1.4). $B < 0$ or $-1 < R < 0$ corresponds to exponential growth of turbulent kinetic energy, and $B > 0$ to exponential decay. Neutral cases are found for both $R = 0$ (no additional rotation) and $R = -1$ (zero absolute vorticity). figure 4.2 illustrates the different behaviours of the kinetic energy evolution in linear inviscid limit with typical values of R. The results are obtained with the proposed model in this thesis, which will be presented in next chapter.

In addition, from the point of view of linear dynamics, the passage from a two-point spectral description to a single-point one implies a loss of nonlocality in the pressure/velocity relationship in physical space. As a consequence, modeling the 'rapid' pressure-strain

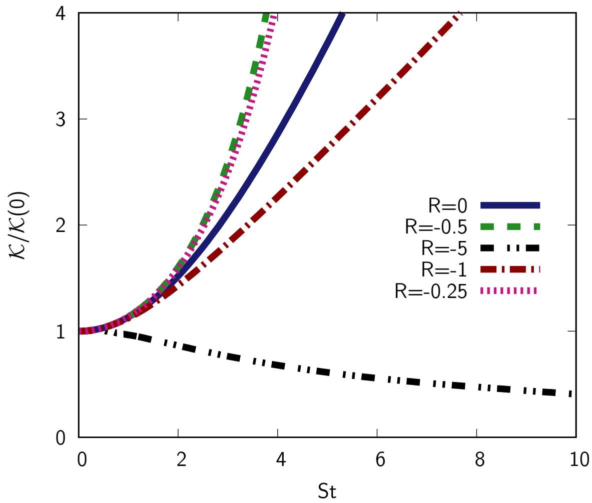

Figure 1.5: Time evolution of turbulent kinetic energy with $R = -5, -1, -1/2, -1/4, 0$ in the linear inviscid limit.

rate tensor in the RSM equations is very difficult and partly hopeless, as recently rediscussed by Mishra & Girimaji (2017) in line with exact SLT analysis. Surprisingly, the Bradshaw criterion is globally relevant for explaining the stability when considering production terms in the RSM equations (see also Brethouwer, 2005). This is also supported by a coarse pressure-less model (Leblanc & Cambon, 1998; Salhi *et al.*, 1997) which also brings forward the role of $R = \frac{2\Omega}{-S}$. A criterion similar to that of Bradshaw was also proposed in the shearing sheet approximation, using the epicyclic frequency $\kappa = \sqrt{2\Omega(2\Omega + S)}$. The stability of the flow is thus related to a Rayleigh criterion, ignoring again the effects of fluctuating pressure. Moreover, $B = \frac{\kappa^2}{S^2}$ in the rotating shear case is sometimes called the 'rotational Richardson number'; it is analogous to the Richardson number $Ri = \frac{N^2}{S^2}$ of the stratified shear case, where N is the Brunt-Väisälä frequency.

1.6 Proposals for the thesis work

As discussed in §1.3.4, even if the MCS model was validated in different flow cases, first comparison to both SLT and DNS for sufficiently long times suggested that the projection on a base of spherical harmonics at low degree was much less satisfactory for the linear terms inherited from SLT than for the nonlinear closure. It appears that the only way to check the validity of the closure model, given the subtle interplay of linear and nonlinear terms, is to conserve the full angular dependence for the linear terms in the equations governing $\boldsymbol{R}$. In addition, this way allows us to check other models which use no assumption for modeling the linear terms, with unexpected results.

On the one hand, for the linear operators, analytical SLT method exhibited difficulties on coupling with nonlinear models for arbitrary mean-velocity gradients. In this thesis, a numerical method based on finite difference scheme is proposed to deal with advection terms directly. On the other hand, the closure technique applied in MCS base on EDQNM-1 drops the components of transfer terms in terms of high degrees anisotropy of $\boldsymbol{R}$. This may result in lack of damping for high degree anisotropy, namely impact on the RTI mechanism, which is essential to the re-growth of $\mathcal{K}$ in pure shear case. To solve the problem induced by the truncation of spherical harmonics expansion for nonlinear terms, we propose a hybrid nonlinear model based on the one used in MCS, partly relevant to Weinstock's model to damp high degree anisotropy with forced RTI term.

Chapter 2

Spectral modeling for homogeneous anisotropic turbulence

In this chapter, we follow the footsteps in our research group to model shear-driven homogeneous anisotropic turbulence. Firstly, we introduce the 3D spectral model EDQNM-1, which closes the nonlinear terms as there is no mean flow acting on the three-point third-order correlation tensor. Next, the spherically-averaged model MCS is revisited, which is based on omitting high degree anisotropy of second-order correlation in terms of spherical harmonics decomposition, in order to decrease the computational cost induced by 3D convolution in EDQNM-1. Then, we propose the present model in this thesis work, retaining exact 3D linear operators as in EDQNM-1 and simplified nonlinear closure as in MCS. In order to recover the damping of high degree anisotropy in nonlinear terms, which is missing in MCS, a hybrid model is proposed partly combined with Weinstock's model that has forced RTI mechanism.

It is worthwhile to clarify that the models presented in this chapter and as well the numerical implementation introduced in next chapter, do not particularly aim at shear-driven flow. Potential applicability is kept for arbitrary forms of mean-velocity gradients.

2.1 Decomposition of the second-order spectral tensor and the three-dimensional nonlinear model

The most general information on two-point second-order velocity correlations is given by the tensor $\hat{R}_{ij}(\boldsymbol{k})$ (and also $R_{ij}(\boldsymbol{r})$), which is *a priori* 9-component. It contains the complete information pertaining to second-order velocity statistics of the flow. Thanks to incompressibility and Hermitian symmetry, it has only four independent components and permits a poloidal-toroidal decomposition. In this section, the classical decomposition for $\hat{\boldsymbol{R}}$ and the consequent decomposition for the governing equations are revisited. Then the 3D nonlinear closure model EDQNM-1 is presented.

2.1.1 Modal decomposition in local frames

In order to use poloidal-toroidal decomposition in Fourier space, which can represent a three-component divergence-free velocity field in terms of two independent scalar terms, a local reference frame of a polar-spherical system of coordinates for $\boldsymbol{\alpha}$ (orientation of $\boldsymbol{k}$) is defined as:

$$\boldsymbol{e}^{(1)}(\boldsymbol{\alpha}) = \frac{\boldsymbol{\alpha}\times\boldsymbol{n}}{|\boldsymbol{\alpha}\times\boldsymbol{n}|}, \quad \boldsymbol{e}^{(2)}(\boldsymbol{\alpha}) = \boldsymbol{e}^{(3)}(\boldsymbol{\alpha})\times\boldsymbol{e}^{(1)}(\boldsymbol{\alpha}), \quad \boldsymbol{e}^{(3)}(\boldsymbol{\alpha}) = \boldsymbol{\alpha}. \tag{2.1}$$

The above frame is usually referred to Craya-Herring frame (Craya, 1957; Herring, 1974) with association to a privileged direction $\boldsymbol{n}$ illustrated in figure 2.1. When $\boldsymbol{k} \parallel \boldsymbol{n}$, the local frame vectors $\boldsymbol{e}^{(1)}$, $\boldsymbol{e}^{(2)}$ and $\boldsymbol{e}^{(3)}$may coincide with the fixed frame of reference, with $\boldsymbol{e}^{(3)} = \boldsymbol{n}$. In the context of HAT, the local frame ($\boldsymbol{e}^{(1)}$, $\boldsymbol{e}^{(2)}$) of the plane is normal to the wavevector and the divergence-free velocity field in Fourier space has only two components in the Craya-Herring frame:

$$\hat{\boldsymbol{u}}(\boldsymbol{k},t) = u^{(1)}\boldsymbol{e}^{(1)}(\boldsymbol{\alpha}) + u^{(2)}\boldsymbol{e}^{(2)}(\boldsymbol{\alpha}). \tag{2.2}$$

An alternative decomposition to the Craya-Herring decomposition is in helical frame (Cambon & Jacquin, 1989; Cambon *et al.*, 1997), and presents some advantages regarding frame-invariance properties, treatment of background nonlinearity, and rotating turbulence. The helical modes are defined from:

$$\boldsymbol{N}(\boldsymbol{\alpha}) = \boldsymbol{e}^{(2)}(\boldsymbol{\alpha}) - \imath\boldsymbol{e}^{(1)}(\boldsymbol{\alpha}), \tag{2.3}$$

and the solenoidal velocity in Fourier space is decomposed as

$$\hat{\boldsymbol{u}}(\boldsymbol{k},t) = \xi_{+}(\boldsymbol{k},t)\boldsymbol{N}(\boldsymbol{\alpha}) + \xi_{-}(\boldsymbol{k},t)\boldsymbol{N}(-\boldsymbol{\alpha}). \tag{2.4}$$

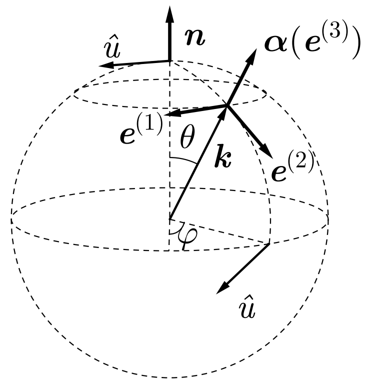

Figure 2.1: Polar-spherical system of coordinates for $\boldsymbol{k}$ and related Craya-Herring frame of reference $\left(\boldsymbol{e}^{(1)}, \boldsymbol{e}^{(2)}, \boldsymbol{\alpha} = \boldsymbol{e}^{(3)}\right)$.

Some properties of the projection vectors are presented in this section. For Craya-Herring frame:

$$\boldsymbol{e}^{(3)}(\boldsymbol{\alpha}) = \epsilon_{\alpha\beta3} e_i^{(\alpha)}(\boldsymbol{\alpha}) e_j^{(\beta)}(\boldsymbol{\alpha}) \qquad (\alpha, \beta = 1, 2) \tag{2.5a}$$

$$P_{ij}(\boldsymbol{\alpha}) = \delta_{ij} - \frac{k_i k_j}{k^2} = \boldsymbol{e}_i^{(1)} \boldsymbol{e}_j^{(1)} + \boldsymbol{e}_i^{(2)} \boldsymbol{e}_j^{(2)}, \tag{2.5b}$$

for helical frame:

$$\imath \boldsymbol{k} \times \boldsymbol{N} = k \boldsymbol{N} \tag{2.6a}$$

$$N_i(-\boldsymbol{\alpha}) = N_i^*(\boldsymbol{\alpha}), \quad N_i(\boldsymbol{\alpha}) N_i(\boldsymbol{\alpha}) = N_i^*(\boldsymbol{\alpha}) N_i^*(\boldsymbol{\alpha}) = 0, \quad N_i^*(\boldsymbol{\alpha}) N_i(\boldsymbol{\alpha}) = 2, \tag{2.6b}$$

and for the relationship between the two frames:

$$N_i^*(\boldsymbol{\alpha}) N_j(\boldsymbol{\alpha}) = P_{ij}(\boldsymbol{\alpha}) + \imath \epsilon_{ijn} \frac{k_n}{k}, \tag{2.7}$$

with simple proof

$$\begin{aligned} N_i^*(\boldsymbol{\alpha}) N_j(\boldsymbol{\alpha}) &= e_i^{(1)} e_j^{(1)} + e_i^{(2)} e_j^{(2)} + \imath (e_i^{(1)} e_j^{(2)} - e_i^{(2)} e_j^{(1)}) \\ &= P_{ij}(\boldsymbol{k}) + \imath \epsilon_{\alpha\beta3} e_i^{(\alpha)} e_j^{(\beta)} \\ &= P_{ij}(\boldsymbol{k}) + \imath \epsilon_{ijn} \frac{k_n}{k}. \end{aligned} \tag{2.8}$$

Eq.(2.6a) indicates that $\boldsymbol{N} e^{\imath \boldsymbol{k} \cdot \boldsymbol{x}}$ and its complex conjugate are eigenmodes of the curl operator.

One can project $\hat{\boldsymbol{R}}(\boldsymbol{k},t)$ in helical frame, which yields the following decomposition

$$\hat{R}_{ij}(\boldsymbol{k},t) = \mathcal{E}(\boldsymbol{k},t)P_{ij}(\boldsymbol{\alpha}) + \mathcal{H}(\boldsymbol{k},t)\imath\epsilon_{ijn}\frac{k_n}{k} + \Re(Z(\boldsymbol{k},t)N_i(\boldsymbol{\alpha})N_j(\boldsymbol{\alpha})), \tag{2.9}$$

with reversed relationship

$$\mathcal{E}(\boldsymbol{k},t) = \frac{1}{2}\hat{R}_{mm}(\boldsymbol{k},t), \quad k\mathcal{H}(\boldsymbol{k},t) = \frac{1}{2}\imath k_m\epsilon_{imj}\hat{R}_{ij}(\boldsymbol{k},t), \quad Z(\boldsymbol{k},t) = \frac{1}{2}\hat{R}_{ij}(\boldsymbol{k},t)N_i^*(\boldsymbol{\alpha})N_j^*(\boldsymbol{\alpha}), \tag{2.10}$$

and symmetric properties

$$\mathcal{E}(-\boldsymbol{k}) = \mathcal{E}(\boldsymbol{k}), \quad Z(-\boldsymbol{k}) = Z^*(\boldsymbol{k}), \quad \mathcal{H}(-\boldsymbol{k}) = \mathcal{H}(\boldsymbol{k}), \tag{2.11}$$

where $\mathcal{E}(\boldsymbol{k},t)$ and $\mathcal{H}(\boldsymbol{k},t)$ are real scalars that represent energy density in three-dimensional $\boldsymbol{k}$-space and helicity spectrum respectively, and $Z(\boldsymbol{k},t)$ is a complex-valued pseudo-scalar (Cambon & Jacquin, 1989). Actually, the preceding decomposition proposed by Chandrasekhar (1961) can be written in any direct orthonormal system of Cartesian coordinates. It can be shown that $\mathcal{E}$, Z and $\mathcal{H}$ are invariants rather than the phase of Z with changing either the fixed frame or $\boldsymbol{n}$. When considering only the symmetric, real part of the spectral tensor, Z describes the anisotropic structure of the real part of the spectral tensor at a given $\boldsymbol{k}$: its modulus is half the difference of the nonzero eigenvalues, whereas its phase is related to the angle for passing from the Craya-Herring frame to the eigenframe by rotation around $\boldsymbol{k}$. In addition, the realizability constraint (Cambon *et al.*, 1997) is

$$\mathcal{E}(\boldsymbol{k},t) \geq \sqrt{|Z(\boldsymbol{k},t)|^2 + \mathcal{H}^2(\boldsymbol{k},t)} \quad, \forall \boldsymbol{k}\,, t. \tag{2.12}$$

The decomposition leads to straightforward physical implications for each components:

$$\hat{R}_{ij}(\boldsymbol{k}) = \hat{R}_{ij}(\boldsymbol{k})^{(\mathrm{iso})} + \hat{R}_{ij}(\boldsymbol{k})^{(\mathrm{dir})} + \hat{R}_{ij}(\boldsymbol{k})^{(\mathrm{pol})} + \hat{R}_{ij}(\boldsymbol{k})^{(\mathrm{h})}, \tag{2.13}$$

and

$$\begin{aligned} \hat{R}_{ij}(\boldsymbol{k})^{(\mathrm{iso})} =& \frac{E(k)}{4\pi k^2}P_{ij}(\boldsymbol{\alpha})\,, \quad \hat{R}_{ij}(\boldsymbol{k})^{(\mathrm{dir})} = \left(\mathcal{E}(\boldsymbol{k}) - \frac{E(k)}{4\pi k^2}\right)P_{ij}(\boldsymbol{\alpha}) = \mathcal{E}^{(\mathrm{dir})}(\boldsymbol{k})P_{ij}(\boldsymbol{\alpha}), \\ \hat{R}_{ij}(\boldsymbol{k})^{(\mathrm{pol})} =& \Re(Z(\boldsymbol{k})N_i(\boldsymbol{\alpha})N_j(\boldsymbol{\alpha}))\,, \quad \hat{R}_{ij}(\boldsymbol{k})^{(\mathrm{h})} = \imath\mathcal{H}(\boldsymbol{k})\epsilon_{ijn}\frac{k_n}{k}. \end{aligned} \tag{2.14}$$

When the turbulence is restricted to isotropy, the state vector $(\mathcal{E}, Z, \mathcal{H})$ reduces to

$$\mathcal{E} = \frac{E(k)}{4\pi k^2}P_{ij}(\boldsymbol{\alpha}), \quad Z = \mathcal{H} = 0. \tag{2.15}$$

Otherwise, the directional anisotropy means that all directions of $\boldsymbol{k}$ on a spherical shell do not have the same amount of energy, and the polarization anisotropy means that the orientations of the vector $\hat{u}_i$, in the plane normal to a given wavevector $\boldsymbol{k}$, are not statistically equivalent, whereas the helical anisotropy is the imaginary and antisymmetric part which has relevance with helicity of turbulence h (see Sagaut & Cambon, 2018, for further details).

Remarks on helicity by Cambon *et al.* (2013): One can define the helicity of turbulence as

$$h = \frac{1}{2}\langle \omega_i(\boldsymbol{x}) u_i(\boldsymbol{x})\rangle, \tag{2.16}$$

where

$$\omega_i(\boldsymbol{x}) = \epsilon_{imn}\frac{\partial u_n(\boldsymbol{x})}{\partial x_m} \tag{2.17}$$

is the curl of velocity fluctuation. Here we introduce a two-point helicity correlation

$$\hbar(\boldsymbol{r}) = \frac{1}{2}\langle \omega_i(\boldsymbol{x}+\boldsymbol{r}) u_i(\boldsymbol{x})\rangle \tag{2.18}$$

Similar to $\hat{R}_{ij}$, we can get

$$\frac{1}{2}\langle \hat{\omega}_i(\boldsymbol{p}) \hat{u}_i(\boldsymbol{k})\rangle = k\mathcal{H}(\boldsymbol{k})\delta(\boldsymbol{k}+\boldsymbol{p}), \tag{2.19}$$

and

$$\mathcal{F}(\hbar(\boldsymbol{r})) = k\mathcal{H}(\boldsymbol{k}). \tag{2.20}$$

A radial helicity spectrum $H(k)$ could be defined by spherically averaging $k\mathcal{H}$, so that

$$h = \hbar(\boldsymbol{r}=\boldsymbol{0}) = \iint_{S_k} H(k)\,\mathrm{d}^2k = \iint k\mathcal{H}(\boldsymbol{k})\,\mathrm{d}^3\boldsymbol{k}. \tag{2.21}$$

If one integrates $\hat{R}_{ij}(\boldsymbol{k})$ and its components in the spheres $\mid \boldsymbol{k} \mid = k$, the corresponding spherically-averaged descriptors can be given by:

$$\varphi_{ij}(k) = \iint_{S_k} \hat{R}_{ij}(\boldsymbol{k})\,\mathrm{d}^2\boldsymbol{k} = 2E(k)\left(\frac{1}{3}\delta_{ij} + H_{ij}^{(\mathrm{dir})}(k) + H_{ij}^{(\mathrm{dir})}(k)\right) \tag{2.22a}$$

$$E(k) = \iint_{S_k} \mathcal{E}(\boldsymbol{k})\,\mathrm{d}^2\boldsymbol{k} \tag{2.22b}$$

$$2E(k)H_{ij}(k)^{(\mathrm{dir})} = \iint_{S_k} \hat{R}_{ij}^{(\mathrm{dir})}(\boldsymbol{k})\,\mathrm{d}^2\boldsymbol{k} = \iint_{S_k}\left(\mathcal{E}(\boldsymbol{k}) - \frac{E(k)}{4\pi k^2}\right)P_{ij}(\boldsymbol{\alpha})\,\mathrm{d}^2\boldsymbol{k} \tag{2.22c}$$

$$2E(k)H_{ij}(k)^{(\mathrm{pol})} = \iint_{S_k} \hat{R}_{ij}^{(\mathrm{pol})}(\boldsymbol{k})\,\mathrm{d}^2\boldsymbol{k} = \iint_{S_k} \Re(Z(\boldsymbol{k})N_i(\boldsymbol{\alpha})N_j(\boldsymbol{\alpha}))\,\mathrm{d}^2\boldsymbol{k} \tag{2.22d}$$

$$2E(k)H_{ij}(k)^{(\mathrm{h})} = \iint_{S_k} \hat{R}_{ij}^{(\mathrm{h})}(\boldsymbol{k})\,\mathrm{d}^2\boldsymbol{k} = \iint_{S_k} \imath\mathcal{H}(\boldsymbol{k})\epsilon_{ijn}\frac{k_n}{k}\,\mathrm{d}^2\boldsymbol{k} = 0, \tag{2.22e}$$

which defines the trace-deviator splitting $\Phi_{ij}(k) = 2E(k)\left(\frac{1}{3}\delta_{ij} + H_{ij}(k)\right)$ with $H_{ij}(k) = H_{ij}^{(\mathrm{dir})}(k) + H_{ij}^{(\mathrm{dir})}(k)$. Furthermore, if one integrates the spherically-averaged descriptors over all k, the decomposed RST can be given by:

$$\mathcal{R}_{ij} = 2\mathcal{K}\left(\frac{1}{3}\delta_{ij} + b_{ij}\right) = 2\mathcal{K}\left(\frac{1}{3}\delta_{ij} + b_{ij}^{(\mathrm{dir})} + b_{ij}^{(\mathrm{pol})}\right), \tag{2.23}$$

with

$$\mathcal{K} = \int E(k)\,\mathrm{d}k, \quad b_{ij}^{(\mathrm{dir})} = \frac{1}{\mathcal{K}}\int E(k)H_{ij}(k)^{(\mathrm{dir})}\,\mathrm{d}k, \quad b_{ij}^{(\mathrm{pol})} = \frac{1}{\mathcal{K}}\int E(k)H_{ij}(k)^{(\mathrm{pol})}\,\mathrm{d}k, \tag{2.24}$$

whereas the helicity components vanish in spherically-averaged level. It is easy to check that all the deviatoric components are trace-free, namely $H_{ii} = H_{ii}^{(\mathrm{dir})} = H_{ii}^{(\mathrm{pol})} = 0$ and $b_{ii} = b_{ii}^{(\mathrm{dir})} = b_{ii}^{(\mathrm{pol})} = 0$. Hence, the three-level descriptors and their connections are built in the context of HAT. Correspondingly, the turbulence models can be classified into 3D spectral models, spherically-averaged spectral models and single-point models.

2.1.2 Lin-type equations for the state vector $(\mathcal{E}\,, Z\,, \mathcal{H})$

The governing equations for $\hat{R}_{ij}(\boldsymbol{k},t)$ can be written as:

$$\dot{\hat{R}}_{ij}(\boldsymbol{k},t) + 2\nu k^2\hat{R}_{ij}(\boldsymbol{k},t) + M_{in}(\boldsymbol{k})\hat{R}_{nj}(\boldsymbol{k},t) + M_{jn}(\boldsymbol{k})\hat{R}_{in}(\boldsymbol{k},t) = T_{ij}(\boldsymbol{k},t), \tag{2.25}$$

benefiting from the characteristic lines defined as $\dfrac{\partial}{\partial t} + A_{ln}x_n\dfrac{\partial}{\partial x_l}$ in physical space and $\dfrac{\partial}{\partial t} - A_{ln}k_l\dfrac{\partial}{\partial k_n}$ in Fourier space by SLT. Then one can derive the equations for the decomposed components with (Cambon & Jacquin, 1989):

$$\dot{\mathcal{E}} = \frac{1}{2}\dot{\hat{R}}_{mm}\,,\; \dot{Z} = \frac{1}{2}\left(\dot{\hat{R}}_{ij}N_i^*N_j^* + \hat{R}_{ij}(\dot{N}_i^*N_j^* + N_i^*\dot{N}_j^*)\right)\,,\; \dot{\mathcal{H}} = \frac{1}{2}\imath\epsilon_{imj}(\dot{\alpha}_m\hat{R}_{ij} + \alpha_m\dot{\hat{R}}_{ij}). \tag{2.26}$$

Final equations for $\mathcal{E}$, Z and H can be obtained as:

$$\begin{aligned}\left(\frac{\partial}{\partial t} - A_{ln}k_l\frac{\partial}{\partial k_n} + 2\nu k^2\right)\mathcal{E}(\boldsymbol{k},t) - \mathcal{E}(\boldsymbol{k},t)S_{ij}\alpha_i\alpha_j& \\ +\Re(Z(\boldsymbol{k},t)S_{ij}N_i(\boldsymbol{\alpha})N_j(\boldsymbol{\alpha})) = T^{(\mathcal{E})}(\boldsymbol{k},t)&\end{aligned} \tag{2.27a}$$

$$\begin{aligned}\left(\frac{\partial}{\partial t} - A_{ln}k_l\frac{\partial}{\partial k_n} + 2\nu k^2\right)Z(\boldsymbol{k},t) - Z(\boldsymbol{k},t)S_{ij}\alpha_i\alpha_j + \mathcal{E}(\boldsymbol{k},t)S_{ij}N_i^*(\boldsymbol{\alpha})N_j^*(\boldsymbol{\alpha})& \\ -\,\imath Z(\boldsymbol{k},t)\underbrace{\left((W_l + 4\Omega_l)\,\alpha_l - \Omega^E\right)}_{\text{stropholysis}} = T^{(Z)}(\boldsymbol{k},t)&\end{aligned} \tag{2.27b}$$

$$\left(\frac{\partial}{\partial t} - A_{ln}k_l\frac{\partial}{\partial k_n} + 2\nu k^2\right)\mathcal{H}(\boldsymbol{k},t) = T^{(\mathcal{H})}(\boldsymbol{k},t), \tag{2.27c}$$

with

$$T^{(\mathcal{E})}(\boldsymbol{k},t) = \frac{1}{2}T_{mm}(\boldsymbol{k},t)\,, \quad T^{(Z)}(\boldsymbol{k},t) = \frac{1}{2}T_{ij}(\boldsymbol{k},t)N_i^*(\boldsymbol{\alpha})N_j^*(\boldsymbol{\alpha}),$$
$$T^{(\mathcal{H})}(\boldsymbol{k},t) = \frac{1}{2}\imath\frac{k_m}{k}\epsilon_{imj}T_{ij}(\boldsymbol{k},t). \tag{2.28}$$

S_{ij} and W_i in Eq.(2.27) are the symmetric part of A_{ij} and the mean vorticity respectively as introduced in §1.2.1 with

$$S_{ij} = \frac{A_{ij}+A_{ji}}{2}\,, \quad W_i = \epsilon_{min}A_{mn}, \tag{2.29}$$

whereas Ω_E is a special rotation induced by the advection operator with

$$\Omega^E = -e_i^{(2)}A_{ij}e_j^{(1)} - k\frac{n_iA_{ij}e_j^{(1)}}{k_\perp}, \quad k_\perp = |\boldsymbol{k}\times\boldsymbol{n}|, \tag{2.30}$$

which corresponds to the rotation required for transforming the Craya-Herring frame at time $t=0$ to that at subsequent time t along characteristic lines. We retain Ω_E here for the sake of completeness, but it can be removed when appropriate $\boldsymbol{n}$ and A_{ij} are chosen.

The **Lagrangian derivations for projections** are listed below.

For $\boldsymbol{k}$ and $\boldsymbol{\alpha}$

$$\dot{k_i} = -A_{ji}k_j\,,\ \dot{k} = \alpha_i\dot{k_i} = -\alpha_iA_{ji}k_j\,,\ \dot{\alpha}_i = -A_{ji}\alpha_j - \alpha_iA_{mn}\alpha_m\alpha_n. \tag{2.31}$$

For arbitrary orthonormal frame under solid-body motion, such as $\boldsymbol{e}^{(1)}, \boldsymbol{e}^{(2)}, \boldsymbol{e}^{(3)}$, we have

$$\dot{\left(e_i^{(m)}e_i^{(n)}\right)} = \dot{e}_i^{(m)}e_i^{(n)} + e_i^{(m)}\dot{e}_i^{(n)} = 0\,, \quad m=1,2,3, \tag{2.32}$$

so that

$$\dot{e}_i^3e_i^3 = 0, \quad \dot{e}_i^{(\alpha)}e_i^{(\beta)} = \epsilon_{\alpha\beta3}\Omega^E, \quad \alpha\,,\beta = 1,2,$$
$$\Omega^E = \dot{e}_i^{(1)}e_i^{(2)} = -\,e_i^{(2)}A_{ij}e_j^{(1)} - k\frac{n_iA_{ij}e_j^{(1)}}{k_\perp}, \quad k_\perp = |\boldsymbol{k}\times\boldsymbol{n}|. \tag{2.33}$$

In the same way, one finds

$$\dot{N_i}N_i = 0, \quad \dot{N_i}N_i^* = -2\imath\Omega^E, \quad \dot{N_i}e_i^{(3)} = -N_i\dot{e}_i^{(3)} = N_iA_{ji}e_j^{(3)} \tag{2.34}$$

so that we have

$$\dot{N_i} = \imath\Omega^EN_i + N_mA_{nm}e_n^{(3)}e_i^{(3)}\,, \tag{2.35}$$

and

$$\dot{N}_i^* = -\imath\Omega^EN_i^* + N_m^*A_{nm}e_n^{(3)}e_i^{(3)}\,. \tag{2.36}$$

The simplest equation is for the spectrum of helicity $\mathcal{H}$, which remains decoupled and is only affected by the mean-flow advection term, but without any 'production'. $\mathcal{H}$ can be used in principle (see Bellet *et al.*, 2006), but it will be neglected in the following: in our case of homogeneous shear-driven turbulence, and probably in almost all cases of HAT, for it must be initialized or forced to be present, and can never emerge spontaneously.

The left-hand sides of equations (2.27) for $\mathcal{E}$ and Z represent the linear effects of the mean flow as in viscous SLT, with geometric coefficients that depend on the orientation of the wavevector $\boldsymbol{\alpha}$ via helical modes. The pure straining process is mediated by the symmetric part of the mean-velocity gradients and is very similar in both equations, which motivates a splitting of the production spectrum in terms of directional anisotropy and polarization anisotropy. The antisymmetric part only affects the equation for polarization, and includes a combination of mean and system vorticity—the 'stropholysis' effect coined by Kassinos *et al.* (2001)— which renders linear solutions complicated. When 'stropholysis' is absent, the linear effect amounts to a simple stretching of the fluctuating vorticity by the irrotational mean strain. In addition, the phase term, which amounts to rotating the plane of polarization, is related to twice the dispersion frequency $2\boldsymbol{\Omega}\cdot\boldsymbol{\alpha}$ of inertial waves for purely rotating turbulence (Cambon & Jacquin, 1989). It is replaced by a similar term, which seems to display the 'tilting vorticity' in Eq.(2.27b), $2\boldsymbol{\Omega}+\boldsymbol{W}/2$, instead of the absolute vorticity $2\boldsymbol{\Omega}+\boldsymbol{W}$.

The right-hand sides of equations (2.27a) and (2.27b) gather the contribution from two-point third-order correlations mediated by the quadratic nonlinearity of basic Navier-Stokes equations and are closed in the following section.

2.1.3 EDQNM closure for transfer terms

As introduced in 1.3.4, it is a hard work to extend EDQNM closure from HIT to HAT. The governing equations for the three-point third-order correlation tensor $\hat{S}_{ijn}(\boldsymbol{k},\boldsymbol{p},t)$ can be written as

$$\left(\frac{\partial}{\partial t}+\nu(k^2+p^2+q^2)\right)\hat{S}_{ijn}(\boldsymbol{k},\boldsymbol{p},t)=L_{ijn}(\boldsymbol{k},\boldsymbol{p},t)+T_{ijn}(\boldsymbol{k},\boldsymbol{p},t)=R_{ijn}(\boldsymbol{k},\boldsymbol{p},t)\,, \quad (2.37)$$

where $L_{ijn}(\boldsymbol{k},\boldsymbol{p},t)$ gathers the linear operators induced by mean-velocity gradients and $T_{ijn}(\boldsymbol{k},\boldsymbol{p},t)$ gathers the contribution from the fourth order as in HIT. Although the $L_{ijn}(\boldsymbol{k},vp,t)$ term is closed in the preceding equation, the simplest strategy is to neglect it.

Similar to the procedure in HIT, with EDQNM assumptions, one can obtain that

$$\hat{S}_{ijn}(\boldsymbol{k},\boldsymbol{p},t)=\theta_{kpq}T^{(\mathrm{QN})}_{ijn}(\boldsymbol{k},\boldsymbol{p},t)\,, \quad (2.38)$$

with

$$\theta_{kpq} = \frac{1 - e^{-\mu_{kpq} t}}{\mu_{kpq}} \,. \tag{2.39}$$

Then, the tensor $\tau_{ij}(\boldsymbol{k}, t)$ defined by Eq.1.35 amounts to

$$\tau_{ij}(\boldsymbol{k}, t) = k_l \iiint \theta_{kpq} T^{(\mathrm{QN})}_{ijl}(\boldsymbol{k}, \boldsymbol{p}, t) \, \mathrm{d}^3\boldsymbol{p}, \tag{2.40}$$

and the transfer terms to be closed are

$$T^{(\mathcal{E})}(\boldsymbol{k}, t) = \frac{1}{2} T_{ii}(\boldsymbol{k}, t) = \frac{1}{2}(\tau_{ii}(\boldsymbol{k}, t) + \tau^*_{ii}(\boldsymbol{k}, t)) \,, \tag{2.41}$$

$$T^{(Z)}(\boldsymbol{k}, t) = \frac{1}{2} T_{ij}(\boldsymbol{k}, t) N^*_i(\boldsymbol{\alpha}) N^*_j(\boldsymbol{\alpha}) = \frac{1}{2}(\tau_{ij}(\boldsymbol{k}, t) + \tau^*_{ji}(\boldsymbol{k}, t)) N^*_i(\boldsymbol{\alpha}) N^*_j(\boldsymbol{\alpha}) \,. \tag{2.42}$$

As mentioned in §1.3.4, $T_{ij}(\boldsymbol{k}, t)$ includes both the 'true' transfer tensor, with zero integral, and a contribution $W_{ij}(\boldsymbol{k}, t)$ involved in the return-to-isotropy effect (Mons *et al.*, 2016). The latter tensor can be generated from a scalar transfer term $T^{(\mathrm{RTI})}(\boldsymbol{k}, t)$ according to

$$W_{ij}(\boldsymbol{k}, t) = -\Re\Big(T^{(\mathrm{RTI})}(\boldsymbol{k}, t)(\alpha_i N_j(\boldsymbol{\alpha}) + \alpha_j N_i(\boldsymbol{\alpha}))\Big), \tag{2.43}$$

consistently with $\tau_{ij}(\boldsymbol{k}, t) k_j = 0$, $\tau_{ij}(\boldsymbol{k}, t) k_i \neq 0$, and

$$T^{(\mathrm{RTI})}(\boldsymbol{k}, t) = \alpha_i(\tau_{ij}(\boldsymbol{k}, t) + \tau^*_{ji}(\boldsymbol{k}, t)) N^*_j(\boldsymbol{\alpha}) = \alpha_i \tau_{ij}(\boldsymbol{k}, t) N^*_j(\boldsymbol{\alpha}) \,. \tag{2.44}$$

Plugging Eq.(1.56) into (2.40) yields

$$\begin{aligned} \tau_{ij}(\boldsymbol{k}, t) = 2k_l \iiint & \theta_{kpq}\big(P_{imn}(\boldsymbol{q}) \hat{R}_{mj}(\boldsymbol{k}, t) \hat{R}_{nl}(\boldsymbol{p}, t) \\ & + P_{jmn}(\boldsymbol{k}) \hat{R}_{ml}(\boldsymbol{p}, t) \hat{R}_{ni}(\boldsymbol{q}, t) + P_{lmn}(\boldsymbol{p}) \hat{R}_{mi}(\boldsymbol{q}, t) \hat{R}_{nj}(\boldsymbol{k}, t)\big) \, \mathrm{d}^3\boldsymbol{p} \,, \end{aligned} \tag{2.45}$$

where $\boldsymbol{k} + \boldsymbol{p} + \boldsymbol{q} = \boldsymbol{0}$. Considering the decomposed expression of $\hat{\boldsymbol{R}}$ in terms of $\mathcal{E}$ and Z in helical mode, the complicated calculation in Eq.(2.45) is actually related to the products of projections in local frame.

First of all, the plane formed by $\boldsymbol{k}$, $\boldsymbol{p}$ and $\boldsymbol{q}$ are determined by the moduli k, p and q, the geometric parameters, and by the unit normal vector $\boldsymbol{\gamma}$ with $\boldsymbol{\gamma} = \dfrac{\boldsymbol{k} \times \boldsymbol{p}}{|\boldsymbol{k} \times \boldsymbol{p}|}$. It is convenient to define a new local frame $(\boldsymbol{\gamma}, \boldsymbol{\beta}, \boldsymbol{\alpha})$ associated to $\boldsymbol{k}$ with $\boldsymbol{\beta} = \dfrac{\boldsymbol{k} \times \boldsymbol{\gamma}}{|\boldsymbol{k} \times \boldsymbol{\gamma}|}$. In the same way, one can define $(\boldsymbol{\gamma}, \boldsymbol{\beta'}, \boldsymbol{\alpha'})$ and $(\boldsymbol{\gamma}, \boldsymbol{\beta''}, \boldsymbol{\alpha''})$ with

$$\boldsymbol{\alpha'} = \frac{\boldsymbol{p}}{p} \,, \quad \boldsymbol{\beta'} = \frac{\boldsymbol{p} \times \boldsymbol{\gamma}}{|\boldsymbol{p} \times \boldsymbol{\gamma}|} \,, \quad \boldsymbol{\alpha''} = \frac{\boldsymbol{q}}{q} \,, \quad \boldsymbol{\beta''} = \frac{\boldsymbol{q} \times \boldsymbol{\gamma}}{|\boldsymbol{q} \times \boldsymbol{\gamma}|} \,. \tag{2.46}$$

Figure 2.2 illustrates the geometry of the triadic plane (Cambon & Jacquin, 1989). The geometric coefficients are expressed by angles a, b and c and their cosines are denoted as

$$x = \cos a = -\frac{\boldsymbol{p} \cdot \boldsymbol{q}}{|\boldsymbol{p} \cdot \boldsymbol{q}|} \,, \quad y = \cos b = -\frac{\boldsymbol{q} \cdot \boldsymbol{k}}{|\boldsymbol{q} \cdot \boldsymbol{k}|} \,, \quad z = \cos c = -\frac{\boldsymbol{k} \cdot \boldsymbol{p}}{|\boldsymbol{k} \cdot \boldsymbol{p}|} \,. \tag{2.47}$$

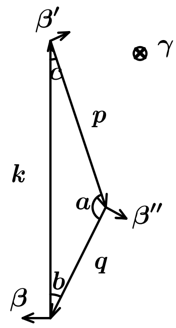

Figure 2.2: Illustration for the geometric information of plane formed by $\boldsymbol{k}$, $\boldsymbol{p}$ and $\boldsymbol{q}$.

Consequently, the sines are

$$\sin a = \sqrt{1-x^2}\,, \quad \sin b = \sqrt{1-y^2}\,, \quad \sin c = \sqrt{1-z^2}\,. \tag{2.48}$$

The rotation of the triadic plane could be characterized by the angles λ, λ' and λ'' around $\boldsymbol{k}$, $\boldsymbol{p}$ and $\boldsymbol{q}$ respectively with

$$\underbrace{\boldsymbol{e}^{(2)}(\boldsymbol{\alpha}) - \imath\boldsymbol{e}^{(1)}(\boldsymbol{\alpha})}_{\boldsymbol{N}(\boldsymbol{\alpha})} = e^{\imath\lambda}\underbrace{(\boldsymbol{\beta}+\imath\boldsymbol{\gamma})}_{\boldsymbol{\mathcal{W}}} \tag{2.49a}$$

$$\underbrace{\boldsymbol{e}^{(2)}(\boldsymbol{\alpha}') - \imath\boldsymbol{e}^{(1)}(\boldsymbol{\alpha}')}_{\boldsymbol{N}(\boldsymbol{\alpha}')} = e^{\imath\lambda}\underbrace{(\boldsymbol{\beta}'+\imath\boldsymbol{\gamma})}_{\boldsymbol{\mathcal{W}}'} \tag{2.49b}$$

$$\underbrace{\boldsymbol{e}^{(2)}(\boldsymbol{\alpha}'') - \imath\boldsymbol{e}^{(1)}(\boldsymbol{\alpha}'')}_{\boldsymbol{N}(\boldsymbol{\alpha}'')} = e^{\imath\lambda}\underbrace{(\boldsymbol{\beta}''+\imath\boldsymbol{\gamma})}_{\boldsymbol{\mathcal{W}}''}\,. \tag{2.49c}$$

Obviously, the rotations λ, λ' and λ'' are dependent on γ. The contribution by polarization component of $\hat{\boldsymbol{R}}$ can be expressed by the geometric coefficients, e.g.

$$Z(\boldsymbol{p})N_i(\boldsymbol{p})N_j(\boldsymbol{p}) = Z(\boldsymbol{p})\mathcal{W}_i'\mathcal{W}_j'e^{2\imath\lambda'}\,, \tag{2.50}$$

so that the final formulae for $T^{(\mathcal{E})}$ and $T^{(Z)}$ should be expressed by triadic geometric parameters, in addition to $\mathcal{E}(\boldsymbol{k})$, $\mathcal{E}(\boldsymbol{p})$, $\mathcal{E}(\boldsymbol{q})$, $Z(\boldsymbol{k})e^{2\imath\lambda}$, $Z(\boldsymbol{p})e^{2\imath\lambda'}$ and $Z(\boldsymbol{q})e^{2\imath\lambda''}$.

Now, all the projections could be projected into the local frame associated to $\boldsymbol{k}$ as:

$$\begin{aligned} \boldsymbol{\alpha}' &= -z\boldsymbol{\alpha} - \sqrt{1-z^2}\boldsymbol{\beta}\,, \quad \boldsymbol{\beta}' = -z\boldsymbol{\beta} + \sqrt{1-z^2}\boldsymbol{\alpha}, \\ \boldsymbol{\alpha}'' &= -y\boldsymbol{\alpha} + \sqrt{1-y^2}\boldsymbol{\beta}, \,, \quad \boldsymbol{\beta}'' = -y\boldsymbol{\beta} - \sqrt{1-y^2}\boldsymbol{\alpha}\,, \end{aligned} \tag{2.51}$$

with

$$\begin{aligned} \boldsymbol{\mathcal{W}}' &= \sqrt{1-z^2}\boldsymbol{\alpha} + \frac{1-z}{2}\boldsymbol{N}e^{-\imath\lambda} - \frac{1+z}{2}\boldsymbol{N}^*e^{\imath\lambda}\,, \\ \boldsymbol{\mathcal{W}}'' &= -\sqrt{1-y^2}\boldsymbol{\alpha} + \frac{1-y}{2}\boldsymbol{N}e^{-\imath\lambda} - \frac{1+y}{2}\boldsymbol{N}^*e^{\imath\lambda}\,. \end{aligned} \tag{2.52}$$

The readers could find details of the derivation in Appendix C. After complicated calculations, the final results are found as:

$$T^{(\mathcal{E})}(\boldsymbol{k},t) = \iiint \theta_{kpq} 2kp\Big[(\mathcal{E}'' + \Re X'')\big[(xy+z^3)(\mathcal{E}'-\mathcal{E}) - z(1-z^2)(\Re X' - \Re X)\big] + \Im X''(1-z^2)(x\Im X - y\Im X')\Big]\,\mathrm{d}^3\boldsymbol{p}\,, \tag{2.53}$$

$$T^{(Z)}(\boldsymbol{k},t) = \iiint \theta_{kpq} 2kp e^{-2\mathrm{i}\lambda}\Big[(\mathcal{E}'' + \Re X'')\big[(xy+z^3)(\Re X' - X) - z(1-z^2)(\mathcal{E}^{'} - \mathcal{E}) + \mathrm{i}(y^2-z^2)\Im X'\big] + \mathrm{i}\Im X''(1-z^2)\big[x(\mathcal{E}+X) - \mathrm{i}y\Im X'\big]\Big]\,\mathrm{d}^3\boldsymbol{p}\,, \tag{2.54}$$

along with

$$T^{(\mathrm{RTI})}(\boldsymbol{k},t) = \iiint \theta_{kpq} 2e^{-\mathrm{i}\lambda} p(xy+z)\sqrt{1-z^2}(\mathcal{E}'' + \Re X'')\Big[(\mathcal{E}+X)(zk-qx) - k\left(z(\mathcal{E}' + \Re X') - \mathrm{i}\Im X'\right)\Big]\,\mathrm{d}^3\boldsymbol{p}\,. \tag{2.55}$$

The above nonlinear model is referred to EDQNM-1 (Sagaut & Cambon, 2018). A remarkable feature of the model is that it makes a distinction between directional and polarization anisotropy, which are treated separately. As discussed in §1.3.4, one has to be very careful when extending EDQNM closure from HIT to HAT. EDQNM-1 ignores the linear operators for third-order correlations, since it is sufficient to take into account the explicit linear effects on the equations for second-order correlations but not on the triple ones when there is production term acting on the former. This is confirmed by accurate quantitative comparisons between EDQNM and DNS, as in the rather recent study by Burlot *et al.* (2015) for Unstably Stratified Homogeneous Turbulence. However, the isotropy simplification is questioned in purely rotating turbulence. In this special case, the Coriolis force does not affect the energy equation directly—no 'production'—so that system rotation cannot be ignored in the equations for the triple ones. Such purely nonlinear dynamics are dominated by nonlinearly interacting inertial waves, and it is possible to match the most elaborate EDQNM2-3 models with inertial wave turbulence theory (Cambon & Jacquin, 1989; Bellet *et al.*, 2006), which renders the tensorial structure of the EDQNM model via a threefold product of Green's functions, and explicitly depends on the type of mean shear, preventing easy further projection on spherical harmonics. The quasi-isotropic form of eddy damping term, by means of a single eddy damping coefficient $\eta(\boldsymbol{k},t)$, can be only supported by DNS/EDQNM cross-validation. At least, it is possible to give an overall isotropized model for the sum of the explicit linear terms and the eddy damping operators as in Burlot *et al.* (2015). The last problem we mentioned in §1.3.4 is the Markovianization. In the case of wave turbulence theory, as in strongly rotating turbulence, the phase-mixing due to interacting inertial waves severely damps the inertial transfers, and there is no need for an 'ad-hoc' eddy-damping. But final equations are similar to 'Markovianized' ones: this is because of the time-scale separation between rapid phases and slow amplitudes. Incidentally, the Markovianization raises the problem of a possible two-time description, in addition to the multipoint one. Discussion of two-time theory is outside our scope, but our long experience is that the usual applications cannot even match 3D anisotropic wave turbulence theory.

Actually, EDQNM-1 for fully anisotropic velocity field has not been implemented numerically, even though the equations are closed. The calculation for $T^{(\mathcal{E})}$, $T^{(Z)}$ and $T^{(\mathrm{RTI})}$ involves 3D convolution, which renders a double-polar system built for each local $\boldsymbol{k}$ and can be very complicated. The computational cost is supposed to be increased with more anisotropy but not sensitive to Reynolds number compared to DNS as confirmed firstly in axisymmetric case by Burlot *et al.* (2015).

2.2 MCS: the spherically-averaged model with truncation

In order to circumvent the difficulties arising from the $\boldsymbol{k}$ dependence, a simplified model was proposed by Mons *et al.* (2016), using a purely technical straightforward procedure: it allowed to pass from EDQNM-1 for spectra depending on a three-dimensional wavevector $\boldsymbol{k}$ to a model in terms of spherically-averaged descriptors, which accomplished a drastic reduction of the complexity and of the numerical cost. This model involves spherically-averaged descriptors along with its governing equations is referred to 'MCS'.

2.2.1 Tensorial expansion and spherically-averaged equations

The solution given by MCS is to integrate analytically the closed Lin equations over a sphere of radius k. This analytical integration requires a representation of the tensor $\hat{R}_{ij}(\boldsymbol{k}, t)$. Here, we use for $\hat{R}_{ij}(\boldsymbol{k}, t)$ the representation proposed by Cambon & Rubinstein (2006). This representation involves spherically-averaged descriptors and is obtained by treating the directional anisotropy and the polarization anisotropy separately. It is written as:

$$
\begin{aligned}
\hat{R}_{ij}(\boldsymbol{k},t) = & \underbrace{\frac{E(k,t)}{4\pi k^2} P_{ij}(\boldsymbol{k})}_{\hat{R}^{(\mathrm{iso})}_{ij}(\boldsymbol{k},t)} \underbrace{-15\frac{E(k,t)}{4\pi k^2} P_{ij}(\boldsymbol{k}) H^{(\mathrm{dir})}_{pq}(k,t)\alpha_p\alpha_q}_{\hat{R}^{(\mathrm{dir})}_{ij}(\boldsymbol{k},t)} \\
& \underbrace{+ 5\frac{E(k,t)}{4\pi k^2}\left(P_{ip}(\boldsymbol{k})P_{jq}(\boldsymbol{k}) + \frac{1}{2}P_{ij}(\boldsymbol{k})\alpha_p\alpha_q\right) H^{(\mathrm{pol})}_{pq}(k,t),}_{\hat{R}^{(\mathrm{pol})}_{ij}(\boldsymbol{k},t)}
\end{aligned}
\tag{2.56}
$$

or equivalently

$$
\mathcal{E}(\boldsymbol{k},t) = \frac{E(k,t)}{4\pi k^2}\left(1 - 15 H^{(\mathrm{dir})}_{ij}(k,t)\alpha_i\alpha_j\right), \quad Z(\boldsymbol{k},t) = \frac{5}{2}\frac{E(k,t)}{4\pi k^2} H^{(\mathrm{pol})}_{ij}(k,t) N^*_i(\boldsymbol{k}) N^*_j(\boldsymbol{k})\,. \tag{2.57}
$$

The final model is in terms of spherically-averaged descriptors for $\hat{R}_{ij}(\boldsymbol{k},t)$, including its isotropic, directional anisotropic and polarization anisotropic components $E(k,t)$, $EH^{(\mathrm{dir})}_{ij}(k,t)$ and $EH^{(\mathrm{pol})}_{ij}(k,t)$ with the relationship introduced in the previous section:

$$
\begin{aligned}
E(k) &= \iint_{S_k} \mathcal{E}(\boldsymbol{k})\,\mathrm{d}^2\boldsymbol{k} \\
2E(k)H_{ij}(k)^{(\mathrm{dir})} &= \iint_{S_k} \hat{R}^{(\mathrm{dir})}_{ij}(\boldsymbol{k})\,\mathrm{d}^2\boldsymbol{k} = \iint_{S_k}\left(\mathcal{E}(\boldsymbol{k}) - \frac{E(k)}{4\pi k^2}\right) P_{ij}(\boldsymbol{\alpha})\,\mathrm{d}^2\boldsymbol{k} \\
2E(k)H_{ij}(k)^{(\mathrm{pol})} &= \iint_{S_k} \hat{R}^{(\mathrm{pol})}_{ij}(\boldsymbol{k})\,\mathrm{d}^2\boldsymbol{k} = \iint_{S_k} \Re(Z(\boldsymbol{k})N_i(\boldsymbol{\alpha})N_j(\boldsymbol{\alpha}))\,\mathrm{d}^2\boldsymbol{k}\,,
\end{aligned}
\tag{2.58}
$$

with $\varphi_{ij}(k) = \iint_{S_k} \hat{R}_{ij}(\boldsymbol{k})\,\mathrm{d}^2\boldsymbol{k} = 2E(k,t)\left(\frac{\delta_{ij}}{3} + H^{(\mathrm{dir})}_{ij}(k,t) + H^{(\mathrm{pol})}_{ij}(k,t)\right)$. For the sake of convenience, we denote the Lin-type equations for $\mathcal{E}(\boldsymbol{k},t)$ and $Z(\boldsymbol{k},t)$ as:

$$
\left(\frac{\partial}{\partial t} + 2\nu k^2\right)\mathcal{E}(\boldsymbol{k},t) = L^{(\mathrm{dir})}(\boldsymbol{k},t) + T^{(\mathcal{E})}(\boldsymbol{k},t) \tag{2.59a}
$$

$$
\left(\frac{\partial}{\partial t} + 2\nu k^2\right) Z(\boldsymbol{k},t) = L^{(\mathrm{pol})}(\boldsymbol{k},t) + T^{(Z)}(\boldsymbol{k},t)\,. \tag{2.59b}
$$

Hence, the equation for $E(k,t)$, $EH^{(\mathrm{dir})}_{ij}(k,t)$ and $EH^{(\mathrm{pol})}_{ij}(k,t)$ can be derived from:

$$
\begin{aligned}
\frac{\partial E(k,t)}{\partial t} &= \iint_{S_k} \frac{\partial \mathcal{E}(\boldsymbol{k},t)}{\partial t}\,\mathrm{d}^2\boldsymbol{k} \\
\frac{\partial\left(E(k)H_{ij}(k,t)^{(\mathrm{dir})}\right)}{\partial t} &= \frac{1}{2}\iint_{S_k}\left(\frac{\partial \mathcal{E}(\boldsymbol{k},t)}{\partial t} - \frac{1}{4\pi k^2}\frac{\partial E(k,t)}{\partial t}\right) P_{ij}(\boldsymbol{\alpha})\,\mathrm{d}^2\boldsymbol{k} \\
\frac{\partial\left(E(k)H_{ij}(k,t)^{(\mathrm{pol})}\right)}{\partial t} &= \frac{1}{2}\iint_{S_k} \Re\left(\frac{\partial Z(\boldsymbol{k},t)}{\partial t} N_i(\boldsymbol{\alpha})N_j(\boldsymbol{\alpha})\right)\mathrm{d}^2\boldsymbol{k}\,.
\end{aligned}
\tag{2.60}
$$

Injecting Eq.(2.59) into the above equations, the spherically-averaged equations are found as:

$$\left(\frac{\partial}{\partial t}+2\nu k^2\right)E(k,t)=\mathcal{S}^{\mathrm{L}}(k,t)+T(k,t)\,, \tag{2.61a}$$

$$\left(\frac{\partial}{\partial t}+2\nu k^2\right)E(k,t)H_{ij}^{(\mathrm{dir})}(k,t)=\mathcal{S}_{ij}^{\mathrm{L(dir)}}(k,t)+\mathcal{S}_{ij}^{\mathrm{NL(dir)}}(k,t)\,, \tag{2.61b}$$

$$\left(\frac{\partial}{\partial t}+2\nu k^2\right)E(k,t)H_{ij}^{(\mathrm{pol})}(k,t)=\mathcal{S}_{ij}^{\mathrm{L(pol)}}(k,t)+\mathcal{S}_{ij}^{\mathrm{NL(pol)}}(k,t)\,, \tag{2.61c}$$

with

$$\begin{aligned}\mathcal{S}^{\mathrm{L}}(k,t)=\iint_{S_k}L^{(\mathcal{E})}(\boldsymbol{k},t)\,\mathrm{d}^2\boldsymbol{k}\,,\quad \mathcal{S}_{ij}^{\mathrm{L(dir)}}(k,t)&=\frac{1}{2}\iint_{S_k}L^{(\mathcal{E})}(\boldsymbol{k},t)P_{ij}(\boldsymbol{\alpha})\,\mathrm{d}^2\boldsymbol{k}-\frac{1}{3}\delta_{ij}S^{\mathrm{L}}(k,t)\,,\\ \mathcal{S}_{ij}^{\mathrm{L(pol)}}(k,t)&=\frac{1}{2}\iint_{S_k}\Re\Big(L^{(Z)}(\boldsymbol{k},t)N_i(\boldsymbol{\alpha})N_j(\boldsymbol{\alpha})\Big)\,\mathrm{d}^2\boldsymbol{k}\,,\end{aligned} \tag{2.62a}$$

$$\begin{aligned}T(k,t)=\iint_{S_k}T^{(\mathcal{E})}(\boldsymbol{k},t)\,\mathrm{d}^2\boldsymbol{k}\,,\quad \mathcal{S}_{ij}^{\mathrm{NL(dir)}}(k,t)&=\frac{1}{2}\iint_{S_k}T^{(\mathcal{E})}(\boldsymbol{k},t)P_{ij}(\boldsymbol{\alpha})\,\mathrm{d}^2\boldsymbol{k}-\frac{1}{3}\delta_{ij}T(k,t)\,,\\ \mathcal{S}_{ij}^{\mathrm{NL(pol)}}(k,t)&=\frac{1}{2}\iint_{S_k}\Re\Big(T^{(Z)}(\boldsymbol{k},t)N_i(\boldsymbol{\alpha})N_j(\boldsymbol{\alpha})\Big)\,\mathrm{d}^2\boldsymbol{k}\,.\end{aligned} \tag{2.62b}$$

The tensors $\mathcal{S}^{\mathrm{L}}(k,t)$, $\mathcal{S}_{ij}^{\mathrm{L(dir)}}(k,t)$ and $\mathcal{S}_{ij}^{\mathrm{L(pol)}}(k,t)$, inherited from SLT, account for the linear terms corresponding to the interactions with the mean flow and the rotation of the frame, whereas $T(k,t)$, $\mathcal{S}_{ij}^{\mathrm{NL(dir)}}(k,t)$ and $\mathcal{S}_{ij}^{\mathrm{NL(pol)}}(k,t)$ correspond to nonlinear transfer terms. The nonlinear terms imply the following relationship:

$$2\left(\frac{\delta_{ij}}{3}T(k,t)+\mathcal{S}_{ij}^{\mathrm{NL(dir)}}(k,t)+\mathcal{S}_{ij}^{\mathrm{NL(pol)}}(k,t)\right)=\mathcal{S}_{ij}(k,t)+\mathcal{P}_{ij}(k,t)\,, \tag{2.63}$$

where the tensor $\mathcal{P}_{ij}(k,t)$ is the spherically integrated spectral counterpart of the 'slow' pressure-strain rate tensor with

$$\mathcal{P}_{ij}(k,t)=-\iint_{S_k}\Re\Big(T^{(\mathrm{RTI})}(\boldsymbol{k},t)\,(\alpha_iN_j\boldsymbol{k}+\alpha_jN_i\boldsymbol{k})\Big)\,\mathrm{d}^2\boldsymbol{k}\,, \tag{2.64}$$

and tensor $\mathcal{S}_{ij}(k,t)$ represents the 'true' transfer tensor whose integrals over k is zero. Since the tensors $H_{ij}^{(\mathrm{dir})}(k,t)$ and $H_{ij}^{(\mathrm{pol})}(k,t)$ are symmetric and trace-free, the system (2.62) forms a set of 11 different equations.

So far, the above expressions are derived without relationship (2.56) or (2.57), which are used next to calculate the spherical integrals.

2.2.2 Linear terms

In order to obtain the spherically-averaged terms $\mathcal{S}^{\mathrm{L}}(k,t)$, $\mathcal{S}_{ij}^{\mathrm{L(dir)}}(k,t)$ and $\mathcal{S}_{ij}^{\mathrm{L(pol)}}(k,t)$, one has to analytically solve the spherical averaging of tensorial products of vectors $\boldsymbol{\alpha}$. This is done as (Cambon *et al.*, 1981):

$$\iint_{S_k} \alpha_{i_1}\alpha_{i_2}\cdots\alpha_{i_{2N}}\,\mathrm{d}^2\boldsymbol{k} = \frac{4\pi k^2}{1\cdot 3\cdots(2N+1)}\delta^N_{i_1 i_2\cdots i_{2N}}, \tag{2.65}$$

where $\delta^N_{i_1 i_2\cdots i_{2N}}$ is defined by:

$$\delta^1_{ij} = \delta_{ij}, \quad \delta^N_{i_1 i_2\cdots i_{2N}} = \sum_{r=1}^{2N-1} \delta_{i_r i_{2N}}\delta^{N-1}_{i_1 i_2\cdots i_{r-1} i_{r+1}\cdots i_{2N-1}}. \tag{2.66}$$

By plugging the relationship (2.57) into (2.62a), in addition with spherical integrations performed thanks to equation (2.65), the final expressions are obtained:

$$\mathcal{S}^{\mathrm{L}}(k,t) = -2S_{lm}\frac{\partial}{\partial k}\left(kEH^{(\mathrm{dir})}_{lm}\right) - 2ES_{lm}\Big(H^{(\mathrm{dir})}_{lm} + H^{(\mathrm{pol})}_{lm}\Big), \tag{2.67}$$

$$\begin{aligned}
\mathcal{S}_{ij}^{\mathrm{L(dir)}}(k,t) &= \frac{2}{15}S_{ij}E - \frac{2}{7}E\Big(S_{jl}H^{(\mathrm{pol})}_{il} + S_{il}H^{(\mathrm{pol})}_{jl} - \frac{2}{3}S_{lm}H^{(\mathrm{pol})}_{lm}\delta_{ij}\Big)\\
&+ \frac{2}{7}\Big(S_{il}\frac{\partial}{\partial k}\left(kEH^{(\mathrm{dir})}_{lj}\right) + S_{lj}\frac{\partial}{\partial k}\left(kEH^{(\mathrm{dir})}_{li}\right) - \frac{2}{3}S_{lm}\frac{\partial}{\partial k}\left(kEH^{(\mathrm{dir})}_{lm}\right)\delta_{ij}\Big)\\
&- \frac{1}{7}E\Big(S_{jl}H^{(\mathrm{dir})}_{li} + S_{il}H^{(\mathrm{dir})}_{lj} - \frac{2}{3}S_{lm}H^{(\mathrm{dir})}_{lm}\delta_{ij}\Big) + \frac{1}{2}E\Big(\epsilon_{jln}W_l H^{(\mathrm{dir})}_{ni} + \epsilon_{iln}W_l H^{(\mathrm{dir})}_{jn}\Big)\\
&- \frac{1}{15}S_{ij}\frac{\partial}{\partial k}(kE),
\end{aligned} \tag{2.68}$$

$$\begin{aligned}
\mathcal{S}_{ij}^{\mathrm{L(pol)}}(k,t) &= -\frac{2}{5}ES_{ij} - \frac{12}{7}E\Big(S_{lj}H^{(\mathrm{dir})}_{li} + S_{il}H^{(\mathrm{dir})}_{lj} - \frac{2}{3}S_{lm}H^{(\mathrm{dir})}_{lm}\delta_{ij}\Big)\\
&- \frac{2}{7}\Big(S_{jl}\frac{\partial}{\partial k}\left(kEH^{(\mathrm{pol})}_{il}\right) + S_{il}\frac{\partial}{\partial k}\left(kEH^{(\mathrm{pol})}_{lj}\right) - \frac{2}{3}S_{ln}\frac{\partial}{\partial k}\left(kEH^{(\mathrm{pol})}_{ln}\right)\delta_{ij}\Big)\\
&+ \frac{1}{7}E\Big(S_{il}H^{(\mathrm{pol})}_{lj} + S_{jl}H^{(\mathrm{pol})}_{li} - \frac{2}{3}S_{lm}H^{(\mathrm{pol})}_{lm}\delta_{ij}\Big) - \frac{1}{6}E\Big(\epsilon_{iml}W_m H^{(\mathrm{pol})}_{lj} + \epsilon_{jml}H^{(\mathrm{pol})}_{li}\Big)\\
&- \frac{4}{3}E\Big(\epsilon_{ilr}\Omega_l H^{(\mathrm{pol})}_{rj} + \epsilon_{jlr}\Omega_l H^{(\mathrm{pol})}_{ri}\Big),
\end{aligned} \tag{2.69}$$

with $E = E(k,t)$, $H^{(\mathrm{dir})}_{ij} = H^{(\mathrm{dir})}_{ij}(k,t)$, $H^{(\mathrm{pol})}_{ij} = H^{(\mathrm{pol})}_{ij}(k,t)$.

Here we give some intermediate results of spherical integrals:

$$\iint_{S_k} H^{()}_{mn}\alpha_m\alpha_n P_{ij}\,\mathrm{d}^2\boldsymbol{k} = -\frac{8\pi k^2}{15}H^{()}_{ij}, \quad \iint_{S_k} H^{()}_{mn}N^*_m N^*_n N_i N_j\,\mathrm{d}^2\boldsymbol{k} = \frac{16\pi k^2}{5}H^{()}_{ij}\,,$$
$$\iint_{S_k} H^{()}_{mn}\alpha_m N^*_n \alpha_i N_j\,\mathrm{d}^2\boldsymbol{k} = \frac{4\pi k^2}{5}H^{()}_{ij}\,,$$
$$\iint_{S_k} A_{ln}H^{()}_{pq}\alpha_i\alpha_j\alpha_l\alpha_n\alpha_p\alpha_q\,\mathrm{d}^2\boldsymbol{k} = \frac{8\pi k^2}{105}\left(2S_{il}H^{()}_{lj} + 2S_{jl}H^{()}_{li} + A_{ln}H^{()}_{ln}\delta_{ij}\right), \tag{2.70}$$

$$\iint_{S_k} A_{ln}k_l\frac{\partial}{\partial k_n}\left(H^{()}_{pq}\alpha_p\alpha_q\alpha_i\alpha_j\right)\mathrm{d}^2\boldsymbol{k} = \frac{8\pi k^2}{105}\Big[S_{il}\big(k\frac{\partial H^{()}_{lj}}{\partial k} + 3H^{()}_{lj}\big)$$
$$+\big(A_{jl}k\frac{\partial H^{()}_{li}}{\partial k} + 3H^{()}_{li}\big) + A_{ln}\big(k\frac{\partial H^{()}_{ln}}{\partial k} + 3H_{ln}\big)\delta_{ij}\Big], \tag{2.71}$$
$$\iint_{S_k} A_{ln}k_l\frac{\partial \mathcal{E}_0\alpha_i\alpha_j}{\partial k_n}\,\mathrm{d}^2\boldsymbol{k} = \frac{8\pi k^2}{15}S_{ij}\left(3\mathcal{E}_0 + k\frac{\partial\mathcal{E}_0}{\partial k}\right),$$

where $\mathcal{E}_0 = \dfrac{E(k,t)}{4\pi k^2}$ and $H^{()}_{ij}$ may refer to either $H^{(\mathrm{dir})}_{ij}(k,t)$ or $H^{(\mathrm{pol})}_{ij}(k,t)$.

2.2.3 Nonlinear closure with EDQNM

The analytical calculation for the transfer terms $T(k,t)$, $S^{\mathrm{NL(dir)}}_{ij}(k,t)$, $S^{\mathrm{NL(pol)}}_{ij}(k,t)$ and $\mathcal{P}_{ij}(k,t)$ is a bit complex. The first step of the derivation consists in injecting in (2.53)-(2.55) the expressions of $\mathcal{E}(\boldsymbol{k},t)$, $\mathcal{E}(\boldsymbol{p},t)$, $\mathcal{E}(\boldsymbol{q},t)$ and $Z(\boldsymbol{k},t)$, $Z(\boldsymbol{p},t)$, $Z(\boldsymbol{q},t)$ given in (2.57). Quadratic contributions of the tensors $H^{(\mathrm{dir})}_{ij}$ and $H^{(\mathrm{pol})}_{ij}$ are disregarded, in accordance with the discussion in the end of this section. The substitution (2.72) is used, and the integral $\iiint S(\boldsymbol{k},\boldsymbol{p},t)\,\mathrm{d}^3\boldsymbol{p}$ is simplified as

$$\iiint S(\boldsymbol{k},\boldsymbol{p},t)\,\mathrm{d}^3\boldsymbol{p} = \iint_{\Delta_k}\frac{pq}{k}\left(\int_0^{2\pi}\tilde{S}(\boldsymbol{k},p,q,\lambda)d\lambda\right)\mathrm{d}p\,\mathrm{d}q\,. \tag{2.72}$$

In anisotropic triadic closure, the new difficulty is to solve the integral over the orientation of the plane of the triad, using the new variables $(\boldsymbol{k},p_1,p_2,p_3)\to(\boldsymbol{k},p,q,\lambda)$. This system of bipolar variables is classical in isotropic turbulence, the integral over p and q is performed over the domain Δ_k (see figure 2.3) so that k, p and q are the lengths of the sides of the triangle formed by $\boldsymbol{k}$, $\boldsymbol{p}$ and $\boldsymbol{q}$. At fixed $\boldsymbol{k}$, p and q give the geometry of the triad around $\boldsymbol{k}$, and the angle λ fixes the orientation of the plane of the triad around $\boldsymbol{k}$, and therefore the azimuthal angle of $\boldsymbol{p}$ (or $\boldsymbol{q}$) around $\boldsymbol{k}$. Of course, in isotropic turbulence, the λ-integral

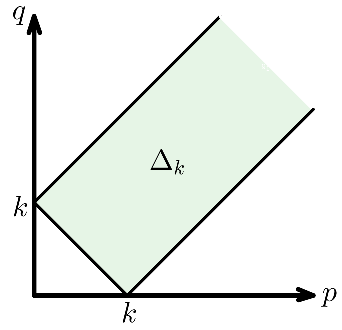

Figure 2.3: Domain of integration Δ_k in the 'triangle integrals'.

amounts to a multiplication by 2π. Here, the anisotropic part of the closure needs integrals such as $\int_0^{2\pi} \alpha_i' \alpha_j' d\lambda$, with $\alpha_i' = p_i/p$. These integrals can be expressed in terms of tensorial products of vectors $\boldsymbol{\alpha}$, and finally spherically integrated using (2.65). After the 'λ-integrals', $T^{(\mathcal{E})}$, $T^{(Z)}$ and $T^{(\mathrm{RTI})}$ are expressed by spherically-averaged descriptors in terms of k, p, q and the projections only in terms of $\boldsymbol{k}$, whereas the integration over p and q in domain Δ_k are retained.

The second step is to plug the above expressions of the transfer terms $T^{(\mathcal{E})}(\boldsymbol{k}, t)$, $T^{(Z)}(\boldsymbol{k}, t)$ and $T^{(\mathrm{RTI})}$ closed by the EDQNM procedure (2.53)-(2.54) into (2.62b) and (2.64). After integrating over k spheres, the final results are:

$$T(k,t) = \iint_{\Delta_k} \theta_{kpq} 16\pi^2 p^2 k^2 q (xy + z^3) \mathcal{E}_0'' (\mathcal{E}_0' - \mathcal{E}_0)\, \mathrm{d}p\, \mathrm{d}q, \tag{2.73}$$

$$\begin{aligned}
\mathcal{S}_{ij}^{\mathrm{NL(dir)}}(k,t) = &\iint_{\Delta_k} \theta_{kpq} 4\pi^2 p^2 k^2 q \mathcal{E}_0'' \Big[(y^2-1)(xy+z^3)(\mathcal{E}_0' - \mathcal{E}_0) H_{ij}^{(\mathrm{pol})''} + z(1-z^2)^2 \mathcal{E}_0' H_{ij}^{(\mathrm{pol})'} \Big]\, \mathrm{d}p\, \mathrm{d}q \\
+ &\iint_{\Delta_k} \theta_{kpq} 8\pi^2 p^2 k^2 q (xy+z^3) \mathcal{E}_0'' \Big[(3y^2-1)(\mathcal{E}_0' - \mathcal{E}_0) H_{ij}^{(\mathrm{dir})''} + (3z^2-1)\mathcal{E}_0' H_{ij}^{(\mathrm{dir})'} - 2\mathcal{E}_0 H_{ij}^{(\mathrm{dir})} \Big]\, \mathrm{d}p\, \mathrm{d}q,
\end{aligned} \tag{2.74}$$

$$\begin{aligned}
\mathcal{S}_{ij}^{\mathrm{NL(pol)}}(k,t) = &\iint_{\Delta_k} \theta_{kpq} 4\pi^2 p^2 k^2 q \mathcal{E}_0'' \Big[(xy+z^3)\Big((1+z^2)\mathcal{E}_0' H_{ij}^{(\mathrm{pol})'} - 4\mathcal{E}_0 H_{ij}^{(\mathrm{pol})} \Big) \\
&+ z(z^2-1)(1+y^2)(\mathcal{E}_0' - \mathcal{E}_0) H_{ij}^{(\mathrm{pol})''} + 2z(z^2-y^2)\mathcal{E}_0' H_{ij}^{(\mathrm{pol})'} + 2yx(z^2-1)\mathcal{E}_0 H_{ij}^{(\mathrm{pol})''} \Big] dp dq \\
+ &\iint_{\Delta_k} \theta_{kpq} 24\pi^2 p^2 k^2 q z (z^2-1) \mathcal{E}_0'' \Big[(y^2-1)(\mathcal{E}_0' - \mathcal{E}_0) H_{ij}^{(\mathrm{dir})''} + (z^2-1)\mathcal{E}_0' H_{ij}^{(\mathrm{dir})'} \Big]\, \mathrm{d}p\, \mathrm{d}q,
\end{aligned} \tag{2.75}$$

$$\mathcal{P}_{ij}(k,t) = \iint_{\Delta_k} \theta_{kpq} 16\pi^2 p^2 k^2 q(yz+x)\mathcal{E}_0'' \Big[\mathcal{E}_0' \Big(y(z^2-y^2)\big(6H_{ij}^{(\mathrm{dir})''} + H_{ij}^{(\mathrm{pol})''}\big) - (xz+y)H_{ij}^{(\mathrm{pol})''}\Big) \\ - y(z^2-x^2)\mathcal{E}_0\big(6H_{ij}^{(\mathrm{dir})''} + H_{ij}^{(\mathrm{pol})''}\big)\Big] \,\mathrm{d}p\,\mathrm{d}q\,, \tag{2.76}$$

with $\mathcal{E}_0 = \frac{E(k,t)}{4\pi k^2}$, $\mathcal{E}_0' = \frac{E(p,t)}{4\pi p^2}$, $\mathcal{E}_0'' = \frac{E(q,t)}{4\pi q^2}$, $H_{ij}^{()} = H_{ij}^{()}(k,t)$, $H_{ij}^{()'} = H_{ij}^{()}(p,t)$ and $H_{ij}^{()''} = H_{ij}^{()}(q,t)$, where $H_{ij}^{()}$ may refer to either $H_{ij}^{(\mathrm{dir})}$ or $H_{ij}^{(\mathrm{pol})}$. The expression of the 'true' transfer $\mathcal{S}_{ij}(k,t)$ can be deduced from equations (2.63) and (2.73)-(2.76). The readers could find details in Appendix D.

2.2.4 Properties of MCS and its application on shear-driven flow

The resulting simplified model is flexible, versatile, and tractable. The model can be used to calculate anisotropic turbulent flows at very high Reynolds number, with good resolution of both large and small scales and over very long evolution times. Its nonlinear part reduces to calculations similar to those of isotropic EDQNM, and it has been validated by Mons *et al.* (2016) for flows submitted to irrotational straining (where A_{ij} is symmetric and can be time-dependent) or plane shear. Another test case was the return-to-isotropy, when the anisotropic flow is no more submitted to mean-velocity gradients.

A previous attempt to close the governing equations of the spherically integrated second-order spectral tensor $\varphi_{ij}(k,t)$ was made by Cambon *et al.* (1981). The model involved a representation of the second-order spectral tensor $\hat{R}_{ij}(\boldsymbol{k},t)$ with a single deviatoric tensor $H_{ij}(k,t)$ and a parameter $a(k,t)$. *A posteriori*, this parameter was interpreted as prescribing an arbitrary link between directional and polarization anisotropies. On the contrary, the representation (2.56) involves no adjustable parameter and is consistent with the directional-polarization decomposition (2.9). Cambon & Rubinstein (2006) considered the following expansions of the scalars $\mathcal{E}(\boldsymbol{k},t)$ and $Z(\boldsymbol{k},t)$ in terms of powers of $\boldsymbol{\alpha} = \boldsymbol{k}/k$:

$$\mathcal{E}(\boldsymbol{k},t) = \frac{E(k,t)}{4\pi k^2}\left(1 + U_{ij}^{(\mathrm{dir})2}(k,t)\alpha_i\alpha_j + U_{ijmn}^{(\mathrm{dir})4}(k,t)\alpha_i\alpha_j\alpha_m\alpha_n + \cdots\right), \tag{2.77}$$

$$Z(\boldsymbol{k},t) = \frac{1}{2}\frac{E(k,t)}{4\pi k^2}\left(U_{ij}^{(\mathrm{pol})2}(k,t) + U_{ijm}^{(\mathrm{pol})3}(k,t)\alpha_m + U_{ijmn}^{(\mathrm{pol})4}(k,t)\alpha_m\alpha_n + \cdots\right) N_i^*(\boldsymbol{k})N_j^*(\boldsymbol{k})\,. \tag{2.78}$$

They also showed that the above expansions of $\mathcal{E}(\boldsymbol{k},t)$ and $Z(\boldsymbol{k},t)$ are equivalent to expansions in terms of respectively scalar and tensor spherical harmonics generated by the rotation group SO^3 decomposition. With the identification

$$U_{ij}^{(\mathrm{dir})2}(k,t) = -15H_{ij}^{(\mathrm{dir})}(k,t), \quad U_{ij}^{(\mathrm{pol})2}(k,t) = 5H_{ij}^{(\mathrm{pol})}(k,t), \tag{2.79}$$

The degree of anisotropy permitted by the representation (2.56) can be derived from realizability conditions. Mons *et al.* (2016) derived a simple condition in terms of the tensors $H_{ij}^{(\mathrm{dir})}(k,t)$ and $H_{ij}^{(\mathrm{pol})}(k,t)$, considering the weaker condition $\mathcal{E}(\boldsymbol{k},t) \geq 0 \ \forall \boldsymbol{k}, t$, which is already proved to be very restrictive. In view of (2.57), this condition is equivalent to:

$$\max_i \Lambda_i \left(\boldsymbol{H}^{(\mathrm{dir})}(\boldsymbol{k},t) \right) \leq \frac{1}{15} \,, \forall \boldsymbol{k}, t \tag{2.80}$$

where $\Lambda_i \left(\boldsymbol{H}^{(\mathrm{dir})}(\boldsymbol{k},t) \right)$ refers to the eigenvalues of $H_{ij}^{(\mathrm{dir})}(k,t)$. Condition (2.80) can help to quantify how small the anisotropy must be to ensure that the present model represents correctly the corresponding turbulent flow. Since the representation (2.57) is restricted to the description of moderate anisotropy, we discard quadratic contributions from the tensors $H_{ij}^{(\mathrm{dir})}(k,t)$ and $H_{ij}^{(\mathrm{pol})}(k,t)$ which appear when the representation (2.57) is injected in (2.53)-(2.55).

The representation (2.57) is interpreted as the first two degree truncation of expansions (2.77)-(2.78). In other words, $E(k,t)$, $E(k,t)H_{ij}^{(\mathrm{dir})}(k,t)$ and $E(k,t)H^{(\mathrm{pol})}(k,t)$ are the first two degree anisotropic components of $\hat{R}_{ij}(\boldsymbol{k},t)$, that means **MCS is a spherically-averaged model for the first two degree anisotropy of $\hat{R}_{ij}(\boldsymbol{k},t)$ essentially, all of the anisotropic information higher than degree-two can not be described at all. Actually, the governing equation for $E(k,t)$ in terms of degree-two spherical descriptors $H_{ij}(k,t)$ is exact without any truncation. However, the contributions to $E(k,t)H_{ij}(k,t)$ from degree-four descriptors are omitted in both linear and nonlinear parts. The dependency on high degree of the governing equation forms another open hierarchy.** Briard (2017) provided the neglected part for $E(k,t)H_{ij}(k,t)$.

The truncation restricts MCS to moderately anisotropic flows. Here, we discuss the linear and nonlinear parts of MCS separately. On the one hand, it is supposed that the truncation in the linear part of equations for $E(k,t)H_{ij}^{(\mathrm{dir})}(k,t)$ and $E(k,t)H^{(\mathrm{pol})}(k,t)$ affects more than in the nonlinear part. In fact, the purely linear limit is no longer exact in the MCS model for it neglects contributions of $H_{ijmn}^{()4}$ to production terms. On the other hand, if we refer to the nonlinear closure in MCS in terms of truncated expression of $T^{(\mathcal{E})}$ and T^{Z} as 'simplified EDQNM' in this thesis, then the simplified EDQNM technique is worthwhile to be studied furthermore for its much cheaper computational cost compared to the 3D EDQNM closure in EDQNM-1. Technically, the simplified EDQNM closure should be validated with an exact linear solution of $\hat{R}_{ij}(\boldsymbol{k},t)$.

2.3 Improved fully angular-dependent model with truncation in nonlinear closure

In order to extend MCS to flows which contain higher degree anisotropy, we propose an improved model here. The new model retains the exact linear operators as in EDQNM-1 or SLT to describe all degree anisotropy of $\hat{R}_{ij}(\boldsymbol{k},t)$ and uses the simplified EDQNM closure which governs the nonlinear performance for the first two degree anisotropy to benefit from its cheap computational cost. To deal with the mismatching between linear and nonlinear parts, a hybrid model is proposed finally to damp higher degree anisotropy with forced RTI mechanism.

2.3.1 Restoration of full angular dependence

Replacing $T^{(\mathcal{E})}$ and $T^{(Z)}$ by the truncated expressions, denoted as $T^{(\mathcal{E})2}$ and $T^{(Z)2}$, the governing equations of $\mathcal{E}$ and Z become

$$\begin{aligned}&\left(\frac{\partial}{\partial t}-A_{ln}k_l\frac{\partial}{\partial k_n}+2\nu k^2\right)\mathcal{E}(\boldsymbol{k},t)-\mathcal{E}(\boldsymbol{k},t)S_{ij}\alpha_i\alpha_j\\&\qquad\qquad+\Re(Z(\boldsymbol{k},t)S_{ij}N_i(\boldsymbol{\alpha})N_j(\boldsymbol{\alpha}))=T^{(\mathcal{E})2}(\boldsymbol{k},t)\end{aligned}\tag{2.81a}$$

$$\begin{aligned}&\left(\frac{\partial}{\partial t}-A_{ln}k_l\frac{\partial}{\partial k_n}+2\nu k^2\right)Z(\boldsymbol{k},t)-Z(\boldsymbol{k},t)S_{ij}\alpha_i\alpha_j+\mathcal{E}(\boldsymbol{k},t)S_{ij}N_i^*(\boldsymbol{\alpha})N_j^*(\boldsymbol{\alpha})\\&\qquad\qquad-\imath Z(\boldsymbol{k},t)\left(\left(W_l+4\Omega_l\right)\alpha_l-\Omega^E\right)=T^{(Z)2}(\boldsymbol{k},t)\end{aligned},\tag{2.81b}$$

which is coined ZCG. Note that it is possible to extract the set of spherically-averaged descriptors $(E,H_{ij}^{(\mathrm{dir})},H_{ij}^{(\mathrm{pol})})$ from an arbitrary anisotropic spectral tensor $\hat{R}_{ij}$, in which directional anisotropy and polarization anisotropy are separated. Conversely, one can reconstruct an approximation of the fully spectral tensor based on these descriptors, by using (2.57). It is consistent to express the generalized transfer terms using the same truncated expansion:

$$\begin{aligned}T^{(\mathcal{E})2}(\boldsymbol{k},t)=&\frac{T(k,t)}{4\pi k^2}\left(1-15\tilde{S}_{mn}^{\mathrm{NL(dir)}}(k,t)\alpha_m\alpha_n\right)\\T^{(Z)2}(\boldsymbol{k},t)=&\frac{5}{2}\frac{T(k,t)}{4\pi k^2}\tilde{S}_{mn}^{\mathrm{NL(pol)}}(k,t)N_m^*(\boldsymbol{\alpha})N_n^*(\boldsymbol{\alpha}),\end{aligned}\tag{2.82}$$

in which the spherically-averaged descriptors are the same as in those equation (2.74) and (2.75) with

$$S_{ij}^{\mathrm{NL(dir)}}(k,t)=T(k,t)\tilde{S}_{ij}^{\mathrm{NL(dir)}}(k,t)\,,\quad S_{ij}^{\mathrm{NL(pol)}}(k,t)=T(k,t)\tilde{S}_{ij}^{\mathrm{NL(pol)}}(k,t)\,,\tag{2.83}$$

given by MCS so that the computation of nonlinear terms is very close to that of isotropic EDQNM. Eq.(2.82) can also be derived by immediate calculation of λ-integrals in 3D integrating expressions for $T^{(\mathcal{E})}$ and $T^{(Z)}$ with truncated $\mathcal{E}$ and Z, which are denoted as:

$$\begin{aligned}\mathcal{E}^{(2)}(\boldsymbol{k},t) =& \frac{E(k,t)}{4\pi k^2}\left(1-15H^{(\mathrm{dir})}_{mn}(k,t)\alpha_m\alpha_n\right)\\ Z^{(2)}(\boldsymbol{k},t) =& \frac{5}{2}\frac{E(k,t)}{4\pi k^2}H^{(\mathrm{pol})}_{mn}(k,t)N^*_m(\boldsymbol{\alpha})N^*_n(\boldsymbol{\alpha})\,.\end{aligned} \tag{2.84}$$

Strictly speaking, from the view of spherical average, the nonlinear terms in ZCG are equivalent to those in MCS but with distributions on spheres.

2.3.2 Hybrid model with forced return-to-isotropy mechanism

As introduced in the beginning of this section, MCS only describes the evolution for the first two degree anisotropy of $\hat{R}_{ij}(\boldsymbol{k},t)$, so that it is reasonable to drop nonlinear evolution for high degree anisotropy. However, it is not the situation for ZCG anymore. Corrections have to be done to consider the nonlinear behaviours of high degree anisotropy, at least of the RTI mechanism which is essential especially in shear flow without system rotation.

In isotropic turbulence, the total anisotropic spectral coefficient $H(k,t) = H^{(\mathrm{dir})}_{mn}(k,t) + H^{(\mathrm{pol})}_{mn}(k,t)$ vanishes, and so do the directional anisotropy or polarization anisotropy terms. One of the simplest proposal for closing nonlinear transfer terms and related RTI effects was coined by Weinstock (1982, 2013). When expressed in terms of equations for $\mathcal{E}$ and Z, it amounts to the following nonlinear transfer terms:

$$\begin{aligned}T^{(\mathcal{E})}(\boldsymbol{k},t) =& \frac{T(k,t)}{4\pi k^2} - \varphi^{(\mathrm{RTI})}(k,t)\left(\mathcal{E}(\boldsymbol{k},t)-\frac{E(k,t)}{4\pi k^2}\right)\\ T^{(Z)}(\boldsymbol{k},t) =& -\varphi^{(\mathrm{RTI})}(k,t)Z(\boldsymbol{k},t)\,.\end{aligned} \tag{2.85}$$

$T(k,t)$ is closed by isotropic EDQNM, in terms of E, as in MCS, but the RTI effect is forced via a single relaxation parameter, here denoted as $\varphi^{(\mathrm{RTI})}(k,t)$. The formulation can be written in the bipolar system of coordinates as in EDQNM:

$$\varphi(k,t)^{(\mathrm{RTI})} = \frac{1}{5\pi}\iint_{\Delta k}\theta_{kpq}\frac{k^3E(p,t)E(q,t)}{pqE(k,t)}(1-y^2)\,\mathrm{d}p\,\mathrm{d}q\,, \tag{2.86}$$

in which θ_{kpq} is the same as the one in EDQNM decorrelation timescale for third-order statistics.

The RTI parameter $\varphi^{(\mathrm{RTI})}$ is suggested by weakly anisotropic EDQNM but it is difficult to recover its exact closure form in terms of E in published papers. It appears that the explicit anisotropic terms generated by $S^{\mathrm{NL(dir)}}_{ij}(k,t)$ and $S^{\mathrm{NL(pol)}}_{ij}(k,t)$ in ZCG are replaced by explicit RTI terms in (2.53)–(2.55). If we consider that the possible rise of angular harmonics of degree larger than two by linear terms cannot be damped by the nonlinear ones, a mixed model, which we call the 'hybrid' model, can be proposed as follows:

$$\begin{aligned} T^{(\mathcal{E})}(\boldsymbol{k},t) =& T^{(\mathcal{E})2} - \varphi^{(\mathrm{RTI})}(k,t)\left(\mathcal{E}(\boldsymbol{k},t) - \mathcal{E}^{(2)}(\boldsymbol{k},t)\right), \\ T^{(Z)}(\boldsymbol{k},t) =& T^{(Z)2} - \varphi^{(\mathrm{RTI})}(k,t)\left(Z(\boldsymbol{k},t) - Z^{(2)}(\boldsymbol{k},t)\right), \end{aligned} \tag{2.87}$$

in which $T^{(\mathcal{E})2}$, $T^{(Z)2}$, $\mathcal{E}^{(2)}$, and $Z^{(2)}$ are the former transfers and spectra given by equations (2.82) and (2.84) respectively.

Chapter 3

Numerical simulation method

The numerical algorithm either for ZCG or for the hybrid model is fairly complex, for the coupled nonlinear differentio-integral equations with advection terms in Fourier space. The advection operator, whose numerical solution is difficult even in the simple hyperbolic equation $\frac{\partial y(x)}{\partial t} + a(x)\frac{\partial y(x)}{\partial x} = f(x)$, is a great challenge to solve numerically. In this thesis work, a straightforward numerical method with finite differences scheme is employed on advection terms rather than conventional characteristic method, in order to improve the computational accuracy and extend the algorithm compatibility to arbitrary mean flow velocity gradients. Then, all the details on numerical implementation are exhibited. Finally, we operate some preliminary tests on the numerical code.

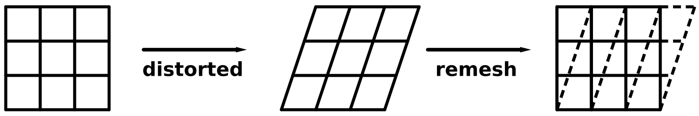

Figure 3.1: Illustration of the resolution grid when using the method of characteristics lines.

3.1 Straightforward method for advection operators

The main difficulty is to solve the advection operator (1.46). In the commonly used approach of SLT (Salhi *et al.*, 2014), as well as in fully nonlinear direct numerical simulation by Rogallo (1981) and Lesur & Longaretti (2005), the scheme amounts to following the characteristic lines in terms of $\boldsymbol{k}(t)$, which is governed by the eikonal equation $\dot{k}_i = -A_{ji}k_j$.

Rogallo (1981) extend the spectral method from isotropic turbulence to homogeneous anisotropic turbulence, in which the original computational domain is confined to a cube for the application of Fast Fourier Transform (**FFT**) in terms of pseudo-spectral method for nonlinear terms. Concerning SLT, as introduced in §1.3, for some special cases that the Green's function tensor $\boldsymbol{G}$ can be solved analytically, the calculation is rather simple without time integration and with flexible coordinate system as illustrated in Appendix 1.3.3. However, for general cases, the equations have to be solved numerically and the computational domain is usually restricted to a cube as well as in DNS. Either for DNS or for numerical SLT, in practice, the computational domain can be strongly distorted at large times, so that periodic remeshing is required. Rogallo (1981) proposed the classical remeshing method for shear flow, which is based on the periodic condition and a spatial extrapolation of the flow field, as illustrated in Fig 3.1. First of all, the restriction to cubic computational domain or the Cartesian coordinate system make the method of characteristics particularly difficult to couple with models based on shell-descriptions, especially considering the accuracy of spherically-averaged statistical quantities. In addition, the remeshing method, which depends on the type of mean flow velocity gradients, is not generalized for any A_{ij}, and can be extremely complicated and even questioned as illustrated in Appendix E. Last but not least, the interpolation has an impact on the accuracy.

A different method is chosen here. We use a finite difference scheme for evaluating the $\frac{\partial}{\partial k_n}$-derivatives, with a discretization of the wavevector consistent with the polar-spherical coordinates presented in figure 2.1. With respect to the method of characteristics, there is no need for interpolation, or remeshing, and the orientation of the wavevector can easily be represented with high accuracy by using a large number of grid points in the spectral space. As a consequence, the algorithm is generalized for arbitrary mean-velocity gradients. This numerical scheme is particularly adapted for the $(\boldsymbol{k}, t)$ development of smooth statistical quantities. We have to admit that the application of FDS raises the difficulty on numerical convergence, so that the numerical implementation must be treated with much attention.

Furthermore, the spectral DNS method for homogeneous turbulence permits deep cross-validation between DNS and spectral theories. On the one hand, the Fourier field in DNS is not only an intermediate product induced by spectral algorithm, but also contains explicit flow information from the view of spectral turbulent theory, although the former is based on discrete Fourier transform, whereas the latter one is based on continuous Fourier transform in mathematics. Therefore, the numerical method for DNS can be evaluated with some theoretical results, which is usually ignored by the studies on numerical methods. On the other hand, the spectral models, e.g. MCS, ZCG, and the hybrid model, can be validated by DNS results even with two-point statistics and spherically averaged descriptors, as long as sufficient accuracy is provided by DNS method. In Appendix E, we firstly obtain Rogallo's method for shear flow from the view of spectral theory, then propose a new DNS method with FDS for homogeneous turbulence.

3.2 Numerical implementation

3.2.1 Computational equations and coordinate system

The computational equations are found as:

$$\left(\frac{\partial}{\partial t} - A_{ln} k_l \frac{\partial}{\partial k_n} + 2\nu k^2\right)(k\mathcal{E})(\boldsymbol{k}, t) + \Re(kZ(\boldsymbol{k}, t) S_{ij} N_i(\boldsymbol{\alpha}) N_j(\boldsymbol{\alpha})) = kT^{(\mathcal{E})}(\boldsymbol{k}, t) \tag{3.1a}$$

$$\begin{aligned} \left(\frac{\partial}{\partial t} - A_{ln} k_l \frac{\partial}{\partial k_n} + 2\nu k^2\right)(kZ)(\boldsymbol{k}, t) + k\mathcal{E}(\boldsymbol{k}, t) S_{ij} N_i^*(\boldsymbol{\alpha}) N_j^*(\boldsymbol{\alpha}) \\ -\imath k Z(\boldsymbol{k}, t)\left((W_l + 4\Omega_l)\,\alpha_l - \Omega^E\right) = kT^{(Z)}(\boldsymbol{k}, t)\,, \end{aligned} \tag{3.1b}$$

in which the computational objects are $k\mathcal{E}(\boldsymbol{k}, t)$ and $Z(\boldsymbol{k}, t)$ rather than $\mathcal{E}(\boldsymbol{k}, t)$ and $Z(\boldsymbol{k}, t)$ to simplify the equations. Thanks to the decoupling of $k\mathcal{E}$ and kZ in advection terms, the computations for them are separate rather than in matrices form, considering $k\mathcal{E}$ and kZ belong to different data types in the memory.

To illustrate the numerical algorithm, the following formulation applies:

$$\left(\frac{\partial}{\partial t}+2\nu k^2\right)(k\mathcal{E})=\mathcal{F}^{(\mathcal{E})}\left(k\mathcal{E},kZ,kT^{(\mathcal{E})}\right)\,,\quad \left(\frac{\partial}{\partial t}+2\nu k^2\right)(kZ)=\mathcal{F}^{(Z)}\left(k\mathcal{E},kZ,kT^{(Z)}\right)\,, \tag{3.2}$$

with

$$\begin{aligned}\mathcal{F}^{(\mathcal{E})}\left(k\mathcal{E},kZ,kT^{(\mathcal{E})}\right)=&\mathcal{A}^{(\mathcal{E})}(k\mathcal{E})+\mathcal{G}^{(\mathcal{E})}(kZ)+kT^{(\mathcal{E})}\\ \mathcal{F}^{(Z)}\left(k\mathcal{E},kZ,kT^{(Z)}\right)=&\mathcal{A}^{(Z)}(kZ)+\mathcal{G}^{(Z)}(k\mathcal{E},kZ)+kT^{(Z)}\,,\end{aligned} \tag{3.3}$$

where $\mathcal{A}^{(\mathcal{E})}(k\mathcal{E})$ and $\mathcal{A}^{(Z)}(kZ)$ represent the advection operators, while $\mathcal{G}^{(\mathcal{E})}(kZ)$ and $\mathcal{G}^{(Z)}(k\mathcal{E},kZ)$ represent the linear operators except viscous terms and advection terms with

$$\begin{aligned}\mathcal{G}^{(\mathcal{E})}(kZ)=&-\Re(kZ(\boldsymbol{k},t)S_{ij}N_i(\boldsymbol{\alpha})N_j(\boldsymbol{\alpha}))\\ \mathcal{G}^{(Z)}(k\mathcal{E},kZ)=&-k\mathcal{E}(\boldsymbol{k},t)S_{ij}N_i^*(\boldsymbol{\alpha})N_j^*(\boldsymbol{\alpha})+\imath kZ(\boldsymbol{k},t)\left((W_l+4\Omega_l)\,\alpha_l-\Omega^E\right)\,.\end{aligned} \tag{3.4}$$

$\mathcal{G}^{(\mathcal{E})}(kZ)$ and $\mathcal{G}^{(Z)}(k\mathcal{E},kZ)$ are simple to deal with because of their locality.

In polar-spherical coordinates , the advection operator is transformed from $(k_1,k_2,k_3)\to(k,\theta,\varphi)$ as:

$$\frac{\partial}{\partial k_n}=\frac{\partial}{\partial k}\alpha_n+\frac{1}{k}\frac{\partial}{\partial\theta}e_n^{(2)}-\frac{1}{k\sin\theta}\frac{\partial}{\partial\varphi}e_n^{(1)}. \tag{3.5}$$

So that

$$\begin{aligned}\mathcal{A}^{(\mathcal{E})}(k\mathcal{E})=&A_{ln}k_l\alpha_n\frac{\partial(k\mathcal{E})}{\partial k}+A_{ln}\alpha_l e_n^{(2)}\frac{\partial(k\mathcal{E})}{\partial\theta}-\frac{1}{\sin\theta}A_{ln}\alpha_l e_n^{(1)}\frac{\partial(k\mathcal{E})}{\partial\varphi}\\ \mathcal{A}^{(Z)}(kZ)=&A_{ln}k_l\alpha_n\frac{\partial(kZ)}{\partial k}+A_{ln}\alpha_l e_n^{(2)}\frac{\partial(kZ)}{\partial\theta}-\frac{1}{\sin\theta}A_{ln}\alpha_l e_n^{(1)}\frac{\partial(kZ)}{\partial\varphi}\,,\end{aligned} \tag{3.6}$$

where $\frac{\partial}{\partial k}, \frac{\partial}{\partial\theta}, \frac{\partial}{\partial\varphi}$ will be approximated with finite differences scheme and contribute the most numerical convergence problem.

Calculations for $kT^{(\mathcal{E})}(\boldsymbol{k},t)$ and $kT^{(Z)}(\boldsymbol{k},t)$ are not as difficult as advection terms but very cumbersome. Either when ZCG or hybrid model is solved, the algorithm can be exhibited as:

$$\begin{aligned}&k\mathcal{E}(\boldsymbol{k},t)\,,\;kZ(\boldsymbol{k},t)\\ &\Downarrow\ \text{Spherical integral}\\ &E(k,t)\,,\;EH_{ij}^{(\mathrm{dir})}(k,t)\,,\;EH_{ij}^{(\mathrm{pol})})(k,t)\\ &\Downarrow\ \text{Triadic integral}\\ &T(k,t)\,,\;S_{ij}^{\mathrm{NL(dir)}}(k,t)\,,\;S_{ij}^{\mathrm{NL(dir)}}(k,t)\\ &\Downarrow\ \text{distributed on spheres}\\ &kT^{(\mathcal{E})}(\boldsymbol{k},t)\,,kT^{(Z)}(\boldsymbol{k},t)\end{aligned}$$

with twice integrals required, which demands highly accurate numerical algorithm for spherical integrations and triadic integration in polar-spherical coordinates. Actually, $kT^{(\mathcal{E})}(\boldsymbol{k},t)$ and $kT^{(Z)}(\boldsymbol{k},t)$ can be written as:

$$\begin{aligned} kT^{(\mathcal{E})}(\boldsymbol{k},t) &= \mathcal{T}^{(\mathcal{E})}(S_{ij}^{\mathrm{NL(dir)}}, S_{ij}^{\mathrm{NL(pol)}}) = \mathcal{T}^{(\mathcal{E})}(E, EH_{ij}^{(\mathrm{dir})}, EH_{ij}^{(\mathrm{pol})}) = \mathcal{T}^{(\mathcal{E})}(k\mathcal{E}, kZ) \\ kT^{(Z)}(\boldsymbol{k},t) &= \mathcal{T}^{(Z)}(S_{ij}^{\mathrm{NL(dir)}}, S_{ij}^{\mathrm{NL(pol)}}) = \mathcal{T}^{(Z)}(E, EH_{ij}^{(\mathrm{dir})}, EH_{ij}^{(\mathrm{pol})}) = \mathcal{T}^{(Z)}(k\mathcal{E}, kZ)\,. \end{aligned} \tag{3.7}$$

One has to keep in mind that $\mathcal{T}^{(\mathcal{E})}(\boldsymbol{k},t)$ and $\mathcal{T}^{(Z)}(\boldsymbol{k},t)$, as functions of $k\mathcal{E}$ and kZ in terms of spatial integrations, are not dependent on $\boldsymbol{k}$ locally.

In the numerical implementation, $(T(k,t)\,,\ S_{ij}^{\mathrm{NL(dir)}}(k,t)\,,\ S_{ij}^{\mathrm{NL(dir)}}(k,t))$ are treated as intermediate computational variables, whereas $(E(k,t)\,,\ EH_{ij}^{(\mathrm{dir})}(k,t)\,,\ EH_{ij}^{(\mathrm{pol})})(k,t))$—which indicate flow state and are frequently used in post processing—are taken into account as part of the flow state vector in addition with $k\mathcal{E}(\boldsymbol{k},t)$ and $kZ(\boldsymbol{k},t)$. Hence, the computational state vector is $\left(k\mathcal{E}(\boldsymbol{k},t), kZ(\boldsymbol{k},t), E(k,t), E(k,t)H_{ij}^{(\mathrm{dir})}(k,t), E(k,t)H_{ij}^{(\mathrm{pol})}\right)$ and the completed state equations are in following:

$$\left\{\begin{aligned} &\left(\frac{\partial}{\partial t} + 2\nu k^2\right)(k\mathcal{E}) = \mathcal{F}^{(\mathcal{E})}\left(k\mathcal{E}(\boldsymbol{k},t), kZ(\boldsymbol{k},t), E(k,t), E(k,t)H_{ij}^{(\mathrm{dir})}(k,t), E(k,t)H_{ij}^{(\mathrm{pol})}\right) \\ &\left(\frac{\partial}{\partial t} + 2\nu k^2\right)(kZ) = \mathcal{F}^{(Z)}\left(k\mathcal{E}(\boldsymbol{k},t), kZ(\boldsymbol{k},t), E(k,t), E(k,t)H_{ij}^{(\mathrm{dir})}(k,t), E(k,t)H_{ij}^{(\mathrm{pol})}\right) \\ &E(k,t) = \frac{1}{k}\iint_{S_k} k\mathcal{E}(\boldsymbol{k},t)\,\mathrm{d}^2\boldsymbol{k} \\ &E(k,t)H_{ij}^{(\mathrm{dir})}(k,t) = \frac{1}{6}\delta_{ij}E(k,t) - \frac{1}{2k}\iint_{S_k} k\mathcal{E}(\boldsymbol{k},\boldsymbol{t},t)\alpha_i\alpha_j\,\mathrm{d}^2\boldsymbol{k} \\ &E(k,t)H_{ij}^{(\mathrm{pol})}(k,t) = \frac{1}{2k}\iint_{S_k} \Re\left(kZ(\boldsymbol{k},t)N_i(\boldsymbol{\alpha})N_j(\boldsymbol{\alpha})\right)\,\mathrm{d}^2\boldsymbol{k}\,. \end{aligned}\right. \tag{3.8}$$

At last, local projections in polar-spherical coordinates are listed below.

If the polar axis is chosen as $\boldsymbol{n} = \delta_{i3} = (0,0,1)$, then all the related local projections turn into:

$$\boldsymbol{\alpha} = (\sin\theta\cos\varphi\,,\sin\theta\sin\varphi\,,\cos\theta)\,, \tag{3.9a}$$

$$\boldsymbol{e}^{(1)}(\boldsymbol{\alpha}) = (\sin\varphi\,, -\cos\varphi\,, 0)\,, \tag{3.9b}$$

$$\boldsymbol{e}^{(2)}(\boldsymbol{\alpha}) = (\cos\theta\cos\varphi\,,\cos\theta\sin\varphi\,, -\sin\theta)\,, \tag{3.9c}$$

$$\boldsymbol{N}(\boldsymbol{\alpha}) = (\cos\theta\cos\varphi\,,\cos\theta\sin\varphi\,, -\sin\theta) + \imath(\sin\varphi\,, -\cos\varphi\,, 0)\,. \tag{3.9d}$$

In addition, the special rotation rate Ω_E becomes

$$\Omega_E = -\frac{1}{\sin\theta}\left(A_{31}\sin\varphi - A_{32}\cos\varphi\right) - A_{ln}e_l^{(2)}e_n^{(1)}\,. \tag{3.10}$$

3.2.2 Time integration

The discretization methods for computational domain on time and space are independent. Classical fourth-order Runge-Kutta (**RK4**) method is employed for time integration combined with an integrating-factor technique by Rogallo (1977); Canuto *et al.* (2007). The discrete time steps are denoted as $t_0, t_1, \ldots, t_N$ with the total computational time domain from t_0 to t_N. For arbitrary time-dependent variable $a(t)$, a^n represents $a(t = t_n)$. The equations to be solved can be formally written as:

$$\left(\frac{\partial}{\partial t} + 2\nu k^2\right)(k\mathcal{E}) = \mathcal{F}^{(\mathcal{E})}\left(k\mathcal{E}, kZ, \mathcal{T}^{(\mathcal{E})}(k\mathcal{E}, kT)\right) \tag{3.11a}$$

$$\left(\frac{\partial}{\partial t} + 2\nu k^2\right)(kZ) = \mathcal{F}^{(Z)}\left(k\mathcal{E}, kZ, \mathcal{T}^{(Z)}(k\mathcal{E}, kT)\right) , \tag{3.11b}$$

which is equal to

$$\frac{\partial\left(e^{2\nu k^2 t} k\mathcal{E}\right)}{\partial t} = e^{2\nu k^2 t}\mathcal{F}^{(\mathcal{E})}\left(k\mathcal{E}, kZ, \mathcal{T}^{(\mathcal{E})}(k\mathcal{E}, kT)\right) . \tag{3.12}$$

Therefore the forward Euler approximation is reduced to

$$(k\mathcal{E})^{n+1} = \exp(-2\nu k^2\Delta t)\left[(k\mathcal{E})^n + \Delta t\mathcal{F}^{(\mathcal{E})n}\left((k\mathcal{E})^n, (kZ)^n, \mathcal{T}^{(\mathcal{E})}\left((k\mathcal{E})^n, (kT)^n\right)\right)\right] . \tag{3.13}$$

Similarly, one obtains

$$(kZ)^{n+1} = \exp(-2\nu k^2\Delta t)\left[(kZ)^n + \Delta t\mathcal{F}^{(Z)n}\left((k\mathcal{E})^n, (kZ)^n, \mathcal{T}^{(Z)}\left((k\mathcal{E})^n, (kT)^n\right)\right)\right] . \tag{3.14}$$

The final algorithm with classical Runge-Kutta method is divided into four steps with step 1:

$$\begin{cases} (k\mathcal{E})_0 = (k\mathcal{E})^n , \quad (kZ)_0 = (kZ)^n \\ d_1^{(\mathcal{E})} = \mathcal{F}^{(\mathcal{E})}\left((k\mathcal{E})_0, (kZ)_0, \mathcal{T}^{(\mathcal{E})}\left((k\mathcal{E})_0, (kZ)_0\right)\right) \\ d_1^{(Z)} = \mathcal{F}^{(Z)}\left((k\mathcal{E})_0, (kZ)_0, \mathcal{T}^{(Z)}\left((k\mathcal{E})_0, (kZ)_0\right)\right) , \end{cases} \tag{3.15}$$

step 2:

$$\begin{cases} (k\mathcal{E})_1 = \exp(-2\nu k^2(\frac{1}{2}\Delta t))\left[(k\mathcal{E})_0 + \frac{1}{2}\Delta t d_1^{(\mathcal{E})}\right] \\ (kZ)_1 = \exp(-2\nu k^2(\frac{1}{2}\Delta t))\left[(kZ)_0 + \frac{1}{2}\Delta t d_1^{(Z)}\right] \\ d_2^{(\mathcal{E})} = \mathcal{F}^{(\mathcal{E})}\left((k\mathcal{E})_1, (kZ)_1, \mathcal{T}^{(\mathcal{E})}\left((k\mathcal{E})_1, (kZ)_1\right)\right) \\ d_2^{(Z)} = \mathcal{F}^{(Z)}\left((k\mathcal{E})_1, (kZ)_1, \mathcal{T}^{(Z)}\left((k\mathcal{E})_1, (kZ)_1\right)\right) , \end{cases} \tag{3.16}$$

step 3:

$$\begin{cases} (k\mathcal{E})_2 = \exp(-2\nu k^2(\frac{1}{2}\Delta t))\left[(k\mathcal{E})_0 + \frac{1}{2}\Delta t d_2^{(\mathcal{E})}\right] \\ (kZ)_2 = \exp(-2\nu k^2(\frac{1}{2}\Delta t))\left[(kZ)_0 + \frac{1}{2}\Delta t d_2^{(Z)}\right] \\ d_3^{(\mathcal{E})} = \mathcal{F}^{(\mathcal{E})}\Big((k\mathcal{E})_2, (kZ)_2, \mathcal{T}^{(\mathcal{E})}\left((k\mathcal{E})_2, (kZ)_2\right)\Big) \\ d_3^{(Z)} = \mathcal{F}^{(Z)}\Big((k\mathcal{E})_2, (kZ)_2, \mathcal{T}^{(Z)}\left((k\mathcal{E})_2, (kZ)_2\right)\Big) \,, \end{cases} \tag{3.17}$$

step 4:

$$\begin{cases} (k\mathcal{E})_3 = \exp(-2\nu k^2\Delta t)\left[(k\mathcal{E})_0 + \Delta t d_3^{(\mathcal{E})}\right] \\ (kZ)_3 = \exp(-2\nu k^2\Delta t)\left[(kZ)_0 + \Delta t d_3^{(Z)}\right] \\ d_4^{(\mathcal{E})} = \mathcal{F}^{(\mathcal{E})}\Big((k\mathcal{E})_3, (kZ)_3, \mathcal{T}^{(\mathcal{E})}\left((k\mathcal{E})_2, (kZ)_2\right)\Big) \\ d_4^{(Z)} = \mathcal{F}^{(Z)}\Big((k\mathcal{E})_3, (kZ)_3, \mathcal{T}^{(Z)}\left((k\mathcal{E})_2, (kZ)_2\right)\Big) \,. \end{cases} \tag{3.18}$$

Finally,

$$\begin{cases} (k\mathcal{E})^{n+1} = \exp(-2\nu k^2\Delta t)\left[(k\mathcal{E})^n + \frac{\Delta t}{6}\left(d_1^{(\mathcal{E})} + 2d_2^{(\mathcal{E})} + 2d_3^{(\mathcal{E})} + d_4^{(\mathcal{E})}\right)\right] \\ (kZ)^{n+1} = \exp(-2\nu k^2\Delta t)\left[(kZ)^n + \frac{\Delta t}{6}\left(d_1^{(Z)} + 2d_2^{(Z)} + 2d_3^{(Z)} + d_4^{(Z)}\right)\right] \,. \end{cases} \tag{3.19}$$

3.2.3 Space discretization and boundary conditions

Thanks to the Hermitian symmetry of $\mathcal{E}(-\boldsymbol{k},t) = \mathcal{E}(\boldsymbol{k},t)$ and $Z(-\boldsymbol{k},t) = Z^*(\boldsymbol{k},t)$, the space computational domain reduces to a hemisphere with $k \in [k_0, k_{\max}]$, $\theta \in [0, \frac{\pi}{2}]$ and $\varphi \in (0, 2\pi]$, in which the original point is excluded because of the singularity of polar-spherical coordinates at it. According to Eq. (3.5), k, θ and φ can be discretized independently as:

$$k_I\,,\ I = 0,1,2,\ldots,N_k\,;\quad \theta_J\,,\ J = 1,2,\ldots,N_\theta\,;\quad \varphi_L\,,\ L = 1,2,\cdots,N_\varphi\,. \tag{3.20}$$

The finite difference approximation for advection terms of $k\mathcal{E}$ and kZ becomes

$$\mathcal{A}(\cdot) = a_k\frac{\tilde{(\cdot)}_{I+\frac{1}{2},J,L} - \tilde{(\cdot)}_{I-\frac{1}{2},J,L}}{2} + a_\theta\frac{\tilde{(\cdot)}_{I,J+\frac{1}{2},L} - \tilde{(\cdot)}_{I,J-\frac{1}{2},L}}{2} + a_\varphi\frac{\tilde{(\cdot)}_{I,J,L+\frac{1}{2}} - \tilde{(\cdot)}_{I,J,L-\frac{1}{2}}}{2}\,, \tag{3.21}$$

with

$$a_k = \frac{1}{J_k}A_{ln}k_l\alpha_n\,,\quad a_\theta = \frac{1}{J_\theta}A_{ln}\alpha_l e_n^{(2)}\,,\quad a_\varphi = -\frac{1}{J_\varphi}\frac{1}{\sin\theta}A_{ln}\alpha_l e_n^{(1)}\,, \tag{3.22}$$

where $(\cdot)_{I,J,L}$ represents $(\cdot)(k=k_I, \theta=\theta_J, \varphi=\varphi_L)$. J_k, J_θ and J_φ are the Jacobi coefficients from discrete coordinates to original continuous coordinates so that

$$\frac{\mathrm{d}}{\mathrm{d}k}f(k) \simeq \frac{\tilde{f}_{I+\frac{1}{2}} - \tilde{f}_{I-\frac{1}{2}}}{2}\cdot\frac{1}{J_k}\,, \quad \frac{\mathrm{d}}{\mathrm{d}\theta}g(\theta) \simeq \frac{\tilde{g}_{J+\frac{1}{2}} - \tilde{g}_{J-\frac{1}{2}}}{2}\cdot\frac{1}{J_\theta}\,, \quad \frac{\mathrm{d}}{\mathrm{d}\varphi}h(\varphi) \simeq \frac{\tilde{h}_{L+\frac{1}{2}} - \tilde{h}_{L-\frac{1}{2}}}{2}\cdot\frac{1}{J_\varphi}\,, \tag{3.23}$$

where $\frac{\tilde{f}_{I+\frac{1}{2}} - \tilde{f}_{I-\frac{1}{2}}}{2}$, $\frac{\tilde{g}_{J+\frac{1}{2}} - \tilde{g}_{J-\frac{1}{2}}}{2}$ and $\frac{\tilde{h}_{L+\frac{1}{2}} - \tilde{h}_{L-\frac{1}{2}}}{2}$, along with the similar expressions in (3.21) represent finite difference schemes.

In the numerical implementation, the access to customized grids is supported, provided that the distributions have good smooth properties. In most situations, a logarithmic distribution of discretized k, as in conventional EDQNM calculations and shell-models (Plunian & Stepanov, 2007), along with uniform distributions of θ and φ performs well. Correspondingly, $k_I = k_0 r^{I-1}$, $\theta_J = J\cdot\Delta\theta$, and $\varphi_L = L\cdot\Delta\varphi$, and the Jacobi coefficients are $J_k = k\ln r$, $J_\theta = \Delta\theta$ and $J_\varphi = \Delta\varphi$.

To describe the turbulence field in all significant scales, the computational domain for k usually promises $[10^{-3}k_l\,, 10k_\eta] \subseteq [k_0\,, k_{\max}]$, where $k_l = 1/l$ is the wavenumber corresponding to integral length scale defined by $l = \dfrac{3\pi}{4\mathcal{K}}\displaystyle\int \frac{E(k)}{k}\,\mathrm{d}k$, and k_η is the one corresponding to Kolmogorov microscale defined by $\eta = \left(\dfrac{\nu^3}{\varepsilon}\right)^{\frac{1}{4}}$. For k, we have two boundaries when $k=k_0$ and $k=k_{\max}$ respectively. Technically, the boundary conditions for advection ought to be very complicated, and usually physical boundary conditions and numerical boundary conditions should be treated with much attention in accordance with the direction of information transfer. However, in our situation, thanks to the very small values quantitatively at k_0 and $k_{\max}$, the boundary conditions are dealt with some complemented extra points with extrapolation. It is worthwhile to point out that, for the extrapolation of the complemented points which are smaller than k_0, $\mathcal{E}(\mathbf{0},t)=0$ and $Z(\mathbf{0},t)=0$ derived from $\hat{\boldsymbol{u}}(\mathbf{0},t)=0$ are used, which improves the convergence at largest scales significantly.

The simplest boundary to deal with is for φ, which contains periodic property $\mathcal{E}(k,\theta,\varphi\pm 2\pi) = \mathcal{E}(k,\theta,\varphi)$ and $Z(k,\theta,\varphi\pm 2\pi) = Z(k,\theta,\varphi)$, whereas θ contributes the most complexity to solve on boundary conditions. Near the region $\theta=\frac{\pi}{2}$, we just complement some extra points with the Hermite symmetry that $\mathcal{E}(k,\theta+\frac{\pi}{2},\varphi) = \mathcal{E}(k,\frac{\pi}{2}-\theta,\varphi\pm\pi)$ and $Z(k,\theta+\frac{\pi}{2},\varphi) = Z^*(k,\frac{\pi}{2}-\theta,\varphi\pm\pi)$. Obviously, Craya frame is not uniquely defined at the pole, so that the governing equations for $k\mathcal{E}(\boldsymbol{k},t)$ and $kZ(\boldsymbol{k},t)$ become singular (along $\boldsymbol{n}$). For the flows in which the advection along θ direction is small compared to those along other directions, the pole can be dug out from the computational domain. However, this prevents the model from applications on arbitrary mean flow velocity gradients. We solve this by using a degenerate equation for $\hat{R}_{ij}(\boldsymbol{k},t)$ at the pole by replacing the Craya frame by the Cartesian frame. Then $\hat{R}_{ij}(\boldsymbol{k},t)$ reduces to $\hat{R}_{\alpha\beta}(k,\boldsymbol{n},t)$ with

$$\left(\frac{\partial}{\partial t}+2\nu k^2\right)\hat{R}_{\alpha\beta}+(A_{\alpha\gamma}+2\epsilon_{\alpha m\gamma}\Omega_m)\hat{R}_{\gamma\beta}+(A_{\beta\gamma}+2\epsilon_{\beta m\gamma}\Omega_m)\hat{R}_{\alpha\gamma}=T_{\alpha\beta}, \tag{3.24}$$

in which, the spectral tensor $\hat{R}_{ij}$ reduces to four non-zero components because of incompressibility so that Greek indices are restricted to 1,2, with $n_i=\delta_{i3}$, and the advection operator vanishes providing $A_{mn}n_m=0$. In the present model, the regular form for right-hand side of Eq. (2.25) can be expressed as:

$$\begin{cases} T_{ij}(\boldsymbol{k},t)=T_{ij}^{(2)}=T^{(\mathcal{E})}P_{ij}(\boldsymbol{\alpha})+\Re(T^{(Z)}N_i(\boldsymbol{\alpha})N_j(\boldsymbol{\alpha}))\,, & \text{for ZCG} \\ T_{ij}(\boldsymbol{k},t)=T_{ij}^{(2)}-\varphi^{(\mathrm{RTI})}\left(\hat{R}_{ij}(\boldsymbol{k},t)-\hat{R}_{ij}^{(2)}(\boldsymbol{k},t)\right)\,, & \text{for hybrid model}\,, \end{cases} \tag{3.25}$$

with

$$\hat{R}_{ij}^{(2)}(\boldsymbol{k},t)=\mathcal{E}(\boldsymbol{k},t)P_{ij}(\boldsymbol{\alpha})+\Re(ZN_i(\boldsymbol{\alpha})N_j(\boldsymbol{\alpha}))\,. \tag{3.26}$$

However, at the pole it reduces to

$$\begin{cases} T_{\alpha\beta}=T_{\alpha\beta}^{(2)}=\dfrac{T}{4\pi k^2}\left(\delta_{\alpha\beta}\left(1-15\tilde{S}_{33}^{\mathrm{NL(dir)}}\right)+5\left(\tilde{S}_{\alpha\beta}^{\mathrm{NL(pol)}}+\dfrac{1}{2}\delta_{\alpha\beta}\tilde{S}_{33}^{\mathrm{NL(dir)}}\right)\right)\,, & \text{for ZCG} \\ T_{\alpha\beta}=T_{\alpha\beta}^{(2)}-\varphi^{(\mathrm{RTI})}\left(\hat{R}_{\alpha\beta}-\hat{R}_{\alpha\beta}^{(2)}\right)\,, \quad \text{for hybrid model}\,, \end{cases} \tag{3.27}$$

with

$$\hat{R}_{\alpha\beta}^{(2)}==\frac{E}{4\pi k^2}\left(\delta_{\alpha\beta}\left(1-15H_{33}^{(\mathrm{dir})}\right)+5\left(H_{\alpha\beta}^{(\mathrm{pol})}+\frac{1}{2}\delta_{\alpha\beta}H_{33}^{(\mathrm{pol})}\right)\right)\,. \tag{3.28}$$

We compute $\hat{R}_{ij}(\boldsymbol{k},t)$ rather than the set $(\mathcal{E}(\boldsymbol{k},t),\ Z(\boldsymbol{k},t))$ in a neighborhood of the pole, and we exchange values with neighbor grid points to provide the required boundary conditions (see Figure 3.2). Overall, the special treatment of the pole has no consequence on the global accuracy, since it is only employed as a local regularization of the equations.

After the space discretization, an adaptive time step is proposed. Δt is in principle constrained by a simple condition of convergence for advection term as:

$$\Delta t\leq\frac{C}{\max(a_k+a_\theta+a_\varphi)}\,, \tag{3.29}$$

in which C is the CFL number and its critical value is determined by trial. In addition, the time resolution for the smallest time scale in turbulence is considered as well, namely $\Delta t\leq10^{-3}\tau$ in accordance with the choice of k_0 and $\Delta t\leq\tau_\eta$. τ is the turn-over time

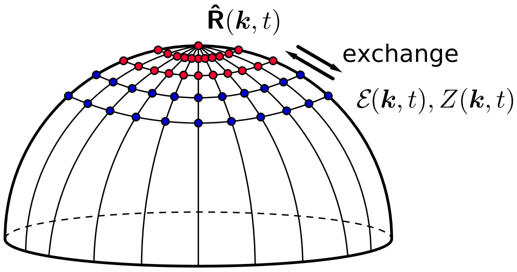

Figure 3.2: Illustration of the interaction between the two numerical regions in the latitude direction. In the polar region, fixed-frame equations are specifically used, and both regions exchange information to recover the complete spectral information.

scale for largest eddy defined by $\tau = \dfrac{\mathcal{K}}{\varepsilon}$, while τ_η is the Kolmogorov time scale given by $\tau_\eta = \left(\dfrac{\nu}{\eta}\right)^{\frac{1}{2}}$. Thus, the adaptive time step is expressed as

$$\Delta t = \min\left(\frac{C}{\max(a_k + a_\theta + a_\varphi)}\,,\ 10^{-3}\tau\,,\ \tau_\eta\right)\,, \tag{3.30}$$

in order to promise convergence even for isotropic flow or for flow in which only viscous effects are considered.

3.2.4 Spherical integration and triadic integral for EDQNM

Since the accuracy of spherical integrals and triadic integrals plays important roles for the numerical resolution, a compound Simpson integral scheme with fourth-order accuracy for uniform grids is employed, along with slight correction at the pole. When $f(\boldsymbol{k}) = f(\theta, \varphi)$ has Hermite symmetry with $f(-\boldsymbol{k}) = f(\boldsymbol{k})$ and discretized as $f_{J,L} = f(\theta_J, \varphi_L)$, the spherical integration is

$$\iint_{S_k} f(\boldsymbol{k})\,\mathrm{d}^2\boldsymbol{k} = 2k^2\left[\int_0^{\theta_1}\int_0^{2\pi} f(k,\theta,\varphi)\sin\theta\,\mathrm{d}\varphi\,\mathrm{d}\theta + \int_0^{2\pi}\int_{\theta_1}^{\frac{\pi}{2}} f(k,\theta,\varphi)\sin\theta\,\mathrm{d}\varphi\,\mathrm{d}\theta\right]\,. \tag{3.31}$$

Then the discrete approximation can be found as:

$$\iint_{S_k} f(\boldsymbol{k})\,\mathrm{d}^2\boldsymbol{k} = 4\pi k^2 f(k\boldsymbol{n})(1-\cos\theta_1) + \frac{4}{9}k^2\sum_{L=1}^{N_\varphi/2}\left[2G_{2L-1}J_\varphi(\varphi_{2L-1}) + G_{2L}J_\varphi(\varphi_{2L})\right]\,, \tag{3.32}$$

with

$$G_L = \sum_{J=1}^{(N_\theta+1)/2}\left[2f_{2J-1,L}J_\theta(\theta_{2J-1}) + 4f_{2J,L}J_\theta(\theta_{2J})\right] - f_{1,L}J_\theta(\theta_1)\sin(\theta_1) - f_{N_\theta,L}J_\theta(\frac{\pi}{2})\,. \tag{3.33}$$

Obviously, this integral scheme restricts N_θ to odd number and N_φ to even number.

The basic integral for 1D EDQNM can be simplified as

$$g(k) = \iint_{\Delta k} f(k,p,q)\,\mathrm{d}p\,\mathrm{d}q = \int_0^{+\infty} \mathrm{d}p \int_{q_{\min}}^{q_{\max}} f(k,p,q)\,\mathrm{d}q\,, \tag{3.34}$$

with a symmetry if p and q are exchanged, where the integral domain is illustrated in (2.3). The popular code for 1D EDQNM is originated from late 1970s, which uses constant approximation in the integral schemes in addition with complicated corrections for volume elements, in order to reduce computational cost. However, the computational cost of triadic integrals is insignificant for modern computers, whereas the accuracy provided by old algorithm is not sufficient anymore. Furthermore, ancient code restricted the grids for k in logarithmic distribution. New integral scheme for 1D EDQNM is proposed here for any smooth distribution of k grids. Discrete k, p, q as k_I, p_M and q_N with same distribution, then $f_{I,M,N} = f(k_I, p_M, q_N)$. Using a compound trapezoid formula, the integral sum for discrete $g_I = g(k_I)$ can be approximated as:

$$g_I = \frac{1}{4}\left[h_1 J_k(p_1) + h_{N_k} J_k(p_{Nk}) + 2\sum_{M=2}^{M=N_k-1} h_M J_k(p_M)\right]\,, \tag{3.35}$$

where

$$h_M = f_{I,M,N_{\min}} J_k(q_{N_{\min}}) + f_{I,M,N_{\max}} J_k(q_{N_{\max}}) + 2\sum_{N=N_{\min}+1}^{N=N_{\max}-1} f_{I,M,N} J_k(q_N)\,. \tag{3.36}$$

3.2.5 Parallelization and the flow diagram for final program

In order to improve computational efficiency, the program is parallelized with hybrid distributed memory and shared memory computing technique, via Message Passing Interface (**MPI**)—the standard for passing data among processes, and Open Multi-Processing (**OpenMP**)—an application programming interface that supports multi-threads work together using shared memory within the single process.

The Single Program Multiple Data (**SPMD**) technique is employed to achieve distributed memory parallelism, through computation domain division in space. Figure 3.3 is a schematic diagram to illustrate the uniform 2D domain division and the topology to processes. MPI 3.x, the latest standard supports to match the calculation domain to the process grid, and also supports flexible communicating operators in sub-dimensions, which is extremely useful when dealing with internal boundaries that are necessary for FDS induced by parallelization, as shown in blue color in the diagram. 2D decomposition decreases

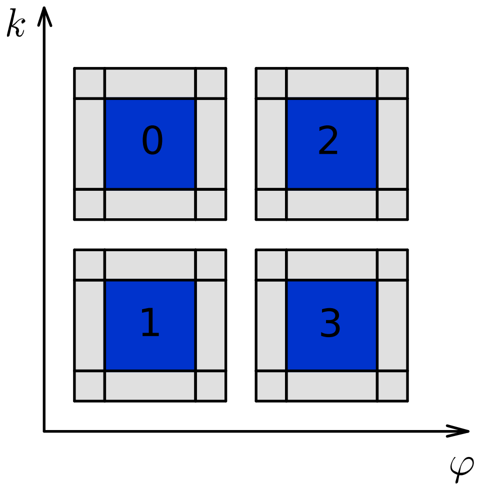

Figure 3.3: Illustration of parallelization based on computational domain division

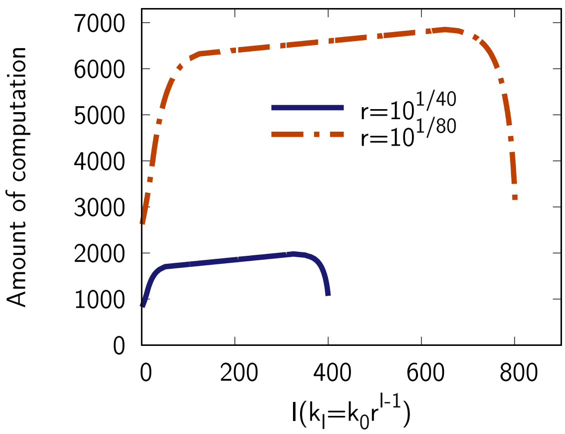

Figure 3.4: Illustration of the nonuniform computation cost distribution for EDQNM integrals

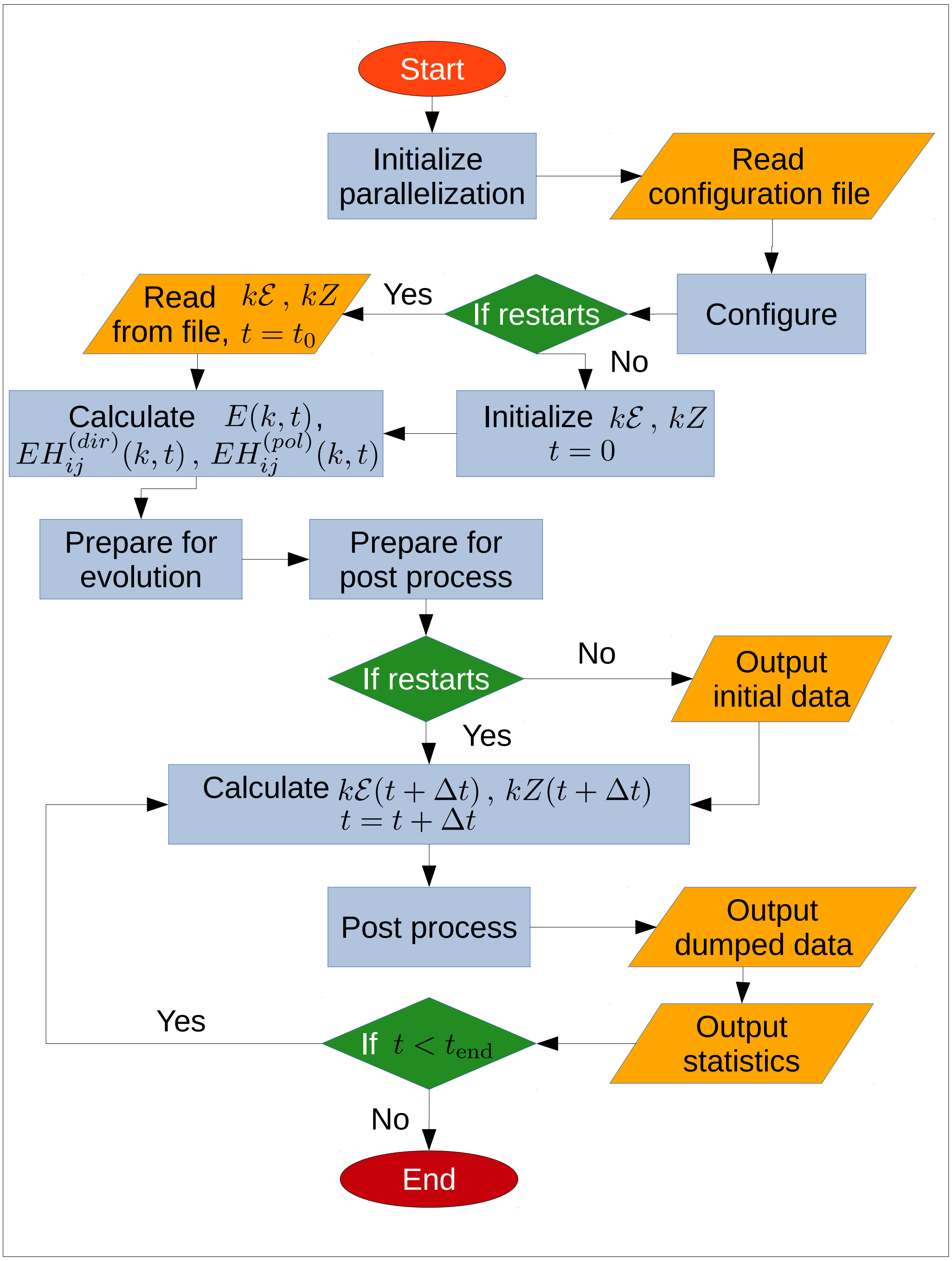

Figure 3.5: Flowchart of the program

the cost of communications for internal boundaries compared to 1D decomposition when refined division is performed, while the domain for θ direction is kept complete for the complex boundary around pole to deal with.

The algorithm for spherical integrals is slightly modified correspondingly, whereas an special domain decomposition method for 1D EDQNM integrals is applied to improve load balance. The EDQNM integrals are done for each single discrete wavenumber $k_0\,, k_1\,, \dots k_{N_\theta}$, and the calculation is independent on main computational domain shown in figure 3.3. Figure 3.4 illustrates the nonuniform distribution of 1D EDQNM integral computational cost in terms of k_I with $k_0 = 10^-5$, $k_{\max} = 10^5$ and with different resolutions, which shows that it is affected more obviously when higher resolution are required for k. In the program, the domain division for EDQNM integrals is to provide almost equal computation cost for each process based on a estimation at the very beginning, instead of simple uniform division regarding to the domain. The simulation tests are given in §3.3.5.

Regarding OpenMP, the parallelization is rather simple through forcing multi threads to divide some work such as loops with permits to share memories, if each process of MPI has been assigned more than one thread.

The numerical code is programmed in latest Fortran standard—Fortran 2008, which permits to design the interfaces of modules in the 'minimum coupling and maximum cohesion principle' for further development. In addition, MPI provides advanced accesses to paralleling input/output operators, Figure 3.5 is a simplified flowchart of the final program, in which flexible customized configurations are supported via an input file.

At last, table 3.1 lists all the statistic quantities calculated in post process.

3.3 Tests of the numerical implementation

Plenty of tests are operated to correct and optimize the program, e.g. simple tests to check correctness of numerical code, comparison among various FDSs, effects of some special treatment, such as around the pole and the EDQNM algorithm, convergence study and parallelization effects.

In this section, all the simulations are initialized with isotropic field constraint to the following energy spectrum:

$$E(k,0) = C_0 \varepsilon^{2/3} k^{-5/3} f(kl) g(k\eta)\,, \tag{3.37}$$

Table 3.1: Statistic quantities calculated in post-process.

quantity	symbol	formula
turbulent kinetic energy	$\mathcal{K}$	$\int E(k)\,\mathrm{d}k$
dissipation rate	ε	$\int \nu k^2 E(k)\,\mathrm{d}k$
directional anisotropy tensor of RST	$b_{ij}^{(\mathrm{dir})}$	$\int E(k) H_{ij}^{(\mathrm{dir})}\,\mathrm{d}k/\mathcal{K}$
polarization anisotropy tensor of RST	$b_{ij}^{(\mathrm{pol})}$	$\int E(k) H_{ij}^{(\mathrm{pol})}\,\mathrm{d}k/\mathcal{K}$
anisotropy tensor of RST	b_{ij}	$b_{ij}^{(\mathrm{dir})} + b_{ij}^{(\mathrm{pol})}$
length scale of the larger eddies	L	$\mathcal{K}^{3/2}/\varepsilon$
eddy turn-over time	τ	$\mathcal{K}/\varepsilon$
integral length scale	l	$3\pi/4 \int E(k)/k\,\mathrm{d}k/\mathcal{K}$
integral wavenumber	k_l	$1/l$
integral Reynolds number	Re_l	$l\sqrt{2\mathcal{K}/3}/\nu$
Taylor microscale	λ	$\sqrt{10\nu\mathcal{K}/\varepsilon}$
Taylor Reynolds number	Re_λ	$\lambda\sqrt{2\mathcal{K}}/\nu$
Taylor wavenumber	k_λ	$1/\lambda$
Kolmogorov length scale	η	$(\nu^3/\varepsilon)^{1/4}$
Kolmogorov wavenumber	k_η	$1/\eta$
Kolmogorov time scale	τ_η	$(\nu/\eta)^{1/2}$
Kolmogorov Reynolds number	Re_η	$\sqrt{20Re_l/3}$

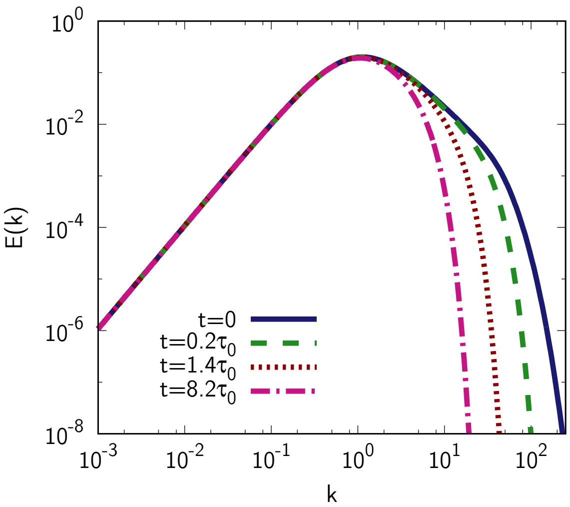

Figure 3.6: Turbulent kinetic energy spectra. Only viscosity effect is considered.

with

$$f(x) = \left(\frac{x}{\left(x^{1.5} + 1.5 - \frac{\sigma}{4}\right)^{2/3}} \right)^{5/3+\sigma}, \quad g(x) = \exp\left(-5.2 \left(x^4 - 0.4^4 \right)^{1/4} - 0.4 \right), \quad (3.38)$$

in which C_0 is the normalized coefficient to make $\mathcal{K}(0) = 1$, and $\sigma = 2$ in this thesis corresponding to Saffman turbulence. The initial spectrum follows Mons *et al.* (2016), in which the functions defined by (3.38) have been proposed by Pope (2001)and Fathali *et al.* (2008) respectively. Initial integral length scale l, integral Reynolds number Re_l and dissipation rate ε are read from the configuration file at the beginning, then η can be calculated thanks to $\frac{\eta}{l} = Re_l^{-\frac{3}{4}}$.

3.3.1 Test for the correctness of numerical code

$$\left(\frac{\partial}{\partial t} + 2\nu k^2 \right) (k\mathcal{E})(\boldsymbol{k}, t) = 0 \,. \quad (3.39)$$

The first task is testing the operators in Eq. (3.2) and (3.3) separately, to exclude any code incorrectness. Three tests with different governing equations are operated, to check viscous terms, EDQNM integrals and advection terms respectively, with $Re_l(0) = 460$.

Figure 3.6 illustrates the time evolution of energy spectra, when only viscous effect is considered, namely Eq. (3.39). Obvious decay at small scales are observed as expected. Figure 3.7 shows the time evolution of turbulent kinetic energy in HIT, namely

$$\left(\frac{\partial}{\partial t} + 2\nu k^2 \right) (k\mathcal{E})(\boldsymbol{k}, t) = kT^{(\mathcal{E})}(\boldsymbol{k}, t) \,. \quad (3.40)$$

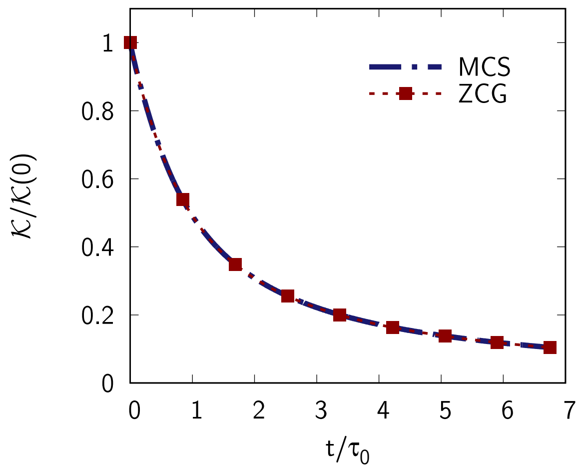

Figure 3.7: Time evolution of turbulent kinetic energy for HIT as a function of non dimensional time τ/τ_0. Comparison with the results from the present model and MCS.

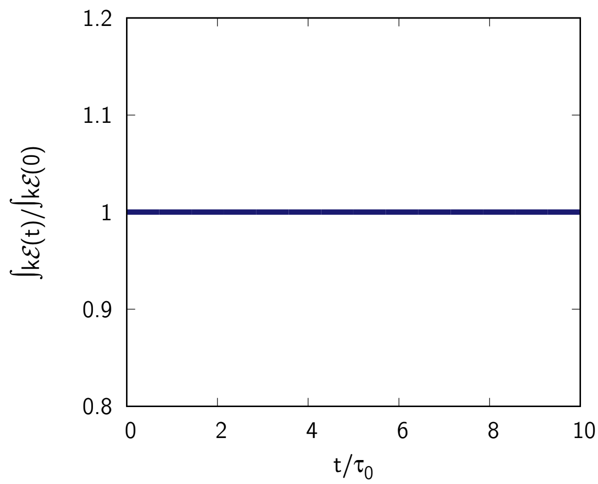

Figure 3.8: Time evolution of kinetic turbulent energy. Only advection term works.

Table 3.2: Illustration of finite differences schemes.

FDS	formula	accuracy
2nd-order central scheme	$\frac{1}{2}f(x_1) - \frac{1}{2}f(x_{-1})$	$O(h^2)$
4th-order central scheme	$-\frac{1}{12}f(x_2) + \frac{2}{3}f(x_1) - \frac{2}{3}f(x_{-1}) + \frac{1}{12}f(x_{-2})$	$O(h^4)$
6th-order central scheme	$\frac{1}{60}f(x_3) - \frac{3}{20}f(x_2) + \frac{3}{4}f(x_1)$ $-\frac{1}{60}f(x_{-3}) + \frac{3}{20}f(x_{-2}) - \frac{3}{4}f(x_{-1})$	$O(h^6)$
8th-order central scheme	$-\frac{1}{280}f(x_4) + \frac{4}{105}f(x_3) - \frac{1}{5}f(x_2) + \frac{4}{5}f(x_1)$ $+\frac{1}{280}f(x_{-4}) - \frac{4}{105}f(x_{-3}) + \frac{1}{5}f(x_{-2}) - \frac{4}{5}f(x_{-1})$	$O(h^8)$
2nd-order upwind scheme	$-\frac{1}{2}f(x_2) + 2f(x_1) - \frac{3}{2}f(x_0)$ if $a < 0$ $\frac{1}{2}f(x_{-2}) - 2f(x_{-1}) + \frac{3}{2}f(x_0)$ if $a > 0$	$O(h^2)$
4th-order upwind scheme	$-\frac{1}{4}f(x_4) + \frac{4}{3}f(x_3) - 3f(x_2) + 4f(x_1) + \frac{25}{12}f(x_0)$ if $a < 0$ $\frac{1}{4}f(x_{-4}) - \frac{4}{3}f(x_{-3}) + 3f(x_{-2}) - 4f(x_{-1}) - \frac{25}{12}f(x_0)$ if $a > 0$	$O(h^4)$

Comparison to MCS proves that present model agrees with MCS well in nonlinear models, as referred in Chapter 2 that these two models are equivalent in nonlinear terms, at least from a spherically-averaged view. The advection term is tested with simple configuration of A_{ij} in accordance with Eq. (1.6). $D = 10$ and $W = 5$ in this simulation, and thanks to Appendix B, the analytical solution for

$$\left(\frac{\partial}{\partial t} - A_{ln}k_l\frac{\partial}{\partial k_n}\right)(k\mathcal{E})(\boldsymbol{k}, t) = 0\,. \tag{3.41}$$

can be obtained. Here, the time evolution for integral of $k\mathcal{E}$ over the whole space is observed by figure 3.8, and the figure shows the conservation of $k\mathcal{E}$ under advection.

3.3.2 Tests of various finite difference schemes

The most challenging case in terms of numerical convergence is in inviscid linear limit with mean shear, so various finite difference schemes are tested in this limit, in order to determine optimized one which can provide relatively long stable simulations with demanded accuracy and whose computational cost is acceptable.

Table 3.2 lists the FDSs for the first order derivative that have been tested, where h represents a uniform grid spacing between each finite difference interval, $x_n = x_0 + nh\,, n = 0, \pm1, \pm2\ldots,$ a is the coefficient for the model equation $\dfrac{\partial f(x)}{\partial t} + a(x)\dfrac{\partial f(x)}{\partial x} = 0$. The numerical error $error_0$ is defined as $\dfrac{|\mathcal{K} - \mathcal{K}_a|}{\mathcal{K}_a}$, in which the analytical solution $\mathcal{K}_a$ is solved in Appendix B.

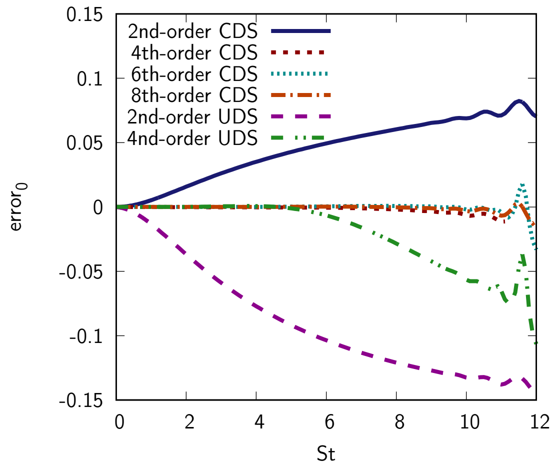

Figure 3.9: Time evolution of the numerical error, as a function of non dimensional time St. Comparison with the results from various FDSs, where CDS represents central scheme and UDS represents upwind scheme.

All the tests are operated with same initial conditions that $Re_l(0) = 1.23\times 10^5$, and with the same grids that $N_\theta = 40, N_\varphi = 1600, r = 1/40$. Figure 3.9 shows the time evolution of numerical errors with central finite difference schemes and upwind schemes. The results indicates that upwind schemes are over dissipative numerically, whereas central schemes perform well in accuracy even their stabilities are not as good as upwind schemes. Taking into account the accuracy and stabilities together, 6th-order central FDS is employed by all the simulations in this thesis, and the reason why so high scheme is needed will be explained in §3.3.4. Actually, some other frequent FDSs have also been tested, such as Lax-Wendroff scheme and McCormack scheme, but they are all excluded for their low accuracy and for that they are complicated when nonlinear terms are considered.

3.3.3 The effects of special treatment at the pole zone

Special treatment at the pole zone is taken to recover the singularity of the governing equations for $k\mathcal{E}$ and kZ. The test is still in inviscid linear limit with mean shear $A_{ij} = S\delta_1\delta_3$ acted, where $Re_l(0) = 460$. We define the norm $\mathrm{error}_2 = \iiint \frac{|k\mathcal{E} - k\mathcal{E}_a|^2}{(k\mathcal{E}_a)^2}\,\mathrm{d}^3\boldsymbol{k}$ to assess the overall numerical error, and the numerical error at a grid point in the pole zone is traced, defined as $\mathrm{error}_1 = \frac{|k\mathcal{E} - k\mathcal{E}_a|}{k\mathcal{E}_a}$ and $\mathrm{error}_1 = \frac{||kZ| - |kZ_a||}{|kZ_a|}$ for $k\mathcal{E}$ and kZ respectively.

The time evolution of the numerical errors is plotted in figure 3.10. The figure illustrates that the special treatment at the pole zone reduces the numerical errors via calculating the

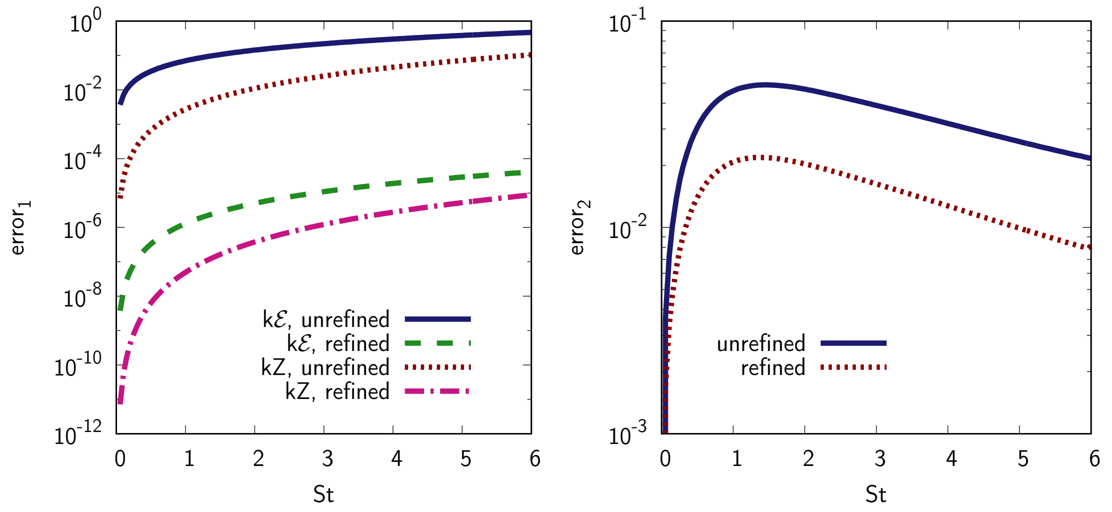

(a) Results at the point in pole zone.

(b) Overall numerical errors.

Figure 3.10: Time evolution of the numerical errors for $k\mathcal{E}$ and kZ. Comparison of the results from the algorithms with and without special treatment at the pole zone.

degenerated equations for $\hat{\boldsymbol{R}}$ at the pole.

3.3.4 Convergence study with numerical grids and CFL number

As introduced in the tests for FDSs, the most challenging case in terms of numerical convergence is the one with mean shear acted without any system rotation. Actually, appropriate nonlinear terms can refine the simulation through their physical influence, just as viscous flow is not so difficult to simulate numerically as inviscid flow in general, since the former is more natural in physics.

Therefore, the strategy to test grids and CFL number is to test them in linear limit with mean shear acted without any system rotation, for any given type of initial condition and mean flow configuration. The simulation cases operated here have basic discretization configuration with $N_\theta = 361$, $N_\varphi = 400$, $C = 0.15$, and the initial Reynolds number Re_l is 90. The convergence study regarding to N_θ, N_φ and the CFL number is plotted in figure 3.11, and study on k grids is plotted in figure 3.12.

Basically, one can finds that the refined grids and smaller CFL number refine the numerical convergence in different extents, except the cases from $N_\varphi = 400$ to $N_\varphi = 600$. A possible explanation is that in this flow, the advection in φ direction is smaller compared to the one in θ direction, so overcrowding grid points are not necessary and even reduces

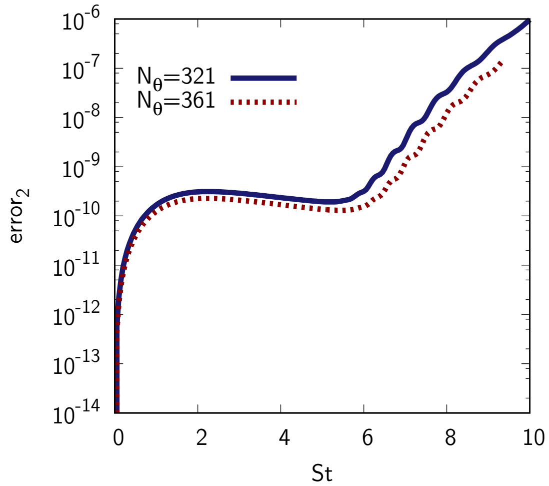

(a) Convergence study on N_θ.

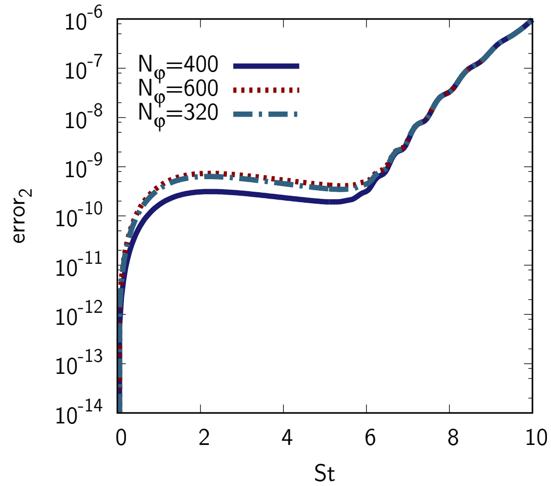

(b) Convergence study on N_φ.

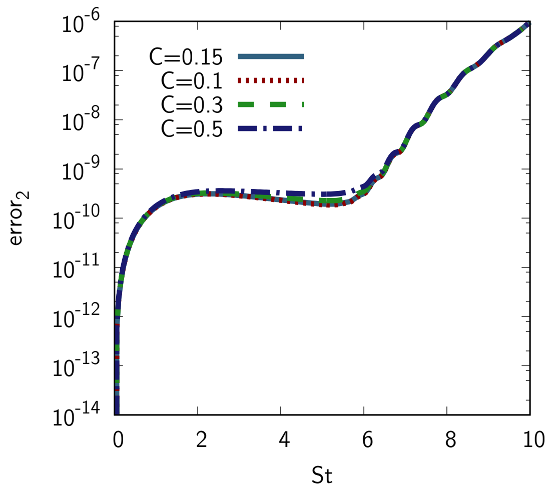

(c) Convergence study on CFL number C.

Figure 3.11: Time evolution of overall numerical error. Comparisons of the results from various grid configuration and CFL number for: (a) N_θ; (b) N_φ; and (c) CFL number.

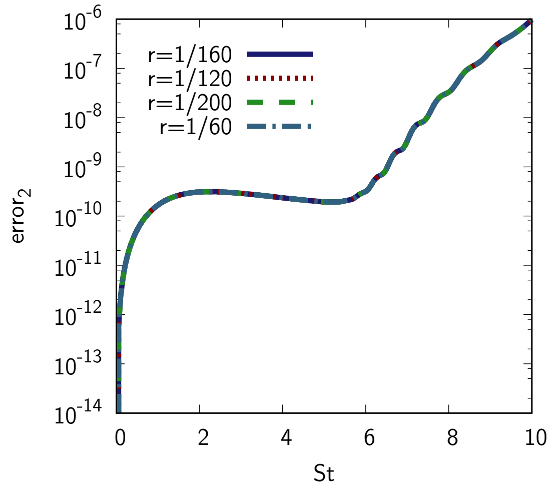

(a) Time evolution of overall numerical error.

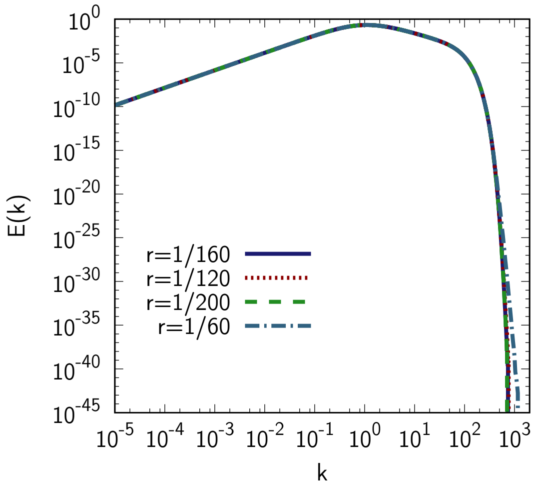

(b) Turbulent kinetic energy spectra.

Figure 3.12: Convergence study on k grids with various resolutions.

the accuracy. It is worthwhile to notice the influence of r, which does not affect the overall numerical accuracy too much, but refined grids in k improve the accuracy in small scales. Actually, the orders of magnitude for $k\mathcal{E}$ and kZ decrease rapidly along with k in the dissipative zone and after, which resulted in loss of significant digits when doing subtraction in FDS (large numbers 'eat' small numbers). The logarithmic distribution of k points leads to sparse mesh elements in the small-scale range. If the grids are refined in this range, then over dense grids are generated in large scales. This is why high order FDS is necessary in this model and upwind schemes perform rather badly. When the Reynolds number is not too large, the computational cost is acceptable with simple refining the k grids. Otherwise, significant computational cost must be reduced by other smooth customized k grids with not too dense grids in large scales and not too sparse grids in the small-scale range.

For the flow we test here, $N_\theta = 321$, $N_\varphi = 400$, $r = 1/120$ and $C = 0.3$ is a nice choice if stable simulations more than $St = 10$ are expected.

3.3.5 The improvements on EDQNM integral

The algorithm of EDQNM integrals is improved, either on the integral accuracy or on the discretization. The tests are performed without action of mean flow and system rotation, namely in HIT, with $Re_l = 880$. Two simulations start with same initial energy spectrum as shown in figure 3.13a with new code and old code respectively. Figure 3.13b indicates that the integral result by new code agrees very well with the one from old code, and figure 3.13c

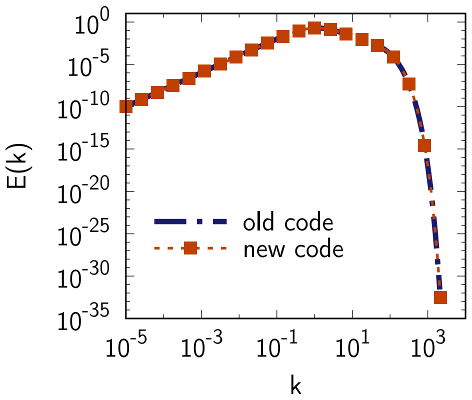

(a) Initial energy spectra at $t = 0$.

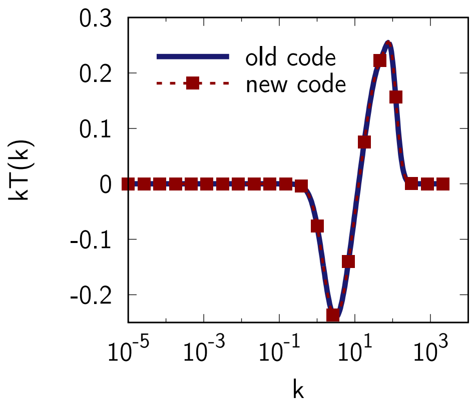

(b) Transfer spectra at $St = 0$.

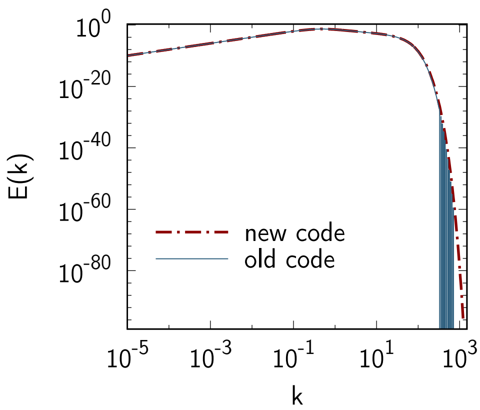

(c) Energy spectrum at $t/\tau_0 = 6.4$.

Figure 3.13: Validation and improvements of the new EDQNM algorithm. Comparisons of the results between old code and new code.

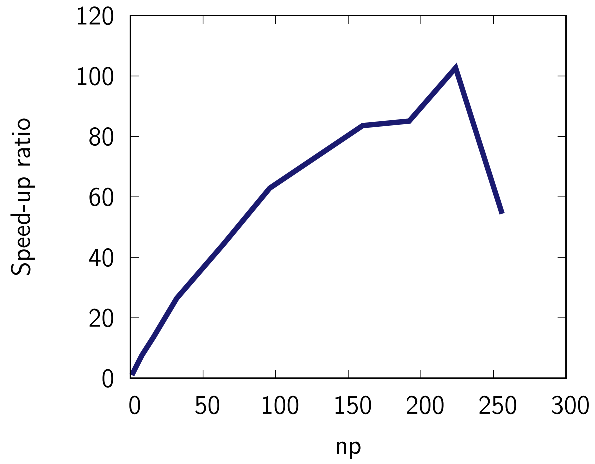

Figure 3.14: Parallel efficiency

shows the remarkable reduction of the numerical error at small scales, which is perhaps partly considered as model problem at past.

3.3.6 Parallelization effects

The parallel efficiency with MPI technique is tested for given flow with $Re_l = 1000$, in viscous linear limit with mean shear acted, and the grids configuration that $N_\theta = 400$, $N_\varphi = 400$ and $r = 1/80$. Figure 3.14 illustrates the speed-up ratio along with increasing number of processes np. Technically, after the peak point, namely when np is large than around 220, the hybrid parallelization can improve the efficiency further. However, it is beyond the current simulation demands and is not tested in this thesis.

Table 3.3 exhibits the effects of refined domain division method for EDQNM integrals. Comparisons of the maximum and minimum CPU time of process are listed out for one integral, with different k resolution and various np. It turns out that the refined method can reduce the maximum CPU time remarkably, especially for dense k grids, although the values of minimum time are similar.

3.4 Conclusion and perspectives

In this chapter, the numerical algorithm for the present model is introduced, and the biggest difference from conventional method is that we use finite difference scheme rather than characteristic method, in order to avoid remeshing and improve the numerical accuracy.

Table 3.3: Optimization effects for paralleled EDQNM integral

r	np	optimized	Min. CPU time	Max. CPU time
1/40	4	no	0.029	0.042
1/40	4	yes	0.029	0.039
1/40	8	no	0.015	0.027
1/40	8	yes	0.016	0.020
1/40	16	no	0.008	0.018
1/40	16	yes	0.008	0.012
1/80	4	no	0.219	0.346
1/80	4	yes	0.205	0.271
1/80	8	no	0.117	0.196
1/80	8	yes	0.113	0.145
1/80	16	no	0.054	0.127
1/80	16	yes	0.058	0.101

Next, plenty of preliminary tests are operated to correct, validate and optimize the numerical implementation.

It is worth well to mention that, a new numerical finite difference—pseudo-spectral method is proposed in Appendix E for incompressible homogeneous, to improve the numerical accuracy and to make the algorithm more universal for any type of mean flow velocity gradients. In addition, the new code for EDQNM integral with improved accuracy, breaks the restriction of logarithmic k grid points distribution, which can plays a role on the simulation of inertial wave.

Chapter 4

Dynamics of homogeneous rotating shear turbulence with the improved model

The validation of the present model is started by considering different flows in both the inviscid and viscous linear limits, and compare with results from Salhi *et al.* (2014) denoted as 'SLT' and obtained by the characteristics technique, and with results of MCS. Then, we compare fully nonlinear results provided by different models and nonlinear closure techniques: the present model with nonlinear terms in Eq. (2.82), denoted as 'ZCG', the hybrid model with nonlinear terms in Eq. (2.87), the MCS model, Weinstock's model with the nonlinear terms in Eq. (2.85), and direct numerical simulations by Salhi *et al.* (2014).

4.1 Linear dynamics: validation, comparison to MCS

4.1.1 Numerical configuration

In order to compare to the SLT results given by Salhi *et al.* (2014), we consider a flow with mean plane shear S such that the mean velocity gradient is $A_{ij} = S\delta_{i1}\delta_{j2}$. The indices 1, 2 and 3 refer to streamwise, cross-gradient, and spanwise directions respectively as illustrated in figure 1.4. In our first application in the linear limit, the additional system vorticity 2Ω is chosen in the spanwise direction, namely $\Omega_i = \Omega\delta_{i2}$. The theoretical predictions for the cases without system rotation are obtained corresponding to the exact solution of equation (1.54) for $\hat{R}_{ij}(\boldsymbol{k}, t)$ in which an integral Green's function (B.5) is computed analytically (details in Appendix B).

All the flow parameters and initial spectrum are following those in Salhi *et al.* (2014). The initial energy spectrum is found as

$$E(k, 0) = C_d k^2 \exp(-2\frac{k}{k_p}), \tag{4.1}$$

where C_d is a normalization constant, and $1/k_p$ is a characteristic length scale with $k_p = 10.6515$ in this section. The initial Taylor-scale-based Reynolds number is $Re = 56$, and the initial shear number $S^+ = S\mathcal{K}/\varepsilon = 2$. Rotation is chosen such that the Rossby number R is -5, -1, $-1/2$ and 0.

The linear limit regime is obtained by considering only the left-hand sides of Eq. (2.81) with zero right-hand sides. It is very subtle to capture because local angle-dependent terms in Fourier space coexist with the nonlocal advection operator (1.46), that induces a linear transfer in wave space.

4.1.2 Turbulent kinetic energy

The present model's numerical predictions of turbulent kinetic energy are shown in figure 4.1, along with those of MCS and the results of SLT. Typical cases with different combinations of strain and rotation are plotted: $R = -5$ or $\Omega = 5S/2$ corresponds to a stabilizing, anticyclonic case; $R = -1$ or $\Omega = S/2$ is a neutral case with zero absolute vorticity, as encountered in the central region of a rotating channel; $R = -1/2$ or $\Omega = S/4$ is a maximum destabilization, anticyclonic case, as in the pressure side of a rotating channel; and $R = 0$ with no rotation.

Concerning this validation of the models, it is important to note that the results of the SLT reference are almost entirely analytical, with a very dense discretization in terms of

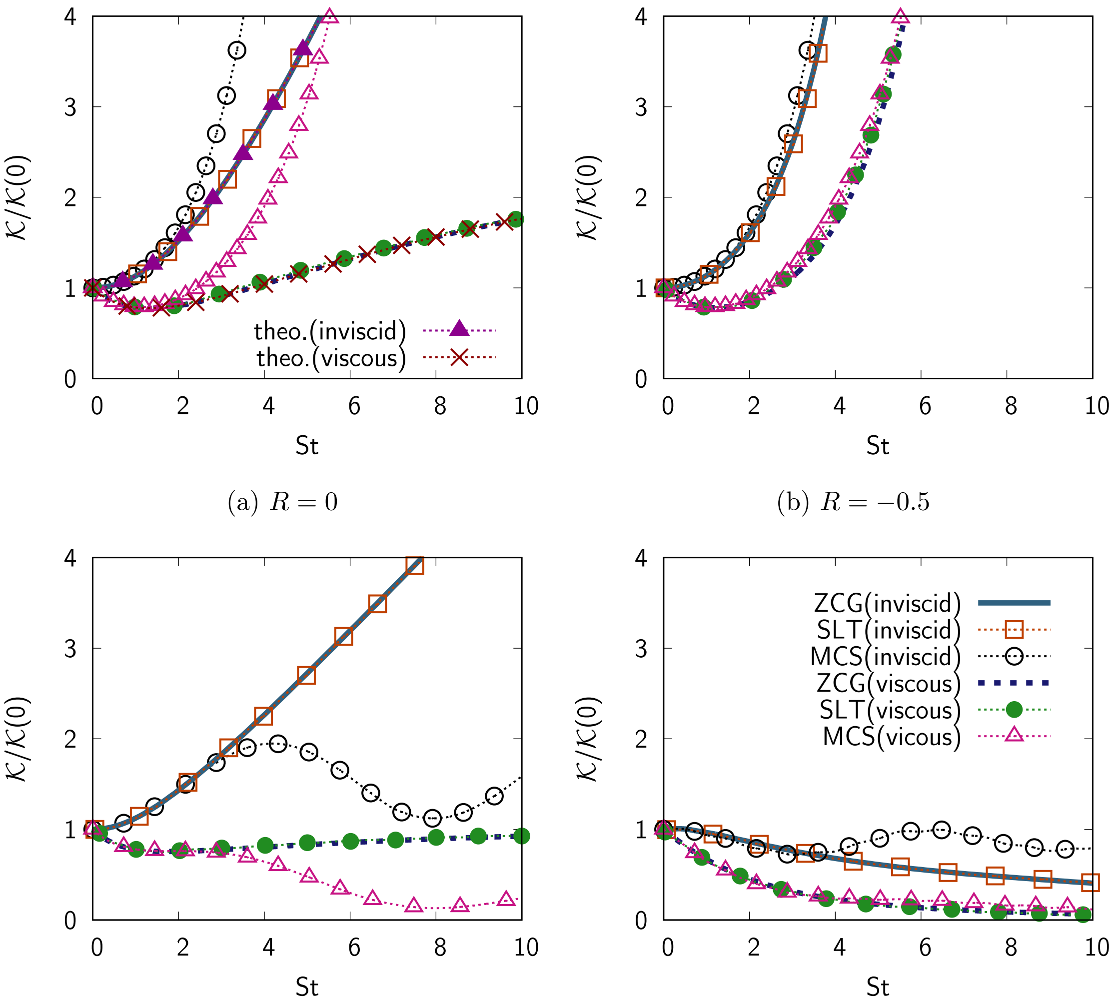

(a) $R = 0$

(b) $R = -0.5$

(c) $R = -1$

(d) $R = -5$

Figure 4.1: Time evolution of turbulent kinetic energy in inviscid and viscous linear limit, as a function of non dimensional time St. ZCG-MCS-SLT comparisons with four typical R ratios: (a) $R = 0$, in which the inviscid and viscous analytical exact solution is also plotted; (b) $R = -0.5$; (c) $R = -1$; and (d) $R = -5$.

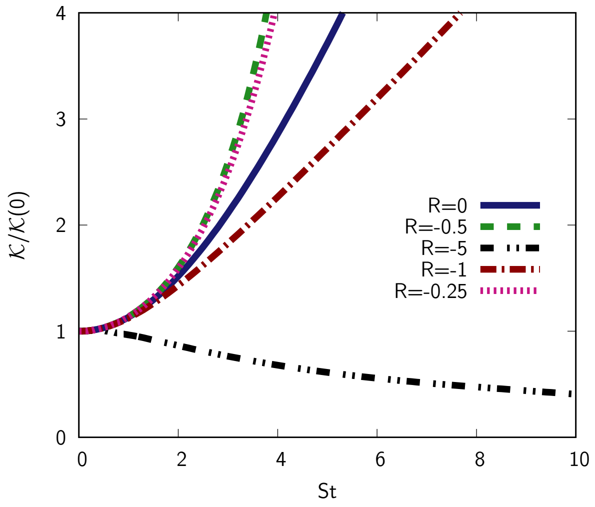

Figure 4.2: Time evolution of turbulent kinetic energy with $R = -5, -1, -1/2, -1/4, 0$ in the linear inviscid limit by the ZCG model.

wavenumbers and angles for performing integrals. For instance, the linear results from Salhi *et al.* (2014) are not obtained by simply cancelling the nonlinear terms in pseudo-spectral DNS, as sometimes done but using an accurate resolution of the time-dependent linear equations recalled in §1.3.3.

First of all, the figure shows excellent agreement between results of the ZCG model and SLT results of Salhi *et al.* (2014) for all the four cases. This is true for the inviscid runs but also, without surprise, for the viscous ones. In contrast, the MCS model departs rapidly from SLT at $St \gtrsim 3$, for both viscous or inviscid cases at $R = 0, -1$ (figures 4.1a and c), and for the inviscid case at $R = -5$ (figure 4.1d). In the viscous exponentially stable $R = -5$ case, which is stabilizing, the damping of energy is strong so that the relative departure of MCS from SLT is not as clear but still noticeable. MCS is close to SLT in the maximum destabilization case $R = -1/2$ (figure 4.1b), exponentially unstable, where the kinetic energy growth is largest. Clearly, for the $R = 0$ case, the algebraic growth of kinetic energy is missed by MCS and exponential growth is predicted instead.

Note that, in the inviscid case of zero absolute vorticity $R = -1$, inviscid MCS gives an evolution not far from periodic, probably close to the evolution of a one-point Reynolds-Stress-Model (RSM), in strong contrast with the expected algebraic growth.

Predictions concerning the pure shear case without additional system vorticity are also given by figure 4.1a in both inviscid and viscous linear limits, and compared with the theoretical analytical result of Appendix 1.3.3. The figure shows that the exact theoretical solution for the time-evolution of kinetic energy is accurately reproduced by our present model, thus confirming that our discretization and choice of numerical FD scheme are adequate in this limit. Moreover, the linear growth of kinetic energy is rightly predicted by the ZCG model, in contrast with the exponential growth of MCS.

We have finally gathered in figure 4.2 the kinetic energy evolution for all the previous inviscid cases, as well as for the intermediate case at $R = -1/4$ which is not documented in Salhi *et al.* (2014). The figure shows that kinetic energy decays only in the case at $R = -5$, and that kinetic energy grows in all others, including the neutral case $R = -1$. Moreover, there is very few difference between cases $R = -1/2$ and $-1/4$.

4.1.3 Kinetic energy spectra for pure shear

Spherically averaged kinetic energy spectra obtained from ZCG-MCS and a theoretical solution are plotted in figure 4.3 for $R = 0$ at $St = 5$, and figure 4.4 from ZCG-SLT at different times.

Figure 4.3 shows that the present ZCG model not only predicts correctly the total kinetic energy evolution but the scale-distribution agrees also very well with the theoretical prediction at all ranges. This is the case for both the inviscid limit (figure 4.3a) and the viscous one (figure 4.3b), so that the agreement cannot be accounted only on the effect of viscosity. As expected from the above comparison on the total kinetic energy, the energy spectra of the viscous or inviscid MCS model do not match the theoretical prediction. The departure is observed in the infrared range at small scales and in the inertial spectral range, less so in the viscous subrange where viscous dissipation is dominant and is solved exactly in the models.

The time evolution of the kinetic energy spectra is shown in figure (4.4), where the ZCG model spectra are compared to SLT spectra up to $St = 8$. The agreement is excellent, and it is particularly worth noticing that the peak of the ZCG spectra follow closely those of the SLT solution, indicating that the large scales are well resolved. The correspondence between the models in terms of the peak wavenumber evolution can also be observed in the nonlinear validation in section 4.2.

4.1.4 Production terms

The analysis of production in one-point statistics is obtained by spherically averaging the $\mathcal{E}$-equation (2.81). Since the mean shear is in the (x_1, x_2) plane, the production term we consider is $\langle u_1 u_2 \rangle$, but we rather compute the corresponding component b_{12} of the deviatoric

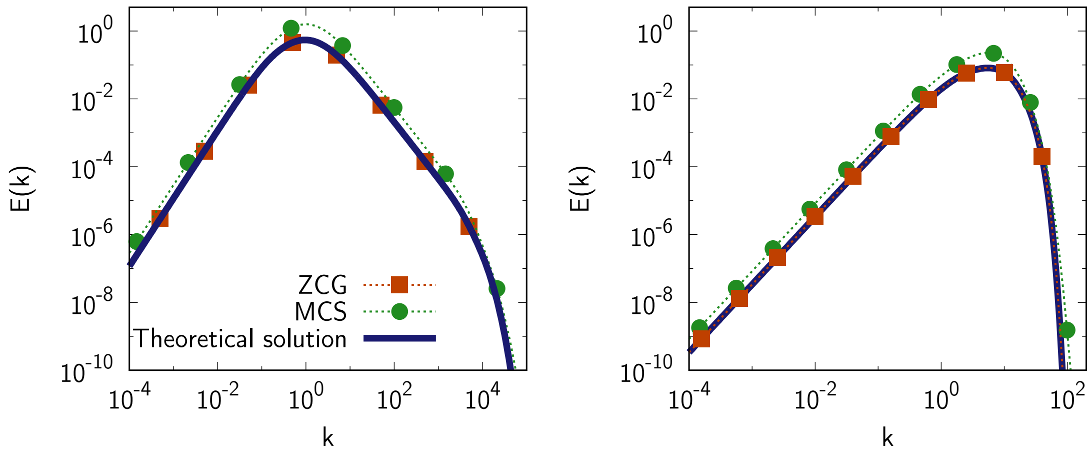

(a) Inviscid linear limit

(b) Viscous linear limit

Figure 4.3: Spherically averaged energy spectra for pure shear case at $St = 5$. MCS-ZCG-theoretical solution comparisons in both (a) inviscid linear and (b) viscous linear limit.

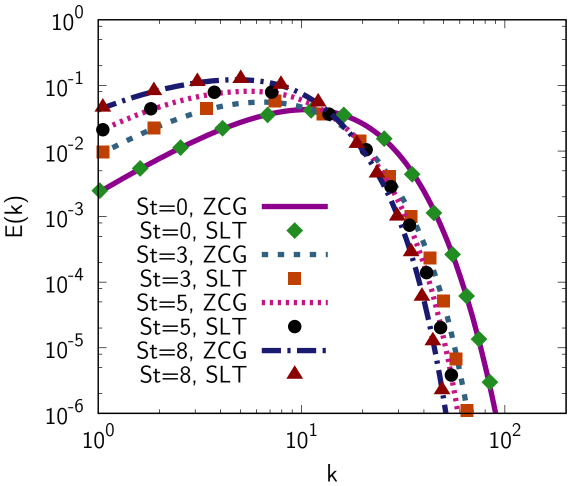

Figure 4.4: Time evolution of spherically averaged energy spectra. Comparison of results from the present model with SLT in the viscous linear limit for the pure shear case $R = 0$.

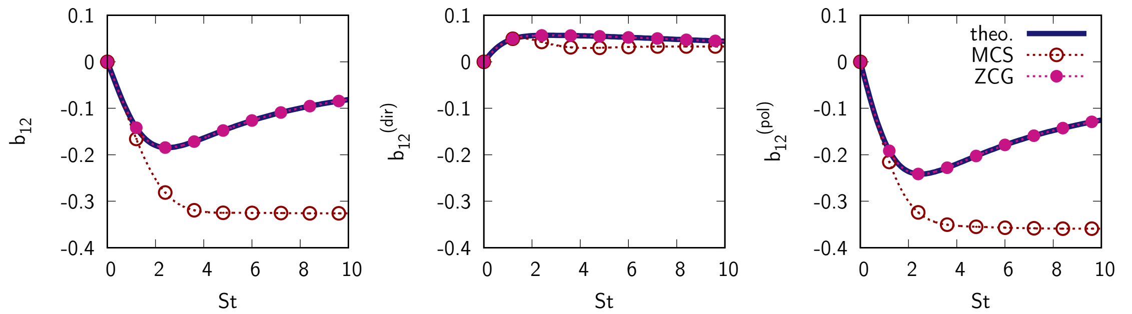

(a) total anisotropy (b) directional anisotropy (c) polarization anisotropy

Figure 4.5: Time evolution of (a) the deviatoric part of the Reynolds stress tensor, which is a production-related term, and its contributions from (b) directional and (c) polarization anisotropies. MCS-ZCG-theoretical solution comparisons for pure shear case $R = 0$ in the viscous linear limit.

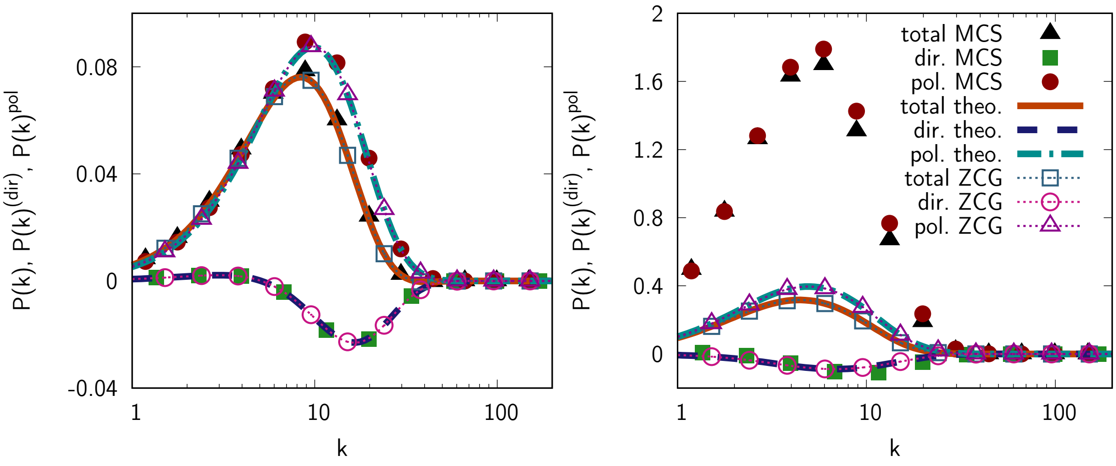

(a) $St = 0.5$ (b) $St = 5$

Figure 4.6: Spherically averaged spectra $P(k)$ of the production term, with both directional and polarization anisotropies for non rotating shear case $R = 0$ in viscous linear limit. MCS-ZCG-theoretical solution comparisons at (a) $St = 0.5$ and (b) $St = 5$.

of the Reynolds-stress tensor, namely $b_{ij} = \mathcal{K}^{-1}\langle u_i u_j \rangle - \delta_{ij}/3$, which can be computed from the kinetic energy spectrum $E(k)$ and the anisotropic tensor $\mathcal{H}(k)$ as

$$b_{ij}(t) = \mathcal{K}(t)^{-1} \int_0^\infty E(k,t) H_{ij}(k,t) dk.$$

At $R = 0$, the time development of b_{12} is shown in figure 4.5 in the viscous linear limit. The present model allows to correctly capture the total deviatoric part of the Reynolds stress tensor (figure 4.5a), along with its directional (figure 4.5b) and polarization contributions (figure 4.5c). The figures also show that MCS predicts quite well the development of the directional component $b_{12}^{(dir)}$, but not that of the polarization component $b_{12}^{(pol)}$, so that its prediction for b_{12} is not correct after $St \simeq 1$. The overestimation of the magnitude of $b_{12}^{(pol)}$ by MCS, with its plateau at large St, is connected to the erroneous prediction of the exponential growth of total kinetic energy, in accordance with

$$\frac{1}{\mathcal{K}} \frac{d\mathcal{K}}{dt} = -S b_{12} - \frac{\varepsilon}{\mathcal{K}}. \tag{4.2}$$

The time evolution of the spectrum $E(k,t)$ is itself obtained via

$$\left(\frac{\partial}{\partial t} + 2\nu k^2 \right) E(k,t) + S^L(k,t) - P(k,t) = T(k,t), \tag{4.3}$$

in which the spherically averaged production spectrum is

$$P(k,t) = -2SE(k,t)H_{12}(k,t). \tag{4.4}$$

Predictions of the production spectrum by the ZCG model with comparison to the results of MCS and the theoretical ones are reported in figure 4.6. Figure 4.6a at short time $St = 0.5$ shows a good agreement between both models and the theoretical predictions, due to the fact that anisotropy development is still limited at this time. However, figure 4.6b at longer time $St = 5$ shows that the MCS model prediction is not correct, mainly due to the polarization spectrum whose amplitude is not adequately captured, notwithstanding the proper prediction of the directional anisotropy production spectrum. The ZCG model compares very well with the theoretical prediction for both production spectra. This indicates clearly that the representation of anisotropy has to be complete, in terms of accumulation of directional accumulation of energy (in latitude in spectral space), but importantly also in terms of the more complex polarization anisotropic contents of the flow, which is related to its structure. This was also observed in homogeneous turbulence, in magnetohydrodynamics, rotating, or stratified flows. (Sagaut & Cambon (2018) and references therein)

These results are confirmed when rotation is added, on figure 4.7. Polarization anisotropy of the production spectrum is overestimated by MCS, except in the most unstable case (figure 4.7b). The directional part is much better reproduced than the polarization part in almost all other cases except the one in figure 4.7d. MCS is not good even for the directional part of anisotropy for this case at $R = -5$ in contrast with figure 4.7b at $R = -0.5$.

Note finally from figure 4.7 that the amplitude of production spectrum peak is larger for the case $R = -1/2$ and decreases with absolute value of R from -1 to -5, in which case it is only a hundredth of that of $R = -1/2$.

Figure 4.8 plots the time evolution of b_{12} for all four cases in viscous linear limit. It is difficult to evaluate what is the apparent frequency of these oscillations, but they seems to result from the bad consequence of the linear modelling of the stropholysis term in the Z-equation. In the 'exact' linear 3D equations, when dominated by system rotation, the term $(\boldsymbol{W} + 4\boldsymbol{\Omega}) \cdot \boldsymbol{\alpha}$ is very close to twice the dispersion frequency of inertial waves $\sigma = 2\boldsymbol{\Omega} \cdot \boldsymbol{\alpha}$. If this term is correctly accounted for in single-point statistics obtained by spectral averaging, it amounts to damped oscillations, and even their suppression after a short time, typically a quarter of a revolution. The physical mechanism is phase mixing, and this effect was also foreshadowed by Kassinos *et al.* (2001) as textitrotational randomization (misleading nomenclature). Unfortunately, such eventual damping of temporal oscillations cannot be captured if the angle-dependent frequency is evaluated by a little number of angular harmonics, as in MCS. Even in DNS's, the phase mixing can be missed at small k, given the sparsity of the angular discretization.

4.2 Nonlinear dynamics

4.2.1 Numerical configuration

The addition of a Coriolis force dramatically changes the linear dynamics with respect to the pure shear case. It is expected that the most difficult term to account for in SLT equation for second-order statistics is the *stropholysis* factor $-\mathrm{i}kZ(\boldsymbol{k}, t)\left((\boldsymbol{W} + 4\boldsymbol{\Omega}) \cdot \boldsymbol{\alpha} - 2\Omega_E\right)$ in (2.81), which reflects the direct effect of mean vorticity, shear-vorticity as well as system vorticity. As already discussed by Leblanc & Cambon (1998), both absolute mean vorticity $\boldsymbol{W} + 2\boldsymbol{\Omega}$ and tilting mean vorticity $\boldsymbol{W} + 4\boldsymbol{\Omega}$ are called into play. The result in figure 4.1 suggests that the simplest case without stropholysis term explains the good behaviour of MCS. Unfortunately, the stropholysis effect includes also the Ω_E term in (2.81), which is non zero in our first system of axes. To identify more clearly stropholysis and tilting mean

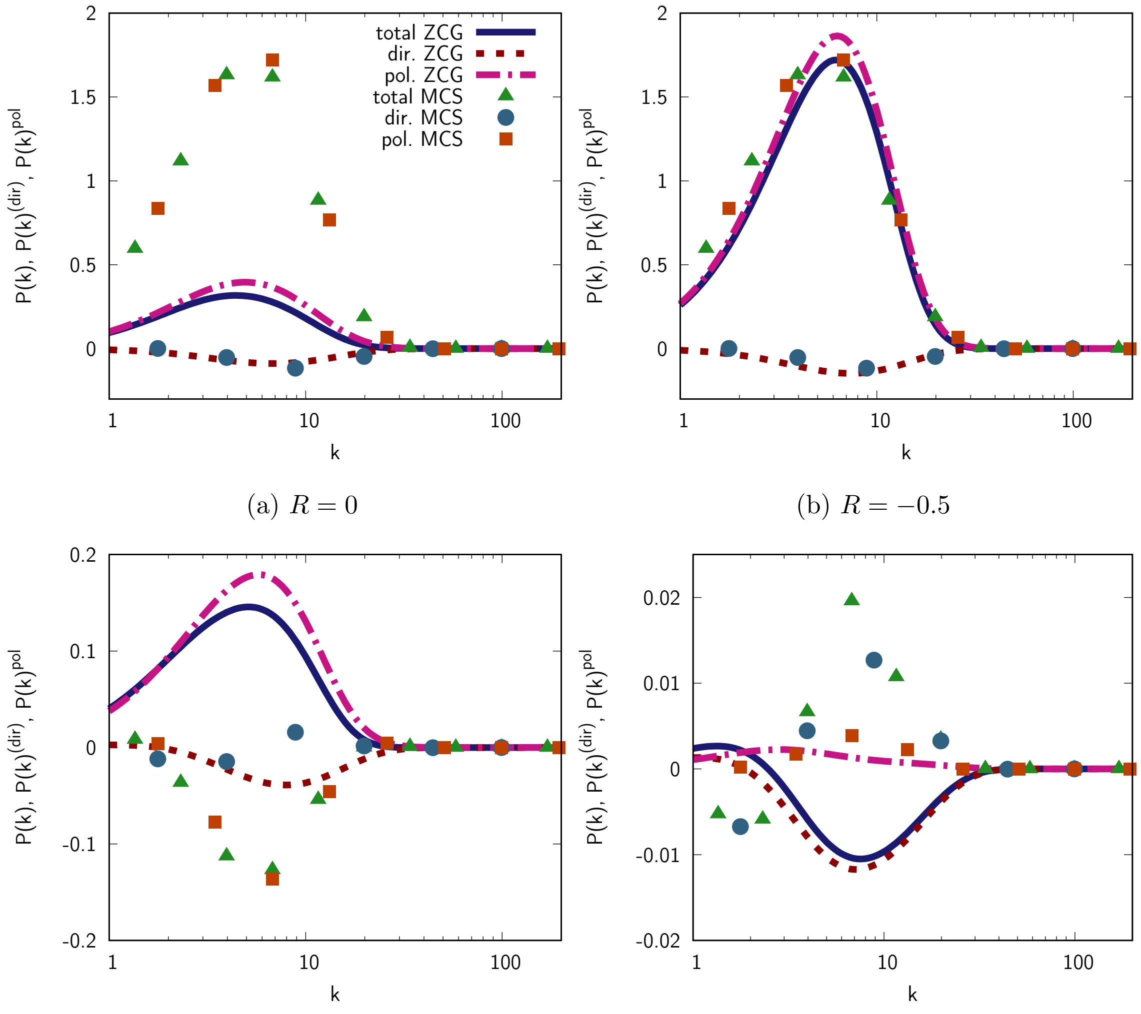

(a) $R = 0$

(b) $R = -0.5$

(c) $R = -1$

(d) $R = -5$

Figure 4.7: Spherically averaged spectra $P(k)$ of the production term with both directional and polarization anisotropies in viscous linear limit. Comparison of results at $St = 5$ from the present model and MCS with : (a) $R = 0$; (b) $R = -0.5$; (c) $R = -1$; and (d) $R = -5$.

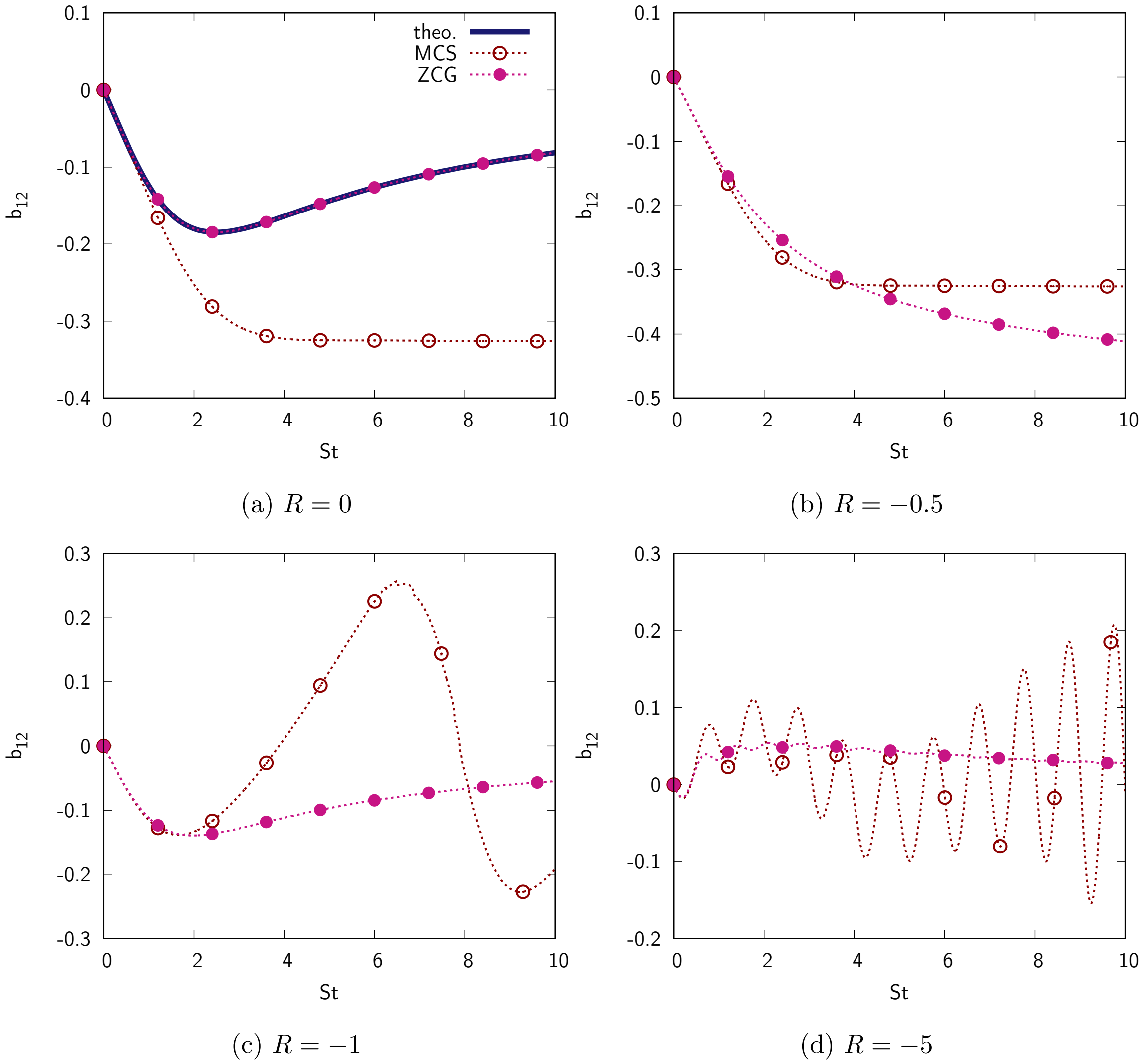

Figure 4.8: Time evolution of b_{13} in viscous linear limit for: (a) $R = 0$; (b) $R = -0.5$; (c) $R = -1$; and (d) $R = -5$.

vorticity, the mean plane shear is changed to $A_{ij} = S\delta_{i1}\delta_{j3}$ in the following fully nonlinear cases so that Ω_E and the complete stropholysis terms vanish. In addition, the robustness of the present ZCG model can be tested and one can also obtain simpler analytical linear solutions with this mean-velocity configuration.

Consequently, in this new configuration, indices 2 and 3 refer to spanwise and cross-gradient directions, and the Coriolis force is along axis 2. Accordingly, the ratio R changes to $2\Omega/S$. The relevant component for single-point anisotropy then becomes b_{13} instead of b_{12} and the corresponding production term is $P(k,t) = -2SE(k,t)H_{13}(k,t)$. The initial energy spectrum is the same as in the direct numerical simulations by Salhi *et al.* (2014) and we use the flow parameters from the linear cases since some computational parameters of the DNS are not document in their article.

4.2.2 Turbulent kinetic energy

Results for the nonlinear evolution of turbulent kinetic energy are presented in figure 4.9, for quantitative comparisons between DNS, MCS and the ZCG model, and with ZCG in the viscous linear limit. First of all, figure 4.9d shows that all approaches agree for the $R = -5$ case, showing that the flow regime is mostly viscous linear with very small production, also echoed by the small amplitude of the production spectrum in figure 4.7d. This is not the case for other flows at $R = 0, -1/2$ and -1 in which nonlinearity and anisotropy are larger. Figures 4.7a-c for these flows show a very good agreement between DNS and ZCG, although in the pure shear case the ZCG model saturates in terms of kinetic energy with respect to DNS, which suggests rather an exponential re-growth. The MCS model predictions are not satisfactory in the most unstable case, in spite of its good behaviour in the linear limit (figure 4.1b for $R = -1/2$). The disappointing behaviour of the ZCG model for the case $R = 0$ without system rotation (figure 4.9) suggests to introduce an additional term of forced Return To Isotropy (RTI) in line with the proposition of Weinstock (2013). Accordingly, Weinstock's model and its hybrid with the ZCG model are introduced in chapter 2, which is dedicated to the case of shear flow without system rotation, and we will comment figure 4.9 further in this section.

4.2.3 Production terms

Figure 4.10 plots the time evolution of b_{12} for all four cases with fully nonlinear models. MCS shows the misleading behaviors in all the cases and the apparent frequency of oscillations in the cases with $R = -1$ and $R = -5$, similar to the results in linear limit. For the

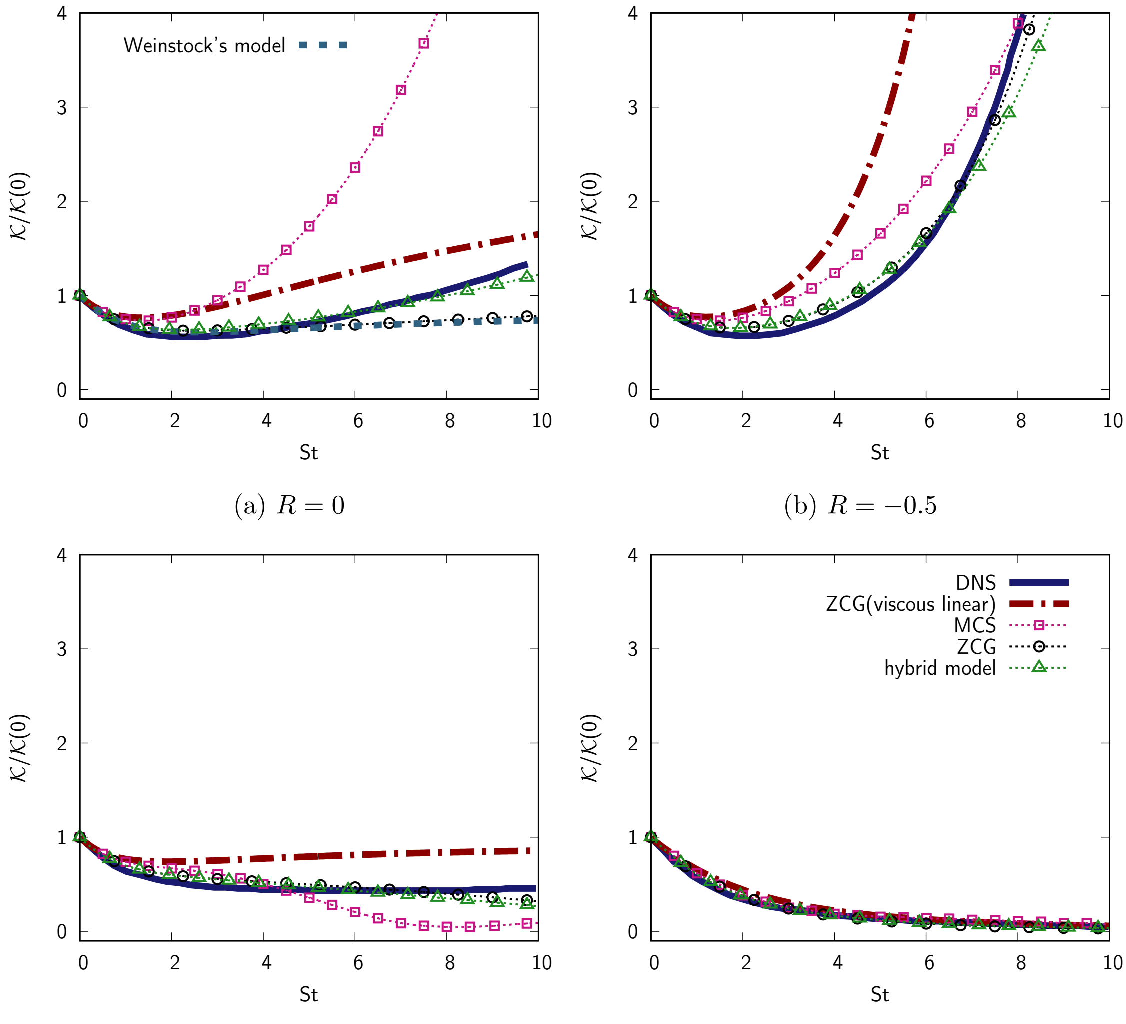

(a) $R = 0$

(b) $R = -0.5$

(c) $R = -1$

(d) $R = -5$

Figure 4.9: Time evolution of turbulent kinetic energy with: (a) $R = 0$; (b) $R = -0.5$; (c) $R = -1$; and (d) $R = -5$. Comparisons of the results from the different fully nonlinear models: full ZCG and viscous linear ZCG, MCS, Weinstock's and hybrid model, and from DNS.

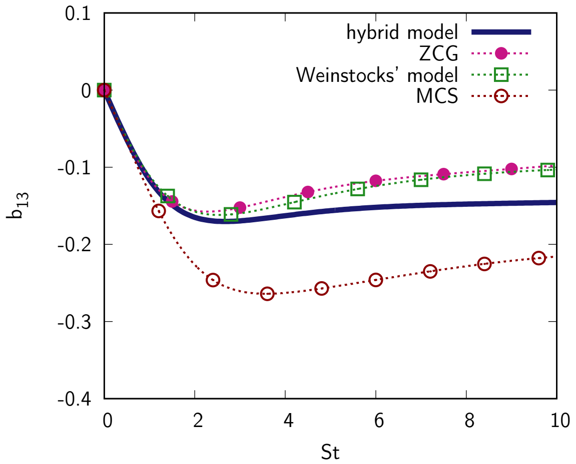

(a) $R = 0$

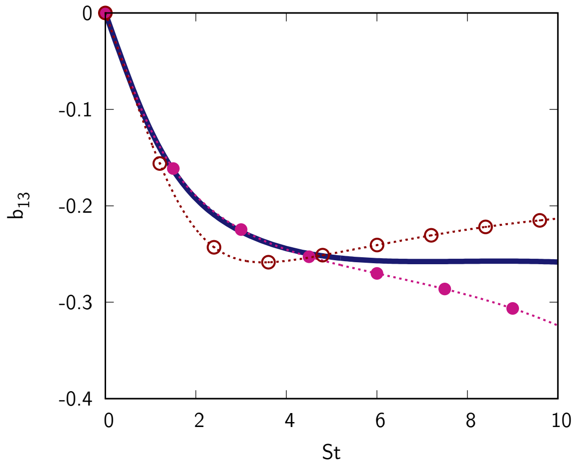

(b) $R = -0.5$

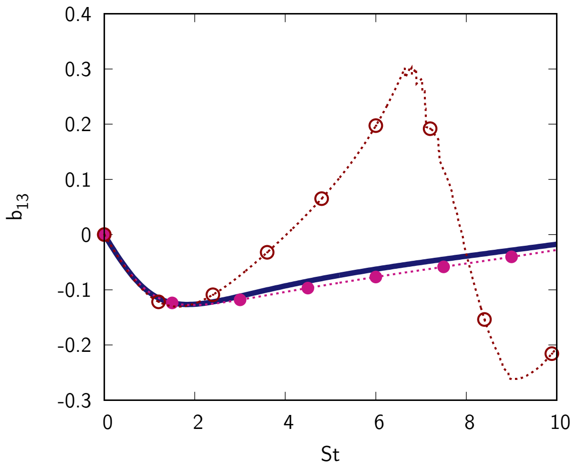

(c) $R = -1$

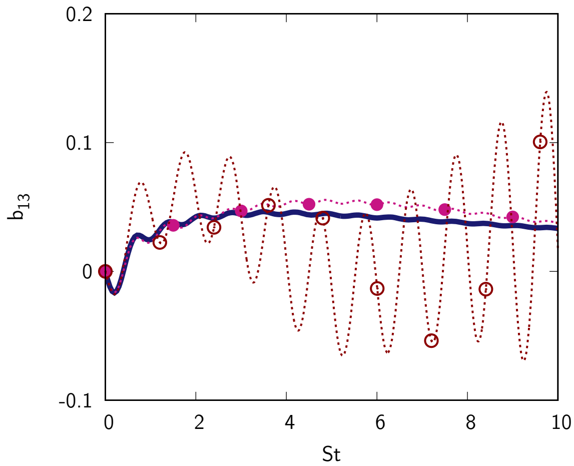

(d) $R = -5$

Figure 4.10: Time evolution of b_{13} with fully nonlinear models for: (a) $R = 0$; (b) $R = -0.5$; (c) $R = -1$; and (d) $R = -5$.

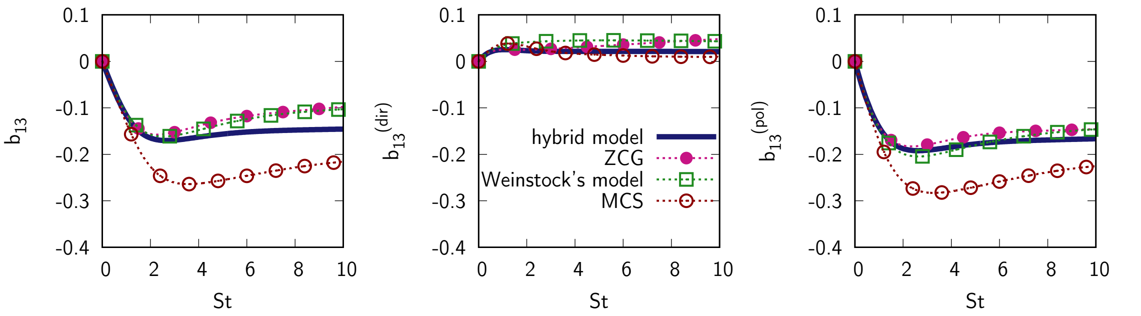

(a) total anisotropy (b) directional anisotropy (c) polarization anisotropy

Figure 4.11: Time development of (a) the deviatoric part of the Reynolds stress tensor component, b_{13}, typical of production-related term; (b) directional and (c) polarization anisotropies by the different fully nonlinear models in the non rotating shear case $R = 0$. Predictions by MCS-ZCG-Weinstock's and hybrid models.

pure shear case, the results given by Weinstock's model and ZCG are similar, which result in their missing exponential growth of the turbulent kinetic energy in figure 4.9a. The predictions given by ZCG and the hybrid model are similar in the neutral case and in the stabilizing case. ZCG predicts a wrong evolution of turbulent kinetic energy in the pure shear case. Moreover, it is worthwhile to notice that ZCG departs from the hybrid model in the maximum destabilization case as well.

4.3 Discussion for pure shear case

Going back to figure 4.9a, the results of both Weinstock's and hybrid model are plotted. Weinstock's model misses the exponential regrowth, as does our ZCG model, but a very satisfactory result is given by the hybrid model (Eq. (2.87)) The hybrid model remains satisfactory in all cases with system rotation, with only a slight underestimation of energy in the most unstable case (vs. DNS and our present model.) The fact that the hybrid model performs better than ZCG or Weinstock's alone indicates that both models have different complementary features which add up correctly to produce a better model for pure shear turbulence.

Still focusing on the case without system rotation, the deviatoric part of the Reynolds stress tensor is plotted in figure 4.11. Unfortunately, this information is not available from DNS, but the hybrid model gives the clearer steady limit of b_{13} that is consistent with the exponential re-growth of energy, with a value $b_{13} = -0.14$ very close to the one

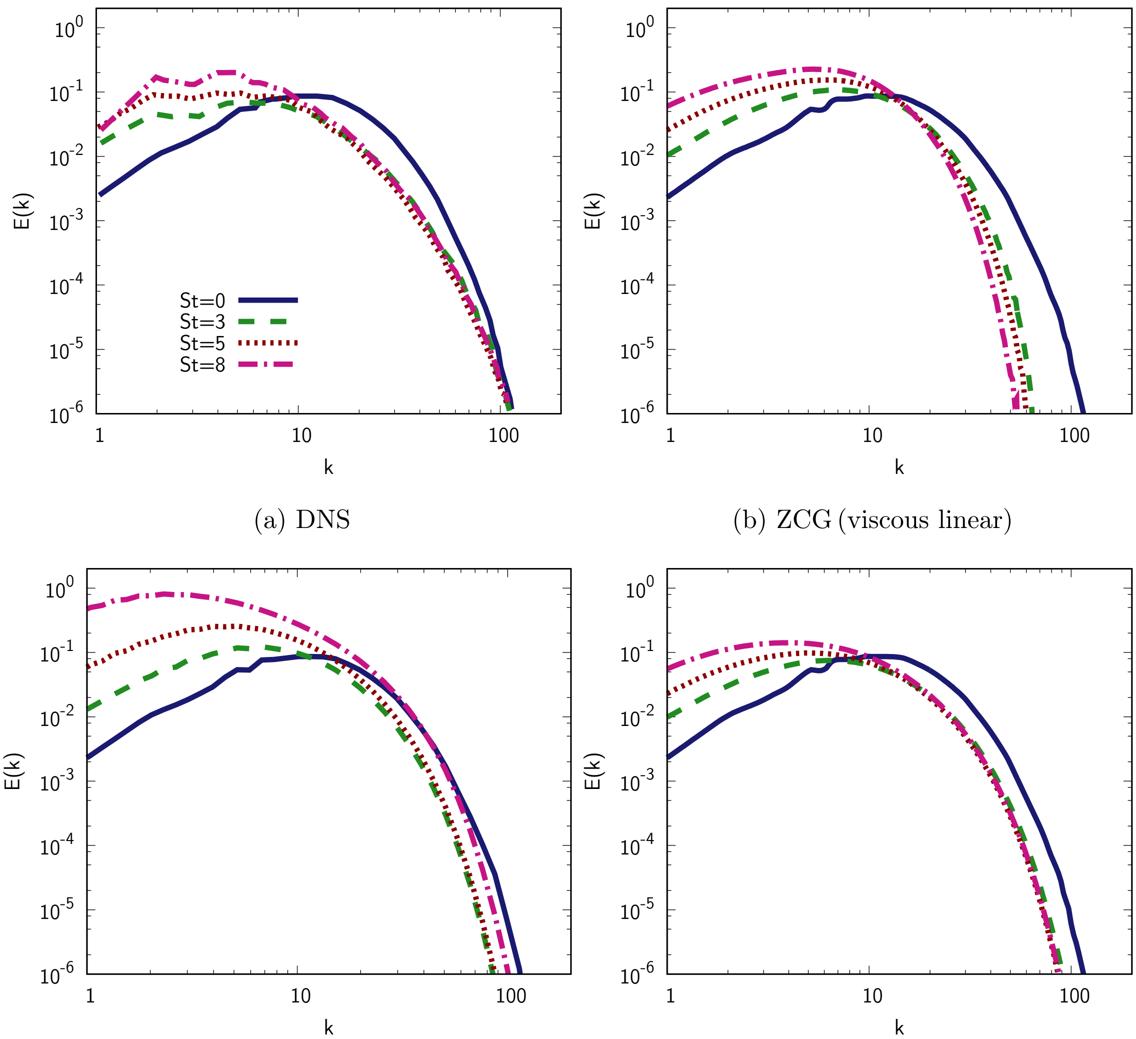

(a) DNS

(b) ZCG (viscous linear)

(c) MCS

(d) hybrid model

Figure 4.12: Time development of spherically averaged energy spectra in the non rotating shear case. Comparisons of the results among different fully nonlinear models, viscous linear and DNS: (a) DNS; (b) ZCG viscous linear; (c) MCS; and (d) hybrid model.

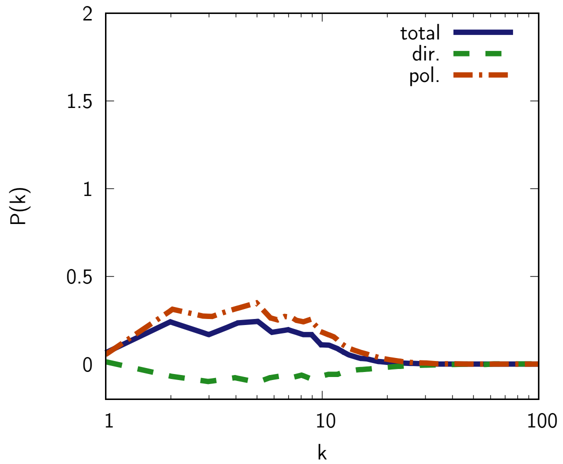

(a) DNS

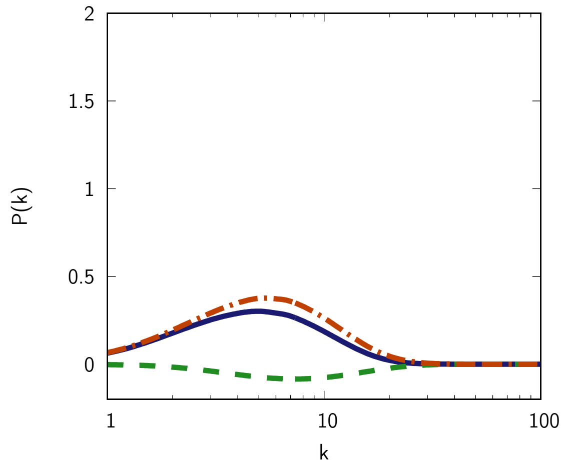

(b) ZCG (viscous linear)

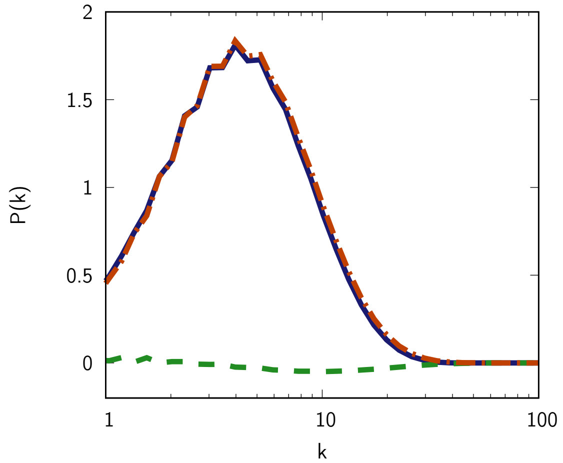

(c) MCS

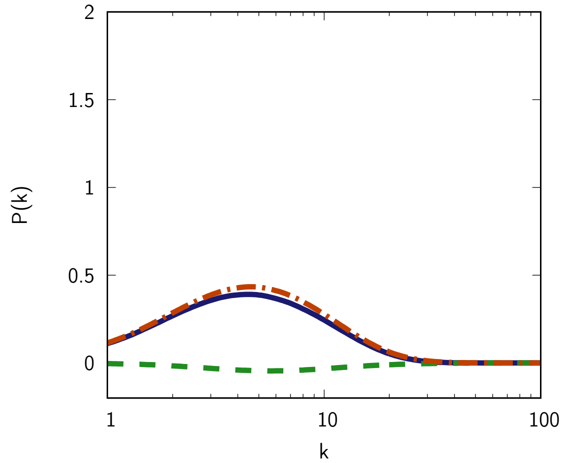

(d) hybrid model

Figure 4.13: Spherically averaged spectrum $P(k)$ of the production term with both directional and polarization anisotropies in pure shear case at $St = 5$. Comparisons of the results among different fully nonlinear models, DNS and viscous linear ZCG: (a) DNS, (b) ZCG (viscous linear), (c) MCS, and (d) hybrid model.

classically expected, in the range $[-0.16; -0.1]$ (see table p. 443 in Sagaut & Cambon (2018)). This stabilization of b_{13} to a constant by the hybrid model explains the constant rate of exponential growth equal to $-b_{13} - \varepsilon/(S\mathcal{K})$ (see equation (4.2), allowing for the change of 2 and 3 reference directions). Contribution of polarization anisotropy is dominant (figure 4.11c), and overestimated only by MCS, as usual, with a negative sign opposite to the one of directional contribution. The latter is correctly reproduced by MCS as well.

The spherically averaged energy spectrum $E(k,t)$ is plotted in figure 4.12 at increasing elapsed times $St = 0, 3, 5, 8$. Some differences between the results of various models with respect to the DNS ones are partly due to a forced isotropic precomputation only performed in DNS, in order to increase the Reynolds number before applying the mean shear. Accordingly, the initial spectrum (at $St = 0$) is closer to the one before the forced isotropic precomputation than the actual one in DNS. Nevertheless, qualitative comparisons remain informative. In figure 4.12c, the MCS model again is not relevant, especially at large scales up to wavenumbers of about 10, and at small scales where too much evolution is observed. The ZCG model in its viscous linear limit, in 4.12b, satisfactorily predicts the large scales growth, but not the decrease of the smallest ones. The latter decrease continuously, instead of being saturated, as in DNS in figure 4.12a. The prediction of large scales evolution is almost unchanged with respect to the linear behaviour in the ZCG model (not shown) and in the hybrid model in figure 4.12d, but the collapse of smallest scales at increasing times is very well reproduced by the hybrid model, slightly better than in the ZCG model and in the Weinstock one. Because all models except MCS reproduce correctly the linear dynamics, dominant at large scales, it is difficult to distinguish them from this viewpoint. The scrambling of large scales in DNS, due to the poor discretization at small wavenumber, and cumulated errors of remeshing, especially at long times, does not permit to establish a hierarchy of the models' predictions quality in the infrared spectral subrange. One can however focus on the large scales growth, or equivalently on the decrease of the wavenumber k_p at the peak of $E(k)$ for each approach. DNS does predict the expected decrease of k_p in time, from $k_p \simeq 16$ at $St = 0$ to $k_p \simeq 4.2$ at $St = 8$, and so do the ZCG and hybrid models ($k_p \simeq 4.1$ at $St = 8$ for the latter), but the decrease by the linear ZCG model is smaller ($k_p \simeq 5.3$ at $St = 8$), and similarly for Weinstock's model (not shown).

Finally, the production spectrum $P(k,t)$ is plotted in figure 4.13 for DNS , viscous linear ZCG, MCS and hybrid models, at a significantly large non dimensional time $St = 5$. Again, all models behave satisfactorily at first glance, except MCS due to the polarization contribution to production (figure 4.13c), which is overestimated, as in the linear limit.

Close examination of directional terms still shows small differences between the models — for instance, the peak production occurs at larger scales in Weinstock's model, and the complete ZCG model decreases both directional and polarization production slightly (not shown), but the amplitudes and shapes of production spectra are very similar to that of DNS in all models but MCS.

4.4 Conclusion and perspectives

Spectral modelling seems to be the best approach to statistics of two-point second-order correlations for homogeneous anisotropic turbulence, in the presence of uniform mean gradients and body forces, using a smart combination of SLT and EDQNM closure. This allows a scale-by-scale and angle-dependent analysis of anisotropy, disentangling directional and polarization anisotropy. Given the cost and the complexity of models in which the full angle-dependence of spectra is retained, especially for the EDQNM part, simplified models in terms of spherically-averaged descriptors are of interest. This was illustrated by Cambon *et al.* (1981) and materialized by a general development at the second order in MCS. Our approach with detailed calculations in this chapter first confirms some general tendencies, as follows:

1. When the linear dynamics gives exponential growth, models similar to MCS (in terms of spherically-averaged descriptors) work well. Generally, the nonlinear evolution results in a reduction of the exponential growth rate of energy, but without saturation. This is illustrated in figure 4.1, in which the special 4.1(b) case merits further discussion.

2. This is no longer true when the linear dynamics yields *algebraic* growth. Our best example is the plane shear flow without rotation. In this case, any model using a truncated expansion in terms of spherical harmonics gives a wrong exponential growth instead of algebraic. In spite of satisfactory results at short time, MCS — even with further introduction of fourth-degrees harmonics (Briard *et al.*, 2018) — is disqualified for a quantitative comparison with DNS. A similar comment applies to the other 'neutral case' (figure 4.1c), although to a lower extent. This is confirmed in this chapter, thanks to the accurate calculation of exact SLT.

The second point suggested to us to focus on the pure shear case, in which the exponential re-growth is mediated by fully nonlinear mechanisms. The combination of exact calculation of linear terms in the $(\mathcal{E}, Z)$ equations, and MCS model for reconstructing the nonlinear transfer terms from EDQNM at the degree 2, was not sufficient, so that kinetic energy was found to saturate, without regrowth. This disappointing result is attributed to insufficient scale-by-scale Return To Isotropy, as proposed by Rotta (1951*b*) for single-point statistics. There is indeed a large consensus on the fact that the RTI is essential for re-distributing the kinetic energy from the streamwise component of the RST to the vertical (cross-gradient) one. The nonlinear feeding of this vertical component is the key for obtaining the re-growth, even if the 'Rotta operator' damps all components of RST anisotropy, including b_{12} (for linear limit cases or b_{13} for fully nonlinear cases in the present paper) that is directly involved in the production of kinetic energy. This suggested the recourse to Weinstock's model, in which the spectral RTI is prescribed, and yields two new results:

3. Weinstock's model alone does not work, when implemented, with a saturation of kinetic energy instead of regrowth (figure 4.9a). This result is obtained by employing an *accurate* calculation of the linear terms.

4. Satisfactory results were eventually obtained by an hybrid of our first ZCG model, with a spectral RTI restricted to higher degree harmonics. This means that the nonlinear closure needs an elaborate degree-two expansion (in MCS but absent in Weinstock's model), but supplemented by a spectral RTI term for clipping higher degrees (as in Weinstock, and ignored in ZCG).

The latter result is perhaps our best achievement. It merits more specific studies for the pure shear, with parametric analysis and use of other DNS results, extrapolated to very high Reynolds number by our hybrid model. Fortunately, our hybrid model does not introduce new parameters to be tuned: the single 'isotropised' eddy-damping parameter is used in MCS and is closely related to φ^{RTI} in (2.85) to (2.87), as initially proposed by Weinstock.

Other perspectives concern improvement of simpler models, keeping the description in terms of angular harmonics, but with ad-hoc corrections and possible outcome for the improvement of single-point closures is expected as well.

Chapter 5

High degree anisotropy analysis with spherical harmonics decomposition on homogeneous rotating shear turbulence

In MCS, and also in the present model, SO^3-type decompositions for scalar $\mathcal{E}(\boldsymbol{k})$ and pseudo-scalar $Z(\boldsymbol{k})$ are employed and only first two degree decompositions of $\boldsymbol{R}$ are modelled in MCS. In addition, the fully nonlinear results of the flow with pure plane shear acted show that, damping of high degree anisotropy is essential to the modeling. Hence, it merits to perform further study on high degree anisotropy of flows. The tensorial expansion is independent of the choice of the polar direction $\boldsymbol{n}$, but it is difficult to apply at really high degree. Generating tensors are difficult to simplify only using rules of permutation and contraction of indices. In addition, it is not obvious to recombine them, at a given degree, in order to derive orthogonal bases. Accounting for this, the classical spherical harmonics decomposition for scalar is recalled in this chapter.

We validate the equivalency of the tensorial expansion and spherical harmonics decomposition, with their applications on $\mathcal{E}(\boldsymbol{k})$ firstly. Then the spherical harmonics decomposition are applied on typical rotating shear cases. In linear limit, we observe the effects of 'stropholysis' term. The fully nonlinear results are calculated with hybrid model, and the interaction between linear and nonlinear mechanisms are studied in the view of evolution of anisotropy in high degrees.

5.1 SO^3 decompositions with tensorial expansions and spherical harmonics

Here we recall the tensorial expansion for $\mathcal{E}(\boldsymbol{k})$, or more generally for any scalar with the symmetry that $\mathcal{E}(-\boldsymbol{k}) = \mathcal{E}(\boldsymbol{k})$, which vanishes all the odd degrees. The expansion is found as:

$$\mathcal{E}(\boldsymbol{k}) = \frac{E(k)}{4\pi k^2} + \sum_{n=1}^{\infty} H^{2n(\mathrm{dir})}_{l_1 l_2 \dots l_{2n}}(k) a_{l_1} a_{l_2} \dots a_{l_{2n}} \,, \tag{5.1}$$

where $2n$ is called the degree. Usually the expansion is mediated at a given degree $2n = 2N$, such as $2n = 2$ in MCS and nonlinear terms of ZCG.

Rubinstein *et al.* (2015) pointed out some properties of the coefficient tensors: They can be assumed symmetric under any interchange of indices, and also trace-free, in the extended sense that the contraction of any two indices vanishes identically; there are $2n+1$ linearly independent tensors with this property for each degree $2n$. Note that degree zero corresponds to the isotropic part $\dfrac{E(k)}{4\pi k^2}$, and the second degree is found as $H^{2(dir)}_{ij} = -15 H^{(\mathrm{dir})}_{ij}$, which is applied on MCS. Rubinstein *et al.* (2015) extended a practical expansion for degree 4, as

$$E(k) H^{4(dir)}_{mnpq} = \iint_{S_k} \mathcal{E}(\boldsymbol{k}) P_{mnpq}(\boldsymbol{\alpha}) \, \mathrm{d}^2\boldsymbol{k} \,, \tag{5.2}$$

with

$$\begin{aligned} P_{ijpq}(\boldsymbol{\alpha}) =& \alpha_i \alpha_j \alpha_p \alpha_q - \frac{1}{7}\big(\delta_{ij}\alpha_p\alpha_q \\ & + \delta_{ip}\alpha_j\alpha_q + \delta_{iq}\alpha_j\alpha_p \\ & + \delta_{jp}\alpha_i\alpha_q + \delta_{jq}\alpha_i\alpha_p + \delta_{pq}\alpha_i\alpha_j\big) \\ & + \frac{1}{35}\left(\delta_{ij}\delta_{pq} + \delta_{ip}\delta_{jq} + \delta_{iq}\delta_{pj}\right) . \end{aligned} \tag{5.3}$$

It is unrealistic to extend to higher expression for its complexity.

Correspondingly, the angular harmonics decomposition for $\mathcal{E}(\boldsymbol{k})$ can be expressed as:

$$\mathcal{E}(\boldsymbol{k}) = \frac{E(k)}{4\pi k^2} + \sum_{n=1}^{\infty} \sum_{m=-2n}^{2n} e_{2n,m}(k) Y_{2n,m}(\theta_k, \phi_k) \,, \tag{5.4}$$

where the basis in real form is applied for $\mathcal{E}(\boldsymbol{k})$. With respect to Eq. (5.2), only even degrees are relevant, from the Hermitian symmetry restricted to a purely real term. In contrast with the expansion in terms of tensors, the properties of orthogonality are obvious. The basis depends on the choice of the polar axis, but not the degree, so that at any given degree, there are simple linear relationships to pass from $Y_{2n,m}(\theta_k, \phi_k)$ to $Y'_{2n,m}(\theta'_k, \phi'_k)$ from a system of

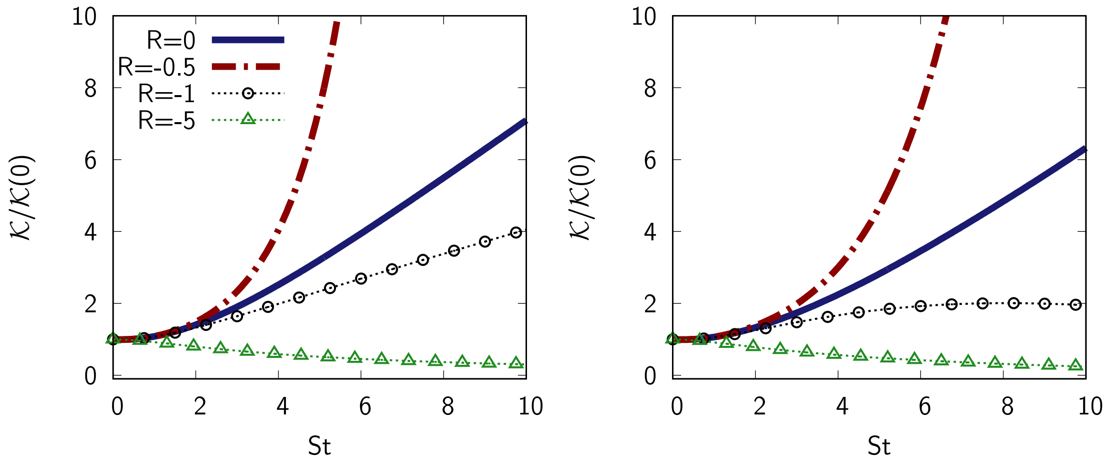

(a) Viscous linear limit

(b) Fully nonlinear results with hybrid model

Figure 5.1: Time evolution of turbulent kinetic energy, comparisons of results from the cases with typical values of R: (a) in viscous linear limit; (b) fully nonlinear results with hybrid model.

polar-spherical coordinates to another one. Note that the number of degree freedom is recovered from the tensorial decomposition to the scalar spherical one as $2n+1$ for degree $2n$.

Here, we denote:

$$\begin{aligned}
\mathcal{E}_0(\boldsymbol{k}) =& \mathcal{E}_0^t(\boldsymbol{k}) = \mathcal{E}_0^s(\boldsymbol{k}) = \frac{E(k)}{4\pi k^2} \\
\mathcal{E}_{2n}^t(\boldsymbol{k}) =& H_{l_1 l_2 \dots l_{2n}}^{2n(\mathrm{dir})}(k) a_{l_1} a_{l_2} \dots a_{l_{2n}} \\
\mathcal{E}_{2n}^s(\boldsymbol{k}) =& \sum_{m=-2n}^{m=2n} e_{2n,m}(k) Y_{2n,m}(\theta_k, \phi_k), \quad n = 1, 2, 3 \dots ,
\end{aligned} \tag{5.5}$$

for the sake of convenience. The coefficients for Eq. (5.4) can be found simply by the integrals:

$$e_{2n,m} = \frac{1}{k^2} \iint_{S_k} \mathcal{E}(\boldsymbol{k}) Y_{2n,m}(\theta_k, \phi_k) \,, \tag{5.6}$$

where all the basis $Y_{2n,m}(\theta_k, \phi_k)$ can be found in Appendix F. Four cases with typical values of R are observed in this chapter in viscous linear limit and with hybrid model respectively. The initial energy spectrum is just follow the one given by Eq. (3.37), with initial Reynolds number $Re_l = 880$. The mean shear is $A_{ij} = S\delta_{i1}\delta_{j3}$ to vanish the term of Ω_E in Eq. (2.27). The time evolution of kinetic energy for all cases is plotted in figure 5.1 and the related characteristic wavenumbers at $St = 5$ are listed in table 5.1. Figure 5.2 plots the

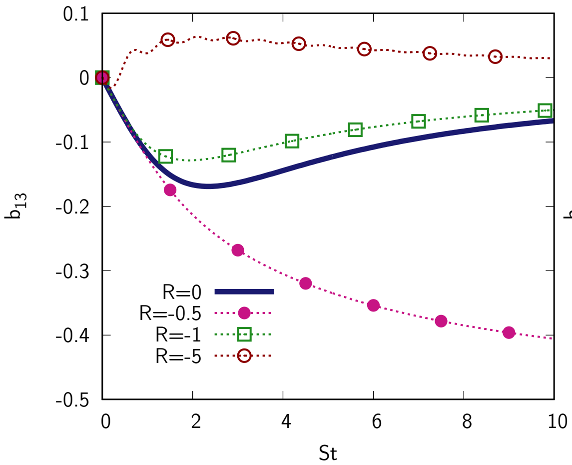

(a) Viscous linear limit

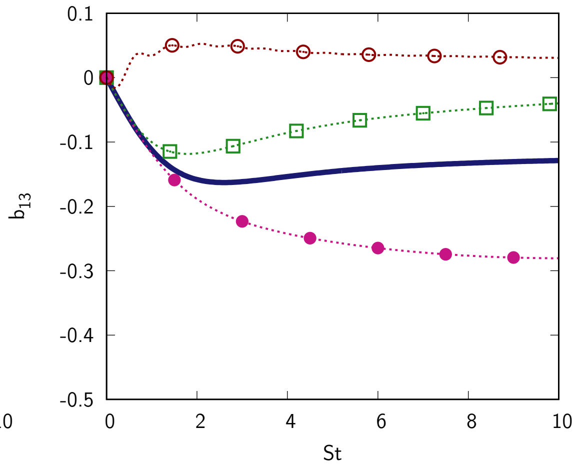

(b) Fully nonlinear results with hybrid model

Figure 5.2: Time evolution of the deviatoric part of the Reynolds stress tensor b_{13}, comparisons of results from the cases with typical values of R: (a) in viscous linear limit; (b) fully nonlinear results with hybrid model.

Table 5.1: Characteristic wavenumbers for all the cases at $St = 5$.

R	limit	k_l	k_λ	k_η
0	linear	0.81	5.08	170
0	fully nonlinear	0.78	11.6	304
-0.5	linear	0.81	4.58	198
-0.5	fully nonlinear	0.67	7.40	225
-1	linear	0.80	5.03	156
-1	fully nonlinear	0.72	8.65	192
-5	linear	0.84	8.53	137
-5	fully nonlinear	0.79	5.72	114

time evolution of the deviatoric part of the Reynolds stress tensor b_{13}, with comparisons of results from typical values of R.

5.2 Numerical validation for directional anisotropy

We consider the maximum destabilization case with $R = -0.5$ in viscous linear limit at $St = 5$ for the sake of concision, and other cases exhibit similar results. The components $\mathcal{E}_2(\boldsymbol{k})$ and $\mathcal{E}_4(\boldsymbol{k})$ are plotted in figures (5.3–5.5), which are calculated by tensorial expansion and spherical harmonics decomposition respectively, with the spherical distributions at characteristic wavenumber, from integral length scale to Taylor micro scale and Kolmogorov length scale.

In order to describe the scale effects of anisotropy with different degrees, we define the normalized spherically integral anisotropy for degree $2n$ as:

$$a_{2n}(k) = \frac{1}{E(k)} \iint_{S_k} |\mathcal{E}_{2n}(\boldsymbol{k})| \, \mathrm{d}^2\boldsymbol{k} \, , \tag{5.7}$$

with a^t_{2n} and a^s_{2n} for tensorial expansion and spherical harmonics decomposition respectively. Figure 5.6 exhibits the results in both linear limit and with fully nonlinear model for $2n = 2$ and $2n = 4$, still at $St = 5$ with the maximum destabilization case.

All the figures indicate that, the spherical harmonics decomposition agrees with tensorial expansion very well with high accuracy in terms of degrees, either with or without nonlinear mechanism, at any length scales. Actually, the two decomposition methods are equivalent in mathematics. The readers can see further details on representation methods in Rubinstein *et al.* (2015).

5.3 High degree anisotropy evolution

In this section, we obtain the high degree directional and polarization anisotropy at moderate dimensionless time $St = 5$ with $2n = 2\,,4\,,6\,,8$, both in linear limit and with fully nonlinear results.

5.3.1 Spherical expansion of polarization anisotropy

Although $Z(\boldsymbol{k})$ can not be decomposed by spherical harmonics directly since it is singular at pole, as introduce in chapter 3, the modulus $|Z(\boldsymbol{k})|$ is frame-invariant and can be

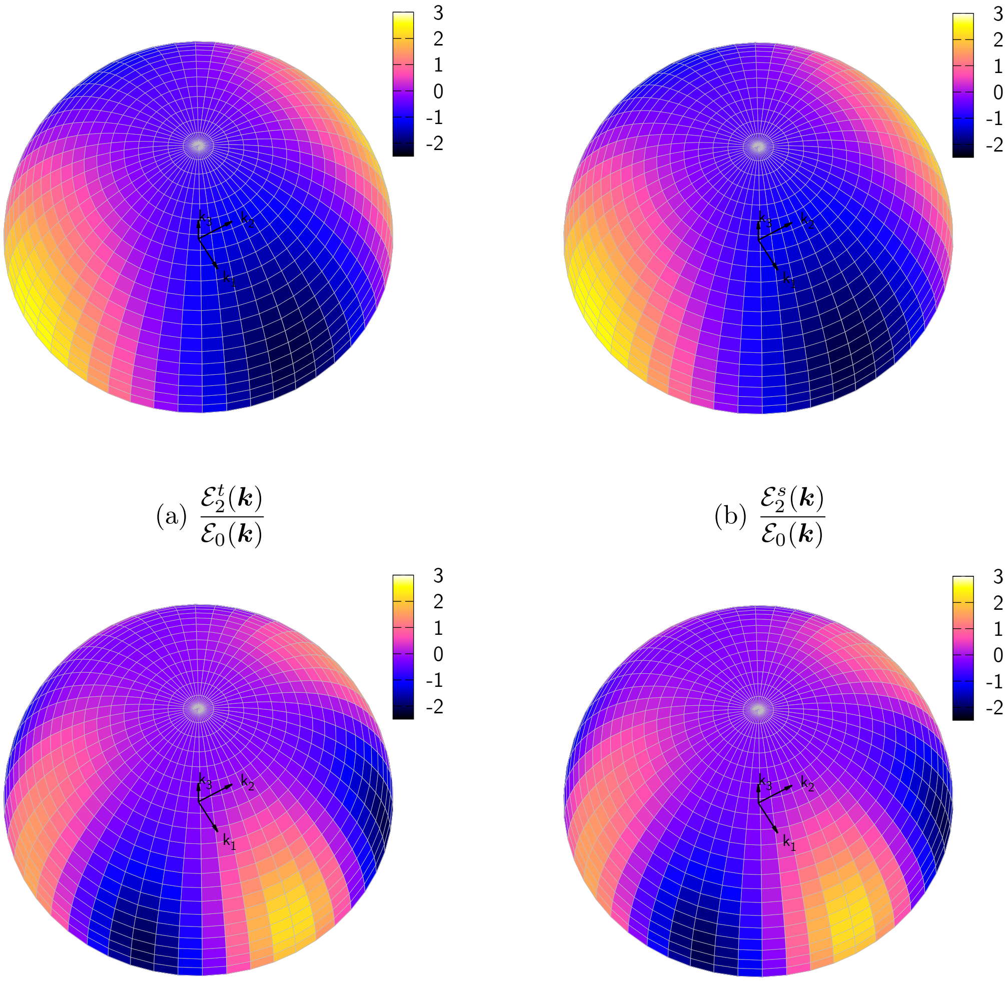

(a) $\dfrac{\mathcal{E}_2^t(\boldsymbol{k})}{\mathcal{E}_0(\boldsymbol{k})}$ (b) $\dfrac{\mathcal{E}_2^s(\boldsymbol{k})}{\mathcal{E}_0(\boldsymbol{k})}$

(c) $\dfrac{\mathcal{E}_4^t(\boldsymbol{k})}{\mathcal{E}_0(\boldsymbol{k})}$ (d) $\dfrac{\mathcal{E}_4^s(\boldsymbol{k})}{\mathcal{E}_0(\boldsymbol{k})}$

Figure 5.3: Spherical distributions of $\mathcal{E}_2$ and $\mathcal{E}_4$ in viscous linear limit with $R = -0.5$ at $St = 5$ at characteristic wavenuber $k = k_l$ for: (a) $\dfrac{\mathcal{E}_2^t(\boldsymbol{k})}{\mathcal{E}_0(\boldsymbol{k})}$; (b) $\dfrac{\mathcal{E}_2^s(\boldsymbol{k})}{\mathcal{E}_0(\boldsymbol{k})}$; (c) $\dfrac{\mathcal{E}_4^t(\boldsymbol{k})}{\mathcal{E}_0(\boldsymbol{k})}$; (d) $\dfrac{\mathcal{E}_4^s(\boldsymbol{k})}{\mathcal{E}_0(\boldsymbol{k})}$.

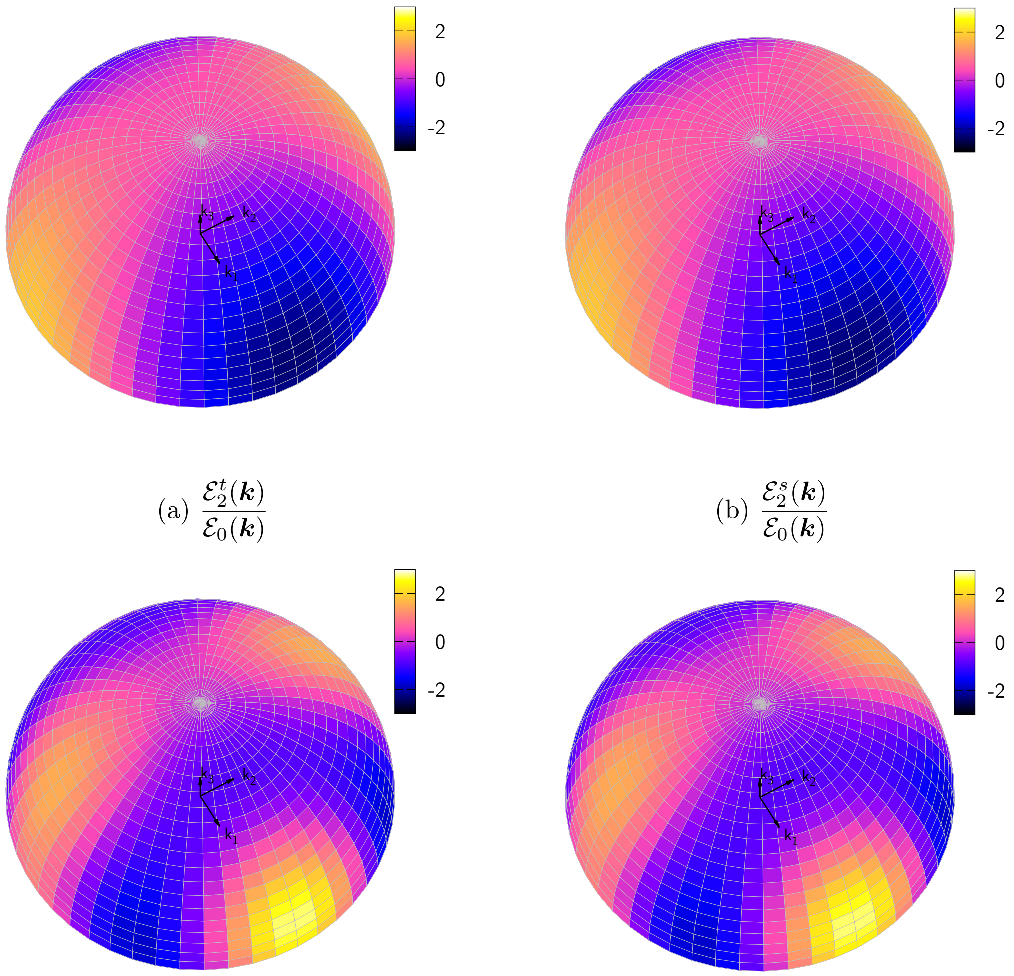

(a) $\dfrac{\mathcal{E}_2^t(\boldsymbol{k})}{\mathcal{E}_0(\boldsymbol{k})}$ (b) $\dfrac{\mathcal{E}_2^s(\boldsymbol{k})}{\mathcal{E}_0(\boldsymbol{k})}$

(c) $\dfrac{\mathcal{E}_4^t(\boldsymbol{k})}{\mathcal{E}_0(\boldsymbol{k})}$ (d) $\dfrac{\mathcal{E}_4^s(\boldsymbol{k})}{\mathcal{E}_0(\boldsymbol{k})}$

Figure 5.4: Spherical distributions of $\mathcal{E}_2$ and $\mathcal{E}_4$ in viscous linear limit with $R = -0.5$ at $St = 5$at characteristic wavenuber $k = k_\lambda$ for: (a) $\dfrac{\mathcal{E}_2^t(\boldsymbol{k})}{\mathcal{E}_0(\boldsymbol{k})}$; (b) $\dfrac{\mathcal{E}_2^s(\boldsymbol{k})}{\mathcal{E}_0(\boldsymbol{k})}$; (c) $\dfrac{\mathcal{E}_4^t(\boldsymbol{k})}{\mathcal{E}_0(\boldsymbol{k})}$; (d) $\dfrac{\mathcal{E}_4^s(\boldsymbol{k})}{\mathcal{E}_0(\boldsymbol{k})}$.

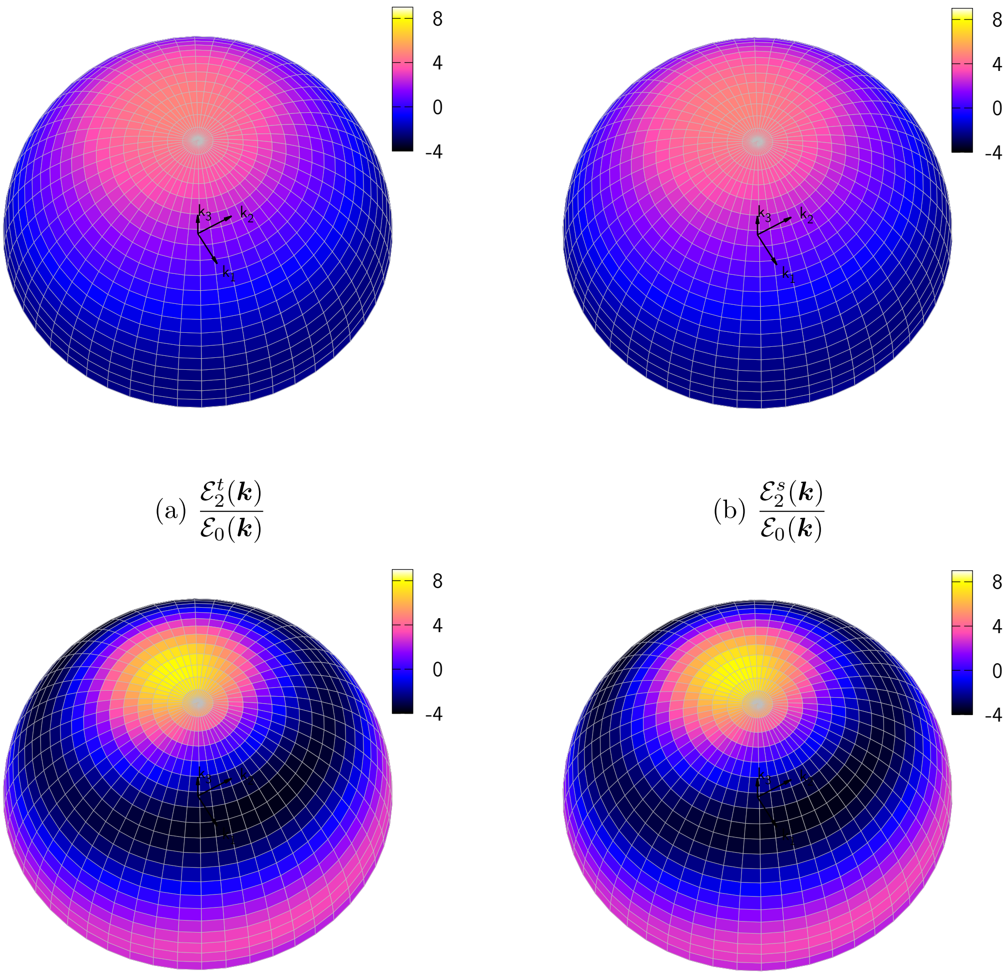

(a) $\dfrac{\mathcal{E}_2^t(\boldsymbol{k})}{\mathcal{E}_0(\boldsymbol{k})}$ (b) $\dfrac{\mathcal{E}_2^s(\boldsymbol{k})}{\mathcal{E}_0(\boldsymbol{k})}$

(c) $\dfrac{\mathcal{E}_4^t(\boldsymbol{k})}{\mathcal{E}_0(\boldsymbol{k})}$ (d) $\dfrac{\mathcal{E}_4^s(\boldsymbol{k})}{\mathcal{E}_0(\boldsymbol{k})}$

Figure 5.5: Spherical distributions of $\mathcal{E}_2$ and $\mathcal{E}_4$ in viscous linear limit with $R = -0.5$ at $St = 5$ at characteristic wavenuber $k = k_\eta$ for: (a) $\dfrac{\mathcal{E}_2^t(\boldsymbol{k})}{\mathcal{E}_0(\boldsymbol{k})}$; (b) $\dfrac{\mathcal{E}_2^s(\boldsymbol{k})}{\mathcal{E}_0(\boldsymbol{k})}$; (c) $\dfrac{\mathcal{E}_4^t(\boldsymbol{k})}{\mathcal{E}_0(\boldsymbol{k})}$; (d) $\dfrac{\mathcal{E}_4^s(\boldsymbol{k})}{\mathcal{E}_0(\boldsymbol{k})}$.

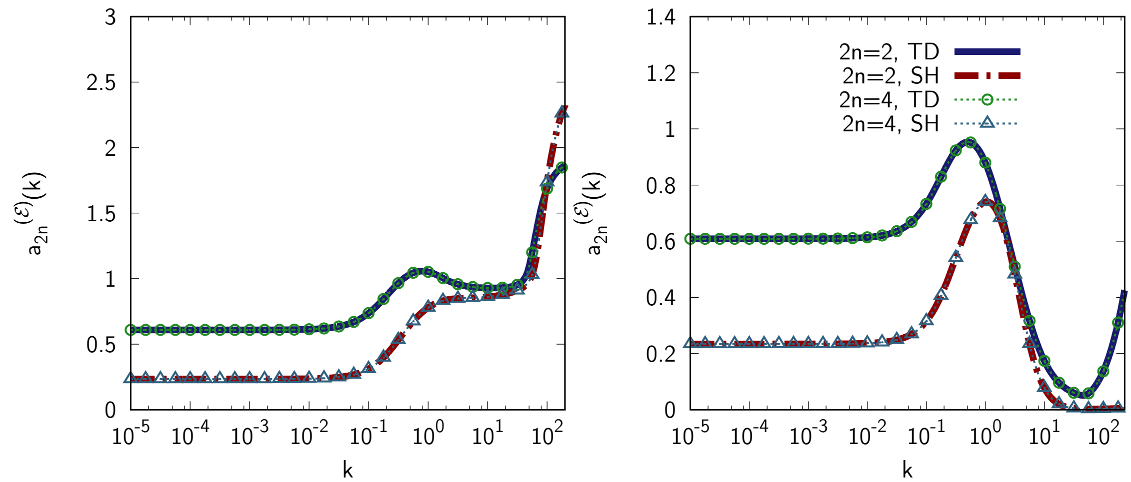

(a) Viscous linear limit

(b) with hybrid model

Figure 5.6: Spherically averaged anisotropy spectra for $\mathcal{E}(\boldsymbol{k})$ with $2n = 2$ and $2n = 4$ at $St = 5$. 'TD' represents 'tensorial decomposition' and 'SH' represents 'spherical harmonics decomposition'. Comparisons of the results from tensorial expansion and spherical harmonics decomposition: (a) in viscous linear limit; (b) with hybrid model.

decomposed by spherical harmonics. Similar to (5.4), one finds

$$|Z(\boldsymbol{k})| = z_0 + \sum_{n=1}^{\infty} \sum_{m=-2n}^{2n} z_{2n,m}(k) Y_{2n,m}(\theta_k, \phi_k) \,, \tag{5.8}$$

with

$$z_0 = \frac{1}{4\pi k^2} \iint_{S_k} |Z(\boldsymbol{k})| \, \mathrm{d}^2\boldsymbol{k} \,, \tag{5.9}$$

Also, we can define

$$Z(\boldsymbol{k})_{2n} = \sum_{m=-2n}^{m=2n} z_{2n,m}(k) Y_{2n,m}(\theta_k, \phi_k), \quad n = 1, 2, 3 \ldots \,, \tag{5.10}$$

and

$$a_{2n}^{(\mathrm{Z})}(k) = \frac{1}{4\pi k^2 z_0} \iint_{S_k} |Z(\boldsymbol{k})_{2n}| \, \mathrm{d}^2\boldsymbol{k} \,. \tag{5.11}$$

The decomposition permits to obtain high degree polarization anisotropy.

5.3.2 Stropholysis dynamical effect in linear limit

Figure 5.7 and figure 5.8 plot the spherically integral anisotropic spectra in viscous linear limit, for $\mathcal{E}(\boldsymbol{k})$ and $|Z(\boldsymbol{k})|$ respectively, with the results of first 8 degrees.

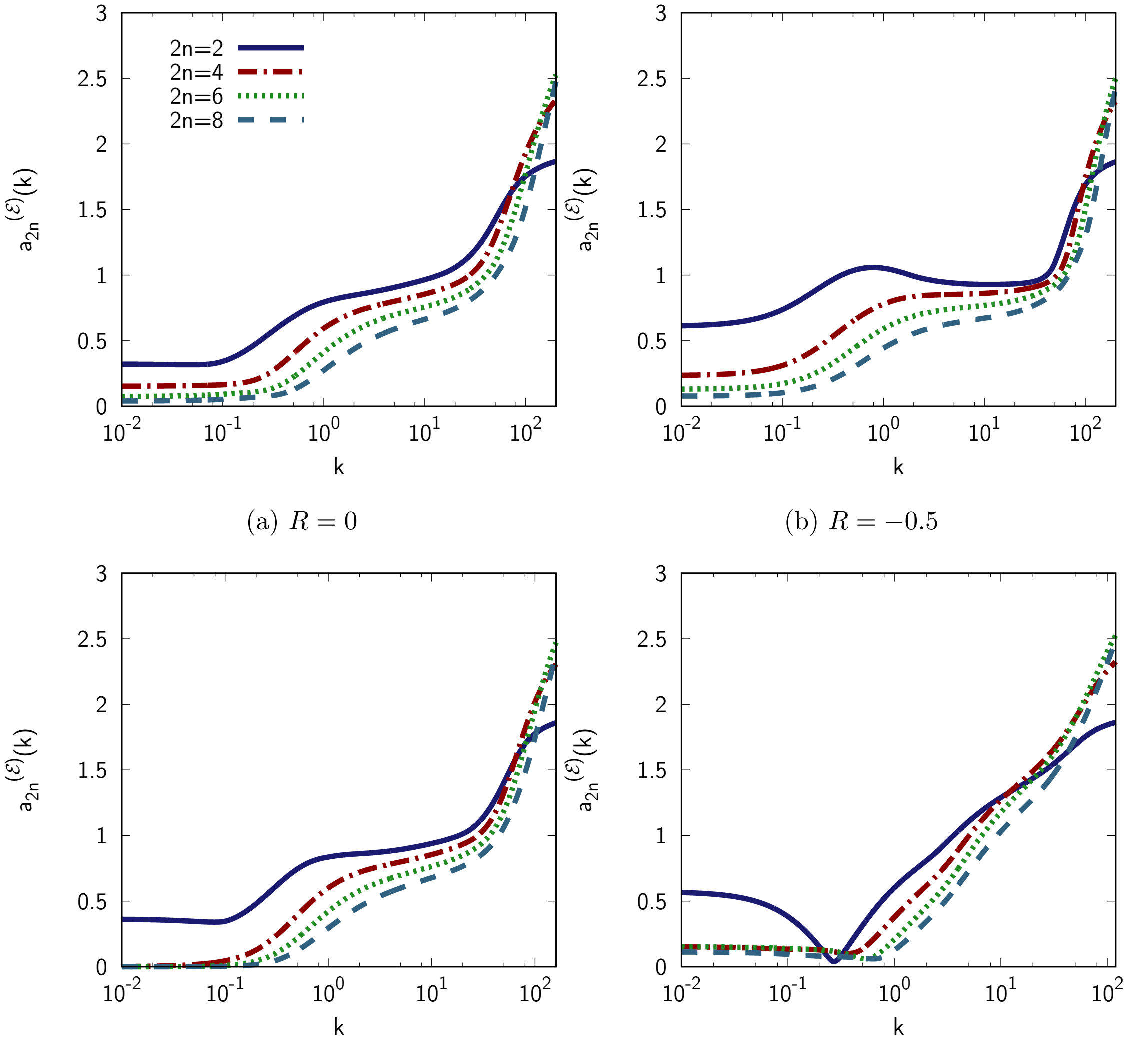

(a) $R = 0$ (b) $R = -0.5$

(c) $R = -1$ (d) $R = -5$

Figure 5.7: Spherically integral anisotropy for $\mathcal{E}(\boldsymbol{k})$ in $2n = 2\,,4\,,6\,,8$, in viscous linear limit at $St = 5$ for: (a) $R = 0$; (b) $R = -0.5$; (c) $R = -1$; (d) $R = -5$.

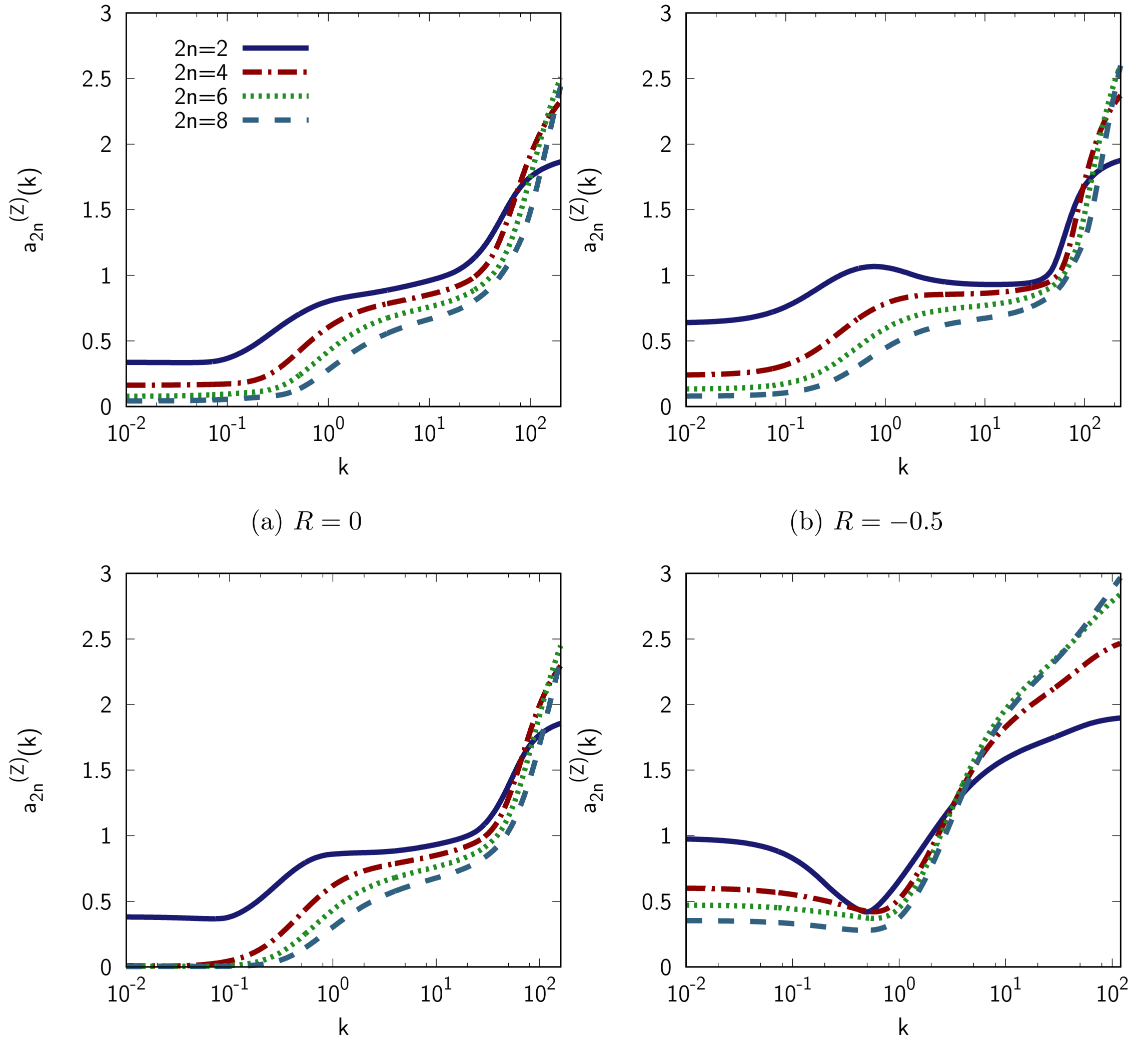

(a) $R = 0$

(b) $R = -0.5$

(c) $R = -1$

(d) $R = -5$

Figure 5.8: Spherically integral anisotropy for $|Z(\boldsymbol{k})|$ in $2n = 2\,,4\,,6\,,8$, in viscous linear limit at $St = 5$ for: (a) $R = 0$; (b) $R = -0.5$; (c) $R = -1$; (d) $R = -5$.

The 'stropholysis' term is the only explicitly different term for all the cases with various R and the same mean shear rate S: $\boldsymbol{W} + 4\boldsymbol{\Omega} = (0, S, 0)$ for the pure shear case; $\boldsymbol{W} + 4\boldsymbol{\Omega} = (0, 0, 0)$ vanishes in the maximum destabilization case; $\boldsymbol{W} + 4\boldsymbol{\Omega} = (0, -S, 0)$ for the neutral case, with the same net mean vorticity but opposite sign to $R = 0$; $\boldsymbol{W} + 4\boldsymbol{\Omega} = (0, -9S, 0)$ for the stabilizing case $R = -5$ with relatively large net mean vorticity.

These two figures indicates that, at the large sales around k_l, the maximum destabilization case has the largest anisotropy in degree 2, while the case with pure shear and the neutral case are similar and the stabilizing case has small anisotropy in degree 2. Concerning higher degree anisotropy, still for large scales, the cases have similar behaviours except the one with $R = -5$, in which the higher degree anisotropy is in the similar level with the one in degree 2. Hence, in the energy containing zone, the case with $R = -0.5$, has the smallest higher anisotropy compared to the one in degree 2.

All the cases show strong anisotropy at large k and non-monotonic k-distribution, especially for the case with $R = -5$. The stabilizing case contributes the most different behaviour, with more obvious higher degree anisotropy than others at small scales, especially in the results of $Z(\boldsymbol{k})$.

5.3.3 Interactions between linear dynamics and nonlinear transfer

Figure 5.9 and figure 5.10 plot the spherically integral anisotropic spectra with hybrid model, corresponding to Figure 5.7 and figure 5.8. First of all, strong RTI effects by the nonlinear terms can be observed in all the cases, in which the anisotropy almost reduce remarkably in viscous zone.

Concerning the large scales, the results do not change too much compared to those in linear limit. In addition, The neutral case and stabilizing cases keep strong anisotropy in the range $k_l < k < k_\eta$.

5.4 Conclusion and perspectives

In this chapter, we validate the equivalency of tensorial expansion and spherical harmonics, then the latter help us analyze the high degree anisotropy of homogeneous rotating shear turbulence both in linear limit and with fully nonlinear terms.

The results, especially in linear limit, support our hypothesis that the 'stropholysis' term plays an essential role to generate anisotropy. The anisotropy in degree 2 is the major anisotropic component in the case $R = -0.5$, that means the influence from higher degree

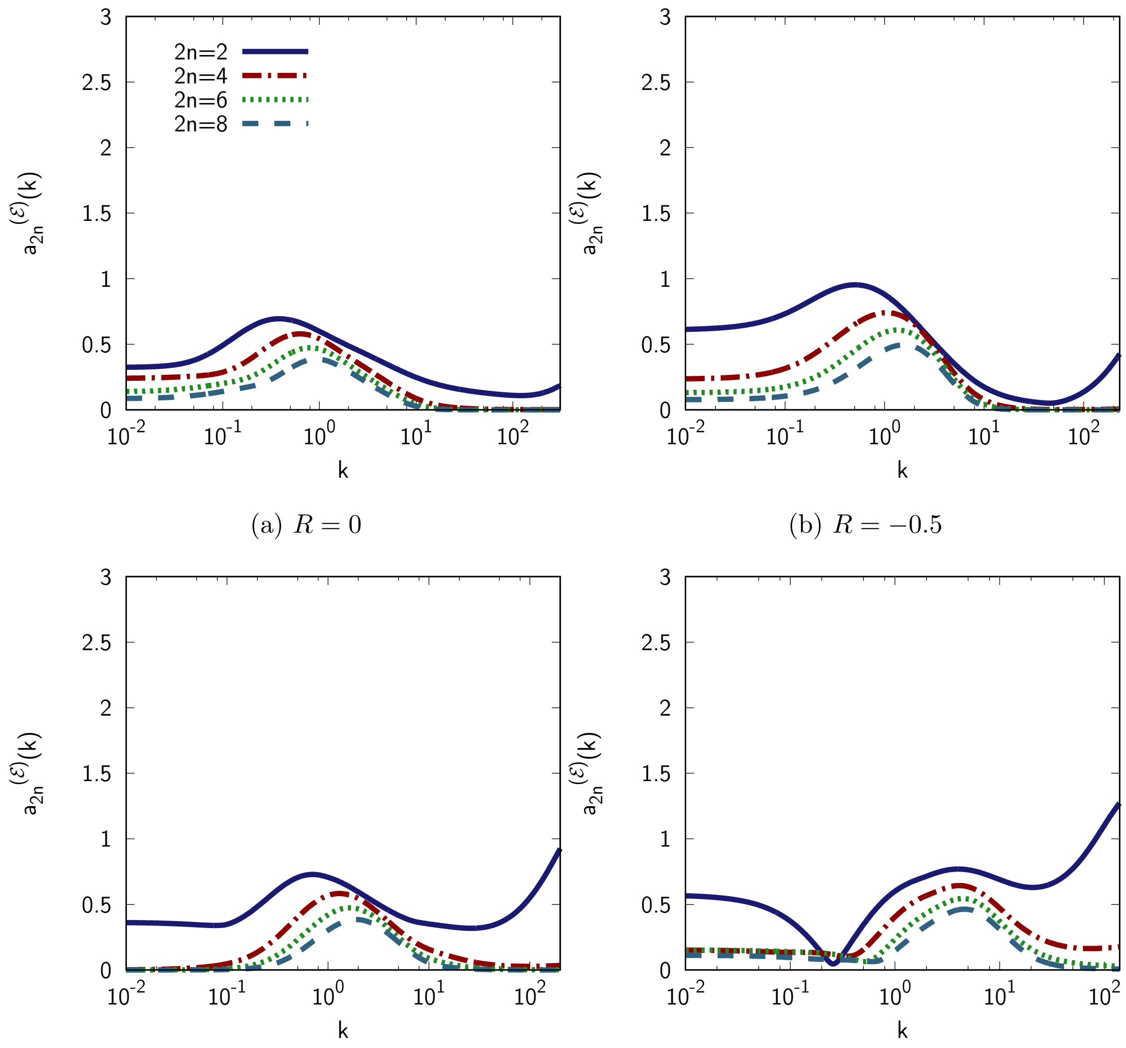

(a) $R = 0$

(b) $R = -0.5$

(c) $R = -1$

(d) $R = -5$

Figure 5.9: Spherically integral anisotropy for $\mathcal{E}(\boldsymbol{k})$ in $2n = 2, 4, 6, 8$, with the hybrid model at $St = 5$ for: (a) $R = 0$; (b) $R = -0.5$; (c) $R = -1$; (d) $R = -5$.

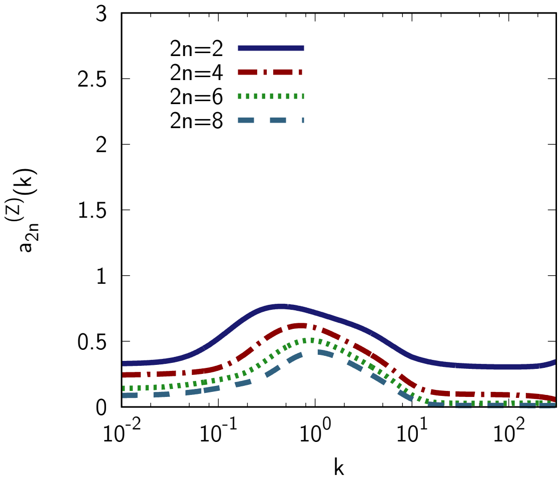

(a) $R = 0$

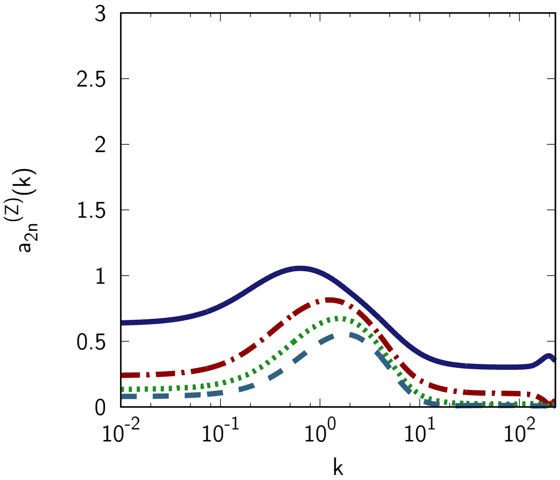

(b) $R = -0.5$

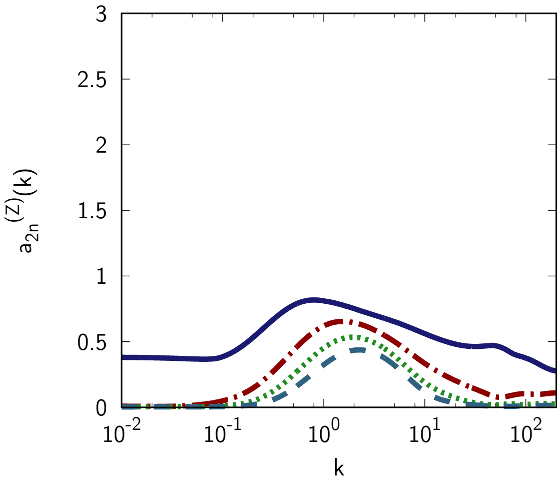

(c) $R = -1$

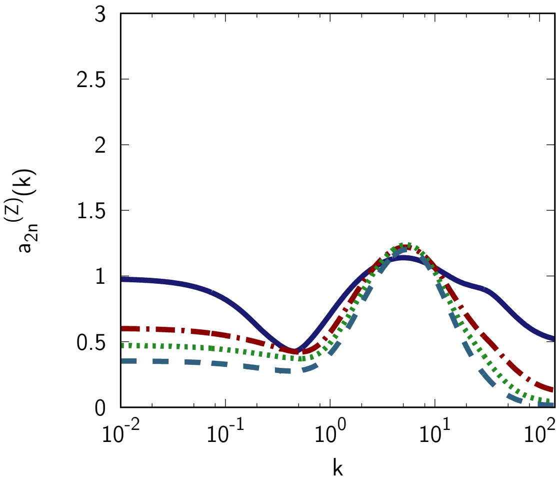

(d) $R = -5$

Figure 5.10: Spherically integral anisotropy for $|Z(\boldsymbol{k})|$ in $2n = 2\,,4\,,6\,,8$, with the hybrid model at $St = 5$ for: (a) $R = 0$; (b) $R = -0.5$; (c) $R = -1$; (d) $R = -5$.

anisotropy on the one in degree 2 does not make much sense. This partly explains why MCS performs well in this case rather than in other cases.

The linear results exhibit the influence on anisotropy by stropholysis terms in some extent. It seems that stropholysis terms can reduce anisotropy in large scales more in lower degrees than in higher degrees. The scale effects on anisotropy are proposed to be induced by viscosity, which acts on flow in terms of wavenumber k. Further study ought to be performed in inviscid linear limit to exclude the impact of viscosity, especially when the phase-mixing reflected by the 'stropholysis' term is significant. Although the 'stropholysis' effects on directional anisotropy and polarization anisotropy can not be distinguished clearly from the current results, it is still worthwhile to do further analyses, in order to figure out the misleading behaviours of MCS resulted from the spherical harmonics.

Thanks to the spherical harmonics decomposition, we can do anisotropy analysis in very high degree. It also provides a possibility to model higher degree anisotropic components of $\boldsymbol{R}$ in the nonlinear terms, which is extremely difficult with tensorial expansions. The difficulty is the spherical harmonics decomposition of $Z(\boldsymbol{k})$ for its singularity at pole. Appendix F gives the first attempt.

Chapter 6

Dynamics of homogeneous flow with mean shear

The shear flow without system rotation is the most challenging case to model in this thesis. In chapter 4, we do some preliminary analysis on pure shear case, and further analysis are continued in this chapter. Firstly, the essential connections among of ZCG, Weinstock's model and the hybrid model, even the isotropic model is discussed, based on different treatments of the anisotropy. Then we exploit the impacts of various initial conditions. At last, a preliminary discussion on Reynolds effects is performed.

6.1 Fully nonlinear spectral models for shear flows without rotation

6.1.1 Hierarchy of the nonlinear models

Here, we return to the original form of $T_{ij}(\boldsymbol{k},t)$. In this view, ZCG, which can be denoted as:

$$T_{ij}^{(\mathrm{ZCG})}(\boldsymbol{k},t) = T_{ij}^{(2)}(\boldsymbol{k},t)\,, \tag{6.1}$$

basically amounts to the truncation of first two degree of $T_{ij}(\boldsymbol{k},t)$ from EDQNM-1. Concerning to Weinstock's model, it can be expressed as

$$T_{ij}^{(\mathrm{Wein})}(\boldsymbol{k},t) = T_{ij}^{(\mathrm{iso})}(\boldsymbol{k},t) - \varphi(k,t)\left(\hat{R}_{ij}(\boldsymbol{k},t) - \hat{R}_{ij}^{(\mathrm{iso})}(\boldsymbol{k},t)\right)\,, \tag{6.2}$$

which means EDQNM evolution for the isotropic component

$$T_{ij}^{(\mathrm{iso})}(\boldsymbol{k},t) = \frac{1}{4\pi k^2} T(k,t)\,, \tag{6.3}$$

and forced damping for higher degree anisotropy. As to our hybrid model,

$$T_{ij}^{(\mathrm{hybrid})}(\boldsymbol{k},t) = T_{ij}^{(\mathrm{iso})}(\boldsymbol{k},t) - \varphi(k,t)\left(\hat{R}_{ij}(\boldsymbol{k},t) - \hat{R}_{ij}^{(2)}(\boldsymbol{k},t)\right)\,, \tag{6.4}$$

maintains the EDQNM evolution for the first two degree anisotropy and forced damping for higher degree anisotropy. Therefore, based on the difference treatments on high degree anisotropic components of $T_{ij}(\boldsymbol{k},t)$, and further different influence on the evolution of $\hat{R}_{ij}(\boldsymbol{k},t)$ and its anisotropic components in high degree, these four models form a hierarchy.

In order to figure out the different behaviours of these models, the simulations are started with the same initial condition as in Eq. (3.37) and with the same flow parameters. The initial $\mathrm{Re}_\lambda = 210$.

6.1.2 Turbulent kinetic energy evolution and production terms

The time evolution of turbulent kinetic energy by various nonlinear models: the isotropic model, ZCG, Weinstock's model and the hybrid model is plotted in figure 6.1. It it not surprising that only the hybrid model realize eventual exponential growth. It is interesting to find that the isotropic model follows the hybrid model when $St \leq 4$.

Table 6.1 lists out the values of γ at $St = 10$, given in chapter 4 as:

$$\gamma = -2b_{13} - \frac{\varepsilon}{\mathcal{K}S}\,,$$

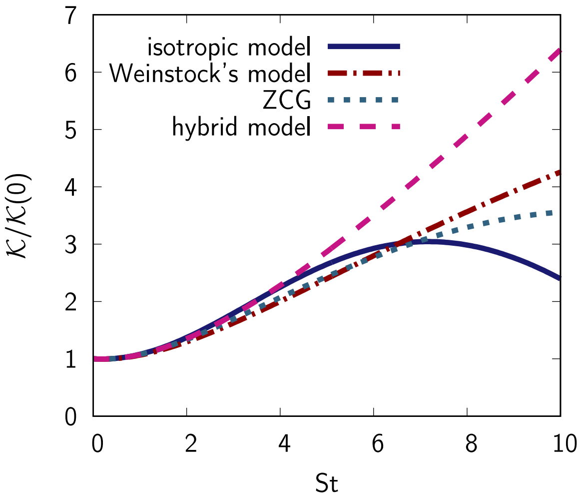

Figure 6.1: Time evolution of turbulent kinetic energy. Comparison of results by various nonlinear models: the isotropic model, ZCG, Weinstock's model and the hybrid model.

Table 6.1: Dimensionless exponential growth rate of kinetic energy by various nonlinear models.

model	b_{13}	$\mathcal{K}(m^2/s^2)$	$\varepsilon(m^2/s^3)$	γ
isotropic model	0.0344	2.4097	2.7927	-0.1847
ZCG	-0.0629	3.5797	3.9256	0.0161
Weinstock's model	-0.0832	4.2824	3.8542	0.0763
hybrid model	-0.1287	6.4312	8.7430	0.1215

which is the dimensionless exponential growth rate of $\mathcal{K}$. The hybrid model gives the value 0.1215 , which is very close to those given by DNS 0.1–0.2, and experiments 0.08–0.12 , and improves the value 0.337 given by MCS remarkably (Mons *et al.*, 2016).

For further observation, the production terms at $St = 4$ and $St = 8$ are plotted in figures 6.2 and 6.3 respectively. The time evolution of b_{13} with its contribution of directional anisotropy and polarization anisotropy are plotted in figure 6.11. The figures show rather bad predictions by the isotropic model.

6.1.3 Anisotropy analysis

Thanks to the spherical harmonics decomposition method proposed in chapter 5, we perform the high anisotropy analysis at $St = 5$. The results for $\mathcal{E}(\boldsymbol{k})$ and $Z(\boldsymbol{k})$ are plotted in figure

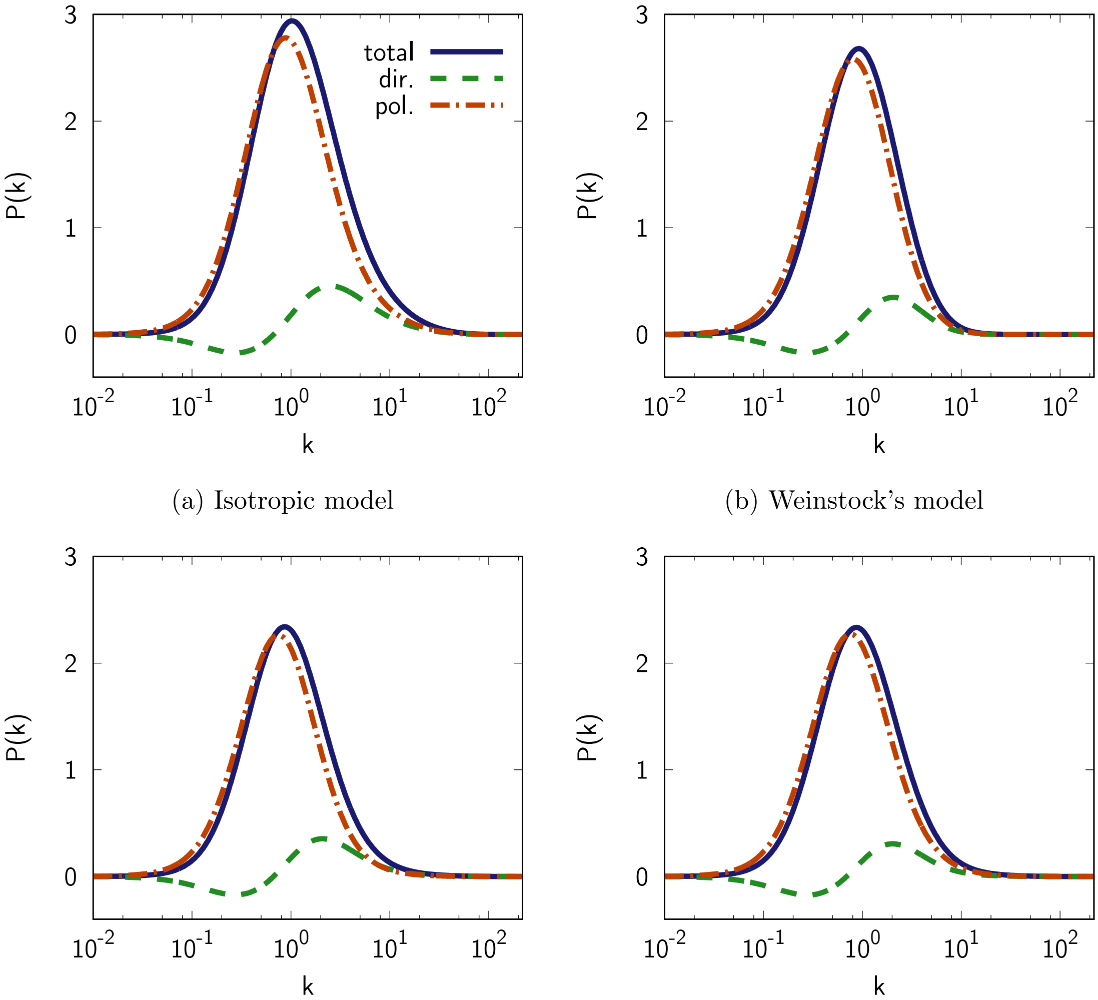

(a) Isotropic model

(b) Weinstock's model

(c) ZCG

(d) Hybrid model

Figure 6.2: Production terms at $St = 4$ by various nonlinear models: (a) the isotropic model; (b) ZCG; (c) Weinstock's model; (d) the hybrid model.

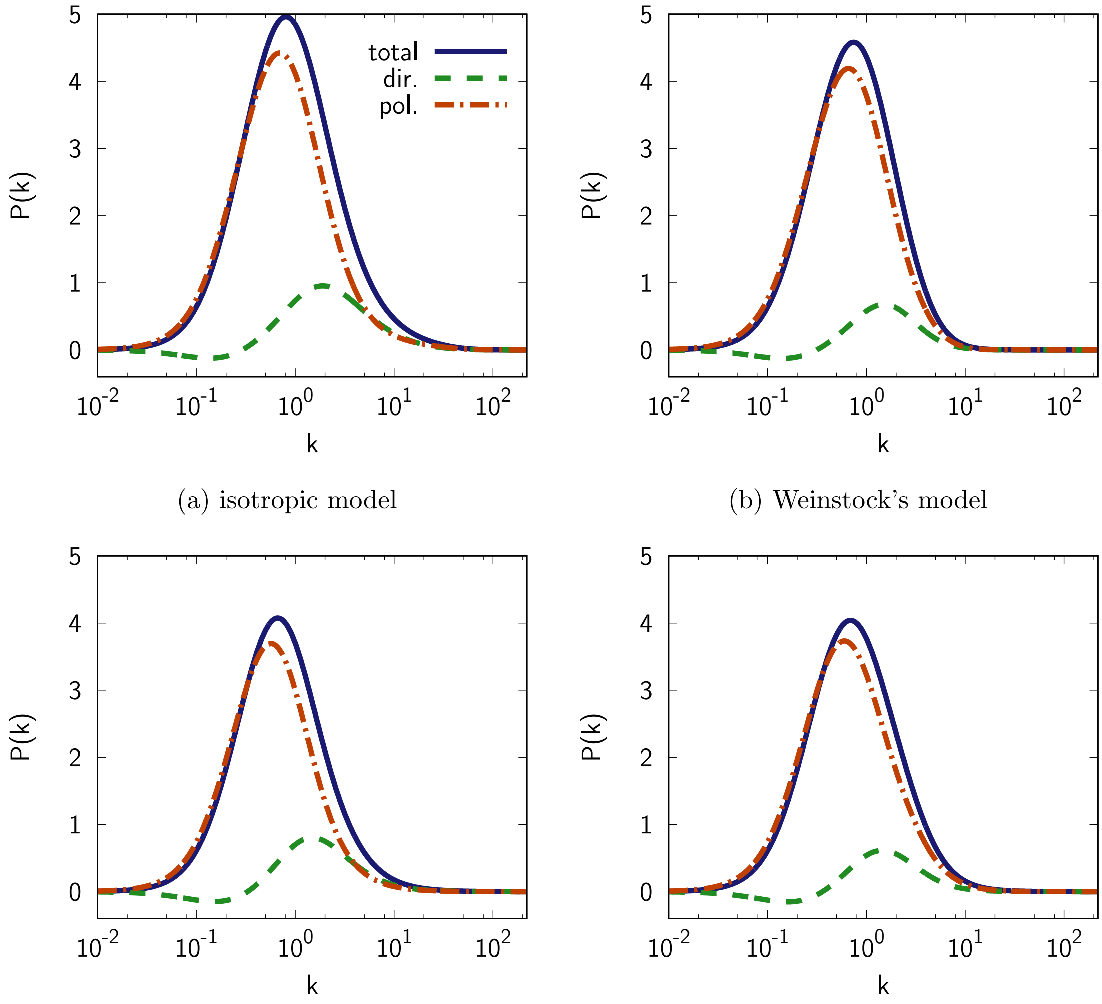

(a) isotropic model

(b) Weinstock's model

(c) ZCG

(d) Hybrid model

Figure 6.3: Production terms at $St = 4$ by various nonlinear models: (a) the isotropic model; (b) ZCG; (c) Weinstock's model; (d) the hybrid model.

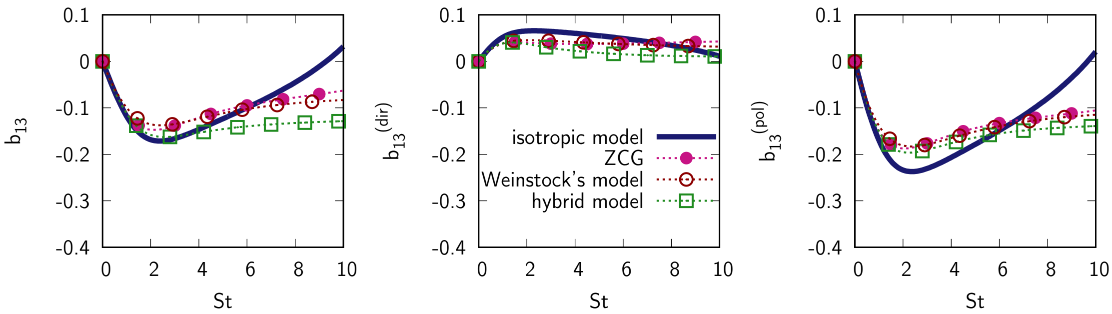

(a) total anisotropy (b) directional anisotropy (c) polarization anisotropy

Figure 6.4: Time evolution of the deviatoric part (a) of the Reynolds stress tensor, and its contributions from (b) directional and (c) polarization anisotropies. Comparisons of results from the isotropic model, ZCG, Weinstock's model, and the hybrid model.

6.5 and 6.6 respectively.

The figures identify the different nonlinear dynamics provided by different nonlinear models. The isotopic model generates the larges anisotropy in all the degrees, which means the least damping of anisotropy. The anisotropy produced by Weinstock's model is smaller compared to the isotropic model, and all the components are damped at small scales, especially the directional anisotropy. Our hybrid model provides smaller anisotropy at degrees higher than 2 compared to the isotropic model, and maintains significant anisotropy in degree 2 smaller than the one produced by ZCG, which neglects the evolution or damping of anisotropic components in all degrees higher than 2.

6.2 Analysis on initial conditions with hybrid model

6.2.1 Introduction to initial conditions

We also consider the effects by various initial conditions. Four typical initial conditions are employed here: isotropic initial spectrum as Eq. 3.37 with k^2 law for large scales, which is used in previous section; isotropic initial spectrum as Eq. 3.37 with k^4 law for large scales, namely $\sigma = 4$ in Eq. 3.37; The isotropic initial spectrum used in chapter 4, Eq. 4.1 for linear limit, which is usually employed in DNS; the flow with shear rapidity from original isotropic field with spectrum following k^2 law, that amounts to a flow with precomputation in viscous linear limit for very short time.

All the cases are performed with the initial parameters that provide the same initial

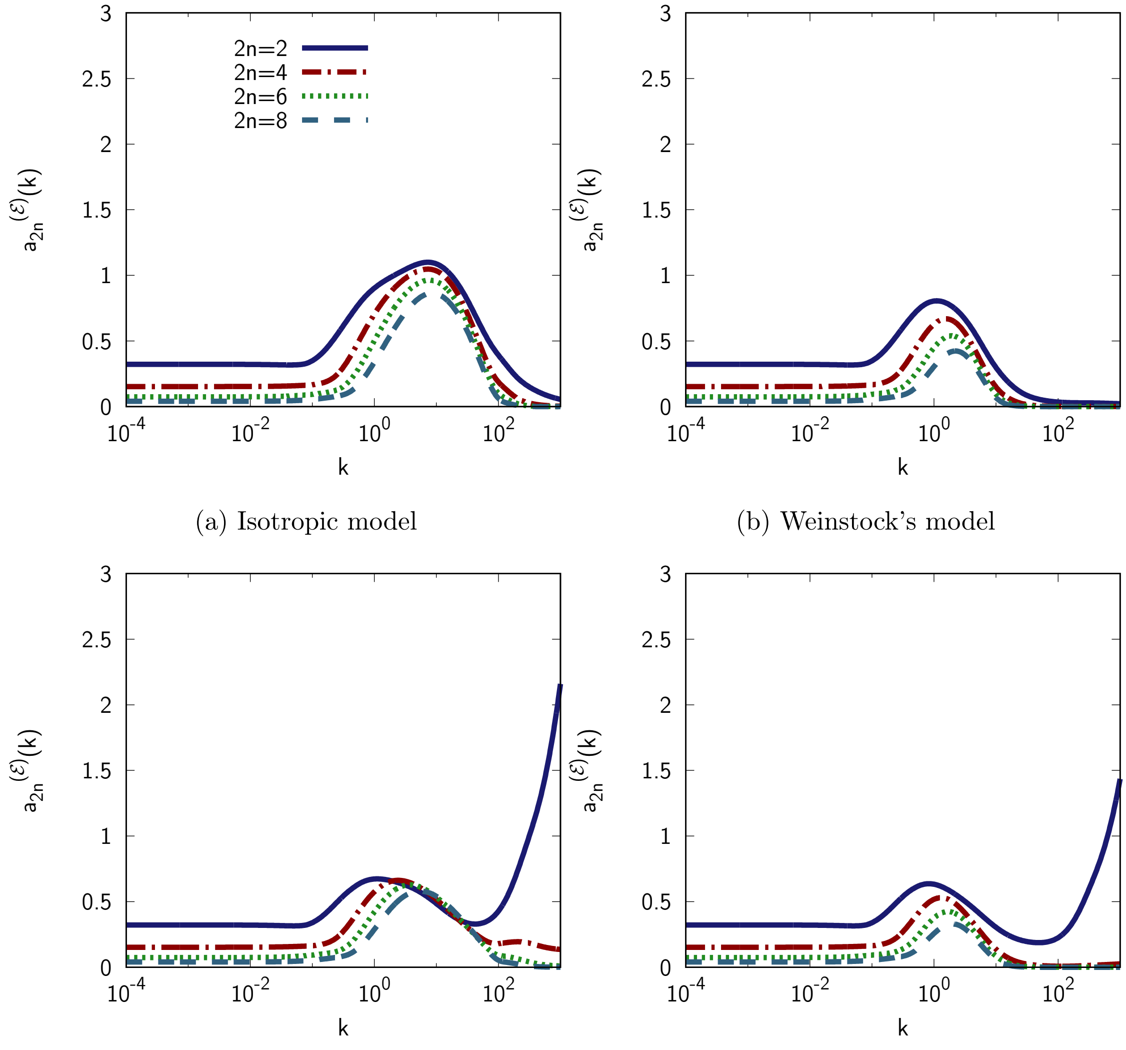

(a) Isotropic model

(b) Weinstock's model

(c) ZCG

(d) Hybrid model

Figure 6.5: High degree anisotropy analysis for $\mathcal{E}(\boldsymbol{k})$ at $St = 5$.

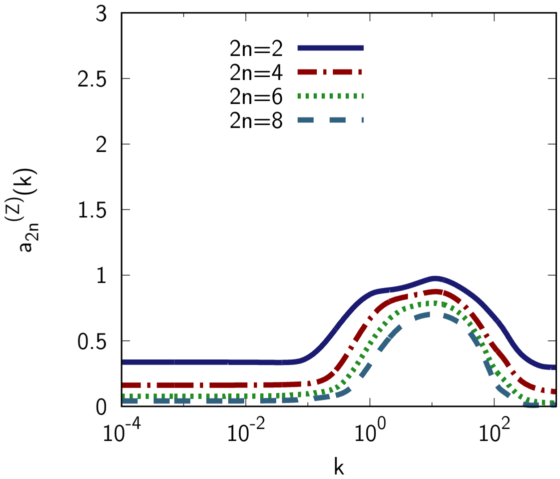

(a) Isotropic model

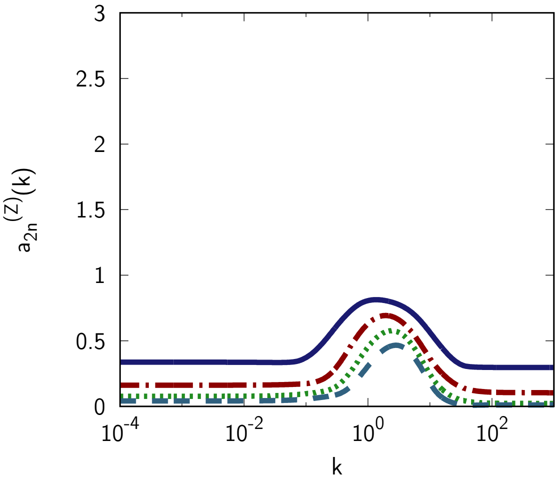

(b) Weinstock's model

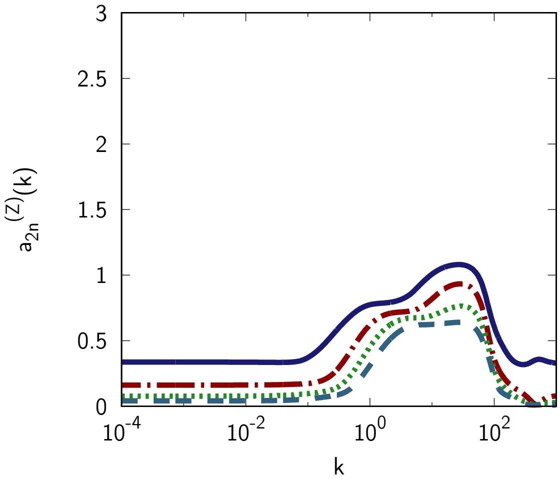

(c) ZCG

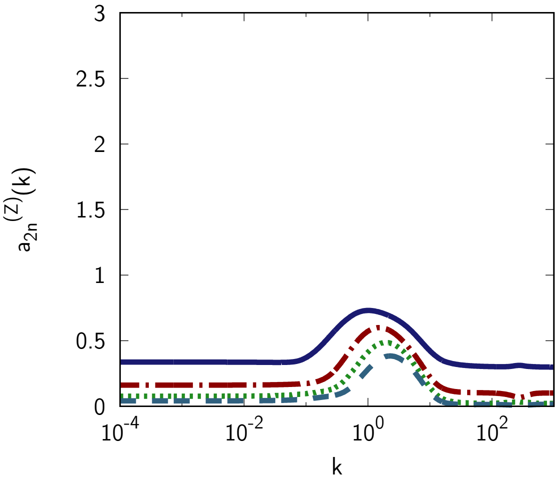

(d) Hybrid model

Figure 6.6: High degree anisotropy analysis for $|Z(\boldsymbol{k})|$ at $St = 5$.

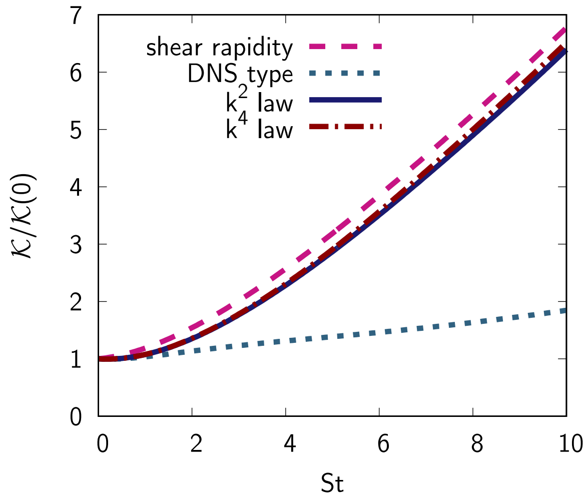

Figure 6.7: Time evolution of turbulent kinetic energy. Comparison of results with different initial conditions: k^2 law. k^4 law. DNS type and shear rapidity.

$\mathrm{Re}_\lambda = 210$ and $S^+ = 22$.

6.2.2 Turbulent kinetic energy and kinetic energy spectra

Figure 6.7 plots the time evolution of turbulent kinetic energy with the different initial conditions. The energy spectra at $St = 0$, $St = 5$ and $St = 10$ are given in figure 6.8

These results indicate that the influence of initial conditions is mainly at large scales rather than at small scales, at which the energy spectra turn out to be aligned after moderate dimensionless time.

6.2.3 Evolution of b_{13}

Time evolution of b_{13} and its contributions of directional anisotropy and polarization are plotted in figure 6.9. All the cases achieve similar asymptotic values of b_{13}, which are around -0.14 and very close to the ones given by Sagaut & Cambon (2018). Table 6.2 lists the dimensionless exponential growth rate γ of kinetic energy at $St = 10$, and all the cases except the one with DNS-type initial spectrum achieve good values of γ, around 0.12. The case with DNS-type initial spectrum departs from others because of the obvious different initial spectrum at large scales.

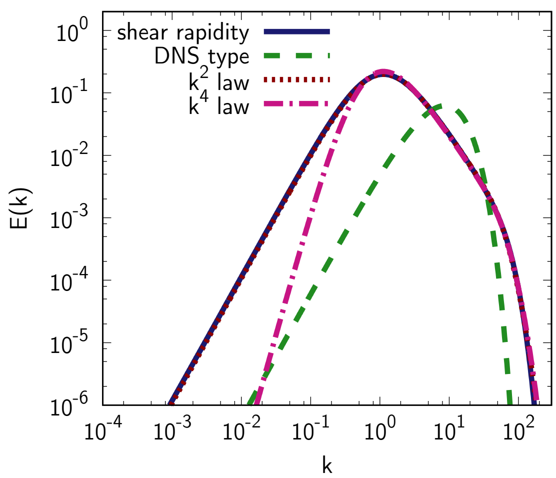

(a) $St = 0$

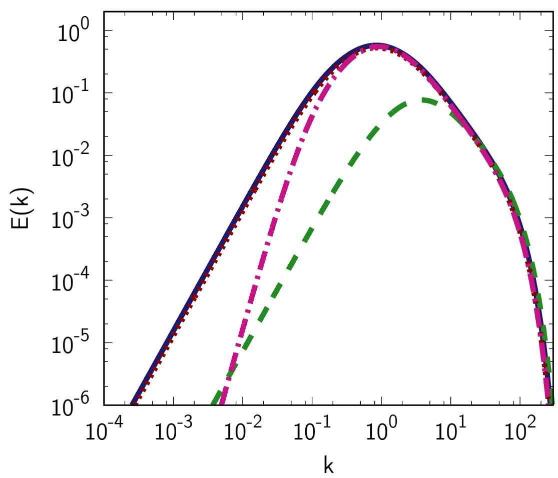

(b) $St = 5$

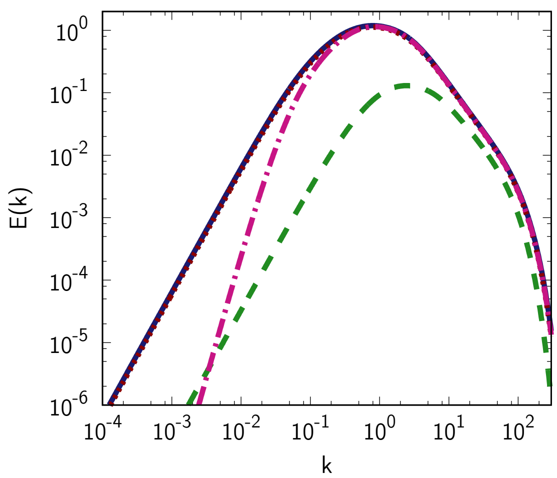

(c) $St = 10$

Figure 6.8: Time evolution of energy spectra. Comparisons of the results with different initial conditions: k^2 law. k^4 law. DNS type and shear rapidity at (a) $St = 0$; (b) $St = 5$, and (c) $St = 10$.

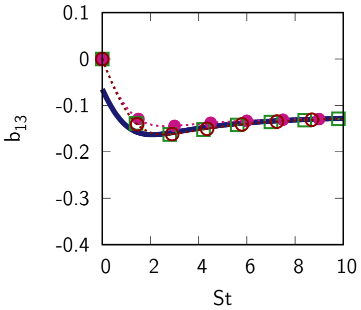

(a) total anisotropy

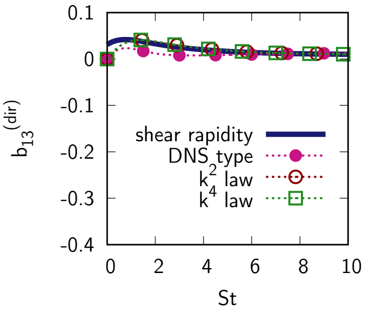

(b) directional anisotropy

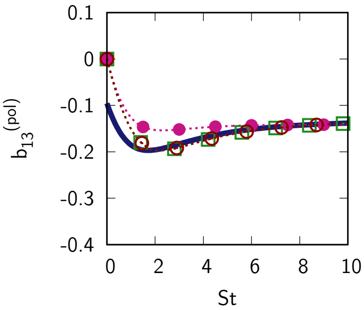

(c) polarization anisotropy

Figure 6.9: Time evolution of the deviatoric part (a) of the Reynolds stress tensor, and its contributions from (b) directional and (b) polarization anisotropies. Comparisons of results with k^2 law. k^4 law. DNS type and shear rapidity initial condition.

Table 6.2: Dimensionless exponential growth rate of kinetic energy by cases with various initial conditions.

initial condition	b_{13}	$\mathcal{K}(m^2/s^2)$	$\varepsilon(m^2/s^3)$	γ
k^2 law	-0.1287	6.4312	8.7430	0.1215
k^4 law	-0.1286	6.5571	8.9990	0.1200
DNS type	-0.1285	1.8579	3.6165	0.0623
shear rapidity	-0.1279	6.8169	9.5275	0.1160

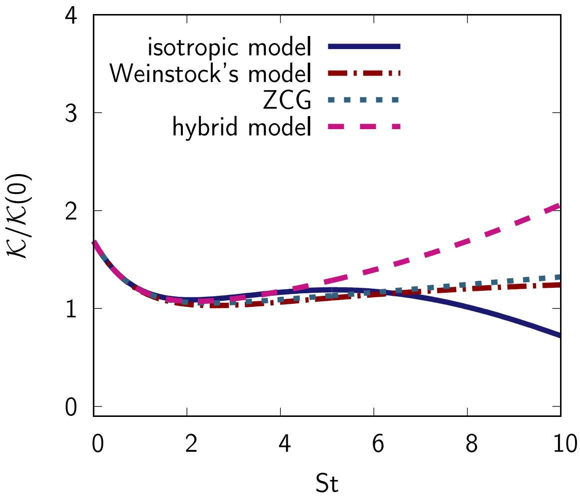

Figure 6.10: Time evolution of turbulent kinetic energy. Comparison of results by various nonlinear models: the isotropic model, ZCG, Weinstock's model and the hybrid model. Initial $\mathrm{Re}_\lambda = 30$

6.3 Preliminary study on Reynolds number effects

We revisit the pure shear case performed in chapter 4, with an extra case using the isotopic nonlinear model. The initial Reynolds number in this case is rather low with $\mathrm{Re}_\lambda = 30$. The time evolution of turbulent kinetic energy is plotted in figure 6.10 and the time evolution of b_{13} is plotted in figure 6.11. The hybrid model predicts $\gamma = 0.100$ at $St = 10$. With respect to the case we performed in the beginning of this chapter with moderate initial $\mathrm{Re}_\lambda = 210$, some interesting results can be found: it seems that Weinstock's model performs better than ZCG at relatively high Reynolds numbers.

6.4 Conclusion and perspectives

In this chapter, we introduce our hierarchy of the nonlinear models, and perform further analysis on the behaviours of pure shear flow governed by these models. This hierarchy provides method of extending nonlinear models to consider higher degree anisotropy evolution. We analyze the effects of initial conditions and Reynolds numbers preliminarily.

The future comparison to high resolution DNS results are expected. In addition, further study on the Reynolds effects will be performed.

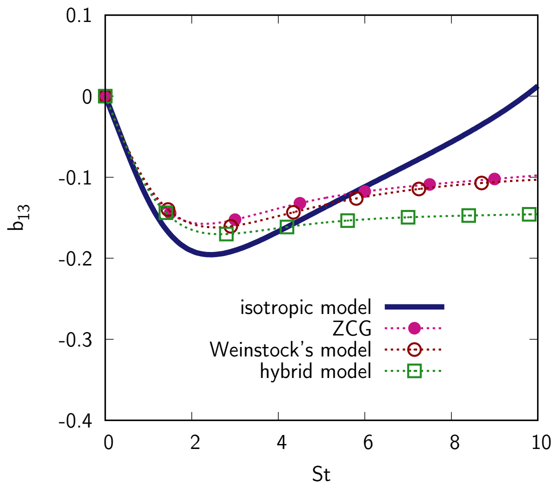

Figure 6.11: Time evolution of the deviatoric part of the Reynolds stress tensor with initial $Re_\lambda = 30$. Comparisons of results from the isotropic model, ZCG, Weinstock's model, and the hybrid model.

Conclusion and perspectives

We propose a new model for predicting the dynamics of homogeneous anisotropic turbulence in this thesis, with or without system rotation. The model separates linear distortion effects from nonlinear turbulent dynamics, so that each contribution can be treated with an adapted model. Our model deals with equations governing the spectral tensor of two-point second-order velocity correlations, and is developed for arbitrary mean-velocity gradients with or without system rotation. The direct linear effect of mean gradients is exact in our model, whereas nonlinear effects come from two-point third-order correlations which are closed by an anisotropic EDQNM model. In the closure, the anisotropy is restricted to an expansion in terms of low-degree angular harmonics (Mons *et al.*, 2016). For the case of sheared turbulence, whose modelling resists most one-point approaches and even the two-point model by Mons, we propose an adaptation of our two-point model in a new hybrid model, in which return-to-isotropy is explicitly introduced in the guise of Weinstock (2013)'s model.

In contrast with pseudo-spectral DNS adapted to shear flow by Rogallo (1981) in engineering and by Lesur & Longaretti (2005) in astrophysics, the advection operator in our model is not solved by following characteristic lines in spectral or physical space, but by an original high-order finite-difference scheme for calculating derivatives $\dfrac{\partial}{\partial k_i}$ with respect to the wavevector $\boldsymbol{k}$ to avoid mesh deformation and remeshing and to extract angular harmonics at any time easily. All the details on the numerical implementation of the present model is exhibited in chapter 3.

The proposed new model is versatile since it is implemented for several cases of mean-velocity gradients consistent with the homogeneity assumption. The first application for the present model is on homogeneous rotating sheared turbulent flow in this thesis. The present model has been validated in the linear regime, by comparison to the accurate solution of viscous SLT, in several cases; stabilizing, destabilizing or neutral. It turns out that, with the new direct numerical approach, we improve the prediction of the previous model by Mons *et al.* (2016) remarkably, in which the linear resolution is questioned at large time, especially in the case without rotation. In respect to fully nonlinear models, validations have been done for several cases of plane deformations, with comparisons to the DNS results given by Salhi *et al.* (2014). The predictions of the new hybrid model are extremely good, especially in the case without system rotation, in which expected exponential growth of turbulent kinetic energy is achieved. These are presented in chapter 4.

In chapter 5, the SO^3-type decompositions for scalers in form of tensorial expansions and spherical harmonics decomposition are introduced, and the equivalency of these two decompositions is validated in homogeneous rotating sheared flow. The spherical harmonics decomposition permits high degree anisotropy analysis of $\hat{\boldsymbol{R}}$. We observe the effects of the 'stropholysis' term in viscous linear limit, and with the hybrid model with fully nonlinear terms as well. The results concerning directional anisotropy $\mathcal{E}(\boldsymbol{k})$ and polarization anisotropy $Z(\boldsymbol{k})$ in viscous linear limit indicate that the 'stropholysis' term reduces the anisotopy of $\hat{\boldsymbol{R}}$, especially the low-degree anisotropy at large scales. And the results by the fully nonlinear model show the RTI effects by nonlinear mechanism clearly, mainly at small scales. Generally speaking, the 'stropholysis' term plays an essential role to anisotropy, although the interactions are complicated.

The most challenging case with plane shear and without system rotation is addressed in chapter 6. The hierarchy of nonlinear models formed by the isotropic model, ZCG, Weinstock's model and the hybrid model is introduced, based on their different treatments on anisotropic components. The hybrid model predicts the value of dimensionless exponential growth rate of turbulent kinetic energy very close to the ones given by DNS and experiments. We exploit the impacts of various initial conditions in this chapter, and preliminary Reynolds effects are obtained as well, which indicates that Weinstock's model can achieve the exponential growth of turbulent kinetic energy at high Reynolds number.

The building of the present model is just a beginning, and this thesis inspires significant works in progress or in short future:

1. The function of the 'stropholysis' term is really complex indeed. The results in chapter 5 in viscous linear limit show strong anisotropy at large k and non-monotonic k-distribution, especially for the case with $R = -5$. Such scale effects on anisotropy are proposed to be induced by viscosity, which acts on flow in terms of wavenumber k. Further study ought to be performed in inviscid linear limit to exclude the impact of viscosity, especially when the phase-mixing reflected by the 'stropholysis' term is significant. Although the 'stropholysis' effects on directional anisotropy and polar-

ization anisotropy can not be distinguished clearly from the current results, it is still worthwhile to do further analyses, in order to figure out the misleading behaviours of MCS resulted from the spherical harmonics truncation.

2. For the pure shear flow without system rotation, further study on Reynolds numbers effects is looked forward to, as well as the validation by new high resolution DNS results.

3. The direct numerical approach proposed in this thesis inspires a new mixed finite-difference—pseudo-spectral method for incompressible homogeneous turbulence to improve the numerical accuracy and to make the algorithm more universal for any type of mean flow velocity gradients without remeshing. In addition, the new code for EDQNM integral with improved accuracy breaks the restriction of logarithmic k grid point distribution, which can play a role on the simulation of inertial wave.

4. Last but not least, the present model permits improvements on single-point models, in connection with the structure-based modelling by Kassinos *et al.* (2001), or with the models proposed by Launder *et al.* (1975) (denoted as **LRR** hereinafter) firstly. Restricting RSM equations to HAT, the closure of the 'rapid' pressure-strain correlations remains the most difficult issue. The LRR model used a tuned constant C_2 for the 'rapid' term of the pressure-strain rate model, which is directly related to the constant D used by Lumley (1975) (referred in Cambon *et al.* (1981)), with a fitting given by the behaviour at very short time, starting from isotropy. A better overall agreement for larger times and pure plane shear was found by LRR with $C_2 = 0.4$, corresponding to $D = -\frac{16}{55}$. Very recently, Mishra & Girimaji (2017) offered a very complete overview of modelling the rapid part of the pressure-strain rate tensor. They consider the overall agreement for a very large class of mean-velocity gradients, from hyperbolic to elliptic mean streamlines, with comparison to RDT, and give priority on fulfilling the realizability constraint. Their most crucial results allow to replace the D constant by a new parameter A_5 that depends on the ellipticity ratio β. The relationship from D to C_2 is

$$C_2 = -\frac{1}{3}(2 + 11D)\,. \tag{6.5}$$

The fact that the 'constant' D is recovered allows us to go back to the seminal study by Cambon *et al.* (1981). This study introduced a spectral parameter $a(k,t)$ in a model equation for the spherically-integrated spectral tensor $\varphi_{ij}(k,t)$. Compared to

MCS, this parameter can be interpreted as giving a partition of $H_{ij}(k,t)$ in terms of its directional component and its polarization one, or

$$H_{ij}^{((\mathrm{dir}))}(k,t) = \left(1+\frac{2}{5}a(k,t)\right) H_{ij}(k,t)\,, \quad H_{ij}^{((\mathrm{pol}))}(k,t) = -\frac{2}{5}a(k,t)H_{ij}(k,t)\,. \quad (6.6)$$

By integrating over k-modulus the related spectrum, it is found that the parameter

$$\frac{2}{7}\left(1+\frac{4}{5}a(k,t)\right) \quad (6.7)$$

is the exact spectral counterpart of $A_5(\beta)$, also equal to D.

In addition to a new insight into the 'rapid' pressure-strain rate tensor, these considerations open the way to a possible improvement of both the models in Cambon *et al.* (1981) and MCS, for the linear part, by means of a tuned parameter, which is in close connection with improving the conventional single-point models.

The LRR model is firstly extended to describe rotating shear flow in Appendix G, which was originally for pure shear flow. The first check to be done is in the case with plane shear, with once-for-all tuned constants, especially with typical value of C_2, then to done in the cases with system rotation. Tests on the sensitivity of varying C_2 (or equivalently D) will be performed afterwards. Accordingly, we can expect a very interesting comparison based on our 'exact' 3D spectral linear model in which the relevant rotational parameter is $(\boldsymbol{W}+4\boldsymbol{\Omega})\cdot\boldsymbol{\alpha}$ that affects only the polarization term. $\boldsymbol{W}+4\boldsymbol{\Omega}$ is also the relevant rotation part of the mean flow in RSM equations, whereas the 'rapid' pressure-strain rate tensor is affected by the absolute vorticity $\boldsymbol{W}+2\boldsymbol{\Omega}$.

Further perspectives can also be concerned, including but not limited to:

1. Improvements on shell-models (models in terms of k-modulus, but not stochastic ones), e.g. , the model proposed by Cambon *et al.* (1981) and MCS, based on high degree anisotropy analysis and possible spherical harmonics decomposition for $\mathcal{E}(\boldsymbol{k})$ and $Z(\boldsymbol{k})$.

2. Study on purely HAT, but with more coupled fields, using modal decomposition, such as buoyancy-driven flows, magnetohydrodynamics (**MHD**) (Linkmann *et al.*, 2016, 2017; Sagaut & Cambon, 2018), and even towards compressible flows.

3. Application to other instabilities — from hyperbolic (strain-dominated) to elliptic (vorticity-dominated) — with nonlinear saturation or not.

4. Towards an extended discussion, with multiscale and directional approach to 'Philosophies and fallacies in modeling turbulence' (Spalart, 2015, essentially RANS).

5. A first attempt to extend towards inhomogeneous flows is to restore the feed-back from fluctuation to mean field. It is almost ignored, or roughly mimicked by effective diffusivity in general studies. On the other hand, a promising strategy could be transferred from weakly inhomogeneous buoyancy-driven flows to weakly inhomogeneous shear-driven flows: in the first approach, from USHT to Rayleigh-Taylor turbulence, the rapid acceleration model of Gréa (2013) couples SLT with the feed-back, whereas the nonlinear EDQNM model from Burlot *et al.* (2015) is being reintroduced in a model with all interactions. Accordingly, the linear stratification parameter N could evolve, in contrast with USHT, as could evolve our shear rate S.

Appendix A

Details for the equations of three-point third-order correlation tensor

Eq.(1.39) defines the four-point fourth-order spectral correlation tensor $\hat{S}_{ijmn}(\boldsymbol{k},t)$. Similar to $\hat{S}_{ijn}(\boldsymbol{k},t)$, $\hat{S}_{ijmn}$ has its corresponding definition in physical space:

$$S_{ijmn}(\boldsymbol{r},t) = \langle u_i(\boldsymbol{x}+\boldsymbol{r})u_j(\boldsymbol{x})u_m(\boldsymbol{x}+\boldsymbol{s})u_n(\boldsymbol{x}+\boldsymbol{x'})\rangle\,. \tag{A.1}$$

First of all, one can obtain the important relationship on convolution

$$\widehat{u_iu_j}(\boldsymbol{q})\hat{u}_m(\boldsymbol{k})\hat{u}_n(\boldsymbol{p}) = \delta(\boldsymbol{q}+\boldsymbol{k}+\boldsymbol{p})\iiint \hat{S}_{ijmn}(\boldsymbol{q}',\boldsymbol{k},\boldsymbol{p})\,\mathrm{d}^3\boldsymbol{q}'. \tag{A.2}$$

It is not difficult to get

$$\delta(\boldsymbol{q}+\boldsymbol{k}+\boldsymbol{p})\frac{\partial\hat{S}_{ijn}(\boldsymbol{k},\boldsymbol{p},t)}{\partial t} = \imath\langle\frac{\partial\hat{u}_i(\boldsymbol{q})}{\partial t}\hat{u}_j(\boldsymbol{k})\hat{u}_n(\boldsymbol{p}) + \hat{u}_i(\boldsymbol{q})\frac{\partial\hat{u}_j(\boldsymbol{k})}{\partial t}\hat{u}_n(\boldsymbol{p}) + \hat{u}_(\boldsymbol{q})\hat{u}_j(\boldsymbol{k})\frac{\partial\hat{u}_n(\boldsymbol{p})}{\partial t}\rangle\,, \tag{A.3}$$

so that the following equations can be observed:

$$\delta(\boldsymbol{q}+\boldsymbol{k}+\boldsymbol{p})\frac{\partial\hat{S}_{ijn}(\boldsymbol{k},\boldsymbol{p},t)}{\partial t} + \mathcal{L}_{ijn}(\boldsymbol{q},\boldsymbol{k},\boldsymbol{p},t) = \mathcal{T}_{ijn}(\boldsymbol{q},\boldsymbol{k},\boldsymbol{p},t)\,, \tag{A.4}$$

with

$$\begin{aligned}\mathcal{L}_{ijn}(\boldsymbol{q},\boldsymbol{k},\boldsymbol{p},t) =& - A_{lm} q_l \langle \frac{\partial \hat{u}_i(\boldsymbol{q})}{\partial q_m} \hat{u}_j(\boldsymbol{k}) \hat{u}_n(\boldsymbol{p}) \rangle + \nu q^2 \hat{S}_{ijn}(\boldsymbol{k},\boldsymbol{p},t)\delta(\boldsymbol{q}+\boldsymbol{k}+\boldsymbol{p}) \\ & - A_{lm} k_l \langle \hat{u}_i(\boldsymbol{q}) \frac{\partial \hat{u}_j(\boldsymbol{k})}{\partial k_m} \hat{u}_n(\boldsymbol{p}) \rangle - \nu k^2 \hat{S}_{ijn}(\boldsymbol{k},\boldsymbol{p},t)\delta(\boldsymbol{q}+\boldsymbol{k}+\boldsymbol{p}) \\ & - A_{lm} q_l \langle \hat{u}_i(\boldsymbol{q}) \hat{u}_j(\boldsymbol{k}) \frac{\partial \hat{u}_n(\boldsymbol{k})}{\partial p_m} \rangle - \nu p^2 \hat{S}_{ijn}(\boldsymbol{k},\boldsymbol{p},t)\delta(\boldsymbol{q}+\boldsymbol{k}+\boldsymbol{p}) \\ & + M_{im}(\boldsymbol{q}) \hat{S}_{mjn}(\boldsymbol{k},\boldsymbol{p},t)\delta(\boldsymbol{q}+\boldsymbol{k}+\boldsymbol{p}) + M_{jm} \hat{S}_{imn}(\boldsymbol{k},\boldsymbol{p},t)\delta(\boldsymbol{q}+\boldsymbol{k}+\boldsymbol{p}) \\ & + M_{nm} \hat{S}_{ijm}(\boldsymbol{k},\boldsymbol{p},t)\delta(\boldsymbol{q}+\boldsymbol{k}+\boldsymbol{p})\,,\end{aligned} \tag{A.5a}$$

$$\begin{aligned}\mathcal{T}_{ijn}(\boldsymbol{q},\boldsymbol{k},\boldsymbol{p},t) =& P_{imp}(\boldsymbol{q}) \langle \widehat{u_m u_p}(\boldsymbol{q}) \hat{u}_j(\boldsymbol{k}) \hat{u}_n(\boldsymbol{p}) \rangle + P_{jmp}(\boldsymbol{k}) \langle \widehat{u_m u_p}(\boldsymbol{k}) \hat{u}_i(\boldsymbol{q}) \hat{u}_n(\boldsymbol{p}) \rangle \\ & + P_{nmp}(\boldsymbol{p}) \langle \widehat{u_m u_p}(\boldsymbol{p}) \hat{u}_i(\boldsymbol{q}) \hat{u}_j(\boldsymbol{k}) \rangle\,.\end{aligned} \tag{A.5b}$$

The linear part can be simplified with distribution property of Dirac functions, when $\boldsymbol{k}+\boldsymbol{p}+\boldsymbol{q}=\boldsymbol{0}$, $\boldsymbol{k}+\boldsymbol{p}\neq\boldsymbol{0}$, $\boldsymbol{k}+\boldsymbol{q}\neq\boldsymbol{0}$ and $\boldsymbol{p}+\boldsymbol{q}\neq\boldsymbol{0}$,

$$\begin{aligned}\mathcal{L}_{ijn}(\boldsymbol{q},\boldsymbol{k},\boldsymbol{p},t) =& \delta(\boldsymbol{q}+\boldsymbol{k}+\boldsymbol{p}) \Big[- A_{lm} \left(k_l \frac{\partial}{\partial k_m} + p_l \frac{\partial}{\partial p_m} \right) \hat{S}_{ijn}(\boldsymbol{k},\boldsymbol{p},t) \\ & + M_{im}(\boldsymbol{q}) \hat{S}_{mjn}(\boldsymbol{k},\boldsymbol{p},t) + M_{jm} \hat{S}_{imn}(\boldsymbol{k},\boldsymbol{p},t) + M_{nm} \hat{S}_{ijm}(\boldsymbol{k},\boldsymbol{p},t) \Big]\,.\end{aligned} \tag{A.6}$$

The nonlinear part can be simplified with Eq.(A.2),

$$\begin{aligned}\mathcal{T}_{ijn}(\boldsymbol{q},\boldsymbol{k},\boldsymbol{p},t) =& \delta(\boldsymbol{q}+\boldsymbol{k}+\boldsymbol{p}) \Big[P_{imp}(\boldsymbol{q}) \iiint \hat{S}_{mpjn}(\boldsymbol{q}',\boldsymbol{k},\boldsymbol{p})\,\mathrm{d}^3\boldsymbol{q}' \\ & + P_{jmp}(\boldsymbol{k}) \iiint \hat{S}_{mpin}(\boldsymbol{q}',\boldsymbol{q},\boldsymbol{p})\,\mathrm{d}^3\boldsymbol{q}' + P_{nmp}(\boldsymbol{k}) \iiint \hat{S}_{mpij}(\boldsymbol{q}',\boldsymbol{q},\boldsymbol{k})\,\mathrm{d}^3\boldsymbol{q}' \Big]\,.\end{aligned} \tag{A.7}$$

Then Eq.(1.37) is proved.

Appendix B

Analytical SLT solutions

B.1 Shear case without rotation

Suppose $A_{ij} = S\delta_{i1}\delta_{j2}$, namely

$$\boldsymbol{A} = \begin{bmatrix} 0 & S & 0 \\ 0 & 0 & 0 \\ 0 & 0 & 0 \end{bmatrix} . \tag{B.1}$$

Setting initial time $t_0 = 0$, then one can obtain the characteristic lines as

$$k_1(t) = K_1, \quad k_2(t) = K_2 - StK_1, \quad k_3(t) = K_3 \,, \tag{B.2}$$

so that the linear governing equations in inviscid limit become

$$\frac{\mathrm{d}\hat{u}_1(\boldsymbol{k}(t),t)}{\mathrm{d}t} = (\frac{2k_1^2}{k^2} - 1)S\hat{u}_2(\boldsymbol{k}(t),t) \tag{B.3a}$$

$$\frac{\mathrm{d}\hat{u}_2(\boldsymbol{k}(t),t)}{\mathrm{d}t} = \frac{2k_1k_2}{k^2}S\hat{u}_2(\boldsymbol{k}(t),t) \tag{B.3b}$$

$$\frac{\mathrm{d}\hat{u}_1(\boldsymbol{k}(t),t)}{\mathrm{d}t} = -\frac{2k_1k_3}{k^2}S\hat{u}_2(\boldsymbol{k}(t),t) \,. \tag{B.3c}$$

Since $(\dot{k^2}) = 2k_i\dot{k_i} = -Sk_1k_2$, one finds that $k^2\hat{u}_2(\boldsymbol{k},t)$ is conservative, which leads to

$$\begin{pmatrix} \hat{u}_1(\boldsymbol{k},t) \\ \hat{u}_2(\boldsymbol{k},t) \\ \hat{u}_3(\boldsymbol{k},t) \end{pmatrix} = \begin{bmatrix} 1 & G_{12} & 0 \\ 0 & \frac{K^2}{k^2} & 0 \\ 0 & G_{32} & 1 \end{bmatrix} \begin{pmatrix} \hat{u}_1(\boldsymbol{K}) \\ \hat{u}_2(\boldsymbol{K}) \\ \hat{u}_3(\boldsymbol{K}) \end{pmatrix} , \tag{B.4}$$

where the Green's function components are

$$G_{12} = -S\int_0^t \left(1 - 2\frac{K_1^2}{k^2(\tau)}\right)\frac{K^2}{k^2(\tau)}\,\mathrm{d}\tau, \quad G_{32} = 2S\frac{K_1K_3}{K^2}\int_0^t \frac{K^4}{k^4(\tau)}\,\mathrm{d}\tau \,. \tag{B.5}$$

The analytical solution comes from the integrals of $\int \frac{1}{k^2}\,\mathrm{d}t$ and $\int \frac{1}{k^4}\,\mathrm{d}t$:

$$
\begin{aligned}
\int_0^t \frac{1}{k^2}\,\mathrm{d}t &= \frac{1}{K_1 S\sqrt{K_1^2+K_3^2}} \arctan \frac{K_1 St\sqrt{K_1^2+K_3^2}}{K^2 - K_1K_2St} \\
\int_0^t \frac{1}{k^4}\,\mathrm{d}t &= \frac{1}{2K_1S(K_1^2+K_3^2)}\left(\frac{1}{\sqrt{K_1^2+K_3^2}} \arctan \frac{K_1 St\sqrt{K_1^2+K_3^2}}{K^2 - K_1K_2St}\right. \\
&\quad \left. + \frac{StK_1\left(K^2 - 2K_1^2 + StK_1K_2\right)}{k^2K^2}\right),
\end{aligned}
\tag{B.6}
$$

and we finally obtain

$$
\begin{aligned}
G_{12} &= \frac{K^2}{K_1^2+K_3^2}\left(-\frac{K_3^2}{K_1\sqrt{K_1^2+K_3^2}} \arctan \frac{K_1 St\sqrt{K_1^2+K_3^2}}{K^2 - K_1K_2St} + \frac{StK_1^2\left(K^2 - 2K_1^2 + StK_1K_2\right)}{K^2k^2}\right) \\
G_{32} &= \frac{K_1K_3}{K_1^2+K_3^2}\left(\frac{K^2}{K_1\sqrt{K_1^2+K_3^2}} \arctan \frac{K_1 St\sqrt{K_1^2+K_3^2}}{K^2 - K_1K_2St} + \frac{St\left(K^2 - 2K_1^2 + StK_1K_2\right)}{k^2}\right).
\end{aligned}
\tag{B.7}
$$

For the 2D modes such that $K_1 = 0$, the simple solution is $k/K = 1$, $G_{12} = -St$ and $G_{32} = 0$.

B.2 Solution for pure advection operator

As introduced in §1.2.1, for steady irrotational mean flow , $\boldsymbol{A}$ with constant rates of strain and of vorticity can be found as

$$
\boldsymbol{A} = \begin{pmatrix} 0 & D-W & 0 \\ D+W & 0 & 0 \\ 0 & 0 & 0 \end{pmatrix}.
\tag{B.8}
$$

The case of pure plane shear, $W = D$, with rectilinear streamlines, delineates the case of elliptic (closed) streamlines $W > D$ from the case of hyperbolic (open) $W < D$ streamlines.

Consider the advection alone, namely

$$
\frac{\mathrm{d}\hat{u}_i(\boldsymbol{k}(t),t)}{\mathrm{d}t} = \frac{\partial \hat{u}_i(\boldsymbol{k},t)}{\partial t} - A_{ln}k_l\frac{\partial \hat{u}_i(\boldsymbol{k},t)}{\partial k_n} = 0 \tag{B.9a}
$$

$$
\text{and} \quad \frac{\mathrm{d}k_i}{\mathrm{d}t} = -\,A_{ji}k_j\,. \tag{B.9b}
$$

It is not difficult to obtain $\dot{F}_{ij}(t) = A_{im}F_{mj}(t)$ with $x_i = F_{im}X_m$ and $\dot{x}_i = A_{ij}X_j$, so that we have

$$
\ddot{F}_{\alpha\beta} = (S^2 - W^2)F_{\alpha\beta}, \quad \alpha = 1,2, \quad \beta = 1,2, \tag{B.10}
$$

from $A_{mn}A_{mn} = (D^2 - W^2)$ in the plane $x_1\,, x_2$. Accordingly, in the elliptic case, it is found as

$$F_{\alpha\beta} = \delta_{\alpha\beta}\cos(\omega_0 t) + A_{\alpha\beta}\frac{\sin(\omega_0 t)}{\omega_0}\,, \tag{B.11}$$

with $\omega_0 = \sqrt{W^2 - D^2}$, using $\boldsymbol{F}|_{t=0} = \boldsymbol{I}$ and $\dot{\boldsymbol{F}}_{t=0} = \boldsymbol{A}$, where $\boldsymbol{I}$ is the second-order unit tensor. The inverse of $\boldsymbol{F}$ is found by changing the sign of t, so that the characteristic lines are

$$k_1 = K_1\cos(\omega_0 t) - (D+W)\frac{\sin(\omega_0 t)}{\omega_0}K_2 \tag{B.12a}$$

$$k_2 = K_2\cos(\omega_0 t) - (D-W)\frac{\sin(\omega_0 t)}{\omega_0}K_1 \tag{B.12b}$$

$$k_3 = K_3\,. \tag{B.12c}$$

In a similar way, the solution for hyperbolic case can be found with $\omega_0 = \sqrt{D^2 - W^2}$

$$k_1 = \frac{1}{2}\left(\mathrm{e}^{\omega_0 t} + \mathrm{e}^{-\omega_0 t}\right)K_1 + \frac{D+W}{2\omega_0}\left(\mathrm{e}^{-\omega_0 t} - \mathrm{e}^{\omega_0 t}\right)K_2 \tag{B.13a}$$

$$k_2 = \frac{1}{2}\left(\mathrm{e}^{\omega_0 t} + \mathrm{e}^{-\omega_0 t}\right)K_2 + \frac{D-W}{2\omega_0}\left(\mathrm{e}^{-\omega_0 t} - \mathrm{e}^{\omega_0 t}\right)K_1 \tag{B.13b}$$

$$k_3 = K_3\,. \tag{B.13c}$$

The pure plane shear case is found with the limit $\omega_0 = 0$,

$$k_1 = K_1 - (D+W)tK_2 \tag{B.14a}$$

$$k_2 = K_2 - (D-W)tK_1 \tag{B.14b}$$

$$k_3 = K_3\,. \tag{B.14c}$$

The solution of $\dot{\Phi} = 0$ for an arbitrary function Φ in terms of $\boldsymbol{k}$ and t can be found as:

$$\Phi(\boldsymbol{k}(t), t) = \Phi(\boldsymbol{K})\,. \tag{B.15}$$

so that, in terms of variables $\boldsymbol{k}$ and t, it is found

$$\Phi(\boldsymbol{k}, t) = \Phi(\boldsymbol{F}^{-1}(t).\boldsymbol{k})\,, \tag{B.16}$$

with $K_i = F_{ji}(t)k_j$, or

$$\boldsymbol{K} = \boldsymbol{F}^{-1}(t).\boldsymbol{k}\,, \tag{B.17}$$

in which (.) represents inner product of second order tensors.

Appendix C

Nonlinear algebra for EDQNM-1

The quasi-normal approximation yields

$$\begin{aligned}\frac{1}{2}T^{(\mathrm{QN})}_{ijl}(\boldsymbol{k},\boldsymbol{p},t) =& P_{imn}(\boldsymbol{q})\hat{R}_{mj}(\boldsymbol{k},t)\hat{R}_{nl}(\boldsymbol{p},t) + P_{jmn}(\boldsymbol{k})\hat{R}_{ml}(\boldsymbol{p},t)\hat{R}_{ni}(\boldsymbol{q},t)\\ &+ P_{lmn}(\boldsymbol{p})\hat{R}_{mi}(\boldsymbol{q},t)\hat{R}_{nj}(\boldsymbol{k},t)\,.\end{aligned} \tag{C.1}$$

For further integrated relationship, generalizing terms such as $E(k)\,, E(q)$, one can gather the first term, permuting $\boldsymbol{p}$ and $\boldsymbol{q}$, and the third one, so that the total contribution is

$$\tau^{-}_{ij} = P_{imn}(\boldsymbol{p})\hat{R}_{mj}(\boldsymbol{k},t)\hat{R}_{nl}(\boldsymbol{q},t)k_l + k_l P_{lmn}(\boldsymbol{p})\hat{R}_{mi}(\boldsymbol{q},t)\hat{R}_{nj}(\boldsymbol{k},t)\,, \tag{C.2}$$

after multiplication by k_l. We will use the slightly different form:

$$\tau^{-}_{ij} = \hat{R}_{mj}\left(P'_{imn}\hat{R}''_{nl}k_l + k_l P'_{lmn}\hat{R}''_{ni}\right)\,, \tag{C.3}$$

with obvious abridged notations for $\boldsymbol{q}$ and $\boldsymbol{p}$ dependence as follows:

$$P'_{imn} = P_{imn}(\boldsymbol{p})\,,\quad P''_{imn} = P_{imn}(\boldsymbol{q})\,,\quad \hat{R}'_{ij} = \hat{R}_{ij}(\boldsymbol{p})\,,\quad \hat{R}'_{ij} = \hat{R}_{ij}(\boldsymbol{q})\,. \tag{C.4}$$

C.1 General contribution to T_{ij} and to $\mathcal{W}_{ij}$

In the integrands for the generalized transfer terms, the contribution τ^{+}_{ij} can be written in a symmetrized $\boldsymbol{p} \leftrightarrow \boldsymbol{q}$ form

$$\tau^{+}_{ij} = \frac{1}{2}\left(P_{jmn}\hat{R}'_{ml}\hat{R}''_{ni} + P_{jmn}\hat{R}''_{ml}\hat{R}'_{ni}\right)k_l\,, \tag{C.5}$$

so that the total contribution to the ‘true’ transfer term is

$$\tau^{-}_{ij} + \tau^{+}_{ij} = \hat{R}''_{ml}\left(k_l\delta_{ip} + k_p\delta_{il}\right)\left(P'_{pmn}\hat{R}'_{mj} + \frac{1}{2}P_{jnm}\hat{R}'_{np}\right)\,. \tag{C.6}$$

Accordingly, the integrand of T_{ij} is recovered as

$$2P_{ilp}\hat{R}''_{nl}\left(P'_{pmn}\hat{R}'_{mj}+\frac{1}{2}P_{jnm}\hat{R}'_{np}\right)+\mathrm{sym}(i\leftrightarrow j)^*\,. \tag{C.7}$$

The integrand of $\mathcal{W}_{ij}$ is

$$2k\alpha_i\alpha_l\alpha_p\hat{R}''_{nl}\left(P'_{pmn}\hat{R}'_{mj}+\frac{1}{2}P_{jnm}\hat{R}'_{np}\right)+\mathrm{sym}(i\leftrightarrow j)^*\,. \tag{C.8}$$

C.2 Detailed 'input' contributions

From

$$P'_{imn}\hat{R}''_{nl}k_l=\frac{1}{2}\left(\left(\frac{p_ip_m}{p^2}-P'_{im}\right)k_n\hat{R}''_{nl}k_l+p_m\left(\hat{R}''_{il}k_l+\frac{p_i}{p^2}k_n\hat{R}''_{nl}k_l\right)\right)\,, \tag{C.9}$$

and

$$P'_{lmn}\hat{R}''_{ni}k_l=\frac{1}{2}\left(p_mk_lP'_{ln}\hat{R}''_{ni}+p_n\hat{R}''_{ni}P'_{lm}k_l\right)=\frac{1}{2}k_l\hat{R}''_{li}\left(p_m\left(1-2\frac{kz}{p}\right)-k_m\right)\,, \tag{C.10}$$

rearrangement of the second factor yields:

$$\tau^-_{ij}=\frac{1}{2}k_l\hat{R}''_{ln}k_n\left(-\hat{R}_{ij}+2\frac{p_ip_m}{p^2}\hat{R}_{mj}\right)+\frac{1}{2}k_l\hat{R}''_{li}\left(2\alpha'_mqx-k_m\right)\hat{R}_{mj}\,, \tag{C.11}$$

using simplifications such that $p_m\hat{R}''_{ml}=-k_m\hat{R}''_{ml}$, from $\boldsymbol{k}+\boldsymbol{p}+\boldsymbol{q}=\boldsymbol{0}$ with solenoidality $q_m\hat{R}''_{ml}=0$, and $p=qx+kz$.

Important blocks to simplify are $k_l\hat{R}''_{li}k_i$ and $k_l\hat{R}''_{li}N_j$. The first one reduces to

$$k_l\hat{R}''_{li}k_j=k^2(1-y^2)\left(\mathcal{E}''+\Re(Z''e^{2\imath\lambda''})\right)\,, \tag{C.12}$$

using $\boldsymbol{k}\cdot\boldsymbol{N}=e^{\imath\lambda''}\boldsymbol{k}\cdot\boldsymbol{\beta}''=-k\sin be^{\imath\lambda''}$. Under a slightly different form, using $k^2\sin^2 b=kp\sin a\sin b$, one finds

$$k_l\hat{R}''_{li}k_j=kp(xy+z)\left(\mathcal{E}''+\Re X''\right)\,. \tag{C.13}$$

Similarly, one could obtain

$$k_l\hat{R}''_{li}N_i=e^{\imath\lambda}k\sin b\left(\mathcal{E}''ky-\frac{1}{2}X''(-y-1)-\frac{1}{2}X''(-y+1)\right)\,, \tag{C.14}$$

using $\boldsymbol{N}\cdot\boldsymbol{N}''=e^{\imath(\lambda+\lambda'')}\boldsymbol{\mathcal{W}}\cdot\boldsymbol{\mathcal{W}}''=-y-1$ and so on. Finally the terms are found as:

$$k_l\hat{R}''_{li}N_i=e^{\imath\lambda}k\sin b\left(y\left(\mathcal{E}''+\Re X''\right)+\imath\Im X''\right)\,, \tag{C.15}$$

and

$$k_l\hat{R}''_{li}N^*_i=e^{-\imath\lambda}k\sin b\left(y\left(\mathcal{E}''+\Re X^{*\prime\prime}\right)-\imath\Im X''\right)\,. \tag{C.16}$$

In addition, contributions from $p_m\hat{R}_{mj}$ yields

$$p_m\hat{R}_{mj}N_j = -p\sin c\left(\mathcal{E}e^{\imath\lambda} + Z^*e^{-\imath\lambda}\right), \tag{C.17}$$

and

$$p_m\hat{R}_{mj}N_j^* = -p\sin c\left(\mathcal{E}e^{-\imath\lambda} + Ze^{\imath\lambda}\right). \tag{C.18}$$

We will now write the contribution from τ_{ij}^+ to the (directional) energy transfer, to the polarization transfer and to the pressure-strain transfer.

The contribution to polarization anisotropy transfer, derived from

$$\begin{aligned}\frac{1}{2}\tau_{ij}^- N_i^* N_j^* = kp(xy+z)\left(\mathcal{E}'' + \Re X''\right)&\left(-Z + (1-z^2)\left(\mathcal{E}e^{-2\imath\lambda} + Z\right)\right)\\ -k\sin b\left(y\left(\mathcal{E}'' + \Re X^{*\prime\prime}\right) - \imath\Im X^{*\prime\prime}\right) qx\sin c&\left(\mathcal{E}e^{-2\imath\lambda} + Z\right),\end{aligned} \tag{C.19}$$

finally is

$$\begin{aligned}\frac{1}{2}\tau_{ij}^- N_i^* N_j^* =&kp\left(\mathcal{E}'' + \Re X''\right)\left(-(xy+z^3)Z + z(1-z^2)\mathcal{E}e^{-2\imath\lambda}\right)\\ &+\imath kp\Im X'' x(1-z^2)\left(\mathcal{E}e^{-2\imath\lambda} + Z\right).\end{aligned} \tag{C.20}$$

The contribution to the directional energy transfer is found from $\frac{1}{2}\tau_{ii}^-$, and is a bit simpler to derive from $\frac{1}{4}\tau_{ij}(N_iN_j^* + N_i^*N_j)$ because $\tau_{ij}^- N_j$ and $\tau_{ij}^- N_j^*$ have already been calculated. From

$$\begin{aligned}\tau_{ij}^- N_i N_j^* =&kp(xy+z)\left(\mathcal{E}'' + \Re X''\right)\left(-\mathcal{E} + (1-z^2)\left(\mathcal{E} + Z^*e^{-2\imath\lambda}\right)\right)\\ &- kpx(1-z^2)\left(y\left(\mathcal{E}'' + \Re X''\right) + \imath\Im X''\right)\left(\mathcal{E} + Ze^{-2\imath\lambda}\right),\end{aligned} \tag{C.21}$$

and

$$\begin{aligned}\tau_{ij}^+ N_i^* N_j =&kp(xy+z)\left(\mathcal{E}'' + \Re X''\right)\left(-\mathcal{E} + (1-z^2)\left(\mathcal{E} + Z^*e^{2\imath\lambda}\right)\right)\\ &- kpx(1-z^2)\left(y\left(\mathcal{E}'' + \Re X''\right) - \imath\Im X''\right)\left(\mathcal{E} + Ze^{2\imath\lambda}\right),\end{aligned} \tag{C.22}$$

one finds

$$\frac{1}{2}\tau_{ii}^+ = kp\left(\mathcal{E}'' + \Re X''\right)\left(-(xy+z^3)\mathcal{E} + z(1-z^2)\Re X\right) + kpx(1-z^2)\Im X\Im X''. \tag{C.23}$$

Extra-contribution $\alpha_i\tau_{ij}N_j$ and $\alpha_i\tau_{ij}N_j^*$ give contribution to the pressure-strain rate tensor, via $T^{(\mathrm{RTI})}$, with $\tau_{ij}^-\alpha_iN_j^* = (k_i\hat{R}_{ij}''k_j)(p_i\hat{R}_{ij}N_j^*)(-\frac{z}{p} + \frac{qx}{kp})$, so that

$$\tau_{ij}^-\alpha_iN_j^* = k(xy+z)\sin c e^{-\imath\lambda}\left(\mathcal{E}'' + \Re X''\right)(qx - kz)\left(\mathcal{E} + Z\right). \tag{C.24}$$

C.3 Detailed 'output' contributions

The contributions from $\tau^+_{ij} = P_{jmn}\hat{R}'_{ml}k_l\hat{R}''_{ni}$ are calculated in a similar way.

$$\tau^+_{ij} = \frac{1}{2}\alpha_l\hat{R}'_{lm}\alpha_m\left(k^2\hat{R}''_{ji} - 2k_jk_n\hat{R}''_{ni}\right) + \frac{1}{2}k_n\hat{R}''_{ni}k_l\hat{R}'_{jl}\,. \tag{C.25}$$

From

$$\alpha_m\hat{R}'_{ml}\alpha_l = (1-z^2)\left(\mathcal{E}' + \Re X'\right) \tag{C.26a}$$

$$\hat{R}''_{ij}N^*_iN^*_j = e^{-2\imath\lambda}\left((1+y^2)\left(\mathcal{E}'' + \Re X''\right) - 2\mathcal{E}'' - 2\imath y\Im X''\right) \tag{C.26b}$$

$$k_n\hat{R}'_{ni}N^*_i = -k\sin ce^{-\imath\lambda}\left(z\left(\mathcal{E}' + \Re X'\right) - \imath\Im X'\right)\,, \tag{C.26c}$$

and previous ones (C.16), under a $\boldsymbol{p} \leftrightarrow \boldsymbol{q}$-symmetrized form, one finds

$$\begin{aligned}\tau^+_{ij}N^*_iN^*_j = &\frac{1}{4}k^2e^{-2\imath\lambda}(1-z^2)\left(\mathcal{E}' + \Re X'\right)\left((1+y^2)\left(\mathcal{E}'' + \Re X''\right) - 2\mathcal{E}'' - 2\imath y\Im X''\right)\\ &+\frac{1}{4}k^2e^{-2\imath\lambda}(1-y^2)\left(\mathcal{E}'' + \Re X''\right)\left((1+z^2)\left(\mathcal{E}' + \Re X'\right) - 2\mathcal{E}' - 2\imath y\Im X'\right)\\ &-\frac{1}{2}k^2e^{-2\imath\lambda}(x+yz)\left(y\left(\mathcal{E}'' + \Re X''\right) - \imath\Im X''\right)\left(z\left(\mathcal{E}' + \Re X'\right) - \imath\Im X'\right)\,.\end{aligned} \tag{C.27}$$

The terms in $(\mathcal{E}' + \Re X')(\mathcal{E}'' + \Re X'')$, after $\boldsymbol{p} \leftrightarrow \boldsymbol{q}$-symmetrization, are therefore affected by the geometric factor $(1-z^2)(1+y^2) + (1-y^2)(1+z^2) - 2(xy+z)yz$, which is equal to $2(1-2y^2z^2-xyz)$.

Some related terms can be simplified as:

$$\begin{aligned}&-k^2(1-z^2)(\mathcal{E}' + \Re X')\mathcal{E}'' - k^2(1-y^2)(\mathcal{E}'' + \Re X'')\mathcal{E}'\\ &\qquad= -2kp(xy+z)(\mathcal{E}'' + \Re X'')\mathcal{E}'\end{aligned} \tag{C.28a}$$

$$\begin{aligned}&\imath k^2\big((\mathcal{E}'' + \Re X'')\Im X'(-2z(1-y^2) - 2y(x+yz))\\ &+(\mathcal{E}' + \Re X')\Im X''(-2y(1-z^2) + 2z(x+yz))\big) = kp(y^2-z^2)(\mathcal{E}'' + \Re X'')\Im X'\end{aligned} \tag{C.28b}$$

$$2k^2(x+yz)\Im X'\Im X'' = 2kpy(1-z^2)\Im X'\Im X'' \tag{C.28c}$$

with symmetrization and with simplification of the geometric factors

$$\begin{gathered}1-2y^2z^2-xyz = 2kp(xy+z^3)\,,\quad qz+py = k(x+yz)(x+2yz)\,,\\ kp(xy+z^3) + kq(xz+y^3) = k^2(1-2y^2z^2-xyz)\,,\quad kpy(1-z^2) + kqz(1-y^2) = 2k^2(x+yz)\,.\end{gathered} \tag{C.29}$$

The final form of $T^{(Z)}$ is

$$\begin{aligned}T^{(Z)}(\boldsymbol{k},t) = \iiint\theta_{kpq}2kpe^{-2\mathrm{i}\lambda}\Big[&(\mathcal{E}'' + \Re X'')\big[(xy+z^3)(\Re X' - X) - z(1-z^2)(\mathcal{E}^{'} - \mathcal{E})\\ &+\mathrm{i}(y^2-z^2)\Im X'\big] + \mathrm{i}\Im X''(1-z^2)\big[x(\mathcal{E} + X) - \mathrm{i}y\Im X'\big]\Big]\mathrm{d}^3\boldsymbol{p}\,.\end{aligned} \tag{C.30}$$

We calculate now the term $\tau^+_{ij}(N_iN_j^*+N_iN_j^*) = 2\tau^+_{ij}P_{ij}$ with $\hat{R}''_{ij}P_{ij} = 2\mathcal{E}''-\alpha_i\hat{R}''_{ij}\alpha_j\hat{R}''_{ij}P_{ij} = \mathcal{E}''(1+y^2) - \Re X''(1-y^2)$. Similarly, one finds

$$k_n\hat{R}''_{ni}N_i = k\sin b\, e^{\imath\lambda}\left(y(\mathcal{E}''+\Re X'') + \imath\Im X''\right) \tag{C.31}$$

and

$$k_nR'_{ni}N_i^* = -k\sin c\, e^{-\imath\lambda}\left(z(\mathcal{E}'+\Re X') - \imath\Im X'\right), \tag{C.32}$$

so that

$$\begin{aligned} 2\tau^-_{ij}P_{ij} =& k^2(1-z^2)(\mathcal{E}'+\Re X')\left(\mathcal{E}''(1+y^2)-(1-y^2)\Re X''\right) \\ &- k^2(yz+x)\left(yz(\mathcal{E}''+\Re X'')(\mathcal{E}'+\Re X') + \Im X'\Im X''\right). \end{aligned} \tag{C.33}$$

Then

$$2\tau^-_{ij}P_{ij} = k^2(\mathcal{E}''+\Re X'')(\mathcal{E}'+\Re X')(y^2-2y^2z^2-xyz)+k^2(1-z^2)(\mathcal{E}'+\Re X')(\mathcal{E}''-\Re X'')-k^2(yz+x)\Im X'\Im X''. \tag{C.34}$$

Symmetrization in terms of $\boldsymbol{p}\leftrightarrow\boldsymbol{q}$ yields

$$\begin{aligned} 2\tau^+_{ij}P_{ij} =& k^2(\mathcal{E}''+\Re X'')(\mathcal{E}'+\Re X')\left(\frac{y^2}{2}+\frac{z^2}{2}-2y^2z^2-xyz\right) \\ &+\frac{1}{2}k^2(1-z^2)(\mathcal{E}'+\Re X')(\mathcal{E}''-\Re X'') + \frac{1}{2}k^2(1-y^2)(\mathcal{E}''+\Re X'')(\mathcal{E}'-\Re X') - k^2(yz+x)\Im X'\Im X'', \end{aligned} \tag{C.35}$$

and finally

$$\begin{aligned} 2\tau^+_{ij}P_{ij} =& k^2(\mathcal{E}''+\Re X'')(\mathcal{E}'+\Re X')(1-2y^2z^2-xyz) \\ &-k^2(1-z^2)(\mathcal{E}'+\Re X')\Re X'' - k^2(1-y^2)(\mathcal{E}''+\Re X'')\Re X' - k^2(yz+x)\Im X'\Im X''. \end{aligned} \tag{C.36}$$

The term $-2kpy(1-z^2)$ is equivalent to $-kpy(1-z^2)-kqz(1-y^2)$ after $\boldsymbol{p}\leftrightarrow\boldsymbol{q}$-symmetrization, which is equal to $-k(qy+pz)(yz+x) = -k^2(yz+x)$, so that the term $-k^2(yz+x)\Im X'\Im X''$ can be replaced by $-2kpy(1-z^2)\Im X'\Im X''$, with the $\boldsymbol{k}\leftrightarrow\boldsymbol{p}$-symmetrized coefficient as in Eq. (C.23) for $2\tau^+_{ii}$.

The term $-k^2(1-z^2)(\mathcal{E}'+\Re X')\Re X'' - k^2(1-y^2)(\mathcal{E}''+\Re X'')\Re X'$ is equal to $-kq(xz+y)(\mathcal{E}'+\Re X')\Re X'' - kp(xy+z)(\mathcal{E}''+\Re X'')\Re X'$, and therefore can be replaced by $-2kp(xy+z)(\mathcal{E}''+\Re X'')\Re X'$. Accordingly, the final form of $T^{(\mathcal{E})}$ is

$$\begin{aligned} T^{(\mathcal{E})}(\boldsymbol{k},t) = \iiint \theta_{kpq}2kp\Big[&(\mathcal{E}''+\Re X'')\left[(xy+z^3)(\mathcal{E}'-\mathcal{E}) - z(1-z^2)(\Re X'-\Re X)\right] \\ &+\Im X''(1-z^2)(x\Im X - y\Im X')\Big]\mathrm{d}^3\boldsymbol{p}, \end{aligned} \tag{C.37}$$

Contributions to $T^{(\mathrm{RTI})}$ are calculated from

$$\alpha_i \tau^+_{ij} N^*_j = \frac{1}{2}(k_i \hat{R}'_{ij} \alpha_j)(\alpha_i \hat{R}''_{ij} N^*_j) + \frac{1}{2}(k_i \hat{R}''_{ij} \alpha_j)(\alpha_i \hat{R}'_{ij} N^*_j)\,, \tag{C.38}$$

which can be replaced by twice the second term, so that

$$\alpha_i \tau^+_{ij} N^*_j = -kp(xy+z)\sin c e^{-\imath\lambda}(\mathcal{E}'' + \Re X'')(z(\mathcal{E}' + \Re X') - \imath X')\,, \tag{C.39}$$

and

$$\begin{aligned} T^{(\mathrm{RTI})}(\boldsymbol{k},t) = \iiint \theta_{kpq} 2e^{-\mathrm{i}\lambda} p(xy+z)\sqrt{1-z^2}(\mathcal{E}'' + \Re X'')\Big[(\mathcal{E}+X)(zk-qx) \\ - k\left(z(\mathcal{E}' + \Re X') - \mathrm{i}\Im X'\right)\Big]\mathrm{d}^3\boldsymbol{p}\,. \end{aligned} \tag{C.40}$$

Appendix D

Spherical average of nonlinear terms for MCS

D.1 λ-integrals

The integration in terms of λ are listed:

$$\int_0^{2\pi} \alpha'_m \alpha'_n d\lambda = \pi[(1-z^2)\delta_{mn} + (3z^2-1)\alpha_m\alpha_n]\,, \tag{D.1}$$

$$\int_0^{2\pi} W'_m W'_n d\lambda = -\pi(1-z^2)(\delta_{mn} - 3\alpha_m\alpha_n)\,, \tag{D.2}$$

$$\int_0^{2\pi} e^{-2\imath\lambda}\alpha'_m \alpha' n d\lambda = \frac{\pi}{2}(1-z^2)N_n^*(\boldsymbol{\alpha})N_m^*(\boldsymbol{\alpha})\,, \tag{D.3}$$

$$\int_0^{2\pi} e^{-2\imath\lambda} W'_m W'_n d\lambda = \frac{\pi}{2}(1+z)^2 N_n^*(\boldsymbol{\alpha})N_m^*(\boldsymbol{\alpha})\,, \tag{D.4}$$

$$\int_0^{2\pi} e^{-2\imath\lambda} W'^*_m W'^*_n d\lambda = \frac{\pi}{2}(1-z)^2 N_n^*(\boldsymbol{\alpha})N_m^*(\boldsymbol{\alpha})\,. \tag{D.5}$$

D.2 Contribution of isotropic and directionally anisotropic transfer terms

Since

$$\int_0^{2\pi} (\mathcal{E}^{(\mathrm{dir})''} + \Re X'')\,\mathrm{d}\lambda = \frac{15\pi}{2}\mathcal{E}_0\left(2(1-3y^2)H_{mn}^{(\mathrm{dir})''} - (1-y^2)H_{mn}^{(\mathrm{pol})''}\right)\alpha_m\alpha_n\,, \tag{D.6}$$

$$\int_0^{2\pi} (\mathcal{E}^{(\mathrm{dir})'} - \mathcal{E}^{(\mathrm{dir})})\,\mathrm{d}\lambda = 15\pi\left((1-3z^2)\mathcal{E}'_0 H_{mn}^{(\mathrm{dir})'} - 2\mathcal{E}_0 H_{mn}^{(\mathrm{dir})}\right)\alpha_m\alpha_n\,, \tag{D.7}$$

$$\int_0^{2\pi} \Re X' \,\mathrm{d}\lambda = \frac{15\pi}{2}\mathcal{E}_0'(1-z^2)H_{mn}^{(\mathrm{pol})'}\alpha_m\alpha_n\,, \tag{D.8}$$

the contribution of $T^{(\mathcal{E})}$ linearized with H, are in terms of $\alpha_m\alpha_n$. Its spherical integral in terms of $\alpha_m\alpha_n P_{ij}$ is found as:

$$\iint_{S_k} H_{mn}^{()}\alpha_m\alpha_n P_{ij}\,\mathrm{d}^2\boldsymbol{k} = -\frac{8}{15}\pi k^2 H_{ij}^{()}\,, \tag{D.9}$$

by using

$$\iint_{S_k} \alpha_m\alpha_n\,\mathrm{d}^2\boldsymbol{k} = \frac{4\pi k^2}{3}\delta_{mn}, \quad \iint_{S_k} \alpha_m\alpha_n\alpha_i\alpha_j\,\mathrm{d}^2\boldsymbol{k} = \frac{4\pi k^2}{15}\left(\delta_{mn}\delta_{ij}+\delta_{mi}\delta_{nj}+\delta_{mj}\delta_{ni}\right)\,. \tag{D.10}$$

In particular, one finds again the relationship

$$\iint_{S_k} \mathcal{E}^{(\mathrm{dir})}P_{ij}\,\mathrm{d}^2(\boldsymbol{k}) = 8\pi k^2\mathcal{E}_0 H_{ij}^{(\mathrm{dir})} = 2E(k)H_{ij}^{(\mathrm{dir})}(k)\,. \tag{D.11}$$

The total contribution of the triple correlations to $EH_{ij}^{(\mathrm{dir})}$, through $H^{(\mathrm{dir})}$, is written as:

$$\mathcal{S}_{ij}^{(\mathrm{dir})\mathcal{E}} + \mathcal{P}_{ij}^{(\mathrm{dir})\mathcal{E}} = \iint_{\Delta_k} \theta_{kpq}8\pi^2p^2k^2q(xy+z^3)\mathcal{E}_0''\left[(3y^2-1)(\mathcal{E}_0'-\mathcal{E}_0)H_{ij}^{(\mathrm{dir})''} + (3z^2-1)\mathcal{E}_0'H_{ij}^{(\mathrm{dir})'} - 2\mathcal{E}_0H_{ij}^{(\mathrm{dir})}\right]\mathrm{d}p\,\mathrm{d}q\,, \tag{D.12}$$

in agreement with the purely isotropic contribution, found as

$$\mathcal{S}_{ij}^{(\mathrm{iso})} = 2T(k)\frac{\delta_{ij}}{3}\,, \tag{D.13}$$

with

$$T(k) = \iint_{\Delta_k} \theta_{kpq}8\pi^2k^2p^2q(xy+z^3)\mathcal{E}_0''\left[\mathcal{E}_0'-\mathcal{E}_0)\right]\,\mathrm{d}p\,\mathrm{d}q. \tag{D.14}$$

Similarly, one obtains the contribution through $H^{(\mathrm{pol})}$ as:

$$\mathcal{S}_{ij}^{(\mathrm{dir})Z} + \mathcal{P}_{ij}^{(\mathrm{dir})Z} = \iint_{\Delta_k} \theta_{kpq}4\pi^2p^2k^2q\mathcal{E}_0''\left[(y^2-1)(xy+z^3)(\mathcal{E}_0'-\mathcal{E}_0)H_{ij}^{(\mathrm{pol})''} + z(1-z^2)^2\mathcal{E}_0'H_{ij}^{(\mathrm{pol})'}\right]\mathrm{d}p\,\mathrm{d}q \tag{D.15}$$

D.3 Contribution of polarization transfer terms

λ-integrals yield

$$\int_0^{2\pi} e^{-2\imath\lambda}\left(\mathcal{E}^{(\mathrm{dir})''} + \Re X''\right)d\lambda = \frac{5}{4}\pi\mathcal{E}_0''\left(6(y^2-1)H_{mn}^{(\mathrm{dir})''} + (1+z^2)H_{mn}^{(\mathrm{pol})''}\right)N_m^*(\boldsymbol{\alpha})N_n^*(\boldsymbol{\alpha})\,, \tag{D.16}$$

$$\int_0^{2\pi} e^{-2\imath\lambda} \Im X' \, \mathrm{d}\lambda = \frac{5}{2}\pi z \mathcal{E}_0' H_{mn}^{(\mathrm{pol})'} N_m^*(\boldsymbol{\alpha}) N_n^*(\boldsymbol{\alpha}) \, , \tag{D.17}$$

$$\int_0^{2\pi} e^{-2\imath\lambda} X \, \mathrm{d}\lambda = 2\pi Z = 5\pi \mathcal{E}_0 H_{mn}^{(\mathrm{pol})} N_m^*(\boldsymbol{\alpha}) N_n^*(\boldsymbol{\alpha}) \, . \tag{D.18}$$

All of the contributions are affected by the term $N_m^*(\alpha)N_n^*(\alpha)$, which leads to the spherical integrals:

$$\iint_{S_k} H_{mn}^{()} N_m^* N_n^* N_i N_j \, \mathrm{d}^2\boldsymbol{k} = \frac{16}{5}\pi k^2 H_{ij}^{()} \, , \tag{D.19}$$

with

$$N_i N_m^* = P_{im} - \imath \epsilon_{imj} \alpha_j \, . \tag{D.20}$$

In particular, on finds again the identity

$$\iint_{S_k} \Re \left(\underbrace{\frac{5}{2} \mathcal{E}_0 H_{mn}^{(\mathrm{pol})} N_m^* N_n^*}_{Z} N_i N_j \right) \mathrm{d}\boldsymbol{k} = 8\pi k^2 \mathcal{E}_0 H_{ij}^{(\mathrm{pol})} = 2E(k) H_{ij}^{(\mathrm{pol})}(k) \, . \tag{D.21}$$

The contributions to the polarization transfer are expressed as

$$\begin{aligned} &\mathcal{S}_{ij}^{(\mathrm{pol})\mathcal{E}} + \mathcal{P}_{ij}^{(\mathrm{pol})\mathcal{E}} = \\ &\iint_{\Delta_k} \theta_{kpq} 24\pi^2 k^2 p^2 q z (z^2-1) \mathcal{E}_0'' \left[(y^2-1)(\mathcal{E}_0' - \mathcal{E}_0) H_{ij}^{(\mathrm{dir})''} - (1-z^2) \mathcal{E}_0' H_{ij}^{(\mathrm{dir})'} \right] \mathrm{d}p \, \mathrm{d}q \, , \end{aligned} \tag{D.22}$$

with

$$\begin{aligned} \mathcal{S}_{ij}^{(\mathrm{pol})Z} + \mathcal{P}_{ij}^{(\mathrm{pol})Z} = &\iint_{\Delta_k} \theta_{kpq} 4\pi^2 p^2 k^2 q \mathcal{E}_0'' \Big[(xy + z^3)\Big((1+z^2) \mathcal{E}_0' H_{ij}^{(\mathrm{pol})'} - 4\mathcal{E}_0 H_{ij}^{(\mathrm{pol})} \Big) \\ &+ z(z^2-1)(1+y^2)(\mathcal{E}_0' - \mathcal{E}_0) H_{ij}^{(\mathrm{pol})''} + 2z(z^2-y^2) \mathcal{E}_0' H_{ij}^{(\mathrm{pol})'} \\ &+ 2yx(z^2-1) \mathcal{E}_0 H_{ij}^{(\mathrm{pol})''} \Big] \mathrm{d}p \, \mathrm{d}q \, . \end{aligned} \tag{D.23}$$

D.4 Contributions to pressure-strain rate tensor

The λ-integrals lead to:

$$\int_0^{2\pi} \alpha_m'' \alpha_n'' e^{-\imath\lambda} \, \mathrm{d}\lambda = -\pi y \sin b (\alpha_m N_n^*(\boldsymbol{\alpha}) + \alpha_n N_m^*(\boldsymbol{\alpha})) \, , \tag{D.24}$$

$$\int_0^{2\pi} W_m'' W_n'' e^{-\imath\lambda} \, \mathrm{d}\lambda = \pi \sin b (1+y)(\alpha_m N_n^*(\boldsymbol{\alpha}) + \alpha_n N_m^*(\boldsymbol{\alpha})) \, , \tag{D.25}$$

$$\int_0^{2\pi} W_m^{``*} W_n^{``*} e^{-\imath\lambda} \, \mathrm{d}\lambda = -\pi \sin b (1-y)(\alpha_m N_n(\boldsymbol{\alpha}) + \alpha_n N_m(\boldsymbol{\alpha})) \, . \tag{D.26}$$

The contribution to the spherical integral is deduced from:

$$\iint_{S_k} H^{()}_{mn} \alpha_m N^*_n \alpha_i N_j \,\mathrm{d}^2\boldsymbol{k} = \frac{4}{5}\pi k^2 H^{()}_{ij} \tag{D.27}$$

with zero contribution of $\alpha_m N_n \alpha_i N_j$.

From

$$\int_0^{2\pi} e^{-\imath\lambda}(\mathcal{E}'' + X'')(\mathcal{E} + X)d\lambda = -5\mathcal{E}_0\mathcal{E}''_0\pi\sin\beta\left(6yH^{(\mathrm{dir})''}_{mn}N^*_n - (1-y)H^{(\mathrm{pol})''}_{mn}N_n\right)\alpha_m,$$

$$\int_0^{2\pi} e^{-\imath\lambda}(\mathcal{E}' + X')\mathcal{E}''_0 d\lambda = 5\mathcal{E}'_0\mathcal{E}''_0\pi\sin\gamma\left(6zH^{(\mathrm{dir})'}_{mn}N^*_n - (1-z)H^{(\mathrm{pol})'}_{mn}N_n\right)\alpha_m,$$

one obtains the contribution of $\iint_{S_k}(\int_0^{2\pi} T^{(\mathrm{RTI})}\,\mathrm{d}\lambda)\alpha_i N^*_j\,\mathrm{d}^2\boldsymbol{k}$ as

$$\mathcal{P}^{\mathcal{E}}_{ij} = \iint\limits_{\Delta_k} 16\pi^2p^2k^2q(yz+x)\mathcal{E}''_0\left[6y(z^2-y^2)\mathcal{E}'_0H^{(\mathrm{dir})''}_{ij} - 6y(z^2-x^2)\mathcal{E}_0H^{(\mathrm{dir})''}_{ij}\right]\mathrm{d}p\,\mathrm{d}q\,, \tag{D.28}$$

and contribution of $\iint_{S_k}(\int_0^{2\pi} T^{(\mathrm{RTI}*)}\,\mathrm{d}\lambda)\alpha_i N_j\,\mathrm{d}^2\boldsymbol{k}$

$$\mathcal{P}^{Z}_{ij} = \iint\limits_{\Delta_k} \theta_{kpq}16\pi^2p^2k^2q(yz+x)\mathcal{E}''_0\left[\mathcal{E}'_0\left(y(z^2-y^2) - xz - y\right)H^{(\mathrm{pol})''}_{ij} - y(z^2-x^2)\mathcal{E}_0H^{(\mathrm{pol})''}_{ij}\right]\mathrm{d}p\,\mathrm{d}q\,. \tag{D.29}$$

Appendix E

Proposal on direct DNS method for homogeneous turbulent flow

E.1 Equations and technical difficulties

In order to avoid the Poisson equation for pressure, usually the fluctuated equations are solved with spectral form in homogeneous incompressible flow by DNS as in follows:

$$\frac{\partial \hat{u}_i}{\partial t} - A_{ln} k_l \frac{\partial \hat{u}_i}{\partial k_n} + A_{ij}\hat{u}_j + 2\epsilon_{imn}\Omega_m \hat{u}_n + \nu k^2 \hat{u}_i = -\imath k_i \hat{p} - \imath k_j \widehat{u_i u_j}\,, \tag{E.1a}$$

$$k_i \hat{u}_i = 0\,. \tag{E.1b}$$

There are two mainly technical challenges, the solution for advection terms and for the convolution. Orszag (1969) and Eliasen *et al.* (1970) proposed pseudo-spectral method independently to calculate the convolution with reduced computational cost, which is not concentrated here. Rogallo (1977, 1981) solved the advection by statistics method and then extended Orszag-Patterson algorithm to all homogeneous turbulent flows.

E.2 Rogallo's transformation

The computations are done in a moving coordinate system $\boldsymbol{x}(t)$, described by $x_i(t) = F_{ij}(t, t_0)X_j$ in accordance with SLT. So the Naiver-Stocks equations for fluctuation turn into

$$\begin{aligned} &\frac{\partial u_i}{\partial t} + A_{ij}u_j + F_{kj}\frac{\partial u_i u_j}{\partial x_k} = -F_{ji}\frac{\partial p}{\partial x_j} + \nu F_{kj}F_{lj}\frac{\partial^2 u_i}{\partial x_k x_k} \\ &F_{ji}\frac{\partial u_i}{\partial x_j}\,, \end{aligned} \tag{E.2}$$

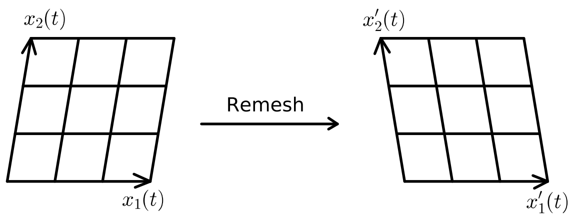

(a) Remeshing in physical space (see Canuto *et al.*, 2007).

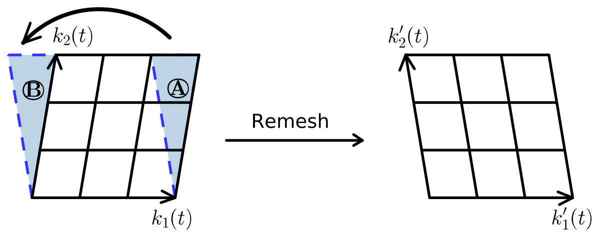

(b) Remeshing in Fourier space

Figure E.1: Illustration of the remeshing for DNS in HAT.

in the moving coordinate system. When $A_{ij} = S\delta_i\delta_j$, namely in shear flow, the remeshing can be illustrated with figure E.1 in both physical space and Fourier space. Usually, the periodic remeshing take place at $St = 0.5\,, 1.5\,, 2.5\,, \ldots$ if the simulation starts at $St = 0$ and the distorted grids in the left of figure E.1 are mapped into the right ones with spatial interpolation of the field on the spatial periodic condition.

However, this produces extra aliasing effects. The aliasing effects can be explained with Fourier expansion before and after remeshing (Canuto *et al.*, 2007) mathematically, or more simply, one can understand immediately from figure E.1b. The remeshing amounts to move the partly velocity field section Ⓑ to section Ⓐ. On the view of turbulent spectral theory, this implies some spectral components in small scales are moved into large scales. Rogallo (1981) referred the aliasing effects but without estimation quantitatively. Figure E.2 shows the impact on statistical quantities after remeshing, in order to illustrate the influence on flow field of remeshing. The simulation is in Fourier space by Lesur & Longaretti (2005) code and $\mathcal{K}(t)$ and $\varepsilon(t)$ are calculated with

$$\mathcal{K}(t) = \iiint \frac{1}{2}\hat{u}_i(\boldsymbol{k},t)\hat{u}_i^*(\boldsymbol{k},t)\,\mathrm{d}^2\boldsymbol{k}\,, \quad \varepsilon(t) = \iiint \frac{1}{2}\nu k^2\hat{u}_i(\boldsymbol{k},t)\hat{u}_i^*(\boldsymbol{k},t)\,\mathrm{d}^2\boldsymbol{k}\,. \tag{E.3}$$

One can find that, remeshing results in obvious unexpected decrease of $\varepsilon(t)$ and slight decrease of $\mathcal{K}(t)$. Delorme (1985) corrected this by a remedy of simply de-aliasing after

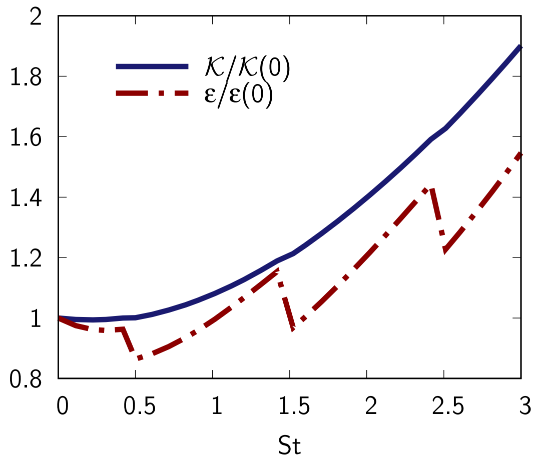

Figure E.2: Illustration of the impact on flow field induced by remeshing.

remeshing only for shear flow, where others usually ignore this problem even without any error estimation. Actually, during the remeshing, a strong spatially periodic condition is employed, which is essential for the aliasing effects. In spectral theory for homogeneous turbulence, there is not periodicity at all, namely it is not physical implication. In practice, the explicit periodicity is applied for numerical method induced by discrete Fourier transform, and should be questioned when involving significant volume rather only in boundaries.

Beyond that, remeshing does result other problems as introduced in chapter 3, e.g. , compatibility problem for arbitrary form of mean flow velocity gradients since complicated and non-universal remeshing algorithm, loss of accuracy induced by extrapolation and by that computational time can not be exact $St = 0.5\,, 1.5\,, 2.5\,, \ldots$ with adaptive time step.

E.3 Compatible numerical method without remeshing

In order to avoid remeshing and the problems resulted by it, here a new numerical method is proposed for incompressible homogeneous turbulent flow with or without system rotation. The new method is referred to "finite difference–pseudo- spectral method", since the advection terms will be solved with FDS directly, while pseudo-spectral method will be retained for convolution term. As a consequence, the numerical method can be implemented universally, and be suitable for specific flow by refined grids and finite difference scheme.

There are two key technologies. First one is the numerical convergence involved to FDS, which is supposed to be solved optimistically. The biggest problem is the potential discontinuity, which is out the scope of FDS. Thanks to the incompressibility, the singularities are primarily generated for geometric reasons, such as sharp edges or corners. In other words, the exact solutions for incompressible Naiver-Stocks equations are smooth if the initial data or boundary conditions are not discontinuous, whereas singularities can arising from non-linear wave propagation in compressible flows. Since the geometry in HAT is really simple, the new method is feasible providing smooth initialization method and boundary conditions are given. For instance, the initialization method by Rogallo (1981) with random anglers must be refined. In addition, the aliasing induced by pseudo-spectral method has to be removed carefully without raising extra discontinuities.

The final goal is to develop a generic numerical code suitable for arbitrary A_{ij} with high accuracy, considering typical initial conditions, then to build system connection between spectral DNS method and spectral turbulent theory.

Appendix F

Scalar and vectorial spherical harmonics decomposition with its application

F.1 Basic decompositions in terms of scalar and vectorial harmonics

Equations for the most general decompositions are given (or recalled) here, for any smooth scalar field or vector field, with their counterpart in Fourier space. A possible time-dependency is implied.

F.1.1 Scalar spherical harmonics (SSH)

The classical SSH decomposition for a scalar s with smooth spatial distribution in a system of polar-spherical coordinates (r, θ, ϕ) is

$$s(\boldsymbol{r}) = \sum_{n=0}^{N} \sum_{m=-n}^{n} s_n^m(r) Y_n^m(\theta, \phi)\,, \tag{F.1}$$

in which $Y_n^m(\theta, \phi)$ are expressed in terms of extended Legendre polynomials $P_n^m(\theta)$ via

$$Y_n^m(\theta, \phi) = P_n^m(\cos\theta) \exp(\imath m \phi)\,. \tag{F.2}$$

The real integer number n is called the degree, with maximum N, and the relative integer number m is the order, that is bounded by n in absolute value.

All the degrees are often not called into play. For a real scalar, as energy distribution, with inversion symmetry, only even degrees are present, and $s_{2p}^{-m} = s_{2p}^{m}$. For a pseudo-scalar, as the instantaneous helicity distribution, with change of sign by inversion symmetry, only odd degrees are present.

A related SO^3-type expansion holds in Cartesian coordinates

$$s(\boldsymbol{r}) = s^0(r) + s^1_m(r)\alpha_m + s^2_{mn}(r)\alpha_m\alpha_n + \cdots , \tag{F.3}$$

with

$$\boldsymbol{\alpha} = \frac{\boldsymbol{r}}{r}, \quad r = \mid \boldsymbol{r} \mid . \tag{F.4}$$

Such an expansion is independent on the choice of the polar direction $\boldsymbol{n}$, but it is difficult to apply at really high degree. Generating tensors $s^n_{i_1 \dots i_n}$ are difficult to simplify only using rules of permutation and contraction of indices. Of course, as the Y_n^m, they rely on the eigenfunctions of the Laplacian operator, so that differential properties are called into play as well (see a lot of references). In addition, it is not obvious to recombine them, at a given degree, in order to derive orthogonal bases.

F.1.2 Vectorial spherical harmonics (VSH)

It is interesting to go beyond SSH, and to look at vectorial spherical harmonics; if a decomposition is valid for a vector $\boldsymbol{V}$, it should apply to a tensor, forming $\boldsymbol{V} \otimes \boldsymbol{V}$.

A *simplified* toroidal-poloidal decomposition (for a solenoidal smooth vector field $\boldsymbol{u}$) follows from the 'vortex-wave' decomposition by Riley *et al.* (1981) with application to stable stratified turbulence (see also Sagaut & Cambon, 2018)

$$\boldsymbol{u}(\boldsymbol{r}) = \boldsymbol{\nabla} \times (s^{(tor)}(\boldsymbol{r})\boldsymbol{n}) + \boldsymbol{\nabla} \times \left(\boldsymbol{\nabla} \times s^{(pol)}(\boldsymbol{r})\boldsymbol{n}\right) . \tag{F.5}$$

It is tempting to decompose both toroidal $s^{(tor)}$ and poloidal $s^{(pol)}$ potentials in terms of SSH, as for 'true' scalars. $s^{(tor)}$ is similar to the streamfunction used in purely 2C-2D flows, if it depends only on horizontal ($\perp \boldsymbol{n}$) coordinates; it yields an extension from 2D-2C flow to 3D-2C toroidal flow, because of its dependency on the vertical coordinate. Unfortunately, the latter equation gives a nul contribution for the purely horizontal ($\perp \boldsymbol{n}$) flow which depends only on the vertical ($\parallel \boldsymbol{n}$) coordinate. Accordingly, the vertically sheared horizontal flow (**VSHF**, e.g. Smith & Waleffe (2002)) mode $\boldsymbol{u}_\perp(\pm r\boldsymbol{n})$— that is essential, especially in stable stratified turbulence! — is missed (zero value). Some empirical attempts to complete the decomposition, as "potosh" (poloidal-toroidal-shear, Galmiche *et al.* (2001)), are not completely satisfactory and thereby will be no longer discussed here.

A more complex decomposition in terms of VSH was used by Rieutord (1987) in order to solve linear operators of rotating flow on spheres in physical space. The essential difference with the simplified toroidal-poloidal decomposition in physical space, closely related to the Craya's one in Fourier space, is a more complex definition of the toroidal mode as

$$\boldsymbol{u}^{(tor+)}(\boldsymbol{r}) = \boldsymbol{\nabla} \times \left(s^{(tor+)}(\boldsymbol{r}) \frac{\boldsymbol{r}}{r} \right), \tag{F.6}$$

following Chandrasekkhar (1982). This amounts to substitute the unit radial vector $\boldsymbol{r}/r$ to the polar axis $\boldsymbol{n}$, and the problem of the zero value always at the pole is avoided. On the other hand, the fact that a smooth distribution always include at least a zero value is still relevant.

From the related decomposition using SSH, or

$$\boldsymbol{u}^{(tor+)}(\boldsymbol{r}) = \sum_{n=0}^{N} \sum_{m=-n}^{n} w_n^m(r) \boldsymbol{\nabla} \times \left(Y_n^m(\theta, \phi) \frac{\boldsymbol{r}}{r} \right), \tag{F.7}$$

and similar relationship for the complementary spheroidal part, also related to a poloidal decomposition for solenoidal fields. Both $\boldsymbol{\nabla} \times (Y_n^m \frac{\boldsymbol{r}}{r})$ and $\boldsymbol{\nabla} Y_n^m$ must be calculated, or $\frac{\partial}{\partial r_n}$ of a function of θ and ϕ.

The use of angular harmonics was investigated in Los Alamos for a long time, in possible connection with RDT, and in possible collaboration with our team (e.g. Cambon & Rubinstein (2006), Rubinstein *et al.* (2015)). Following internal reports from Chuck Zemach, vectorial spherical harmonics were implicitly used, in addition to conventional scalar harmonics. For instance, in a recent study by Clark *et al.* (2018), both Y_n^m scalar functions and their $\boldsymbol{k}$-gradients are used. Note also that this paper does not separate directional anisotropy and polarization anisotropy, and is restricted to pure irrotational mean flow (no stropholysis term), as an application to angular harmonics expansions to the RDT solution by Batchelor & Proudman (1954).

F.1.2.1 Recovering the zonal-meridional-radial local frame

Spatial derivative are calculated in the polar-spherical system of coordinates as follows.

$$\frac{\partial}{\partial r_n} = \frac{\partial}{\partial r}\frac{\partial r}{\partial r_n} + \frac{\partial}{\partial \theta}\frac{\partial \theta}{\partial r_n} + \frac{\partial}{\partial \phi}\frac{\partial \phi}{\partial r_n},$$

and it is shown that the three generating vectors are expressed in terms of the zonal - meridional - radial local frame

$$\boldsymbol{e}^{(1)}(\boldsymbol{\alpha}) = \frac{\boldsymbol{\alpha} \times \boldsymbol{n}}{\mid \boldsymbol{\alpha} \times \boldsymbol{n} \mid}, \quad \boldsymbol{e}^{(2)}(\boldsymbol{\alpha}) = \boldsymbol{\alpha} \times \boldsymbol{e}^{(1)}(\boldsymbol{\alpha}), \quad \boldsymbol{e}^{(3)}(\boldsymbol{\alpha}) = \boldsymbol{\alpha} = \frac{\boldsymbol{r}}{r}, \tag{F.8}$$

whose exact counterpart in Fourier space is called the Craya-Herring frame of reference in the turbulence community. $\frac{\partial r}{\partial r_n} = \alpha_n$ simply derives from $rdr = r_n dr_n$; less obvious are $\frac{\partial \theta}{\partial r_n} = \frac{1}{r} e_n^{(2)}(\boldsymbol{\alpha})$ and $\frac{\partial \phi}{\partial r_n} = -\frac{1}{r\sin\theta} e_n^{(1)}(\boldsymbol{\alpha})$. Finally, is found

$$\frac{\partial}{\partial r_n} = \alpha_n \frac{\partial}{\partial r} + \frac{1}{r} e_n^{(2)}(\boldsymbol{\alpha}) \frac{\partial}{\partial \theta} - \frac{1}{r\sin\theta} \boldsymbol{e}_n^{(1)}(\boldsymbol{\alpha}) \frac{\partial}{\partial \phi}. \tag{F.9}$$

Its singularity at the pole ($\sin\theta = 0$) is clear for the derivative with respect to ϕ.

F.1.3 Counterpart in 3D Fourier space

The similarity between the representation in physical space and the one in 3D Fourier space is obvious for a scalar field, with

$$\hat{s}(\boldsymbol{k}) = \sum_{n=0}^{N} \sum_{m=-n}^{n} s'^m_n(k) Y_n^m(\theta_k, \phi_k), \tag{F.10}$$

and

$$\hat{s}(\boldsymbol{k}) = s'^0(k) + s'^1_m(k)\alpha_m + s'^2_{mn}(k)\alpha_m\alpha_n + \cdots .$$

For the sake of simplicity, we will use the same notation $\boldsymbol{\alpha}$ for both $\boldsymbol{r}/r$ and $\boldsymbol{k}/k$, in the absence of possible confusion.

As mentioned for distribution in physical space, all degrees are not present. For instance if the scalar is the spectrum of energy in homogeneous anisotropic turbulence, only even degrees are present with $s'^{-m}_{2p} = s'^m_{2p}$. In the same conditions, Hermitian symmetry holds for the helicity spectrum, but purely imaginary contributions with odd degree are present as well.

This physical-spectral analogy is conserved in Fourier space for vector fields, but with significant differences. Firstly, the solenoidal property, or $\boldsymbol{\nabla} . \boldsymbol{u} = 0$ in physical space, amounts to the simpler algebraic orthogonality condition $\boldsymbol{k} \cdot \boldsymbol{u} = 0$.

Accordingly, the simplified toroidal-poloidal decomposition (F.5) becomes

$$\boldsymbol{u}h(\boldsymbol{k}) = s'^{(tor)}(\boldsymbol{k})(\boldsymbol{k} \times \boldsymbol{n}) + s'^{(pol)}\left(\boldsymbol{k} \times (\boldsymbol{k} \times \boldsymbol{n})\right).$$

The hole at the pole is even more obvious than in physical space, when $\boldsymbol{k} \times \boldsymbol{n} = 0$. This inconvenience is treated in the Craya-Herring frame of reference by defining

$$\boldsymbol{u}h(\boldsymbol{k}) = u^{(1)}(\boldsymbol{k})\boldsymbol{e}^{(1)}(\boldsymbol{\alpha}) + u^{(2)}(\boldsymbol{k})\boldsymbol{e}^{(2)}(\boldsymbol{\alpha}), \quad if \quad \mid \boldsymbol{k} \times \boldsymbol{n} \mid = \sin\theta_k \neq 0. \tag{F.11}$$

The zonal- meridional -radial frame in Eq. (F.8) is thereby transfered to the sphere in Fourier space ($\boldsymbol{r} \rightarrow \boldsymbol{k}$), and corresponds to a *normalized* simplified toroidal-poloidal decomposition. As a caveat, The zonal-meridional-radial frame, or Craya-Herring, is not defined at the pole. In practical calculation, it is possible to replace this frame by the Cartesian frame $(\boldsymbol{e}^{(1)}, \boldsymbol{e}^{(2)}, \boldsymbol{n})$ exactly at the pole, with for instance $e_i^{(1)} = \delta_{i1}, e_i^{(2)} = \delta_{i2}, n_i = \delta_{i3}$. The helical modes (Cambon & Jacquin, 1989; Waleffe, 1992) are easily derived by

$$\boldsymbol{N}(\boldsymbol{\alpha}) = \boldsymbol{e}^{(2)}(\boldsymbol{\alpha}) - \imath \boldsymbol{e}^{(1)}(\boldsymbol{\alpha}), \quad \boldsymbol{N}^*(\boldsymbol{\alpha}) = \boldsymbol{N}(-\boldsymbol{\alpha}) = \boldsymbol{e}^{(2)}(\boldsymbol{\alpha}) + \imath \boldsymbol{e}^{(1)}(\boldsymbol{\alpha}), \tag{F.12}$$

with the same caveat. Instead of a particular polar definition, an explicit *multiple definition* can be derived from

$$N_1(\boldsymbol{n}) = \exp(-\imath\phi_k), N_2(\boldsymbol{n}) = -\imath \exp(-\imath\phi_k), N_3 = 0,$$

ensuring continuity.

A special definition of the Craya-Herring frame is needed at the pole, when the direction of the wave vector exactly coincides with the polar axis, or $\boldsymbol{\alpha} = \pm \boldsymbol{n}$. We consider half a space, taking into account the Hermitian symmetry, so that we focus on the vicinity of $\boldsymbol{\alpha} = \boldsymbol{n}$. For instance, the Craya frame is replaced by the Cartesian frame at this point, or

$$e_i^{(1)} = \delta_{i1}, e_i^{(2)} = \delta_{i2}, e_i^{(3)} = n_i = \delta_{i3}.$$

The spectral tensor $\hat{R}_{ij}$ again reduces to four non-zero components because of incompressibility, $\hat{R}_{ij}(k, \boldsymbol{n})n_j = \hat{R}_{ij}(k, \boldsymbol{n})n_i = 0$, say $\hat{R}_{\alpha\beta}(k, \boldsymbol{n})$, with Greek indices restricted to $1, 2$.

Accordingly, it is possible to work with only 3 real quantities for its symmetric part (discarding helicity), $\hat{R}_{11}$ $\hat{R}_{22}$, $\frac{\hat{R}_{12}+\hat{R}_{21}}{2}$, or equivalently with $\mathcal{E}(k, \boldsymbol{n}) = \frac{1}{2}(\hat{R}_{11} + \hat{R}_{22})$ (no polar specificity), and with

$$\Psi(k) = \frac{1}{2}\left(\hat{R}_{22} - \hat{R}_{11} + \imath\left(\hat{R}_{12} + \hat{R}_{21}\right)\right), \tag{F.13}$$

as the polar surrogate of Z.

Eq. (F.33) is derived as follows.

$$N_i^* N_j^* \Psi_{ij}(\boldsymbol{k}) = N_3^{*2}\Psi_{33} + N_\alpha^* N_\beta^* \Psi_{\alpha\beta},$$

only assuming that Ψ_{ij} is symmetric with $\Psi_{\alpha 3} = 0$, and using

$$N_\alpha^* N_\beta^* \Psi_{\alpha\beta} = -\frac{1}{2} N_3^{*2} (\Psi_{11} + \Psi_{22}) +$$

$$+\frac{1}{4}(N_2^* - \imath N_1^*)^2 (\Psi_{22} - \Psi_{11} + 2\imath\Psi_{12}) + \frac{1}{4}(N_2^* + \imath N_1^*)^2 (\Psi_{22} - \Psi_{11} - 2\imath\Psi_{12}),$$

with $N_3^2 = \sin^2\theta$, $N_2^* - \imath N_1^* = \imath(1 + \cos\theta)\exp(\imath\phi)$, and $N_2^* + \imath N_1^* = -\imath(1 - \cos\theta)\exp(-\imath\phi)$.

Looking at the toroidal mode defined from Eq. (F.6), its counterpart in Fourier space is no longer purely algebraic. A spectral surrogate of Eq. (F.6) is

$$\boldsymbol{u}h^{(tor)}(\boldsymbol{k}) = \boldsymbol{k} \times \left(\frac{\partial s'^{(tor+)}(\boldsymbol{k})}{\partial \boldsymbol{k}} \right). \tag{F.14}$$

More precisely, if the (new) toroidal mode is expanded as in Eq. (F.7) (Rieutord, 1987), the equation (F.9), first in physical space, then in Fourier space, is directly useful.

F.1.4 New toroidal-poloidal decomposition of the velocity field in Fourier space and VSH expansion

The simplified toroidal-poloidal decomposition by Riley *et al.* (1981) was introduced as a Helmholtz decomposition restricted to the horizontal field ($\boldsymbol{u}_\perp \perp \boldsymbol{n}$), with

$$\boldsymbol{u}_\perp = \boldsymbol{\nabla}_\perp \times (s\boldsymbol{n}) + \boldsymbol{\nabla}_\perp (d\boldsymbol{n}),$$

in which $\boldsymbol{\nabla}_\perp$ is restricted to horizontal ($\boldsymbol{x} \perp \boldsymbol{n}$) coordinates but not the surrogates of solenoidal potential $s(\boldsymbol{x})$ and dilatational potential $d(\boldsymbol{x})$. Taking the divergence of the whole (3D-3C) velocity field $\boldsymbol{u}(\boldsymbol{x})$, one finds

$$\nabla_\perp^2 d + \frac{\partial u_3}{\partial x_3} = 0$$

for solenoidal (divergence-free) property. One can easily recover the Eq. (F.5) from both previous equations, so that

$$\boldsymbol{u}(\boldsymbol{x}) = \boldsymbol{\nabla} \times (s\boldsymbol{n}) + \boldsymbol{\nabla} \times (\boldsymbol{\nabla} \times (\boldsymbol{n}d)),$$

using $\boldsymbol{\nabla} \times (\boldsymbol{\nabla w}) = -\nabla^2 \boldsymbol{w} + \boldsymbol{\nabla}(\boldsymbol{\nabla} \cdot \boldsymbol{w})$.

In Rieutord (1987), the vector field is expanded as

$$\boldsymbol{u}(\boldsymbol{r}) = \sum_{n=0}^{N} \sum_{m=-n}^{n} u_n^m(r) \underbrace{Y_n^m \boldsymbol{\alpha}}_{\boldsymbol{R}_n^m} + v_n^m(r) \underbrace{\boldsymbol{\nabla} Y_n^m}_{\boldsymbol{S}_n^m} + w_n^m(r) \underbrace{\boldsymbol{\nabla} \times (Y_n^m \boldsymbol{\alpha})}_{\boldsymbol{T}_n^m}, \tag{F.15}$$

by means of the normalized SSH Y_n^m. The solenoidal property is not completely explicit. For instance, using

$$\frac{\partial}{\partial r_n} = \boldsymbol{\alpha}_n \frac{\partial}{\partial r} + \frac{1}{k} e_n^{(2)} \frac{\partial}{\partial \theta} - \frac{1}{k \sin\theta} e_n^{(1)} \frac{\partial}{\partial \phi},$$

one finds

$$\boldsymbol{\nabla} \cdot (a(r)\boldsymbol{w}(\theta, \phi)) = a(r)\boldsymbol{\nabla} \cdot \boldsymbol{w} + a'(r)\boldsymbol{\alpha} \cdot \boldsymbol{w}$$

and

$$\boldsymbol{\nabla} \times (a(r)\boldsymbol{w}(\theta,\phi)) = a(r)\boldsymbol{\nabla} \times \boldsymbol{w} + a'(r)\boldsymbol{\alpha} \times \boldsymbol{w}.$$

A more explicit toroidal-poloidal (solenoidal of course) relationship may be inferred from Eq. (F.15) as

$$\boldsymbol{u}(\boldsymbol{r}) = \boldsymbol{\nabla} \times \left(s^{(tor+)}(\boldsymbol{r})\boldsymbol{r}\right) + \boldsymbol{\nabla} \times \left(\boldsymbol{\nabla} \times \left(s^{(pol+)}(\boldsymbol{r})\boldsymbol{r}\right)\right). \tag{F.16}$$

In addition to its explicit toroidal-poloidal property, similarly as Eq. (F.5), we prefer replacing the unit vector $\boldsymbol{\alpha}$ by $\boldsymbol{r}$, with a slight modification of the potentials, in order to allow a simpler expression in 3D Fourier space, as follows.

We can move to the counterpart of the velocity as

$$\boldsymbol{u}(\boldsymbol{k}) = \boldsymbol{\alpha} \times \left(k\frac{\partial}{\partial \boldsymbol{k}}\left(s^{(tor)f}(\boldsymbol{k})\right)\right) + \boldsymbol{\alpha} \times \left(\boldsymbol{\alpha} \times \left(k\frac{\partial}{\partial \boldsymbol{k}}\left(s^{(pol)f}(\boldsymbol{k})\right)\right)\right), \tag{F.17}$$

and a classical SSH decomposition holds, with

$$s^{(tor)f}(\boldsymbol{k}) = \sum_{n=0}^{N}\sum_{m=-n}^{n} t_n^m(k)Y_n^m(\theta_k,\phi_k), \quad s^{(pol)f}(\boldsymbol{k}) = \sum_{n=0}^{N}\sum_{m=-n}^{n} p_n^m(k)Y_n^m(\theta_k,\phi_k). \tag{F.18}$$

The gradient of the new potential terms is given by

$$\partial_p = (t_n^m)'(k)Y_n^m\alpha_p + t_n^m(k)\partial_p Y_n^m,$$

and the first term is null in Eq. (F.17). From

$$\boldsymbol{\alpha} \times (k\boldsymbol{\nabla} Y_n^m) = -\boldsymbol{e}^{(1)}\left(Y_n^m\right)_{,\theta} + \frac{k}{\sin\theta}\boldsymbol{e}^{(2)}\left(Y_n^m\right)_{,\phi},$$

with obvious simplified notations for derivatives with respect to polar and azimutal angles, and

$$\boldsymbol{\alpha} \times (\boldsymbol{\alpha}\,(\times\,(k\boldsymbol{\nabla} Y_n^m))) = -\boldsymbol{e}^{(2)}\left(Y_n^m\right)_{,\theta} - \frac{1}{\sin\theta}\boldsymbol{e}^{(1)}\left(Y_n^m\right)_{,\phi},$$

one has

$$u^{(1)} = \sum_{n=0}^{N}\sum_{m=-n}^{n} t_n^m(k)\left(Y_n^m\right)_{,\theta} + \frac{1}{\sin\theta_k}p_n^m(k)\left(Y_n^m\right)_{,\phi} \tag{F.19}$$

and

$$u^{(2)} = \sum_{n=0}^{N}\sum_{m=-n}^{n} t_n^m(k)\frac{1}{\sin\theta_k}\left(Y_n^m\right)_{,\phi} - p_n^m(k)\left(Y_n^m\right)_{,\theta}. \tag{F.20}$$

Angular derivatives of the SSH modes are

$$\left(Y_n^m\right)_{,\phi} = \imath m Y_n^m, \quad \left(Y_n^m\right)_{,\theta} = \left(P_n^m\right)'(\theta_k)\exp(\imath m\phi_k).$$

Since the Y_n^m are eigenfunctions of the Laplacian operator, they satisfy

$$\left(Y_n^m\right)_{,\theta^2} + \cot\theta_k \left(Y_n^m\right)_{,\theta} - \frac{m^2}{\sin^2\theta_k} Y_n^m + n(n+1)Y_n^m = 0, \tag{F.21}$$

(e.g. from Rieutord, 1987). One recovers

$$k^2\nabla^2 Y_n^m = \left(Y_n^m\right)_{,\theta^2} + \cot\theta_k \left(Y_n^m\right)_{,\theta} + \frac{1}{\sin^2\theta_k}\left(Y_n^m\right)_{,\phi^2}, \tag{F.22}$$

using Eq. (F.9) and $\boldsymbol{e}^{(1)} \cdot \frac{\partial e^{(2)}}{\partial \phi_k} = -\cos\theta_k$.

In terms of helical modes, is found

$$\begin{aligned} \xi_+(\boldsymbol{k}) &= \frac{1}{2}\boldsymbol{u}h\cdot\boldsymbol{N}^* = \frac{1}{2}\left(u^{(2)} + \imath u^{(1)}\right) = \\ &= -\frac{1}{2}\sum_{n=0}^{N}\sum_{m=-n}^{n}\left(p_n^m - \imath t_n^m\right)\left(\left(Y_n^m\right)_{,\theta} - \imath\frac{1}{\sin\theta_k}\left(Y_n^m\right)_{,\phi}\right) \end{aligned} \tag{F.23}$$

and

$$\begin{aligned} \xi_-(\boldsymbol{k}) &= \frac{1}{2}\boldsymbol{u}h\cdot\boldsymbol{N} = \frac{1}{2}\left(u^{(2)} - \imath u^{(1)}\right) = \\ &= -\frac{1}{2}\sum_{n=0}^{N}\sum_{m=-n}^{n}\left(p_n^m + \imath t_n^m\right)\left(\left(Y_n^m\right)_{,\theta} + \imath\frac{1}{\sin\theta_k}\left(Y_n^m\right)_{,\phi}\right). \end{aligned} \tag{F.24}$$

F.2 Application to the two-point second-order velocity tensor in HAT

In arbitrary incompressible HAT, the spectral tensor $\hat{R}_{ij}(\boldsymbol{k})$ is the 3D Fourier transform of the two-point second-order correlation tensor

$$R_{ij}(\boldsymbol{r}) = \langle u_i(\boldsymbol{x})u_j(\boldsymbol{x}+\boldsymbol{r})\rangle. \tag{F.25}$$

Its general form calls into play four contributions

$$\hat{R}_{ij}(\boldsymbol{k}) = \frac{E(k)}{4\pi k^2}P_{ij}(\boldsymbol{\alpha}) + \hat{R}_{ij}^{(dir)}(\boldsymbol{k}) + \hat{R}^{(pol)}(\boldsymbol{k}) + \imath\hat{R}_{ij}^{(hel)}(\boldsymbol{k}), \quad P_{ij}(\boldsymbol{\alpha}) = \delta_{ij} - \alpha_i\alpha_j, \tag{F.26}$$

in which the first one holds for 3D isotropy with mirror symmetry (HIT), whereas the three other ones denote directional anisotropy, polarization anisotropy, and contribution from helicity, respectively. The relationship (F.26) involves two scalars (energy and helicity spectra) and one complex-valued pseudo-scalar Z (polarization anisotropy). The energy spectrum is related to the trace, or $\mathcal{E} = (1/2)\hat{R}_{ii}$, the helicity spectrum $k\mathcal{H}(\boldsymbol{k})$ is related to the purely imaginary and antisymmetric part of $\hat{R}_{ij}$. Last not least, the real and symmetric, deviatoric contribution from polarization, $R_{ij}^{(pol)}$ is much less known: It is generated by Z, $\hat{R}_{ij} = \Re(ZN_iN_j)$, using the helical modes, or directly extracted from the spectral tensor in Cartesian coordinates, from

$$\hat{R}_{ij}^{(pol)}(\boldsymbol{k}) = \frac{1}{2}\left(P_{im}P_{jn} + P_{in}P_{jm} - P_{ij}P_{mn}\right)\hat{R}_{mn}(\boldsymbol{k}). \tag{F.27}$$

Of course, the latter equation, that also corresponds to $Z(\boldsymbol{k}) = (1/2)\hat{R}_{mn}N_m^*N_n^*$, is tautological. Our goal is to replace $\hat{R}_{mm}$ in the latter equations by a simpler tensor, to which classical or modified SH expansions may apply.

F.2.1 SSH decomposition of the anisotropic energy and helicity spectra

A SO^3-type expansion holds for the scalar $\mathcal{E}$, as

$$\mathcal{E}(\boldsymbol{k}) = \frac{E}{4\pi k^2}\left(1 + H_{mn}^{2(dir)}(k)\alpha_m\alpha_n + H_{mnpq}^{4(dir)}(k)\alpha_m\alpha_n\alpha_p\alpha_q + \cdots\right). \tag{F.28}$$

A very useful identity is

$$H_{ij}^{2(dir)} = -15H_{ij}^{(dir)}. \tag{F.29}$$

Nevertheless, it is difficult to extend a practical expansion beyond the degree 2 (degree 4 by Rubinstein *et al.*, 2015; Briard *et al.*, 2017), as we have already discussed for SSH.

Accordingly, the classical expansion in terms of scalar spherical harmonics is much more practical, especially when the degree increases.

$$\mathcal{E}(\boldsymbol{k}) = \frac{E}{4\pi k^2}\left(1 + \sum_{n=1}^{N}\sum_{m=-2n}^{2n} e_{2n}^m(k)Y_{2n}^m(\theta_k,\phi_k)\right). \tag{F.30}$$

With respect to Eq. (F.1), only even degrees are relevant, from the Hermitian symmetry restricted to a purely real term.

In contrast with the expansion (F.28) in terms of tensors, the properties of orthogonality are obvious. The basis depends on the choice of the polar axis, but not the degree, so that at any given degree, there are simple linear relationships to pass from $Y_n^m(\theta_k,\phi_k)$ to $Y_n^{m'}(\theta_k',\phi_k')$ from a system of polar-spherical coordinates to an other one.

Note that the number of degrees of freedom is recovered from the tensorial decomposition to the scalar spherical one: at the degree 2, there are five $e_2^m(k)$ descriptors, with $m = -2,-1,0,1,2$, and five independent components for the symmetric traceless tensor $H_{ij}^{(dir)}$.

Even if physical data for anisotropic helicity spectrum are missing in HAT, a SSH decomposition can be proposed, similarly to to (F.28) and (F.30) but with additional, purely imaginary, terms of odd degree.

F.2.2 Possible forms of the polarization pseudo-scalar Z

A general expansion can be proposed as

$$Z(\boldsymbol{k}) = \frac{1}{2}\frac{E(k)}{4\pi k^2}\left(H^{2(pol)}_{ij}(k) + \imath H^{3(pol)}_{ijm}(k)\alpha_m + H^{4(pol)}_{ijmn}\alpha_m\alpha_n + \cdots\right) N_i^*(\boldsymbol{\alpha})N_j^*(\boldsymbol{\alpha}). \quad \text{(F.31)}$$

Note that the terms with odd degree yield imaginary contribution from generating k-modulus-tensors. As for the energy spectrum, the identity

$$H^{2(pol)}_{ij}(k) = 5H^{(pol)}_{ij}(k), \quad \text{(F.32)}$$

holds, in which $2E(k)H^{(pol)}_{ij}(k)$ is the spherical integral of $\hat{R}^{(pol)}_{ij}(\boldsymbol{k})$. In addition, terms of degree 3 and 4 were investigated by Briard *et al.* (2017) but without practical and systematic way to reach higher degrees (see also Rubinstein *et al.*, 2015).

F.2.2.1 Particular decomposition accounting for the polar value

Of course, the SSH expansion cannot be applied directly to Z. Setting aside a possible direct application of VSH, in next subsection,a simpler method is first proposed. Its goal is to solve, as far as possible, the problem of special definition, or multiple definition, of a vector field in the Craya-Herring frame of reference, that implies a similar problem for Z.

For this purpose one recovers the decomposition by Cambon *et al.* (1985) as

$$Z(\boldsymbol{k}) = \sin^2\theta_k \tilde{Z}(\boldsymbol{k}) - \left(\frac{1+\cos\theta_k}{2}\right)^2 \exp(2\imath\phi_k)\Psi(k) - \left(\frac{1-\cos\theta_k}{2}\right)^2 \exp(-2\imath\phi_k)\Psi^*(k), \quad \text{(F.33)}$$

in which Ψ derives from the value of $\hat{R}_{ij}(k,\boldsymbol{n})$ exactly at the pole $\boldsymbol{\alpha} = \boldsymbol{n}$:

$$\Psi = \frac{1}{2}\left(\hat{R}_{22} - \hat{R}_{11} + \imath\left(\hat{R}_{12} + \hat{R}_{21}\right)\right). \quad \text{(F.34)}$$

This equation derives from the calculation of $(1/2)N_i^*N_j^*\Psi_{ij}(\boldsymbol{k})$: The choice $\Psi_{ij}(\boldsymbol{k}) = \hat{R}_{ij}(k,\boldsymbol{n}) + \sin^2\theta_k\tilde{\Psi}_{ij}(\boldsymbol{k})$ yields Eq. (F.33). This equation expresses explicitly the *multi-definition* of Z at the exact pole, with $Z \to -\exp(2\imath\phi_k)\Psi$. Accordingly, Ψ in Eq. (F.33) and (F.34), is the continuous limit of Z at $\phi_k = \pi/2$, but this is not the case in following any other meridian line (fixed ϕ_k) when converging towards the pole. In the whole spectral domain, this equation can be considered as exact provided that $\hat{R}_{ij}(\boldsymbol{k}) - \hat{R}_{ij}(k, \boldsymbol{n})$ behaves as $\sin^2\theta_k$. The particular axisymmetric case corresponds to $\Psi = 0$, $\tilde{Z} = \tilde{Z}(k, \theta_k)$.

Even though Z cannot be expanded in terms of Y_n^m, Eq. (F.33) suggests to transfer the decomposition in terms of scalar spherical harmonics from Z to $\tilde{Z}$, and preliminary results were very encouraging in Cambon *et al.* (1985). In this case, Ψ gives the polarization of the spectral tensor exactly at the pole, and a correct convergence to this polar value is ensured, with

$$\tilde{Z} = \sum_{n=0}^{N} \sum_{m=n}^{n} z_n^m(k) Y_n^m(\theta_k, \phi_k),$$

with both even and odd degrees. Coefficients with odd degree are imaginary.

As another good property, Eq. (F.33) and the latter are consistent at the degree 2 with MCS, or

$$Z(\boldsymbol{k}, t) = \frac{5}{2} N_i^*(\boldsymbol{\alpha}) N_j^*(\boldsymbol{\alpha}) H_{ij}^{(pol)}(k, t),$$

with $\Psi(k) = \frac{5}{2}(H_{22}^{(pol)} - H_{11}^{(pol} + 2\imath H_{12}^{(pol)})$ and $\tilde{Z}(k) = \frac{15}{4} H_{33}^{(pol)}$.

F.2.2.2 Direct application of VSH modes

A general decomposition of Z follows from Eq (F.17) for the velocity field, with Eq. (F.23) and Eq. (F.1.4). A simple product of expansions yields

$$Z(\boldsymbol{k}) = \frac{1}{2} \sum_{n=0}^{N} \sum_{m=-n}^{n} \sum_{n'=0}^{N} \sum_{m'=-n'}^{n'} \langle (p_n^m - \imath t_n^m) \left(p_{n'}^{m'} - \imath t_{n'}^{m'} \right) \rangle;$$

$$\cdot \left((Y_n^m)_{,\theta} - \imath \frac{1}{\sin\theta_k} (Y_n^m)_{,\phi} \right) \left(\left(Y_{n'}^{-m'} \right)_{,\theta} - \imath \frac{1}{\sin\theta_k} \left(Y_{n'}^{-m'} \right)_{,\phi} \right).$$

At least the degree 3 and the degree 4 merit a particular investigation. The degree 3 expansion corresponds to $n = 2,\ n' = 1,\ n = 1, n' = 2$. The degree 4 should involve $n = 1, n' = 3,\ n = 2, n' = 2,\ n = 3, n' = 1.$.

F.3 Spherical harmonics table in real form

For degree 2:

$$\begin{aligned}
Y_{2,-2} &= \frac{1}{4}\sqrt{\frac{15}{\pi}}\sin^2\theta\sin 2\varphi,\\
Y_{2,-1} &= \frac{1}{2}\sqrt{\frac{15}{\pi}}\sin\theta\cos\theta\sin\varphi,\\
Y_{2,0} &= \frac{1}{4}\sqrt{\frac{5}{\pi}}(3\cos^2\theta - 1),\\
Y_{2,1} &= \frac{1}{2}\sqrt{\frac{15}{\pi}}\sin\theta\cos\theta\cos\varphi,\\
Y_{2,2} &= \frac{1}{4}\sqrt{\frac{15}{\pi}}\sin^2\theta\cos\varphi.
\end{aligned} \tag{F.35}$$

For degree 4:

$$\begin{aligned}
Y_{4,-4} &= \frac{3}{16}\sqrt{\frac{35}{\pi}}\sin^4\theta\sin 4\varphi,\\
Y_{4,-3} &= \frac{3}{4}\sqrt{\frac{35}{2\pi}}\sin^3\theta\cos\theta\sin 3\varphi,\\
Y_{4,-2} &= \frac{3}{8}\sqrt{\frac{5}{\pi}}\sin^2\theta(7\cos^2\theta - 1)\sin 2\varphi,\\
Y_{4,-1} &= \frac{3}{4}\sqrt{\frac{5}{2\pi}}\sin\theta\cos\theta(7\cos^2\theta - 3)\sin\varphi,\\
Y_{4,0} &= \frac{3}{16}\sqrt{\frac{1}{\pi}}(35\cos^4\theta - 30\cos^2\theta + 3),\\
Y_{4,1} &= \frac{3}{4}\sqrt{\frac{5}{2\pi}}\sin\theta\cos\theta(7\cos^2\theta - 3)\cos\varphi,\\
Y_{4,2} &= \frac{3}{8}\sqrt{\frac{5}{\pi}}\sin^2\theta(7\cos^2\theta - 1)\cos 2\varphi,\\
Y_{4,3} &= \frac{3}{4}\sqrt{\frac{35}{2\pi}}\sin^3\theta\cos\theta\cos 3\varphi,\\
Y_{4,4} &= \frac{3}{16}\sqrt{\frac{35}{\pi}}\sin^4\theta\cos 4\varphi.
\end{aligned} \tag{F.36}$$

For degree 6:

$$
\begin{aligned}
Y_{6,-6} &= \frac{1}{32}\sqrt{\frac{3003}{2\pi}}\sin^6\theta\sin 6\varphi,\\
Y_{6,-5} &= \frac{3}{16}\sqrt{\frac{1001}{2\pi}}\sin^5\theta\cos\theta\sin 5\varphi,\\
Y_{6,-4} &= \frac{3}{32}\sqrt{\frac{91}{\pi}}\sin^4\theta(11\cos^2\theta-1)\sin 4\varphi,\\
Y_{6,-3} &= \frac{1}{16}\sqrt{\frac{1365}{2\pi}}\sin^3\theta\cos\theta(11\cos^2\theta-3)\sin 3\varphi,\\
Y_{6,-2} &= \frac{1}{32}\sqrt{\frac{1365}{2\pi}}\sin^2\theta(33\cos^4\theta-18\cos^2\theta+1)\sin 2\varphi,\\
Y_{6,-1} &= \frac{1}{16}\sqrt{\frac{273}{\pi}}\sin\theta\cos\theta(33\cos^4\theta-30\cos^2\theta+5)\sin\varphi,\\
Y_{6,0} &= \frac{1}{32}\sqrt{\frac{13}{\pi}}(231\cos^6\theta-315\cos^4\theta+105\cos^2\theta-5),\\
Y_{6,1} &= \frac{1}{16}\sqrt{\frac{273}{\pi}}\sin\theta\cos\theta(33\cos^4\theta-30\cos^2\theta+5)\cos\varphi,\\
Y_{6,2} &= \frac{1}{32}\sqrt{\frac{1365}{2\pi}}\sin^2\theta(33\cos^4\theta-18\cos^2\theta+1)\cos 2\varphi,\\
Y_{6,3} &= \frac{1}{16}\sqrt{\frac{1365}{2\pi}}\sin^3\theta\cos\theta(11\cos^2\theta-3)\cos 3\varphi,\\
Y_{6,4} &= \frac{3}{32}\sqrt{\frac{91}{\pi}}\sin^4\theta(11\cos^2\theta-1)\cos 4\varphi,\\
Y_{6,5} &= \frac{3}{16}\sqrt{\frac{1001}{2\pi}}\sin^5\theta\cos\theta\cos 5\varphi,\\
Y_{6,6} &= \frac{1}{32}\sqrt{\frac{3003}{2\pi}}\sin^6\theta\cos 6\varphi.
\end{aligned}
\tag{F.37}
$$

For degree 8:

$$
\begin{aligned}
Y_{8,-8} &= \frac{3}{256}\sqrt{\frac{12155}{\pi}}\sin^8\theta\sin 8\varphi,\\
Y_{8,-7} &= \frac{3}{64}\sqrt{\frac{12155}{\pi}}\sin^7\theta\cos\theta\sin 7\varphi,\\
Y_{8,-6} &= \frac{1}{64}\sqrt{\frac{7293}{2\pi}}\sin^6\theta(15\cos^2\theta-1)\sin 6\varphi,\\
Y_{8,-5} &= \frac{3}{64}\sqrt{\frac{17017}{\pi}}\sin^5\theta\cos\theta(5\cos^2\theta-1)\sin 5\varphi,\\
Y_{8,-4} &= \frac{3}{128}\sqrt{\frac{1309}{\pi}}\sin^4\theta(65\cos^4\theta-26\cos^2\theta+1)\sin 4\varphi,\\
Y_{8,-3} &= \frac{1}{64}\sqrt{\frac{19635}{\pi}}\sin^3\theta\cos\theta(39\cos^4\theta-26\cos^2\theta+3)\sin 3\varphi,\\
Y_{8,-2} &= \frac{3}{64}\sqrt{\frac{595}{2\pi}}\sin^2\theta(143\cos^6\theta-143\cos^4\theta+33\cos^2\theta-1)\sin 2\varphi,\\
Y_{8,-1} &= \frac{3}{64}\sqrt{\frac{17}{\pi}}\sin\theta\cos\theta(715\cos^6\theta-1001\cos^4\theta+385\cos^2\theta-35)\sin\varphi,\\
Y_{8,0} &= \frac{1}{256}\sqrt{\frac{17}{\pi}}(6435\cos^8\theta-12012\cos^6\theta+6930\cos^4\theta-1260\cos^2\theta+35), \qquad \text{(F.38)}\\
Y_{8,1} &= \frac{3}{64}\sqrt{\frac{17}{\pi}}\sin\theta\cos\theta(715\cos^6\theta-1001\cos^4\theta+385\cos^2\theta-35)\cos\varphi,\\
Y_{8,2} &= \frac{3}{64}\sqrt{\frac{595}{2\pi}}\sin^2\theta(143\cos^6\theta-143\cos^4\theta+33\cos^2\theta-1)\cos 2\varphi,\\
Y_{8,3} &= \frac{1}{64}\sqrt{\frac{19635}{\pi}}\sin^3\theta\cos\theta(39\cos^4\theta-26\cos^2\theta+3)\cos 3\varphi,\\
Y_{8,4} &= \frac{3}{128}\sqrt{\frac{1309}{\pi}}\sin^4\theta(65\cos^4\theta-26\cos^2\theta+1)\cos 4\varphi,\\
Y_{8,5} &= \frac{3}{64}\sqrt{\frac{17017}{\pi}}\sin^5\theta\cos\theta(5\cos^2\theta-1)\cos 5\varphi,\\
Y_{8,6} &= \frac{1}{64}\sqrt{\frac{7293}{2\pi}}\sin^6\theta(15\cos^2\theta-1)\cos 6\varphi,\\
Y_{8,7} &= \frac{3}{64}\sqrt{\frac{12155}{\pi}}\sin^7\theta\cos\theta\cos 7\varphi,\\
Y_{8,8} &= \frac{3}{256}\sqrt{\frac{12155}{\pi}}\sin^8\theta\cos 8\varphi.
\end{aligned}
$$

Appendix G

LRR model with consideration of the Coriolis effects

G.1 LRR for shear flow in HAT

In HAT, the advection term and flux terms in the evolution equation for the Reynolds Stress tensor (1.64) vanish for homogeneity assumption, so that one can find:

$$\frac{\mathrm{d}\mathcal{R}_{ij}}{\mathrm{d}t} = \mathcal{P}_{ij} + \Pi_{ij} - \varepsilon_{ij} \,, \tag{G.1}$$

where the production term $\mathcal{P}_{ij} = -A_{ik}\mathcal{R}_{kj} - A_{jk}\mathcal{R}_{ki}$ is the only closed term. In this context, the equation for pressure is given by

$$\nabla^2 p = -2A_{ij}\frac{\partial u_j}{\partial x_i} - \frac{\partial(u_i u_j)}{\partial x_i x_j} \,. \tag{G.2}$$

The solution for this Poisson equation can be expressed as an integral over the whole domain based on a Green's function, with both linear and nonlinear contributions from fluctuations. Accordingly, we divide the solution of p into the 'rapid' part and the 'slow' part with

$$\nabla^2 p^{(\mathrm{r})} = -2A_{ij}\frac{\partial u_j}{\partial x_i} \,, \quad \nabla^2 p^{(\mathrm{s})} = -\frac{\partial(u_i u_j)}{\partial x_i x_j} \,. \tag{G.3}$$

Therefore, the pressure-strain correlation Π_{ij} can be divided into the 'rapid' part and the 'slow' part correspondingly, as:

$$\Pi^{(\mathrm{r})}(\boldsymbol{x}) = \frac{1}{2\pi}\iiint \frac{1}{|\boldsymbol{y}-\boldsymbol{x}|} A_{mn} \langle \frac{\partial u_n(\boldsymbol{y})}{\partial y_m}\left(\frac{\partial u_i(\boldsymbol{x})}{\partial x_j} + \frac{\partial u_j(\boldsymbol{x})}{\partial x_i}\right)\rangle \, \mathrm{d}^3\boldsymbol{y} \,, \tag{G.4}$$

$$\Pi^{(\mathrm{s})}(\boldsymbol{x}) = \frac{1}{4\pi}\iiint \frac{1}{|\boldsymbol{y}-\boldsymbol{x}|} \langle \frac{\partial^2 u_m(\boldsymbol{y}) u_n(\boldsymbol{y})}{\partial y_m \partial y_n}\left(\frac{\partial u_i(\boldsymbol{x})}{\partial x_j} + \frac{\partial u_j(\boldsymbol{x})}{\partial x_i}\right)\rangle \, \mathrm{d}^3\boldsymbol{y} \,. \tag{G.5}$$

$\Pi_{ij}^{(\mathrm{s})}$ can be modelled with Rotta (1951*a*), as an isotropic function of b_{ij}

$$\Pi_{ij}^{(\mathrm{r})} = -2C_1 \varepsilon b_{ij} \,, \tag{G.6}$$

with the tuned constant C_1.

The 'slow' pressure-strain correlation term can be written as:

$$\Pi_{ij}^{(\mathrm{r})} = \frac{A_{mn}}{2\pi} \left(\iiint \frac{1}{r} \frac{\partial^2 R_{in}(\boldsymbol{r})}{\partial r_m \partial r_j} \,\mathrm{d}^3\boldsymbol{r} + \iiint \frac{1}{r} \frac{\partial^2 R_{jn}(\boldsymbol{r})}{\partial r_m \partial r_i} \,\mathrm{d}^3\boldsymbol{r} \right) . \tag{G.7}$$

Let

$$M_{ijpq} = \frac{1}{4\pi} \iiint \frac{1}{r} \frac{\partial^2 R_{ij}(\boldsymbol{r})}{\partial r_p \partial r_q} \,\mathrm{d}^3\boldsymbol{r} \,, \tag{G.8}$$

Then $\Pi_{ij}^{(\mathrm{r})}$ becomes

$$\Pi_{ij}^{(\mathrm{r})} = 2A_{mn}(M_{inmj} + M_{jnmi}) \,. \tag{G.9}$$

M_{ijpq} is thought to be a tensorial function of $\mathcal{R}_{ij}$ in Launder *et al.* (1975), similarly in Mishra & Girimaji (2017); Sagaut & Cambon (2018), with properties

$$M_{ijpq} = M_{jipq} \,, \quad M_{ijiq} = M_{ijjq} = 0 \,, \quad M_{ijqq} = R_{ij} \,. \tag{G.10}$$

Therefore, an assumed form for M_{ijpq} is obtained as:

$$\begin{aligned} M_{ijpq} =& \frac{1}{2} \Bigg(\frac{4C_2 + 10}{11} \delta_{pq} \mathcal{R}_{ij} - \frac{2 + 3C_2}{11} \left(\delta_{ip}\mathcal{R}_{jq} + \delta_{iq}\mathcal{R}_{jp} + \delta_{jp}\mathcal{R}_{iq} + \delta_{jq}\mathcal{R}_{ip} \right) \\ & + C_2 \delta_{ij} \mathcal{R}_{pq} + \left(-\frac{50C_2 + 4}{55} \delta_{ij}\delta_{pq} + \frac{20C_2 + 6}{55} (\delta_{ip}\delta_{jq} + \delta_{iq}\delta_{jp}) \right) \mathcal{K} \Bigg) \,, \end{aligned} \tag{G.11}$$

with a tuned constant C_2.

The dissipation term can be modelled in the isotopic form $\varepsilon_{ij} = \frac{2}{3}\delta_{ij}\varepsilon$ with:

$$\frac{\mathrm{d}\varepsilon}{\mathrm{d}t} = -C_{1\varepsilon} \frac{A_{ik}\mathcal{R}_{ik}\varepsilon}{\mathcal{K}} - C_{2\varepsilon} \frac{\varepsilon^2}{\mathcal{K}} \,, \tag{G.12}$$

where $C_{1\varepsilon}$ and $C_{2\varepsilon}$ are two tuned constants.

After some algebra, the final equations of LRR can be found as:

$$
\begin{aligned}
\frac{\mathrm{d}\mathcal{R}_{ij}}{\mathrm{d}t} =& -\mathcal{R}_{jk}A_{ik} - \mathcal{R}_{ik}A_{jk} \\
& -2C_1\varepsilon b_{ij} \\
& +2\mathcal{K}\left[\frac{2}{3}\delta_{ij} + \frac{3(3C_2+2)}{11}(b_{jk}S_{ik} + b_{ik}S_{jk} - \frac{2}{3}\delta_{ij}b_{mn}S_{mn}) - \frac{7C_2+10}{11}(b_{ik}W_{jk} + b_{jk}W_{ik})\right] \\
& -\frac{2}{3}\delta_{ij}\varepsilon \\
\frac{\mathrm{d}\varepsilon}{\mathrm{d}t} =& -C_{1\varepsilon}\frac{A_{ik}\mathrm{R}_{ik}\varepsilon}{\mathcal{K}} - C_{2\varepsilon}\frac{\varepsilon^2}{\mathcal{K}} \\
\mathcal{K} =& \frac{1}{2}\mathcal{R}_{ii}\,, \quad b_{ij} = \frac{\mathcal{R}_{ij}}{2\mathcal{K}} - \frac{1}{3}\delta_{ij}\,,
\end{aligned}
\tag{G.13}
$$

with $S_{ij} = \dfrac{A_{ij}+A_{ji}}{2}$, and $W_{ij} = \dfrac{1}{2}\epsilon_{imj}W_m$.

G.2 Consideration of the Coriolis effects

The original LRR did not consider system rotation. Here, we only consider the Coriolis effects on the production term and on the ‘rapid’ pressure-strain correlation term. The incorporation of the Coriolis force is very easy in the production term of RSM equations, and one can find

$$
\mathcal{P}_{ij} = -A_{ik}\mathcal{R}_{kj} - A_{jk}\mathcal{R}_{ki} - 2\Omega_m(\epsilon_{imn}\mathcal{R}_{nj} + \epsilon_{jmn}\mathcal{R}_{ni})\,, \tag{G.14}
$$

which amounts to replacing the vorticity$\boldsymbol{W}$ by $\boldsymbol{W}+4\boldsymbol{\Omega}$ in the production term. The ‘rapid’ part of the solution of pressure turns into

$$
\nabla^2 p^{(\mathrm{r})} = -2A_{ij}\frac{\partial u_j}{\partial x_i} - 2\epsilon_{imn}\Omega_m\frac{\partial u_n}{\partial x_i}\,, \tag{G.15}
$$

when system rotation acts. In the ‘rapid’ pressure-strain rate tensor, this amounts to replacing the vorticity $\boldsymbol{W}$ by the absolute vorticity $\boldsymbol{W}+2\boldsymbol{\Omega}$. Consequently, the final equations can be obtained as:

$$
\begin{aligned}
\frac{\mathrm{d}\mathcal{R}_{ij}}{\mathrm{d}t} =& - \mathcal{R}_{jk}A_{ik} - \mathcal{R}_{ik}A_{jk} - 2\Omega_m(\epsilon_{imn}\mathcal{R}_{nj} + \epsilon_{jmn}\mathcal{R}_{ni}) \\
& - 2C_1\varepsilon b_{ij} \\
& + 2\mathcal{K}\left[\frac{2}{3}\delta_{ij} + \frac{3(3C_2+2)}{11}(b_{jk}S_{ik} + b_{ik}S_{jk} - \frac{2}{3}\delta_{ij}b_{mn}S_{mn}) - \frac{7C_2+10}{11}(b_{ik}W_{jk} + b_{jk}W_{ik})\right] \\
& - \frac{2}{3}\delta_{ij}\varepsilon \\
\frac{\mathrm{d}\varepsilon}{\mathrm{d}t} =& - C_{1\varepsilon}\frac{A_{ik}\mathcal{R}_{ik}\varepsilon}{\mathcal{K}} - C_{2\varepsilon}\frac{\varepsilon^2}{\mathcal{K}} \\
\mathcal{K} =& \frac{1}{2}\mathcal{R}_{ii}\,, \quad b_{ij} = \frac{\mathcal{R}_{ij}}{2\mathcal{K}} - \frac{1}{3}\delta_{ij}\,,
\end{aligned}
\tag{G.16}
$$

with $S_{ij} = \dfrac{A_{ij} + A_{ji}}{2}$, and $W_{ij} = \dfrac{1}{2}\epsilon_{imj}(W_m + 2\Omega_m)$.

Bibliography

André, J. C. & Lesieur, M. 1977 Influence of helicity on the evolution of isotropic turbulence at high Reynolds number. *Journal of Fluid Mechanics* **81**, 187–207. (Cited on page 22.)

Balbus, S. A. & Hawley, J. F. 1998 Instability, turbulence, and enhanced transport in accretion disks. *Reviews of Modern Physics* **70** (1), 1. (Cited on page 11.)

Batchelor, G. & Proudman, I. 1954 The effect of rapid distortion of a fluid in turbulent motion. *The Quarterly Journal of Mechanics and Applied Mathematics* **7** (1), 83–103. (Cited on pages 10, 18 and 157.)

Bellet, F., Godeferd, F., Scott, J. & Cambon, C. 2006 Wave turbulence in rapidly rotating flows. *Journal of Fluid Mechanics* **562**, 83–121. (Cited on pages 38 and 41.)

Bradshaw, P. 1969 The analogy between streamline curvature and buoyancy in turbulent shear flow. *Journal of Fluid Mechanics* **36** (01), 177–191. (Cited on page 28.)

Brethouwer, G. 2005 The effect of rotation on rapidly sheared homogeneous turbulence and passive scalar transport. Linear theory and direct numerical simulation. *Journal of Fluid Mechanics* **542**, 305–342. (Cited on page 29.)

Briard, A. 2017 Modélisation du transport en turbulence homogène. PhD thesis, Paris 6. (Cited on page 49.)

Briard, A., Gréa, B.-J., Mons, V., Cambon, C., Gomez, T. & Sagaut, P. 2018 Advanced spectral anisotropic modelling for shear flows. *Journal of Turbulence* pp. 1–30. (Cited on page 97.)

Briard, A., Iyer, M. & Gomez, T. 2017 Anisotropic spectral modeling for unstably stratified homogeneous turbulence. *Physical Review Fluids* **2** (4), 044604. (Cited on pages 163 and 164.)

Burlot, A., Gréa, B.-J., Godeferd, F. S., Cambon, C. & Griffond, J. 2015 Spectral modelling of high Reynolds number unstably stratified homogeneous turbulence. *Journal of Fluid Mechanics* **765**, 17–44. (Cited on pages 41, 42 and 133.)

Cambon, C. 2001 Turbulence and vortex structures in rotating and stratified flows. *European Journal of Mechanics-B/Fluids* **20** (4), 489–510. (Cited on page 9.)

Cambon, C., Danaila, L., Godeferd, F. S. & Scott, J. F. 2013 Third-order statistics and the dynamics of strongly anisotropic turbulent flows. *Journal of Turbulence* **14** (3), 121–160. (Cited on page 35.)

Cambon, C. & Jacquin, L. 1989 Spectral approach to non-isotropic turbulence subjected to rotation. *Journal of Fluid Mechanics* **202**, 295–317. (Cited on pages 32, 34, 36, 38, 39, 41 and 159.)

Cambon, C., Jeandel, D. & Mathieu, J. 1981 Spectral modelling of homogeneous non-isotropic turbulence. *Journal of Fluid Mechanics* **104**, 247–262. (Cited on pages 45, 48, 97, 131 and 132.)

Cambon, C., Mansour, N. N. & Godeferd, F. S. 1997 Energy transfer in rotating turbulence. *Journal of Fluid Mechanics* **337**, 303–332. (Cited on pages 32 and 34.)

Cambon, C., Mons, V., Gréa, B.-J. & Rubinstein, R. 2017 Anisotropic triadic closures for shear-driven and buoyancy-driven turbulent flows. *Computers & Fluids* **151**, 73–84. (Cited on pages 9 and 22.)

Cambon, C. & Rubinstein, R. 2006 Anisotropic developments for homogeneous shear flows. *Physics of Fluids* **18** (8), 085106. (Cited on pages 42, 48 and 157.)

Cambon, C., Teissèdre, C. & Jeandel, D. 1985 Etude d'effets couplés de rotation et de déformation sur une turbulence homogène. *Journal de Mécanique Théorique et Appliquée* **5**, 629. (Cited on pages 20, 164 and 165.)

Canuto, C., Hussaini, M. Y., Quarteroni, A. & Zang, T. A. 2007 *Spectral methods: Evolution to complex geometries and applications to fluid dynamics*. Springer Science & Business Media. (Cited on pages 58 and 152.)

Canuto, V., Dubovikov, M., Cheng, Y. & Dienstfrey, A. 1996 Dynamical model for turbulence. III. Numerical results. *Physics of Fluids* **8** (2), 599–613. (Cited on page 21.)

Canuto, V. M. & Dubovikov, M. S. 1996*a* A dynamical model for turbulence. I. General formalism. *Physics of Fluids* **8** (2), 571–586. (Cited on page 21.)

Canuto, V. M. & Dubovikov, M. S. 1996*b* A dynamical model for turbulence. II. Shear-driven flows. *Physics of Fluids* **8** (2), 587–598. (Cited on page 21.)

Chandrasekhar, S. 1961 *Hydrodynamic and hydromagnetic stability*. Oxford-Clarendon Press and New York-Oxford Univ. Press. (Cited on page 34.)

Clark, T. T., Kurien, S. & Rubinstein, R. 2018 Generation of anisotropy in turbulent flows subjected to rapid distortion. *Physical Review E* **97** (1), 013112. (Cited on page 157.)

Craik, A. & Criminale, W. 1986 Evolution of wavelike disturbances in shear flows: a class of exact solutions of the Navier-Stokes equations. *Proceedings of the Royal Society A* **406** (1830), 13–26. (Cited on page 10.)

Craya, A. 1957 Contribution à l'analyse de la turbulence associée à des vitesses moyennes. PhD thesis, Université de Grenoble. (Cited on pages 10, 15 and 32.)

Delorme, P. 1985 Simulation numérique de turbulence homogene compressible avec ou sans cisaillement imposé. *these de docteur ingénieur, Université de Poitiers* . (Cited on page 152.)

Dong, C., McWilliams, J. C. & Shchepetkin, A. F. 2007 Island wakes in deep water. *Journal of Physical Oceanography* **37** (4), 962–981. (Cited on page 5.)

Eliasen, E., Machenhauer, B. & Rasmussen, E. 1970 *On a numerical method for integration of the hydrodynamical equations with a spectral representation of the horizontal fields*. Kobenhavns Universitet, Institut for Teoretisk Meteorologi. (Cited on page 151.)

Eringen, A. C. 1976 *Continuum Physics. Vol. Iii: Mixtures and Em Field Theories*. Academic Press. (Cited on page 19.)

Fathali, M., Meyers, J., Rubio, G., Smirnov, S. & Baelmans, M. 2008 Sensitivity analysis of initial condition parameters on the transitional temporal turbulent mixing layer. *Journal of Turbulence* (9), N12. (Cited on page 68.)

Galmiche, M., Hunt, J., Thual, O. & Bonneton, P. 2001 Turbulence-mean field interactions and layer formation in a stratified fluid. *European Journal of Mechanics-B/Fluids* **20** (4), 577–585. (Cited on page 156.)

Gréa, B.-J. 2013 The rapid acceleration model and the growth rate of a turbulent mixing zone induced by Rayleigh-Taylor instability. *Physics of Fluids* **25** (1), 015118. (Cited on pages 9 and 133.)

Hanazaki, H. & Hunt, J. C. R. 2004 Structure of unsteady stably stratified turbulence with mean shear. *Journal of Fluid Mechanics* **507**, 1–42. (Cited on page 18.)

Herring, J. R. 1974 Approach of axisymmetric turbulence to isotropy. *Physics of Fluids* **17** (5), 859–872. (Cited on page 32.)

Hiwatashi, K., Alfredsson, P. H., Tillmark, N. & Nagata, M. 2007 Experimental observations of instabilities in rotating plane Couette flow. *Physics of Fluids* **19** (4), 048103. (Cited on page 5.)

Johnston, J. P., Halleen, R. M. & Lezius, D. K. 1972 Effects of spanwise rotation on the structure of two-dimensional fully developed turbulent channel flow. *Journal of Fluid Mechanics* **56** (03), 533–557. (Cited on page 5.)

Kassinos, S. C., Reynolds, W. C. & Rogers, M. M. 2001 One-point turbulence structure tensors. *Journal of Fluid Mechanics* **428**, 213–248. (Cited on pages 13, 38, 87 and 131.)

Kraichnan, R. H. 1959 The structure of isotropic turbulence at very high Reynolds numbers. *Journal of Fluid Mechanics* **5** (4), 497–543. (Cited on page 21.)

Kraichnan, R. H. & Herring, J. R. 1978 A strain-based Lagrangian-history turbulence theory. *Journal of Fluid Mechanics* **88** (2), 355–367. (Cited on page 21.)

Launder, B. E., Reece, G. J. & Rodi, W. 1975 Progress in the development of a Reynolds-stress turbulence closure. *Journal of Fluid Mechanics* **68** (3), 537–566. (Cited on pages 13, 26, 131 and 170.)

Leblanc, S. & Cambon, C. 1998 Effects of the Coriolis force on the stability of Stuart vortices. *Journal of Fluid Mechanics* **356**, 353–379. (Cited on pages 29 and 87.)

Lesur, G. & Longaretti, P. Y. 2005 On the relevance of subcritical hydrodynamic turbulence to accretion disk transport. *Astronomy and Astrophysics* **444**, 25–44. (Cited on pages i, iii, 54, 129 and 152.)

Lighthill, M. J. 1958 *An introduction to Fourier analysis and generalised functions*. Cambridge University Press. (Cited on page 14.)

Linkmann, M., Berera, A. & Goldstraw, E. E. 2017 Reynolds-number dependence of the dimensionless dissipation rate in homogeneous magnetohydrodynamic turbulence. *Physical Review E* **95** (1), 013102. (Cited on page 132.)

Linkmann, M., Berera, A., McKay, M. & Jäger, J. 2016 Helical mode interactions and spectral transfer processes in magnetohydrodynamic turbulence. *Journal of Fluid Mechanics* **791**, 61–96. (Cited on page 132.)

Mathieu, J. & Scott, J. 2000 *An introduction to turbulent flow*. Cambridge University Press. (Cited on page 14.)

Mishra, A. A. & Girimaji, S. S. 2017 Toward approximating non-local dynamics in single-point pressure–strain correlation closures. *Journal of Fluid Mechanics* **811**, 168–188. (Cited on pages 29, 131 and 170.)

Moffatt, H. 1967 The interaction of turbulence with strong wind shear. *Atmospheric Turbulence and Radio Wave Propagation* pp. 139–156. (Cited on page 18.)

Mons, V., Cambon, C. & Sagaut, P. 2016 A spectral model for homogeneous shear-driven anisotropic turbulence in terms of spherically averaged descriptors. *Journal of Fluid Mechanics* **788**, 147–182. (Cited on pages i, ii, iii, iv, 2, 24, 39, 42, 48, 49, 68, 117 and 129.)

Ogura, Y. 1963 A consequence of the zero-fourth-cumulant approximation in the decay of isotropic turbulence. *Journal of Fluid Mechanics* **16** (1), 33–40. (Cited on page 21.)

Orszag, S. A. 1969 Analytical theories of turbulence. *Journal of Fluid Mechanics* **41**, 363–386. (Cited on pages 21, 22 and 151.)

Perret, G., Stegner, A., Farge, M. & Pichon, T. 2006 Cyclone-anticyclone asymmetry of large-scale wakes in the laboratory. *Physics of Fluids* **18** (3), 036603. (Cited on page 5.)

Plunian, F. & Stepanov, R. 2007 A non-local shell model of hydrodynamic and magnetohydrodynamic turbulence. *Journal of Turbulence* **9(8)**, 294. (Cited on page 60.)

Pope, S. B. 2001 Turbulent flows. (Cited on page 68.)

Pouquet, A., Lesieur, M., André, J. C. & Basdevant, C. 1975 Evolution of high Reynolds number two-dimensional turbulence. *Journal of Fluid Mechanics* **72**, 305–319. (Cited on page 22.)

Rieutord, M. 1987 Linear theory of rotating fluids using spherical harmonics part I: Steady flows. *Geophysical & Astrophysical Fluid Dynamics* **39** (3), 163–182. (Cited on pages 157, 160 and 162.)

Riley, J. J., Metcalfe, R. W. & Weissman, M. A. 1981 Direct numerical simulations of homogeneous turbulence in density-stratified fluids. *AIP Conference Proceedings* **76** (1), 79–112. (Cited on pages 156 and 160.)

Rogallo, R. S. 1977 An ILLIAC program for the numerical simulation of homogeneous incompressible turbulence . (Cited on pages 58 and 151.)

Rogallo, R. S. 1981 Numerical experiments in homogeneous turbulence . (Cited on pages i, iii, 54, 129, 151, 152 and 154.)

Rotta, J. 1951*a* Statistische theorie nichthomogener turbulenz. *Zeitschrift für Physik* **129** (6), 547–572. (Cited on page 170.)

Rotta, J. 1951*b* Statistische theorie nichthomogener turbulenz I. *z. Phys.* **129**, 547. (Cited on page 98.)

Rubinstein, R., Kurien, S. & Cambon, C. 2015 Scalar and tensor spherical harmonics expansion of the velocity correlation in homogeneous anisotropic turbulence. *Journal of Turbulence* **16** (11), 1058–1075. (Cited on pages 100, 103, 157, 163 and 164.)

Sagaut, P. & Cambon, C. 2018 *Homogeneous Turbulence Dynamics*, 2nd edn. Springer International Publishing. (Cited on pages 7, 10, 13, 19, 22, 24, 35, 41, 86, 96, 123, 132, 156 and 170.)

Salhi, A. & Cambon, C. 1997 An analysis of rotating shear flow using linear theory and DNS and LES results. *Journal of Fluid Mechanics* **347**, 171–195. (Cited on pages 18 and 20.)

Salhi, A. & Cambon, C. 2010 Stability of rotating stratified shear flow: An analytical study. *Physical Review E* **81** (2), 026302. (Cited on page 18.)

SALHI, A., CAMBON, C. & SPEZIALE, C. 1997 Linear stability analysis of plane quadratic flows in a rotating frame. *Physics of Fluids* **9(8)**, 2300–2309. (Cited on page 29.)

SALHI, A., JACOBITZ, F. G., SCHNEIDER, K. & CAMBON, C. 2014 Nonlinear dynamics and anisotropic structure of rotating sheared turbulence. *Physical Review E* **89** (1), 013020. (Cited on pages 2, 3, 20, 54, 79, 80, 82, 83, 90 and 130.)

SMITH, L. M. & WALEFFE, F. 2002 Generation of slow large scales in forced rotating stratified turbulence. *Journal of Fluid Mechanics* **451**, 145–168. (Cited on page 156.)

SMITS, A. J., MCKEON, B. J. & MARUSIC, I. 2011 High-Reynolds number wall turbulence. *Annual Review of Fluid Mechanics* **43**. (Cited on page 9.)

SPALART, P. R. 2015 Philosophies and fallacies in turbulence modeling. *Progress in Aerospace Sciences* **74**, 1–15. (Cited on page 133.)

VON KÁRMÁN, T. & LIN, C. 1951 On the statistical theory of isotropic turbulence. *Advances in Applied Mechanics* **2**, 1–19. (Cited on page 22.)

WALEFFE, F. 1992 The nature of triad interactions in homogeneous turbulence. *Physics of Fluids A: Fluid Dynamics* **4** (2), 350–363. (Cited on page 159.)

WEINSTOCK, J. 1982 Theory of the pressure–strain rate. Part 2. Diagonal elements. *Journal of Fluid Mechanics* **116**, 1–29. (Cited on pages 24 and 51.)

WEINSTOCK, J. 2013 Analytical theory of homogeneous mean shear turbulence. *Journal of Fluid Mechanics* **727**, 256–281. (Cited on pages ii, iv, 24, 51, 90 and 129.)